

UNIVERSITY OF SOUTHAMPTON

FACULTY OF PHYSICAL SCIENCES AND ENGINEERING

Optoelectronics Research Centre

**Development of paper-based point-of-care
biosensors by laser-based direct-write processes**

by

Peijun He

Thesis submitted for the degree of Doctor of Philosophy

March 2017

UNIVERSITY OF SOUTHAMPTON

ABSTRACT

FACULTY OF PHYSICAL SCIENCES AND ENGINEERING

Optoelectronics Research Centre

Doctor of Philosophy

DEVELOPMENT OF PAPER-BASED POINT-OF-CARE BIOSENSORS BY LASER-BASED DIRECT-WRITE PROCESSES

By Peijun He

The demand for low-cost alternatives to conventional point-of-care (POC) diagnostic tools has led to significant developments in the field of microfluidics in porous materials. Several approaches have already been reported for fabricating fluidic devices in such materials, which include photolithography, inkjet printing, wax printing etc.

In this thesis, a new approach towards the fabrication of paper-based POC diagnostic sensors is proposed, which is a simple laser-based direct-write (LDW) procedure that uses polymerisation of a photopolymer to produce the required fluidic channels in porous substrates. Furthermore, this LDW technique is also further developed and explored for the introduction of a range of additional functionalities in paper-based microfluidic devices. Firstly, programmable flow control is enabled via two fluid delay mechanisms, namely, permeable barriers with variable porosity and impermeable barriers with variable depth. The generated flow delays can span times from minutes to over an hour. Secondly, the same LDW approach is also developed for stacking and sealing of multi-layer substrates, for assembly of backing layers for two-dimensional lateral flow devices (LFDs) and eventually for fabrication of three-dimensional devices.

In addition, we also report an idea of enabling fluidic gating in paper-based devices via triggerable wax barriers. The printed wax barrier acts as triggerable fluidic gates, which can be switched on demand via the application of local heating.

Finally, these LDW fabricated paper-based devices were validated via implementation of various clinical diagnostics and analytical chemistry assays using both artificial samples as well as real human bodily fluids.

Overall, a huge number of advantages have been established with this approach for both device fabrication and enabling additional functionalities. Thus, we believe that this technique could be an ideal choice for fabrication of paper-based microfluidic devices.

Table of Contents

Table of Contents.....	i
List of Tables.....	v
List of Figures.....	vii
Declaration of authorship.....	xv
Acknowledgements	xvii
Abbreviations	xix
Chapter 1: Introduction.....	1
1.1 Motivation.....	1
1.2 Outline of this thesis.....	2
1.3 Main achievements.....	4
Chapter 2: Background.....	7
2.1 Laser direct-write techniques	7
2.2 Light-induced photo-polymerisation	7
2.2.1 Depth of laser-induced polymerisation.....	9
2.3 Paper-based microfluidic sensors.....	11
2.4 Capillary action in porous materials.....	14
Chapter 3: Laser-based patterning for fluidic devices.....	17
3.1 Introduction.....	17
3.2 Experimental work.....	18
3.2.1 Experimental setup.....	18
3.2.2 Experimental method	19
3.2.3 Materials and reagents	20
3.3 Experimental results.....	21
3.3.1 Patterning of cellulose paper	21
3.3.1.1 Patterning with a pulsed laser	21
3.3.1.2 Patterning with c. w. laser	23
3.3.2 Patterning of nitrocellulose membrane	30

Table of Contents

3.3.3	Patterning of other porous materials	35
3.4	Performance improvement and optimisation of the LDW procedure.....	37
3.4.1	Introduction of a galvo scanner	38
3.4.2	Introduction of local deposition procedure	41
3.5	Summary	53
Chapter 4:	Fluidic delay strategies in paper-based devices	55
4.1	Introduction.....	55
4.2	Fluidic delay strategies	56
4.3	Experimental results.....	59
4.3.1	Delay via solid barriers created by a pulsed laser.....	61
4.3.2	Delay via porous barriers created by a c.w. laser.....	64
4.3.2.1	Weight measurements of porous barriers	67
4.3.3	Validation of delay barriers for multiple fluid delivery	69
4.4	Summary	72
Chapter 5:	Three-dimensional structures in paper-based devices.....	73
5.1	Introduction.....	73
5.2	Background.....	74
5.3	Experimental results.....	75
5.3.1	Stacking and sealing of multi-layer papers.....	75
5.3.2	Single-sided polymerisation – for backing a paper-based device.....	78
5.3.3	Single-sided polymerisation – for reduction in the dead-volume of a paper-based device	83
5.3.4	Dual-sided polymerisation – for fabrication of a 3D paper-based device	84
5.4	Summary	88
Chapter 6:	Triggerable fluidic gates in paper-based devices	91
6.1	Introduction.....	91
6.2	Background.....	92
6.3	Fluidic gate strategy	93

6.4	Experimental results	94
6.4.1	Triggering via global heating by a hot plate	94
6.4.2	Triggering via localised heating by a wax pen	95
6.4.3	Triggering via localised heating by a c.w. laser	98
6.4.4	Validation of fluidic gates for implementation of assays	99
6.5	Summary	101
Chapter 7:	Implementation of assays on paper-based devices	103
7.1	Introduction	103
7.2	Enzyme-linked immunosorbent assay (ELISA)	104
7.2.1	Limit of detection	107
7.3	Experimental results	108
7.3.1	Implementation of one step colorimetric assays	108
7.3.2	Implementation of multi-step sandwich ELISA	113
7.3.3	Implementation of automatic multi-step assays	122
7.3.4	Detection of CRP in real human bodily fluids	125
7.4	Summary	127
Chapter 8:	Conclusions and future work	129
8.1	Conclusions	129
8.1.1	LDW patterning for fabrication of paper-based devices	129
8.1.2	Introduction of fluidic delays via LDW approach	130
8.1.3	Fabrication of 3D paper-based device via LDW approach	130
8.1.4	Enabling triggerable fluidic gates in paper-based devices	131
8.1.5	Validation of the fabricated paper-based devices	132
8.2	Future work	132
Appendix A	Laser Fluence Calculation	135
Appendix B	BioDot dispensing system	137
Appendix C	Assay protocols	143
C.1	Assay for the detection of BSA	143
C.2	Assay for the detection of glucose	143

Table of Contents

C.3 Assay for the detection of nitrite	143
C.4 Assay for the detection of TNF- α	144
C.5 Assay for the detection of CRP	144
Appendix D Publications.....	147
D.1 Journal Publications.....	147
D.2 Conference Contributions	147
D.3 Other Publications.....	149
Bibliography	151
Reprint of published journal papers	171

List of Tables

Table 2.1 Summary of reported methods for fabrication of paper-based microfluidic devices..... 14

Table 4.1 Summary of the weight measurements of the paper substrate with polymer lines that were patterned with different laser incident powers at a fixed writing speed of 50 mm/s. The weight numbers in this table were the mean number of three measurements. 69

List of Figures

Figure 2.1 Schematic of a light-induced photo-polymerisation process for a photopolymer mixture of oligomer, monomer, and photoinitiator.....	8
Figure 3.1 Schematic of the LDW process used to form polymerised hydrophobic structures in a paper-based substrate.....	18
Figure 3.2 Step-wise schematic showing the typical paper patterning procedure using the LDW approach.....	20
Figure 3.3 Image showing three sets of parallel polymerised lines that were written with a fixed laser average power of 7 mW at different scan speeds. a) 0.06 mm/s, b) 0.07 mm/s and c) 0.09mm/s.....	22
Figure 3.4 Images showing sets of parallel lines that have been photo-polymerised using a 375 nm c.w. laser under different writing conditions: (a) fixed laser power, variable translation speeds, and (b) fixed translation speed, variable laser powers. Photopolymer used was DeSolite®.....	24
Figure 3.5 Graph showing the widths of the laser-patterned lines for different incident laser powers from the 375 nm source at different scan speeds. Error bars indicate the standard deviation for 5 measurements along each line.....	25
Figure 3.6 Plots showing the relationship between the widths of the polymerised lines using a 405 nm c.w. laser and the different incident laser powers at different scan speeds. Error bars indicate the standard deviation for 5 measurements along each line.....	26
Figure 3.7 Plots show the summary of the line-widths for writing wavelengths of 375 nm and 405 nm, at different incident powers up to a maximum value of 50 mW, but a common writing speed of 6.7 mm/s. Error bars indicate the standard deviation for 5 measurements along each line and lines are a simple guide for the eye.....	26
Figure 3.8 Sets of polymerised lines formed using a 405 nm c.w. laser with different incident powers and two different photopolymers. a) DeSolite® and b) SubG.....	27
Figure 3.9 Graph showing the widths of the laser-patterned lines for different incident laser powers and a scan speed of 10 mm/s. The lines were patterned with a c. w. 405 nm laser and the photopolymers used were DeSolite® and SubG. Error bars indicate the standard deviation for 5 measurements along each line.....	28
Figure 3.10 Microscope images showing two parallel lines written in SubG via LDW using a scan speed of 10 mm/s and an incident power of 10 mW at 405 nm, and having widths of ~50 µm.....	28
Figure 3.11 Camera images of a series of square structures before and after the introduction of ink; a) written in Desolite®; b) written in SubG.....	29
Figure 3.12 Camera images show a) four fluidic channels with different widths formed by barrier lines with a width of ~ 120 µm, b) the ~ 80µm fluidic channel in a) guiding red ink.....	30
Figure 3.13 Images showing two fluidic channels formed by writing parallel lines with two different laser powers of 10 and 5 mW at a speed of 10 mm/s.....	31

List of Figures

Figure 3.14 Plots showing the variations in the widths of the polymerised lines for different laser powers at three different scan speeds.	32
Figure 3.15 a) Image showing a set of fluidic channels formed under different patterning conditions; b) after the introduction of red ink into each channel.	32
Figure 3.16 Photographic images showing a set of parallel fluidic channels having different channel widths: a) before, and b) after the introduction of red ink.	33
Figure 3.17 Photographic image showing a) a series of 5 mm × 5 mm square-shaped wells patterned with different laser powers of 0.3, 0.4, 0.5, 1, 5, and 10 mW at a constant scanning speed of 10 mm/s; b) after the introduction of 3 µL of red ink into each square.	34
Figure 3.18 Images showing a) a series of 5 mm × 5 mm wells patterned with a laser power of 1 mW and a scan speed of 10 mm/s; b) after the introduction of red ink in different volumes of 1-15 µL into each square; c) a surface profiler scan across a polymerised barrier-wall.	35
Figure 3.19 Images showing a set of parallel fluidic channels writing in glass fibre filter with different laser power at a fixed scan speed a) before, and b) after introduction of red ink.	36
Figure 3.20 Images showing a T-shape structure patterned in filament polyester wipe a) before, and b) after the introduction of red ink.	36
Figure 3.21 Images show the results of patterning different porous materials using LDW technique. a) PVDF and b) printing paper (photo-copy paper).	37
Figure 3.22 Schematic of the laser-based direct-write setup with the introduction of a galvo scanner used to form polymerised hydrophobic structures in a porous substrate.	40
Figure 3.23 Image shows ‘THANKS FOR YOUR ATTENTION’ text that was patterned in cellulose filter paper using the galvo scanner with a laser output power of 30 mW at a scan speed of 50 mm/s.	41
Figure 3.24 Photographic images showing a) a triple spiral design patterned in NC via a galvo scanner; b) the introduction of yellow dye into one of the spirals and c) the introduction of red dye into the same spiral, which shows no over contamination.	42
Figure 3.25 Schematic of the modified laser-based direct-write setup with the introduction of local deposition of photopolymer for creating polymerised hydrophobic structures in the porous substrate.	43
Figure 3.26 Schematic of the modified LDW paper-patterning procedure: local deposition of photopolymer followed by photo-polymerisation.	44
Figure 3.27 Microscope image showing two sets of parallel lines that were dispensed on NC via the BioDot dispense system with two different photopolymers with a drop volume of 40 nL at 0.5 mm pitch. a) Before and b) after the introduction of red ink into the gap between those polymer lines.	46
Figure 3.28 Photographic images showing sets of parallel-deposited photopolymer lines on NC via the BioDot system with a 40 nL drop volume and 0.5 mm pitch at a valve open time of 600 µs. a) Cured with laser light immediately after dispensing; b) Not cured after deposition and left in the dark overnight.	47
Figure 3.29 Photographic image showing a set of parallel photopolymer lines that are dispensed on NC via the BioDot system with different drop volumes ranging from 10 nL to 50 nL at a fixed	

pitch of 0.5 mm. The dispensed polymer lines were cured via a 405 nm laser immediately after dispensing. Red ink was introduced for testing the performance of these printed lines.	48
Figure 3.30 Photographic image showing a set of parallel photopolymer lines that are dispensed on NC via the BioDot system with different drop volumes ranging from 10 nL to 50 nL at a fixed pitch of 0.5 mm. No laser curing procedure was performed after dispensing and the image was taken after leaving the sample in the dark overnight.	49
Figure 3.31 Image of plots showing the relationship between the resulting dispensed polymer line before width and the dispensed volume. Lines are a simple guide for the eye.	50
Figure 3.32 Microscope image of the dispensed polymer line in Figure 3.29 with a 50 nL drop volume shows a narrow rectangular gap that isolates the inked channel and the deposited polymer line.	51
Figure 3.33 Microscope image of the dispensed polymer line with a 10 nL drop volume as shown in Figure 3.29. Red circles are a simple guide for the eye.	51
Figure 3.34 Photographic images showing the dispensed and cured photopolymer lines with three different drop volumes (40, 80 and 100 nL) at a 0.5 mm drop pitch. Before a) and after b) introduction of different colour inks.	52
Figure 4.1 Schematic of the fabrication of polymerised barriers with: a) variable depth and b) variable porosity.	58
Figure 4.2 Schematic representation of: a) cross-section of a fluidic channel; b) cross-section of a fluidic channel with solid barriers; c) cross-section of a fluidic channel with porous barriers; d) layout of a pre-defined fluidic structure.	59
Figure 4.3 Images showing the delay barriers from both sides of the cellulose paper. a) Depth-variable solid barriers formed by pulsed laser exposure; b) porosity-variable barriers formed by c.w. laser exposure.	60
Figure 4.4 Schematic representation of the layout of the fluidic device and the position of delay barriers (P1, P2, P3 and P4) used for studying the flow delay introduced by delay barriers.	61
Figure 4.5 Comparison between the depth of the polymerisation in the paper and the writing speed of the delay barriers. Error bars indicate the standard deviation for 5 measurements.	62
Figure 4.6 Image showing the delay of the liquid flow after the introduction of blue ink in fluidic channels with barriers created using different writing speeds.	62
Figure 4.7 Plots showing the delay factor for devices with barriers having different depths. Barriers were written with different writing speeds at a fixed average power of 7 mW. Error bars indicate the standard deviation for 5 measurements.	63
Figure 4.8 Plots showing the delay factor of delay-barrier-designed devices. a) Barriers written with different laser output powers at a fixed scan speed; b) barriers written with different scan speeds as a fixed laser output power. Error bars indicate the standard deviation for 5 measurements.	65
Figure 4.9 Plots showing the delay factor of delay-barrier-designed devices. Different numbers of barriers written at a) fixed scan speeds, b) fixed laser output powers. Error bars indicate the standard deviation for 5 measurements and lines are a simple guide for the eye.	66

List of Figures

Figure 4.10 Plots showing the relationship between the fluid delay factor and the position of the delay barriers (distance to the starting line) with the same condition of 200 mm/s scan speed and 20 mW laser output power. Error bars indicate the standard deviation for 5 measurements and lines are a simple guide for the eye.....	67
Figure 4.11 Plot showing the relationship between the laser fluence used to prepare polymer structures and their density (weight/volume).	69
Figure 4.12 Image showing a 2D multi-channel fluidic device used for sequential delivery of three fluids (TBS). Three identical channels modified with different delay barriers (1.Stronger delay barriers; 2.blank; 3.weaker delay barriers).....	71
Figure 4.13 Sequential images showing the arrival and mixing of black and red inks from three separated flow channels in a 2D multi-channel device and the subsequent mixing of the inks.	71
Figure 5.1 Schematic of patterning multi-layer stacks using the LDW technique.	75
Figure 5.2 Images showing the polymerised structures from both sides a) top side, b) bottom side) of a stack with three layers of cellulose paper and images of both sides of the device c) top side, d) bottom side) after introduction of blue ink of different volumes (3-7 μ L) into the designated well.	76
Figure 5.3 a) Schematic image showing the arrangement of a stacked device with different structures in top and bottom layers, which are isolated with a hydrophobic film in between. b) Top and c) bottom images showing the device described in a) after the introduction of different inks from top and bottom surfaces without any cross-contamination or mixing.....	78
Figure 5.4 Schematic of patterning a backing layer inside the paper substrate using the LDW technique.....	80
Figure 5.5 a) Schematic of patterning a backing structure by scanning the laser beam across the substrate in a line-by-line manner with a separation of 1 mm. Cross-sectional images showing polymerised layers (un-inked white layers) on one side of thick cotton fibre filter paper with different thicknesses of: b) $\sim 700 \mu$ m and c) ~ 1 mm, after the introduction of red ink from the other side.	81
Figure 5.6 Plots showing the variation in the depth of the polymerised layers for different laser powers at three different scan speeds. Error bars indicate the standard deviation for 5 measurements.	82
Figure 5.7 Plots showing the variations in the depths of the polymerised layers for different laser powers at a fixed scan speed of 10 mm/s for three different numbers of scans. Error bars indicate the standard deviation for 5 measurements and the straight line for the case of 2 scans is a simple guide for the eye.	82
Figure 5.8 (a) Images showing the results of the introduction of different volumes of red ink into 4 \times 5mm well structures patterned in two samples with different backing thickness. (b) Plots constructed using the grayscale intensity values taken from the images shown in (a). Error bars indicate the standard deviation for 3 measurements.	84
Figure 5.9 a) Schematic showing an enclosed flow-path formed by creating polymerised blocks from both faces of a single paper substrate. b) Schematic representation of the cross-section of	

a 3D fluidic device with two inlets (①②) from either end. c) Photographic images taken from the top and bottom of the device described in b).	86
Figure 5.10 Sequential images taken from the a) top and b) bottom showing the device described in Figure 5.9b after the introduction of red ink from the inlet ①.	86
Figure 5.11 Photographic images showing the top and bottom of the device described in Figure 5.9b after the introduction of red ink from the inlet ②.	87
Figure 5.12 Cross-section image showing the enclosed channels and flow of the red ink in the device described in Figure 5.9b after the introduction of ink from both inlets.	87
Figure 6.1 Sequential photographic images showing the flow of red ink on a NC strip with a triggerable wax gate in the middle of the flow path. The gate was triggered globally via a hot plate.	95
Figure 6.2 Sequential photographic images showing the flow of yellow dye followed with green dye on a cellulose paper strip with a triggerable wax gate in the middle of the flow path. The gate was triggered locally via a wax pen.	96
Figure 6.3 Microscopy images of a wax gate at different positions with different magnifications: a) and c) 10 x; d) and d) 20 x. a) and b) show the unheated area, which remains as a solid barrier, and c) and d) show the heated area, where the fluid (PBS) flowed through.....	97
Figure 6.4 Sequential photographic images show triggering of the wax gate using a locally applied laser light source.	98
Figure 6.5 a) Schematic image shows the arrangement of the device. b) Image shows the introduction of the sample into the inlet well and its containment inside the well. c) – f) Sequential images showing the process of the detection after triggering the wax gates.	100
Figure 6.6 a) Schematic image show the arrangement of a designed lateral-flow strip with a wax gate. b) Image shows the result of implementing a sandwich CRP ELISA on the lateral-flow strip described in a).	101
Figure 7.1 Representative images of the different formats of ELISA. a) Direct ELISA, b) indirect ELISA, c) sandwich ELISA and d) competitive ELISA.	106
Figure 7.2 (a) 5×5 mm wells patterned with a laser power of 1 mW and a scan speed of 10 mm/s and prepared for the detection of nitrite by the Griess reagent, after the introduction of the sodium nitrite samples. (b) Calibration curve constructed using the grayscale intensity values taken from the image shown in (a).	109
Figure 7.3 Patterned cellulose paper after completion of a) the BSA detection assay showing different shades of the blue-green colour, corresponding to the different concentrations of BSA pipetted in each well and b) the glucose assay showing different shades of the pink-brown colour, corresponding to the different concentrations of glucose in each well.	111
Figure 7.4 Calibration curve for the detection of BSA constructed using the grayscale intensity values taken from the image shown in Figure 7.3a.	111
Figure 7.5 Calibration curve for the detection of glucose constructed using the grayscale intensity values taken from the image shown in Figure 7.3b.	112

List of Figures

Figure 7.6 Camera images of the patterned device, designed for the simultaneous detection of glucose and BSA, a) at the time of introduction of the sample solution and b) after detection was completed and measurements were taken.	113
Figure 7.7 Schematic diagram showing the logic sequence for performing direct one-step ELISA on a paper-based device.....	114
Figure 7.8 Image showing the result of the implementation of one-step ELISA on a) cellulose filter paper and b) nitrocellulose membrane.	114
Figure 7.9 Schematic diagram showing the logic sequence for performing a sandwich ELISA on a paper-based device.....	115
Figure 7.10 Image showing the result of the implementation of sandwich TNF- α ELISA on nitrocellulose membrane with a sample concentration of 370 ng/mL.	116
Figure 7.11 Image showing the result of the implementation of sandwich CRP ELISA on nitrocellulose membrane with a sample concentration of 90 ng/mL.	116
Figure 7.12 (a) Selected area of 5 \times 5mm well structure patterned with a laser power of 1 mW and a scan speed of 10 mm/s and results for the detection of CRP by the sandwich ELISA. (b) Calibration curve constructed using the grayscale intensity values taken from the image shown in (a). Error bars indicate the standard deviation for 4 individual measurements.	117
Figure 7.13 Schematic of a lateral flow-type biosensor that consists of four components: sample pad, conjugated pad, reaction pad and absorbent pad.	119
Figure 7.14 a) Schematics showing the arrangement of a lateral flow paper strip for implementation of CRP detection. b) Schematic indicates the method of preparation of the capture antibody. c) Image showing the result of lateral flow detection of CRP on a device as described in a) based on a sandwich ELISA.	120
Figure 7.15 Image of a real device showing the arrangement of a lateral flow paper strip for implementation of CRP detection.....	121
Figure 7.16 Image showing the result of the implementation of an enzyme-based sandwich ELISA for detection of CRP on a paper strip shown in Figure 7.15 with a sample concentration of 90 ng/mL.	121
Figure 7.17 Image showing the result of the implementation of an Au nanoparticle-based sandwich ELISA for detection of CRP on a paper strip shown in Figure 7.15 with the sample concentration of 90 ng/mL.	122
Figure 7.18 Automated multi-step ELISA for CRP detection in a 2D multi-channel fluidic device. a) Image of a device showing its design and indicating reagent locations for the assay. Four blue spots, shown schematically in a), represent the position of immobilised capture antibody in the detection zone. b), c), d) and e) are photos of the CRP ELISA result on the device for different sample concentrations of 10 μ g/mL, 100 ng/mL, 10 ng/mL and no sample respectively.....	124
Figure 7.19 Automated multi-step ELISA for CRP detection in a 2D multi-channel fluidic device. a) Image of a device showing its design and indicating reagent locations for the assay. Four blue spots, shown schematically in a), represent the position of immobilised capture antibody in	

the detection zone. b), c), d) and e) are sequential photos of the device after different times of adding the reagents, and f) is a photo shows the result.	125
Figure 7.20 Detection of CRP in human urine on LDW patterned NC device. The first two rows show detection of various concentrations of CRP in spiked healthy human urine, and the two last rows show detection of the same concentrations of CRP in spiked PBS.	126
Figure 7.21 Detection of CRP in blood plasma on laser-patterned nitrocellulose. Both infected clinical samples and healthy samples were tested.	127
Figure B 1 Schematic of the BioDot AD3220 dispense/aspirate system with a BioJet™ non-contact nanoliter dispenser head [188].	137
Figure B 2 Schematic figure shows the variation of the pressure during a prime, aspirate, and dispense cycle [188].	139
Figure B 3 Flow chart showing the logic sequence of the AxSys™ software program for operation of the BioDot dispensing system.	140
Figure B 4 Step-wise schematic describing a general working protocol for the BioDot aspirate/dispense system, which involves several basic steps in a logic sequence.	141

Declaration of authorship

I, Peijun He, declare that this thesis entitled “Development of paper-based point-of-care biosensors by laser-based direct-write processes” and the work presented in the thesis are both my own, and have been generated by me as the result of my own original research.

I confirm that:

1. This work was done wholly or mainly while in candidature for a research degree at this University;
2. Where any part of this thesis has previously been submitted for a degree or any other qualification at this University or any other institution, this has been clearly stated;
3. Where I have consulted the published work of others, this is always clearly attributed;
4. Where I have quoted from the work of others, the source is always given. With the exception of such quotations, this thesis is entirely my own work;
5. I have acknowledged all main sources of help;
6. Where the thesis is based on work done by myself jointly with others, I have made clear exactly what was done by others and what I have contributed myself;
7. Parts of this work have been published as shown in Appendix D.

Signed:

Date:

Acknowledgements

First of all, I would like to express my heartfelt gratitude to my supervisors Prof. R. W. Eason and Dr. C. L. Sones for their invaluable support, guidance and patience over these years, as well as for all the opportunities they have given me. I would never reach this point without their help. I would also like to thank Dr. I. N. Katis for all his help and discussions that made my project much smoother and also helped me to become a better researcher.

I acknowledge the help and support from all members of the LIFT group, especially, Dr. M. Feinaeugle and Dr. B. Mills for their advice and encouragement during the first half of my studies. I am very grateful to N. Sessions for his technical support. Thanks also to people in the Faculty of Medicine and the Southampton General Hospital for their help in introducing me into the biological field. I am grateful to Dr. S. Pang from LGC for not only providing samples and reagents but also helping in troubleshooting. Also, I thank for Dr. A. Sweet from Hyperteknologies for his advice in implementation and troubleshooting of biological assays.

I would like to thank my family and my friends for their support during my studies.

Finally, I would like to thank my parents who gave me the chance to study abroad and, most importantly, support my Ph.D. financially. Thank you again for all your support and understanding, and thank you for making me who I am now.

Abbreviations

LDW	Laser direct write
ELISA	Enzyme linked immunosorbent assay
IgG	Immunoglobulin G
HRP	Horseradish peroxidase
TMB	Tetramethylbenzidine
PBS	Phosphate buffered saline
TBS	Tris buffered saline
CRP	C-reactive protein
POC	Point of Care
LOC	Lab on Chip
PDMS	Polydimethylsiloxane
TNF- α	Tumor necrosis factor alpha
IL-6	Interleukin 6
BSA	Bovine serum albumin
c.w.	Continuous-wave
LFD	Lateral flow device
μ PAD	Microfluidic paper-based analytical device
DI	Distilled
IPA	Isopropyl alcohol
AKD	Alkyl ketene dimer
TBPB	Tert-butyl peroxybenzoate
NC	Nitrocellulose
PVDF	Polyvinylidene fluoride
SSP	Steady state pressure
USB	Universal serial bus
3D	Three-dimensional

Abbreviations

CAD	Computer-aided design
hCG	Human chorionic gonadotropin
HIV	Human immunodeficiency virus
ALP	Alkaline phosphatase
Au	Gold
LOD	Limit of Detection
LOB	Limit of Blank

Chapter 1: Introduction

1.1 Motivation

In recent years, the requirements for easy-to-use, low-cost and accurate diagnostic solutions have led to a rapid progress in the research of point-of-care (POC) diagnostic devices, especially lab-on-chip (LOC) type POC devices with origins in the 1990s, which are based on microfluidic engineering technology [1, 2]. One of the main reasons behind the use of this LOC-type microfluidic technique for POC diagnostics is the possibility of reducing the quantity of valuable samples or reagents that would be needed and also the possibility to shorten the detection times, which would result primarily from the compact structure and small size of such LOC devices. However, although this technology is promising and there have been a large number of achievements in this field, there is still a bottleneck in the development of commercialized products, which can be attributed to a disconnect between users, academic researchers and manufacturers [3].

This situation is changing however with the emergence of capillary-based microfluidic devices and in particular with the relatively recent adoption of paper, one of the most simple and widely used capillary structures. The field of paper-based microfluidics, which has led to many different LOC type devices for implementing a range of analytical assays, has been a hot topic and is currently widely researched since it was first proposed by the Whitesides' group in 2007 [4, 5]. Microfluidic paper-based analytical device (μ PADs) are regarded as a relatively new class of POC device that are cheap, easy-to-use and possess a rapid modus-operandi especially for use in developing countries which lack basic infrastructure and trained personnel.

To date, paper, or more generally porous material, as the functional substrate has already been widely researched as an alternative to other commonly used substrates such as glass, silicon, SU8, and PDMS (polydimethylsiloxane) and many different kinds of microfluidic devices with a range of structures and applications have been reported [4, 6-12]. This is a direct result of the many advantages offered by paper, namely its low cost, availability, ease of storage and transport and finally being easily disposable in a non-hazardous manner. Paper-based fluidics, therefore, presents itself as a LOC technology that could become the technique of choice for mass-market commercialized POC diagnostic devices.

In addition, when compared with other solid-material-based LOC-type microfluidic devices, those devices based on porous paper do not require any additional pump because of the inherent ability of paper to wick fluids via capillary forces. This provides a real

advantage with regards to both the cost and manufacturability of any such device, and has hence led to the development of many paper-based POC devices based on simple colorimetric bio-assays, i.e. enzymatic-based colorimetric detection [13-17], colorimetric immunoassay [18-20], and nanomaterials-based colorimetric detection [21-24]. In addition, porous nitrocellulose (NC) membranes, since their first demonstration in the 1960's, have been widely used, due to some key features, such as their smooth surface, uniform pore size, and high protein-binding capability [25]. A large number of biological assays, namely blotting assays, flow-through assays, and lateral flow tests have been developed on these porous nitrocellulose membranes, and hence nitrocellulose-based microfluidic devices are currently regarded as the alternative of choice for improving the performance of existing POC assays.

These facts hence form the basic motivation for this research project which aims to develop a novel technique for patterning of these porous materials for fabrication of paper-based POC devices, which are low cost, easy to operate and hence can fill in the gap described above and indeed bring paper-based devices into the real market. Thus, this thesis describes the initial work in exploring the use of a laser direct-write (LDW) procedure based on light-induced photo-polymerisation for development of a novel technology for creating the fluidic patterns in a porous substrate for fabrication of paper-based diagnostic sensors as well as enabling a range of additional functionalities, i.e. flow control, three-dimensional (3D) flow paths etc. In contrast to other reported methods, this approach not only eliminates the requirements for cleanroom-based steps, expensive masks, specialist reagents and custom-designed equipment but is also amenable to large-scale commercialization.

Another main objective of this work is the validation of the effectiveness of these LDW fabricated devices as medical diagnostic sensors. This involves the implementation of a range of real clinical diagnostics and analytical chemistry assays onto those LDW patterned paper-based devices.

These are the main objectives that have been achieved during this thesis, and as a future goal, we intend to build upon these initial results for the further development of this LDW technique for eventual realization of large-scale fabrication of commercialized paper-based POC diagnostic sensors and truly realize paper-based diagnostics in the real world.

1.2 Outline of this thesis

In chapter 2, an introduction to LDW techniques will be presented, with more focus given to laser direct-write modification, which is the main approach that is further explored and

developed for the fabrication of paper-based devices as described in this thesis. Additionally, light-induced photo-polymerisation will be presented, as it is the main principle applied during LDW modification. Finally, an overview of paper-based microfluidic sensors will also be given, including an introduction to paper-based devices, their advantages, limitations and also the current situation.

Chapter 3 will introduce a novel approach for patterning of various porous materials towards the fabrication of paper-based POC diagnostic sensors. Through a simple LDW procedure, which relies on light-induced photo-polymerisation of a photopolymer previously impregnated in the substrate, microfluidic structures can be patterned in a wide range of porous materials, i.e. cellulose filter paper, glass fibre filter, nitrocellulose membranes, fabric etc. In addition, two main improvements to this LDW technique have also been proposed in this chapter including the introduction of a galvo-scanner and a local deposition procedure, which satisfactorily addressed several limitations and further develop this LDW technique to eventually meet all requirements for large-scale commercialized fabrication of paper-based devices.

Chapter 4 is focused on introducing fluid delay mechanisms, which can be intentionally introduced during the same device fabrication procedure that allow programmable fluid delivery in paper-based devices. Two strategies will be presented - solid barriers with variable depths and porous barriers with variable porosities. Through adjustment of the depth and/or the porosity of these barriers, programmable flow delays can be introduced spanning time scales from minutes to over an hour.

In chapter 5, the same LDW technique is utilised to design three-dimensional structures within a single or a stack of porous substrates for fabrication of 3D devices. Through controlling the depths of the produced hydrophobic structures within a substrate, 3D flow paths can be achieved. In addition, this depth-variable patterning protocol can also be explored for stacking and sealing of multi-layer substrates and for assembly of backing layers for lateral flow devices (LFDs).

Chapter 6 describes an idea to enable fluidic gating in paper-based microfluidic devices via triggerable wax barriers that are introduced using a cheap office wax printer. The printed wax barriers act as triggerable fluidic gates, which can be switched on demand via the application of local heating.

Chapter 7 is focused on validation of those LDW fabricated devices by implementing a range of both clinical diagnostics and analytical chemistry assays. Single step colorimetric analyses as well as multi-step enzyme-linked immunosorbent assays (ELISAs) will be

presented for both qualitative and semi-quantitative detection of various markers in artificial laboratory samples as well as real human bodily fluids.

Finally, chapter 8 summarises the works described during this thesis, which are mainly focused on developing a LDW approach for fabrication of paper-based diagnostic biosensors with the possibility of a range of additional functionalities. It also gives some outlook on possible future works for further developing this LDW procedure as a unique technique for commercialised fabrication of paper-based diagnostic sensors.

1.3 Main achievements

The following lists the main achievements attained during the Ph.D. and contained within this thesis.

- We developed a laser-based fabrication procedure to produce fluidic channels and structures in porous materials including cellulose filter paper, glass fibre, nitrocellulose membranes, fabric etc.
- Results showed that laser-patterned polymerised walls/barriers could successfully guide the flow of fluids in channels or contain them in wells.
- The minimum width for the barriers that prevented fluid leakage was $\sim 120\text{ }\mu\text{m}$ and the minimum width for the fluidic channels was $\sim 80\text{ }\mu\text{m}$, both are the smallest reported so far for paper-based fluidic patterns.
- Demonstration of programmable flow-delays on paper-based fluidic devices spanning timescales from minutes to over an hour, which allows programmable and timed fluid delivery which enables implementation of multi-step analytical assays in an automatic manner.
- Demonstration of using the same LDW approach for stacking and sealing of multi-layer paper substrates that can help to solve potential evaporation and contamination problems.
- Fabrication of a polymer backing layer with a specific thickness within the paper substrate itself, which can be used as backing for paper-based devices or to reduce the paper volume, which in turn allows reduction of the required reagent/sample volume and most importantly, can be used to increase the limit of detection.

- Demonstration of using the LDW approach for fabrication of 3D flow paths in a multilayer paper stack or inside a single layer of the substrate for fabrication of 3D devices.
- Fabrication of wax-based triggerable fluidic gates in paper-based devices which allows flow-on-demand control of the fluid in paper-based devices.
- Implementation of single step colorimetric assays on LDW fabricated paper-based devices for both qualitative and semi-quantitative detection of protein, glucose, and nitrite.
- Implementation of complicated multi-step ELISA on LDW fabricated paper-based devices for both qualitative and semi-quantitative detection of C-reactive protein (CRP) and tumor necrosis factor alpha (TNF- α).
- Demonstration of the above assays using real clinical samples: human bodily fluid samples including urine and blood plasma.

Chapter 2: Background

2.1 Laser direct-write techniques

LDW is one of the most versatile direct-write techniques, which uniquely enable adding, removal and modifying target materials without any physical contact. Additionally, it is able to process complex materials with a resolution spanning more than three orders of magnitude, from millimetres to microns, which makes LDW process a unique technique to fabricate structures that are not possible using other techniques [26].

One of the unique features that the LDW technique provides is that it allows processing and modifying of a wide range of materials for fabrication of devices and structures within a research laboratory environment or even as an entire manufacturing system on the factory floor.

The key components of a LDW system normally consist of three parts: the laser source, beam delivery pathway, and substrate translation system. The heart of any LDW process is always the laser source. A wide range of lasers, from ultrafast pulsed systems to continuous wave (c.w.) systems, can be applied during the LDW process as befits different applications. The fundamental interactions of the laser with the target material are usually the main factors in choosing the appropriate laser source, via parameters including the wavelength, pulse duration, divergence, beam quality etc., which directly determine the energy absorption efficiency and the subsequent material response [27].

To date, many kinds of LDW systems have been used in science and engineering, and they can be classified into three main categories: LDW subtraction, where material is removed [28]; LDW addition, where material is added [29, 30]; and finally LDW modification, where material is modified [31, 32]. The technique we have developed and describe in the following sections belongs to the last category (LDW modification), namely using the LDW procedure to modify the material in the substrate in order to form designed patterns based on light-induced photo-polymerisation.

2.2 Light-induced photo-polymerisation

Polymerisation is a process whereby individual small monomer molecules react together via a chemical reaction to produce chains or three-dimensional networks, called polymers. There are a large number of polymerisation processes, including plasma-induced polymerisation, pressure-induced polymerisation, heat-induced polymerisation etc. In

general terms, polymerisation is defined as a process of converting a monomer or a monomer mixture into a polymer [33].

Light-induced photo-polymerisation, also known as photo-induced polymerisation, is a polymerisation reaction initiated by radiation, which is usually taken to mean light. The polymer used in this process is called a photopolymer, which is a polymer that can change its properties when exposed to light [34]. A photopolymer is usually comprised of monomers, oligomers, photoinitiators, or a mixture of these materials. When exposed to light, it undergoes photochemical reactions (cross-linking of monomers or oligomers), also called curing, forming a network polymer that changes its chemical and mechanical properties [35]. A simple schematic in Figure 2.1 describes a typical light-induced photo-polymerisation process. High-intensity light sources such as lasers can be used for selective and high-speed curing and are regarded as one of the main advantages of photo-induced polymerisation. However, most of the monomers and oligomers are not easily activated by light, thus photoinitiators are usually required in the formulation at usually just a few percent concentration of the photopolymer mixture. Photoinitiators are compounds that can be decomposed into two or more parts by radiation, which then help to activate polymerisation of specific functional groups on the monomers and oligomers to link them together [36]. Photoinitiators are only sensitive to light of specific wavelengths, but most of them are sensitive to ultraviolet radiation. Lasers and other types of light sources such as lamps are normally used as the radiation source for curing.

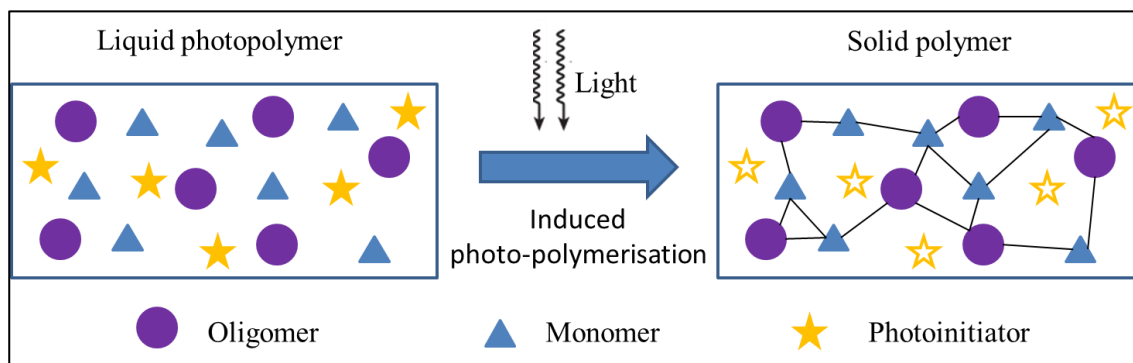


Figure 2.1 Schematic of a light-induced photo-polymerisation process for a photopolymer mixture of oligomer, monomer, and photoinitiator.

There are two main chemical schemes (free radical polymerisation and cationic polymerisation) that are commonly used and each requires different photoinitiators. In cationic polymerisation, the bonding process of monomer and oligomer is induced by a strong acid that is released by the initiator when exposed to light. On the other hand, in free radical polymerisation, the radiation will induce complex radicals that are split off from the initiator, which combine with monomers and oligomers to start the

polymerisation reaction. Most of today's photopolymers are based on the free radical scheme.

During the reaction, the molecules of monomers and oligomers first combine together to form long chain molecules and then during a cross-linking process these longer chains link together to form the final solid material (polymer). As it is a chain reaction, it keeps going once the polymerisation process begins. An additional radical or acid molecule will be liberated every time a monomer and/or oligomer link together, which then cause additional molecules to bond. These chain reactions will continue going until radicals recombine to form non-reactive products or the ingredients needed for the reaction are no longer available in the correct proportions, or finally by trapping reactive molecules in the hardening matrix where they can no longer move into position to combine. Thus in some cases, the polymerisation process can even continue for a short time in the dark after removing the light source. The final properties of the polymer rely on both the composition of the oligomers and monomers and also the way they bond together.

Compared to other polymerisation processes, especially thermal-cured polymerisation, photo-polymerisation allows local curing and is able to achieve much better spatial resolution and higher rates of polymerisation. As a result, photo-curable materials and the photo-polymerisation technique are widely used for a range of applications in medical, imaging and photoresist techniques [34, 37].

As described in this thesis, laser-induced photo-polymerisation was used as a manufacturing tool to create hydrophobic polymer structures within porous material substrates during a LDW procedure for both fabrication of paper-based diagnostic sensors and introduction of additional functionalities.

2.2.1 Depth of laser-induced polymerisation

One of the important parameters in order to study this LDW polymerisation process is the penetration depth of laser light in photopolymer-soaked porous material, which will directly determine the achievable dimension in depth of the solid polymer structure inside the porous substrate.

Attenuation coefficient is used to describe the extent to which the radiant flux of a beam is reduced as it passes through a specific material. A large attenuation coefficient means that the beam is quickly "attenuated" (weakened) as it passes through the medium, and a small attenuation coefficient means that the medium is relatively transparent to the beam.

The Beer–Lambert law, also known as Beer's law, relates the attenuation of light to the properties of the material through which the light is traveling. According to the Beer-Lambert law, the intensity of an electromagnetic wave inside a material falls off exponentially from the surface as:

$$I(z) = I_0 e^{-\alpha z} \quad [1]$$

where I_0 is the incident intensity, $I(z)$ is the axial dependence of the intensity on the depth z into the material and α is the attenuation coefficient.

When a narrow (collimated) beam passes through a volume, the beam will lose intensity due to two processes: absorption and scattering. Absorption of light describes the process by which energy of a photon is absorbed by matter, typically the electrons of an atom. On the other hand, scattering is a general physical process where light is forced to deviate from a straight trajectory by one or more paths due to localized non-uniformities in the medium. As a result, both absorption and scattering lead to the decay of the light intensity in the $+z$ direction. The volume absorption coefficient a for absorption and scattering can be defined in the same way as for attenuation coefficient[38]. Hence, attenuation coefficient of a volume can be described as the sum of absorption coefficient and scattering coefficient:[5]

$$\alpha = \alpha_a + \alpha_s \quad [2]$$

where α_a is the absorption coefficient and α_s is the scattering coefficient.

In terms of the absorption, as described by the Beer law, once inside the material, absorption causes the intensity of the light to decay with depth at a rate determined by the material's absorption coefficient α_a . In general, α_a is a function of wavelength and temperature and can be expressed by the following formula:

$$\alpha_a = \frac{4\pi k}{\lambda} \quad [3]$$

where λ is the wavelength and k is the extinction coefficient.

Finally, by substituting equations [2] and [3] into [1], the Beer's equation can be written as follows:

$$I(z) = I_0 e^{-(\frac{4\pi k}{\lambda} + \alpha_s)z} \quad [4]$$

In order to estimate the depth of the polymerised structure inside the substrate which is directly related to the light penetration depth inside the substrate, the above equation can be rearranged as follows:

$$z = \frac{\lambda}{4\pi k + \lambda \alpha_s} \ln\left(\frac{I_0}{I(z)}\right) \quad [5]$$

As shown in the above equation, for a fixed $I(z)$, the penetration depth of laser light is related to the intensity of the light and the wavelength. Therefore, as the polymerisation depth is directly determined by the light penetration depth, it can be controlled via the laser power and wavelength.

Based on the discussions here, as described in Chapter 4 and 5 in this thesis, by changing the patterning parameter, namely incident power and wavelength, solid hydrophobic polymer structures were created with different depths in the porous substrate for implementation of both flow control and 3D flow path.

2.3 Paper-based microfluidic sensors

POC diagnostics, also known as bed-side testing, is specifically targeted at medical testing at or near the site of the patient care, without further need for a specialist laboratory environment and trained personnel. Such POC testing is facilitated through the use of uncomplicated, user-friendly and portable testing devices and much effort has been directed towards producing diagnostic test-kits that are not only smaller, faster and smarter, but also satisfy the elusive goal of being cost-effective – a vital requirement that ensures economic viability, since such POC test procedures may need to be performed repeatedly over potentially very large sample groups, that could even extend to an entire nation in the case of a pandemic.

It has been recognised that microfluidic-based LOC technology has considerable potential, and hence sustained efforts have been directed towards developing LOC-type fluidic systems for medical diagnostic devices since its origins in the 1990s [39]. The prime reason for this enthusiasm lies in the obvious advantages presented by these compact LOC devices such as the use of smaller reagent volumes, faster reaction times and portability arising from the device sizes, as well as ease of manufacture and distribution.

Compact LOC devices have primarily been developed on platform substrates such as silicon and glass [40-42], using cleanroom-based fabrication processes adapted from the semiconductor processing industry. In an attempt to further reduce the manufacturing costs, a low-cost polymer, PDMS, which can be used in a rapid prototyping environment, was considered as a better choice for implementation of microfluidic-based LOC devices [43-46]. This material still presents certain limitations and comparatively high fabrication costs, however, which has led to a subsequent search for other alternatives, which now include paper, and thread [10].

In particular, paper, with its varied characteristics, is now considered as a highly suitable alternative for fabrication of LOC-type devices, and many labs have focused their attention in this direction [6, 47, 48]. The first demonstration of paper-based diagnostic devices was by the Whitesides' group at Harvard University [4, 49]. In recent years, paper-based POC devices have been thoroughly researched and rapidly developed, especially for medical diagnostics and biochemical analysis [47]. The reason behind this is because of the urgent need for reliable diagnostic tools in developing countries where people suffer from infectious diseases, and also have a lack of infrastructure, trained personnel and cannot afford expensive technologies [50].

Compared with the polymer, silica or silicon-based microfluidic devices, paper-based devices offer considerable advantages. First of all, paper is readily available in a range of different properties, such as porosity, wettability and wicking capability [6]. In addition, it is cheap and biocompatible, which makes it suitable for implementation of simple biological assays [6, 47]. Furthermore, paper is widely manufactured from renewable resources and can be easily stored and transported and it is also biodegradable and can be incinerated [51]. Finally, an important feature that makes paper very attractive for microfluidic devices is its inherent ability to wick fluids via capillary forces, which avoid the need for external pumps which are necessary for the case of microfluidic devices on other platforms [52].

Paper is currently used for analytical and clinical chemistry, and chromatographic tests are routinely performed in commercial analytical laboratories for the detection of different chemical species. Two of the most commonly known paper-based chromatographic clinical tests are the pregnancy test and the lateral flow-based urine dipsticks that can simultaneously detect sugar, pH, ketone etc. [27-30, 53]. However, clinical tests that can yield quantitative information of a multiplexed nature (i.e. can perform a series of parallel tests) using a single test strip are clearly the way forward, and recent reports of microfluidic paper-based analytical devices (μ PADs) suggest that these may be the ideal platform for performing such tests [50].

As their name suggests, paper-based microfluidic devices normally consist of interconnected hydrophilic fluidic channels, which are demarcated by the hydrophobic walls, to guide and transport an analyte fluid, from a point of entry on the device to a reaction zone that has been pre-treated with specific reagents. Unlike glass, silicon or polymer substrates, where the fluidic channels are surface-relief structures that have been inscribed in these substrates, for paper-based devices the fluidic channels are formed inside and extend throughout the full thickness of the paper. A number of methods have been demonstrated for creating these hydrophobic walls, which can be subdivided into

two general categories: (i) physical blocking of pores [54, 55], and (ii) two-dimensional shaping/cutting [56-59]. Table 2.1 provides an overview of the reported techniques for fabrication of paper-based microfluidic devices.

As described in Table 2.1, the earliest approach presented by the Whitesides' group [80, 81], relied on a cleanroom-based lithographic technique that involved exposure of a UV-sensitive polymer (SU8) impregnated in a paper, through a custom-designed mask, to cross-link it and form the required barriers for the intended fluidic channels. In order to reduce the costs associated with such a conventional lithographic procedure, a subsequent approach they presented involved the use of a modified desktop plotter that dispensed an ink composed of the low-cost elastomeric polymer PDMS [82]. Several other groups have also proposed and demonstrated the usefulness of other paper patterning approaches such as inkjet printer-based etching of paper impregnated with polystyrene [52, 83], plasma-treatment through a metal mask of a paper impregnated with hydrophobic AKD [86], paper-cutting using a computer-controlled X-Y knife plotter [55, 56], printing of wax [84, 85], flexographic printing [87], wax-screen printing [54], and laser-ablation [58].

Each of these procedures has its own advantages, as well as some characteristic drawbacks. Techniques such as UV-lithography and plasma-treatment require the use of expensive and fixed-pattern masks as well as dedicated equipment and controlled lab conditions. The wax printing technique has potential for scaling up for commercial use. However, it requires additional post-processing procedures and the achievable feature size is limited by the spread of the wax. In addition, the solid wax barriers are very fragile, ambient (hot) air conditions and long-term storage in the developing world may cause the wax to melt, thus deforming the channels. Inkjet etching method requires the use of organic solvents and multiple printing processes. The knife-plotting technique requires specialised or custom-modified patterning equipment, and when paper is being cut, it is necessary to have at least three sequential overlapping cuts to prevent tearing of the paper. Other important issues include the limitation on achievable feature size resulting from the lateral spreading of the hydrophobic material (for example with wax printing and inkjet printing of hydrophobic materials), and the need for specialised chemicals or inks (for inkjet etching) or the use of harsh chemical etchants.

Fabrication technique	Substrate	Consumables
Photolithography [60, 61]	Chromatography paper	SU-8 photoresist
Polydimethylsiloxane (PDMS) printing [62]	Filter paper	PDMS

Inkjet etching [53, 63]	Filter paper	Polystyrene
Wax printing [64, 65]	Filter paper	Solid wax
Alkenyl ketene dimer (AKD) printing [66]	Filter paper	AKD
Screen printing [55]	Filter paper	Solid wax
Flexographic printing [67]	Chromatography papers	Polystyrene
Knife shaping [56, 57]	Chromatography paper and nitrocellulose	None
CO ₂ laser cutting [59]	Chromatography paper and nitrocellulose	None

Table 2.1 Summary of reported methods for fabrication of paper-based microfluidic devices.

In terms of using these paper-based microfluidic devices to realize diagnoses, a range of detection mechanisms have been proposed, which cover the area of medical diagnostics [68-71], food pathogens [72-74], and environmental testing [75, 76]. So far, the majority of these studies are focused on healthcare with limited studies reported on environmental applications and food safety. The reported sensing mechanisms include colorimetric detection [76-79], electrochemical sensing [2, 72, 80], nanoparticle-based detection [73, 81, 82], fluorescence [83-85], electrochemiluminescence [86-88], etc. To date, most studies are based on more mature sensing mechanisms such as colorimetric and electrochemical sensing in paper-based devices. In chapter 7, several colorimetric detections will be implemented on our LDW fabricated paper-based devices in order to validate the effectiveness of those devices as medical sensors.

2.4 Capillary action in porous materials

As mentioned above, one of the most important features that make paper or porous materials very attractive for microfluidic devices is their inherent ability to wick fluids via capillary forces, which then avoid the need for external pumps which are necessary for the case of microfluidic devices on other platforms [51].

Capillary action is a result of the intermolecular attraction within the liquid and solid materials, which describes the ability of a liquid to flow in narrow spaces without the assistance of, or even in opposition to, external forces such as gravity. It is defined as the

movement of a liquid within the spaces of a porous material due to the forces of adhesion, cohesion, and surface tension [89].

The one-dimensional transport of the fluid in a porous medium (such as paper) during wet-out follows the Washburn equation under two assumptions (a non-limiting source fluid and a constant cross-sectional area) [90]:

$$L^2 = \frac{\gamma D t}{4\mu} \quad [6]$$

where L is distance moved by the fluid front, γ is the effective surface tension of the fluid, t is time, D is the average pore diameter, and μ is viscosity [91].

According to the Washburn equation, the fluid front velocity decreases with time ($L \sim \sqrt{t}$). The force comes from the surface tension that pulls the fluid further into the paper and counteracting this is the viscous resistance, which is proportional to the velocity with a coefficient ($\frac{8\mu L}{D^2}$) that increases as the fluid column lengthens. This results in a decrease in flow velocity as the fluid penetrates the porous medium [92].

As described in Chapter 4, two delay strategies are proposed based on introduction of delay barriers in the flow path to either alter the porous size or the cross-section area, in order to control the flow in paper-based devices.

Chapter 3: Laser-based patterning for fluidic devices

3.1 Introduction

To date, a few methods have been reported for fabrication of paper-based microfluidic devices, and these can be generally classified into three categories: physical blocking of pores in the paper, physical deposition of a hydrophobizing reagent and chemical modification of fibre surfaces that constitute the paper [47]. The techniques reported so far include the use of photolithography [4, 5, 93], inkjet printing [94-96], wax printing [65, 97, 98], plotting [99], shaping [100], plasma oxidation [101, 102], laser cutting [103], flexographic printing [67], screen printing [55] and inkjet etching [53, 63].

Photolithography, as the first approach used for fabrication of paper-based devices, was first proposed by the Whitesides' group in 2007 [4, 5]. Similar to our proposed LDW technique, photolithography also relies on UV exposure of photoresist-saturated paper, however, with the aid of a photomask. Uncured photoresist is removed with solvent, leaving hydrophobic, cured photoresist barriers within the paper. This work was a major breakthrough that led to significant research growth in this field. However, one of the potential problems with the use of photolithography to create a microfluidic channel is that it lacks flexibility as the design totally relies on the photomask. In addition, it also requires expensive cleanroom facilities, otherwise dust particles in the air can settle on lithographic masks and damage the mask hence cause defects in the devices. Since the pioneering work by the Whitesides' group on paper-based microfluidics, a range of alternative approaches have been introduced by other researchers. However, each of these procedures has its own advantages, as well as some characteristic drawbacks as discussed in Chapter 2. In general, the ideal technique should be as simple, cheap, and fast to implement as possible, and therefore multiple printing steps, the use of specialist chemicals, or complex post-processing procedures are to be avoided. The other factor is the feature sizes achievable, which is where procedures such as plotting or wax printing may present restrictions in this context.

This chapter presents the use of a LDW technique based on the principle of light-induced photo-polymerisation for creating fluidic patterns in porous material substrates. This LDW procedure is non-contact, mask-less and non-lithographic in nature. In addition, the patterning process can be simply controlled through choice of the laser parameters such as the laser power, wavelength, pulse duration and finally the laser scanning/writing

speed. More importantly, if desired, it is routinely possible to considerably reduce the dimensions of the patterned features as compared to other existing methods. Finally, this LDW process is also suitable to scale up for mass-production, possibly on a roll-to-roll scale.

3.2 Experimental work

3.2.1 Experimental setup

The basic LDW setup is shown in the schematic in Figure 3.1. During the LDW step, the laser beam is focused onto the substrate through a focusing lens. The substrate, normally a porous material, was mounted on a stage and translated either in two (x, y) or three directions (x, y, and z). By programming the movement of the stage in the x-y plane, a user-defined two-dimensional (2D) structure can be patterned into the substrate. In addition, the axis z was used to adjust the position of the substrate (which was mainly at the focal plane of the lens).

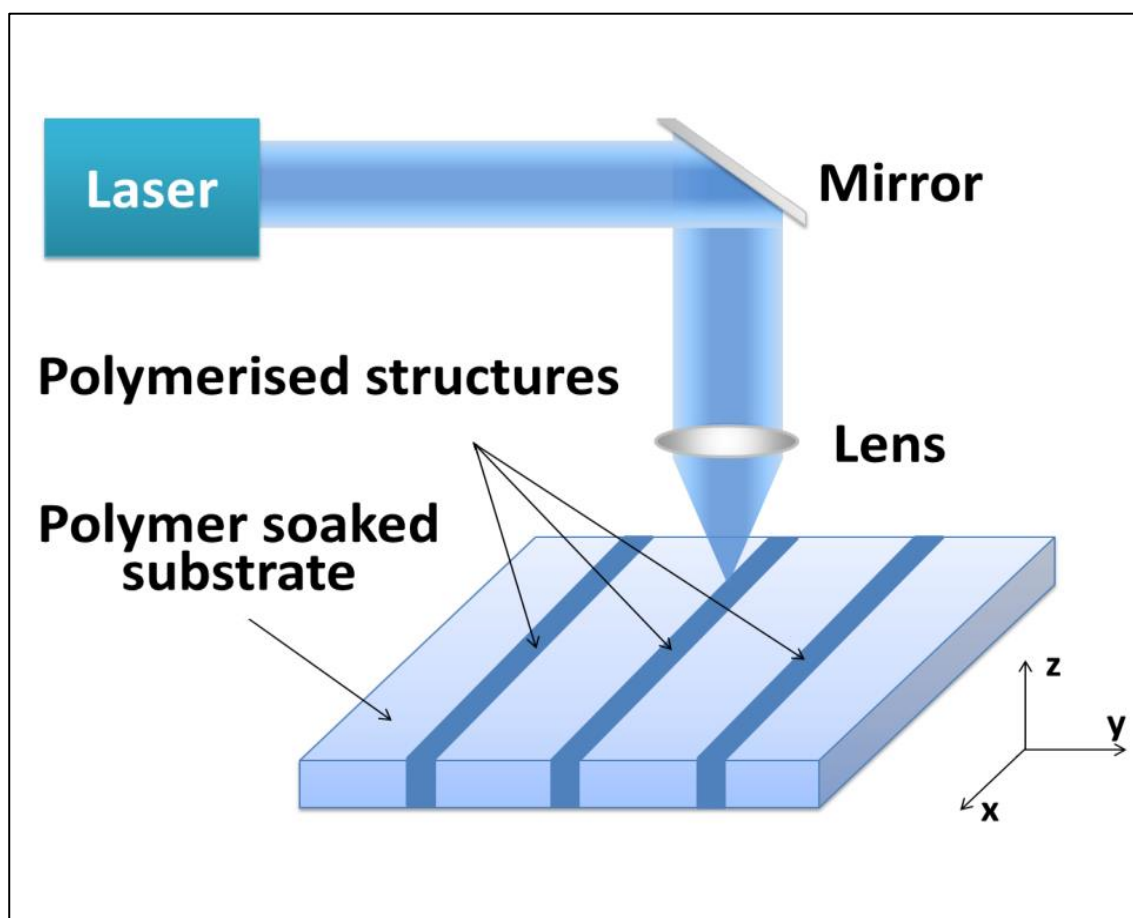


Figure 3.1 Schematic of the LDW process used to form polymerised hydrophobic structures in a paper-based substrate.

The lasers we have tried so far were either a pulsed 266 nm laser (with a pulse duration of 10 ns, a maximum single pulse energy of 2 mJ, and a repetition rate of 20 Hz) or much cheaper and smaller continuous wave (c.w.) diode-lasers, which operated at 375 nm (with a maximum output of 70 mW) and 405 nm (with a maximum output of 110 mW). In addition, the lenses used for LDW experiments were either cylindrical ($f = 25$ mm, 36 mm) or spherical ($f = 15$ cm).

For experiments with the pulsed 266 nm laser, the range of translational speeds was varied from 0.05 mm/s to 0.5 mm/s, together with a variation of incident average powers ranging from ~ 7 mW to ~ 10 mW (corresponding to energies of ~ 0.35 mJ to ~ 0.5 mJ per pulse). The paper was positioned at a distance of 10 mm away from the focal point of the cylindrical lens ($f = 36$ mm), and the corresponding dimension of the laser spot (on the paper substrate) was ~ 0.3 mm \times 1 mm. The corresponding incident fluence hence ranged from 4.6 J/cm² to 66 J/cm². More details on the calculation of the laser fluence can be found in appendix A.

For experiments with the c.w. 375 nm laser, the range of translational speeds was varied from 4 mm/s to 6.7 mm/s, with the corresponding variation of incident power ranging from 1 mW through to 50 mW. The paper was positioned at the focal point of the cylindrical lens ($f = 25$ mm), and the corresponding incident fluence ranged from ~ 1.9 J/cm² to ~ 156 J/cm².

For experiments with the c.w. 405 nm laser, the range of translational speeds was varied from 4 mm/s to 10 mm/s, with a corresponding variation of incident power ranging from 1 mW through to 100 mW. The paper was positioned at the focal point of the cylindrical lens ($f = 25$ mm), and the corresponding incident fluence ranged from ~ 1.25 J/cm² to ~ 312.5 J/cm².

3.2.2 Experimental method

As described above, the paper-based devices were fabricated by forming hydrophobic barriers that extend through the full thickness of the substrate, and demarcate the hydrophilic channels. The method we developed to create fluidic patterns is based on light-induced photo-polymerisation through the LDW technique, and this is described in the step-wise schematic in Figure 3.2. For the first step, the substrate is fully soaked with a photopolymer, and then a laser beam is scanned across the substrate, as a second step, which leads to polymerisation of photopolymer in the laser-exposed areas. Finally, in the third step, a solvent is used during the development step in order to wash away un-polymerised photopolymer in the unexposed regions. After evaporation of the solvent, the

polymerised regions, which remain and extend throughout the thickness of the substrate, serve as hydrophobic barriers that define the channels that contain and guide fluids.

During the paper-patterning procedure, the light-induced photo-polymerisation process is controlled by choosing the laser wavelength or adjusting the incident fluence (through laser output power or exposure time/scanning speed), so that any user-designed fluidic structure (including both the outline of the design and the integrity of the barriers) can be easily achieved in a single step.

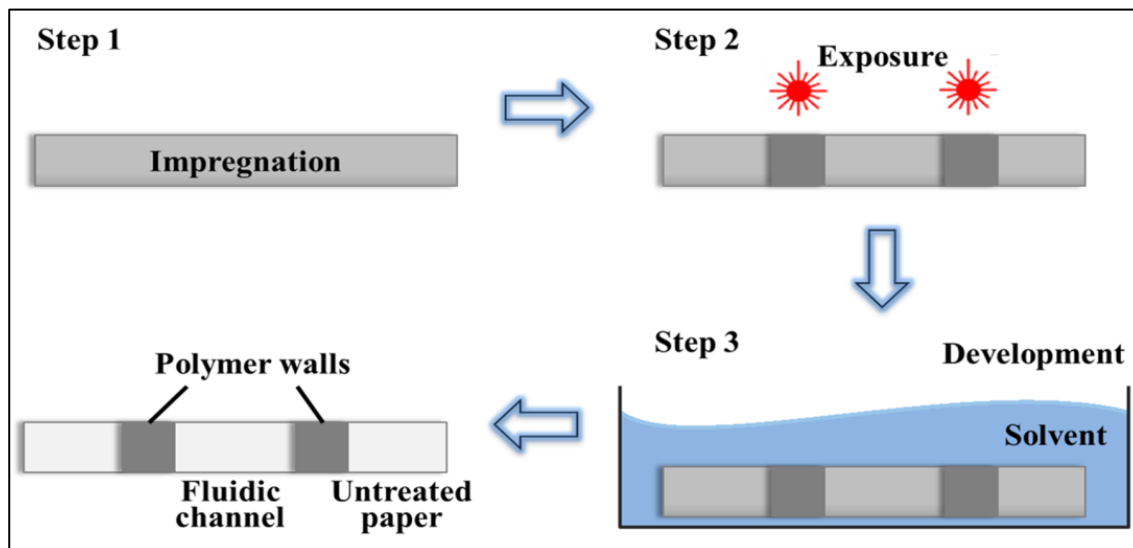


Figure 3.2 Step-wise schematic showing the typical paper patterning procedure using the LDW approach.

3.2.3 Materials and reagents

From the perspective of bioactive paper, critical properties include surface chemistry, porosity and optical properties, such as transmission to laser light and the colorimetric signal produced within the volume of the paper itself. Surface chemistry influences biomolecule immobilization, non-specific binding and colour expression in enzyme-catalysed reporting assays. Porosity, a measure of the void spaces in a material, together with surface chemistry, influences wet properties, which are important for bioactive-paper fabrication by printing or coating. Finally, the optical properties may influence colour-based or fluorescence-based reporting schemes.

Therefore, we have tried to pattern a range of materials with very different properties. The substrates tried so far are cellulose paper, nitrocellulose membrane, polyvinylidene fluoride (PVDF), fabric and normal printing paper (e.g. A4). The initial experiments were performed on cellulose paper (Whatman no. 1 filter paper with pore size of 100 μm and porosity of $\sim 68\%$). The work was then extended to the patterning of nitrocellulose

membranes (Whatman BA85 Protran with pore size of 0.45 μm and porosity of $\sim 0.31\%$). Porous nitrocellulose membranes, since their first demonstration in the 1960s, have been widely used, due to some key features, such as their smooth surface, uniform pore size and high protein-binding capability [25]. Finally, in order to further develop and explore the technique, other porous materials including PVDF, fabric and printing paper were also tested.

The photopolymer we first explored for patterning cellulose paper was a photopolymer used to coat optical fibres (DeSolute® 3471-3-14 from DSM Desotech Inc. USA), followed by a 3D printing polymer (SubG from Maker Juice, USA). However, during the experiments of patterning nitrocellulose membrane, it was observed that the photopolymer applied alters the properties of the nitrocellulose substrate, which is itself a polymer-based porous material. In order to find out an appropriate photopolymer that is compatible with nitrocellulose, several different photopolymers were also tested, such as Ablelux A4061T & A4086 (Henkel AG & Co. Germany), Norland 61 & 68 (Norland Products Inc. USA) and WaterShed® XC 11122 (DSM Desotech Inc. USA). However, most of the photopolymers either dissolved the nitrocellulose or transformed it into an extremely hydrophobic material, which is not desirable. So far, of all tested polymers, DeSolute® 3471-1-14 is the best choice as it seems to only slightly change the hydrophilicity of the nitrocellulose. Meanwhile, we are still trying to explore and discover the most suitable photopolymers, which hopefully would be perfectly benign to the nitrocellulose.

The solvents normally used during the development step are acetone and isopropyl alcohol (IPA). Again, because of the vulnerability of the nitrocellulose, a large number of solvents were tried, such as methanol, ethanol, hexane, dichloromethane etc., and toluene proves to be the best so far, even though it still affects the hydrophilicity of the nitrocellulose to a small extent.

3.3 Experimental results

3.3.1 Patterning of cellulose paper

3.3.1.1 Patterning with a pulsed laser

The initial experiment was started with the patterning of cellulose paper using a 266 nm pulse laser and the DeSolute® polymer. Because of the high viscosity of the photopolymer, we need to dilute it in a solution of IPA with a ratio of 1:2. The initial result is shown in Figure 3.3: three parallel channels, each formed by a pair of identical polymerised lines,

were inscribed with different scan speeds of 0.06 mm/s, 0.07 mm/s and 0.09 mm/s at a fixed incident average laser power of 7 mW.

In order to test the ability of these barriers to contain and guide the liquid, a blue ink was pipetted into each channel from one side. As shown in Figure 3.3, the polymerised barriers start to be able to contain and guide with scan speed down to only 0.06 mm/s. It was found that the polymerisation depths of the barrier walls for channel (c) was only about 60% of the thickness of the paper, whereas for channel (b) this depth was about 75% of the paper thickness. For channel (a) however, the barrier walls extended throughout the full thickness of the paper, enabling leak-free transport of the ink on introduction at one end of the fluidic channel. In contrast, for channels (b) and (c), whose barrier walls do not extend throughout the entire paper thickness, undesirable and irregular leakage of the ink was seen from either side of the channel walls. For speeds slower than 0.06 mm/s, for this pulsed laser source, ablation along a central section of the barrier wall was observed as the local fluence had exceeded the paper ablation threshold at the peak of the Gaussian laser profile.

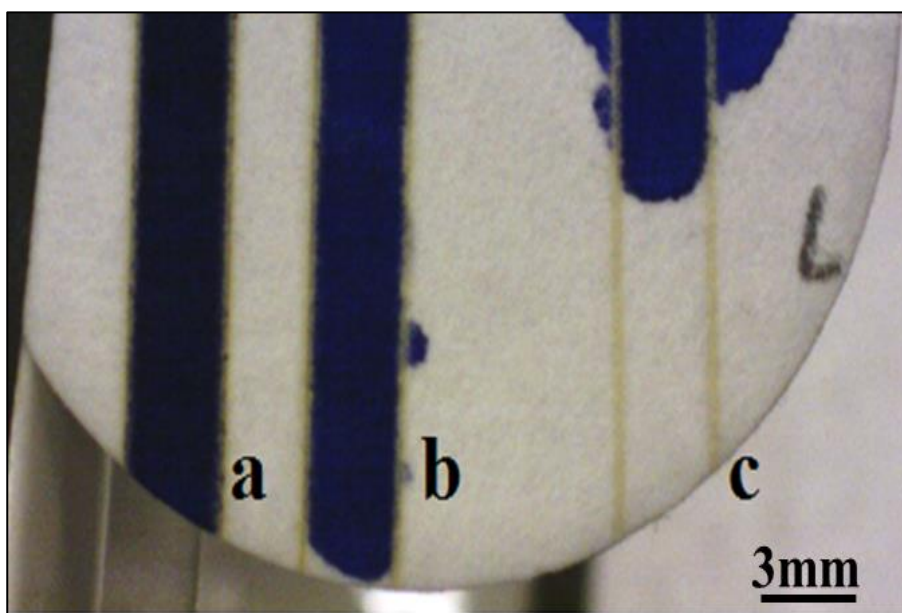


Figure 3.3 Image showing three sets of parallel polymerised lines that were written with a fixed laser average power of 7 mW at different scan speeds. a) 0.06 mm/s, b) 0.07 mm/s and c) 0.09mm/s.

Subsequent experiments were performed with the paper held at a distance of 1 mm from the focal point. Translation speeds were trialled ranging from 0.06 to 0.5 mm/s, and for speeds greater than 0.35 mm/s the photo-polymerised structures did not extend throughout the paper, while for speeds slower than 0.25 mm/s ablation occurred along

the central region of the scanned lines. For speeds lower than 0.2 mm/s the paper was physically cut through along the length of the scanned line.

From the above results, the correlation between spot size of the incident laser source and resultant size of the polymerised regions is easily determined, and hence for a specific choice of laser and photopolymer, it is then possible to deduce the correct exposure regime that will produce any desired line-width. However, for our demonstrations, it is important to note that the smallest barrier widths that are able to contain and guide the fluid flow are of order 100 μm . Since there is a minimum fluence requirement for photopolymerisation at any specific translational speed, this fluence then determines the maximum translational speed and hence device fabrication speed. However, the above demonstration clearly shows the ability to build compact fluidic flow-based devices which encompass the basic needs for smaller volumes of expensive reagents in the fabrication of low-cost LOC-type medical diagnostic devices. These then act as the first proof-of-principle experiment of the technique.

3.3.1.2 Patterning with c. w. laser

In order to explore the usefulness of this technique with different laser parameters, two c.w. lasers (375 nm and 405 nm) were tested instead of a pulsed laser. One of the reasons for choosing these c. w. lasers was because they can avoid the very high peak power from a pulsed laser, which could lead to ablation of the substrate. Most importantly, as longer wavelength translates into greater absorption depth in the substrate, it gives a chance to increase the scan speed.

In order to investigate the relationship between the polymerised barriers and all relevant laser parameters, sets of parallel lines were written with the 375 nm laser with different laser output powers as well as scan speeds. The polymerised line widths were then measured using CorelDRAW based on USB camera images. Figure 3.4 shows a set of lines polymerised with the 375 nm laser, where the line-widths obtained are shown as a function of incident laser power and paper translation speed. Figure 3.4a shows results for a fixed incident laser power of 1 mW, and the line-widths are seen to increase from a value of $\sim 130\ \mu\text{m}$ at 6.7 mm/s to a value of $\sim 320\ \mu\text{m}$ at 4 mm/s. Similarly, as shown in Figure 3.4b, for a fixed scan speed of 6.7 mm/s, the width of the polymerised lines increases with increasing incident laser powers from a value of $\sim 500\ \mu\text{m}$ at 5 mW, to a value of $\sim 1200\ \mu\text{m}$ at 50 mW. This can be attributed to the fact that with an increase in the incident laser power, a larger fraction of the incident Gaussian intensity laser profile would be above the polymerisation threshold, thus resulting in polymerised lines with larger widths.

The graph in Figure 3.5 summarises the above observations and presents the relationship between the line-widths of the polymerised regions for different scan speeds and different laser powers. The data presented in Figure 3.5 show that, for a fixed laser power of 10 mW, the widths of the polymerised lines increased from $\sim 680\text{ }\mu\text{m}$ to $\sim 1000\text{ }\mu\text{m}$ with decreasing scan speeds, and for a fixed scan speed of 6.7 mm/s, the widths of the lines increased from $\sim 130\text{ }\mu\text{m}$ to $\sim 1200\text{ }\mu\text{m}$ with increasing laser powers.

We observed a similar effect for the 405 nm laser, and the relationship between the width of polymerised barriers and different laser parameters are plotted in Figure 3.6: for a fixed scan speed, the width of the lines increases with an increase of the incident laser power. For example, at a fixed scan speed of 4 mm/s, the width of the lines increase from $\sim 200\text{ }\mu\text{m}$ to $\sim 1000\text{ }\mu\text{m}$. A similar tendency was observed with line widths increasing from $\sim 180\text{ }\mu\text{m}$ to $\sim 900\text{ }\mu\text{m}$ and $\sim 80\text{ }\mu\text{m}$ to $\sim 800\text{ }\mu\text{m}$ at a fixed scan speed of 5 mm/s and 6.7 mm/s respectively. For a fixed laser power, the widths of the polymerised lines increase with decreasing scan speeds, i.e. for a fixed laser power of 10 mW, the widths of the polymerised lines increase from $\sim 220\text{ }\mu\text{m}$ to $\sim 330\text{ }\mu\text{m}$ with decreasing scan speeds.

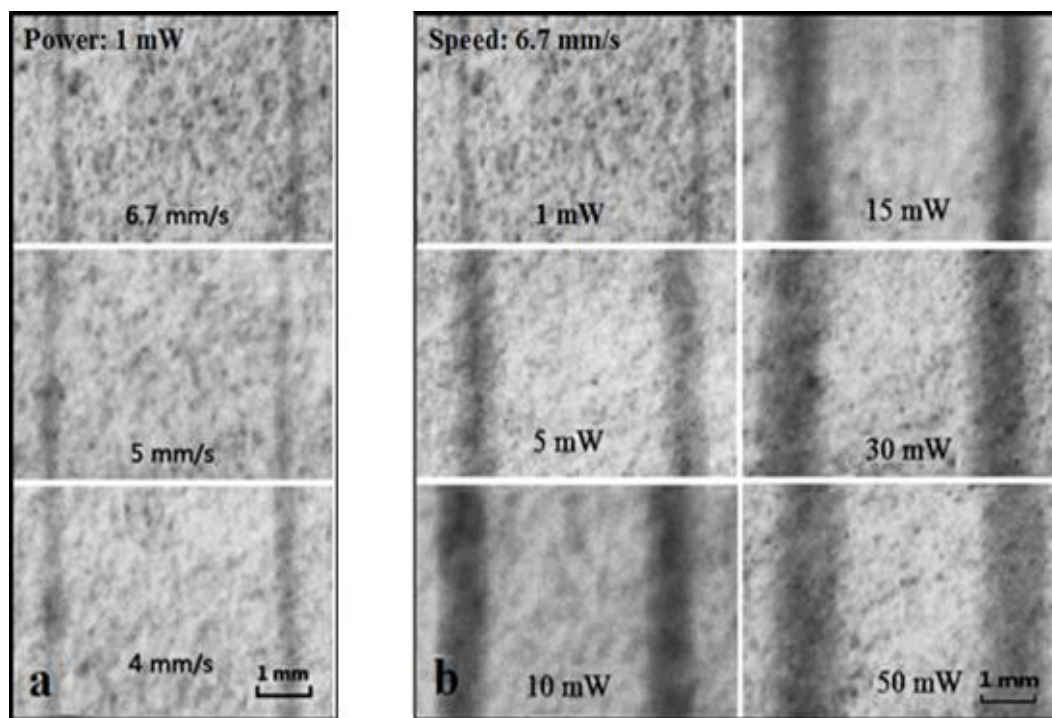


Figure 3.4 Images showing sets of parallel lines that have been photo-polymerised using a 375 nm c.w. laser under different writing conditions: (a) fixed laser power, variable translation speeds, and (b) fixed translation speed, variable laser powers. Photopolymer used was DeSolite®.

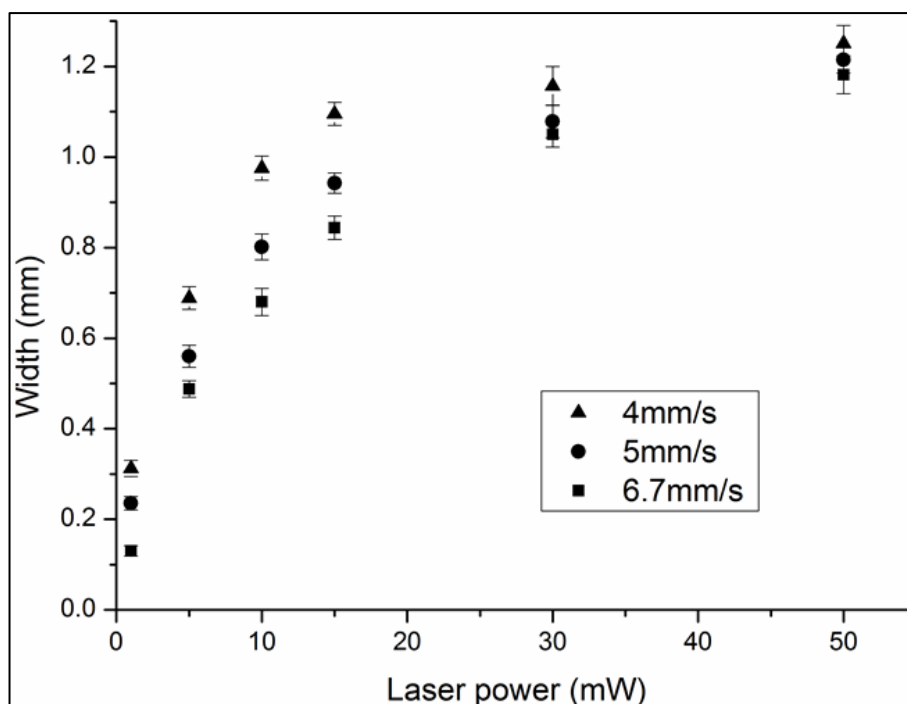


Figure 3.5 Graph showing the widths of the laser-patterned lines for different incident laser powers from the 375 nm source at different scan speeds. Error bars indicate the standard deviation for 5 measurements along each line.

During the experiment, we found that the performance of 375 nm and 405 nm lasers were very similar and the 405 nm laser was finally chosen because of its better beam quality. The smaller line-widths for the irradiation at a wavelength of 405 nm, are a direct consequence of the better beam quality of the 405 nm laser compared to the 375 nm laser and the absence of parasitic lobes in the spatial intensity profile that we saw with the 375 nm source which, though of low intensity, do induce additional photo-polymerisation and therefore produce a broadened line-width compared to the theoretical limit for a perfect single mode laser source. Plots in Figure 3.7 show a summary of the resulting line-widths for the lines polymerised with the two c.w. wavelengths under different laser writing conditions.

For a useful comparison, another photopolymer, SubG, was tested. Due to the extremely low viscosity (12 cP @ 25 °C) of SubG, we soaked the paper directly with the photopolymer solution without the need for any solvent-based dilution, unlike the case for DeSolite®, which had to be diluted in a solution of IPA prior to impregnation into the paper substrates.

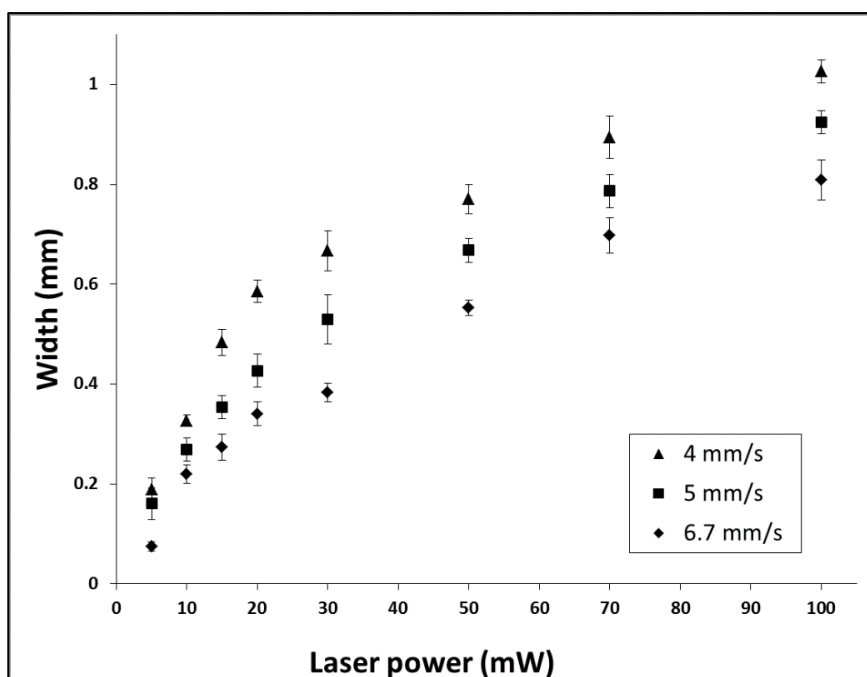


Figure 3.6 Plots showing the relationship between the widths of the polymerised lines using a 405 nm c.w. laser and the different incident laser powers at different scan speeds. Error bars indicate the standard deviation for 5 measurements along each line.

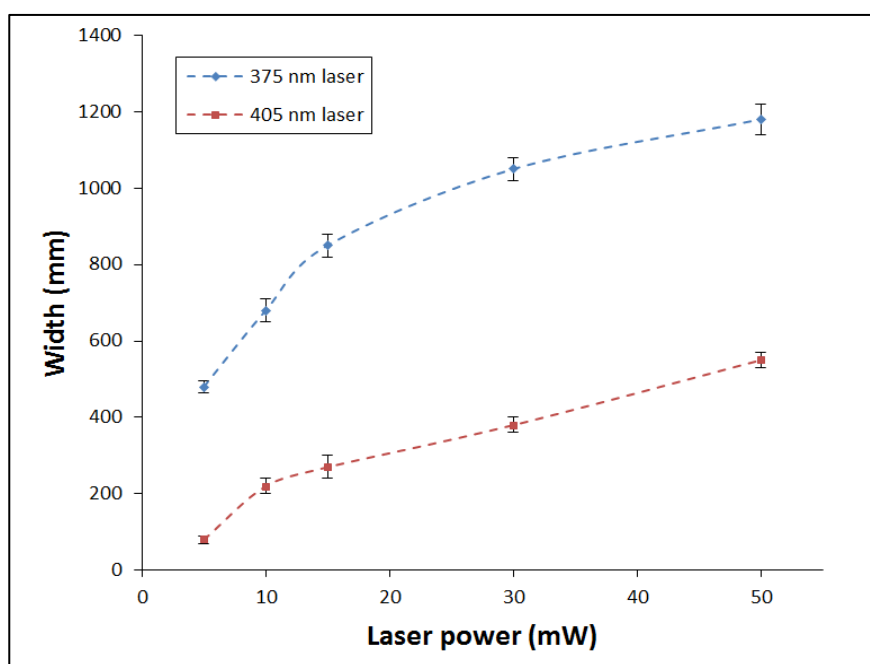


Figure 3.7 Plots show the summary of the line-widths for writing wavelengths of 375 nm and 405 nm, at different incident powers up to a maximum value of 50 mW, but a common writing speed of 6.7 mm/s. Error bars indicate the standard deviation for 5 measurements along each line and lines are a simple guide for the eye.

Figure 3.8 shows a series of parallel lines that were patterned with the same laser-patterning conditions using two different photopolymers. As can be seen, the polymerised

lines written with SubG (Figure 3.8b) were more compact and had edges that were more sharply-defined when compared with those formed with DeSolite® (Figure 3.8a) under the same patterning conditions. Figure 3.9 shows the variations in the width of the lines patterned with the 405 nm laser for the two different photopolymers at different incident laser powers but the same scan speeds of 10 mm/s. The smallest polymerised barriers that can be formed using this technique are $\sim 50\ \mu\text{m}$ (SubG) and $\sim 80\ \mu\text{m}$ (Desolite®).

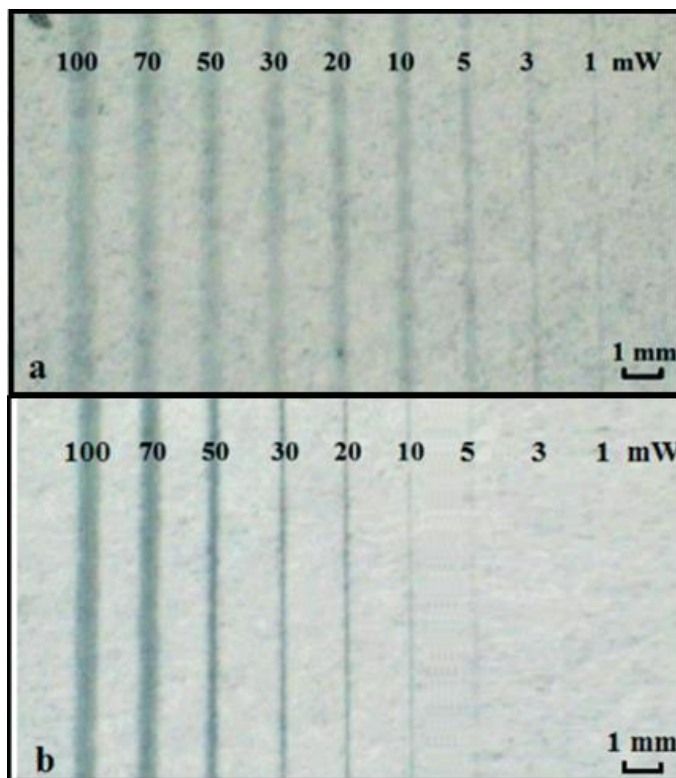


Figure 3.8 Sets of polymerised lines formed using a 405 nm c.w. laser with different incident powers and two different photopolymers. a) DeSolite® and b) SubG.

An important advantage offered by LOC-type fluidic devices is their cost-effectiveness, which is a consequence of their much reduced sizes, so an important requirement is to implement the entire device with the smallest possible footprint. Using our LDW procedure for making such compact devices would require finding the smallest dimensions not only for the fluidic barrier walls but also for the fluidic channels. To this effect, we initially investigated the minimum barrier wall widths that could be created with our procedure using a c.w. 405 nm laser. As shown in Figure 3.10, under the appropriate writing conditions (scan speed of 10 mm/s, incident power of 10 mW), we could polymerise lines with widths of $\sim 50\ \mu\text{m}$, which is smaller than the dimensions we could achieve using the pulsed laser, and to our knowledge, is also the smallest line-width reported so far for barrier-walls in paper-based devices. Although such feature dimensions would have been possible through lithographic procedures, our LDW method presents a far less complicated approach as it does not require lithographic masks or

cleanroom-intensive processing. However, fluidic channels formed with barrier-walls that had such narrow line-widths were found to be unable to contain and guide fluids, and instead, a minimum line-width of $\sim 120\ \mu\text{m}$ was required.

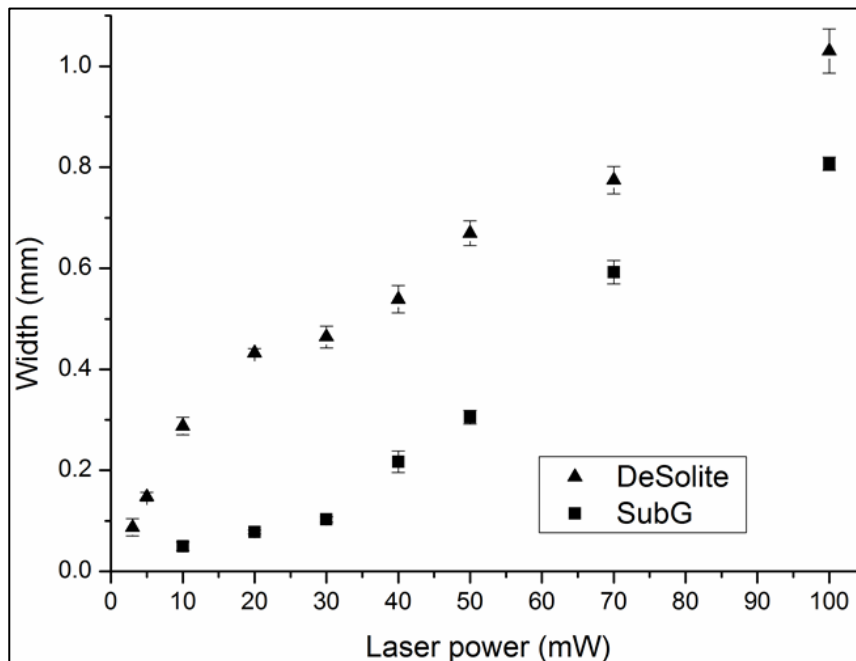


Figure 3.9 Graph showing the widths of the laser-patterned lines for different incident laser powers and a scan speed of 10 mm/s. The lines were patterned with a c. w. 405 nm laser and the photopolymers used were DeSolite® and SubG. Error bars indicate the standard deviation for 5 measurements along each line.

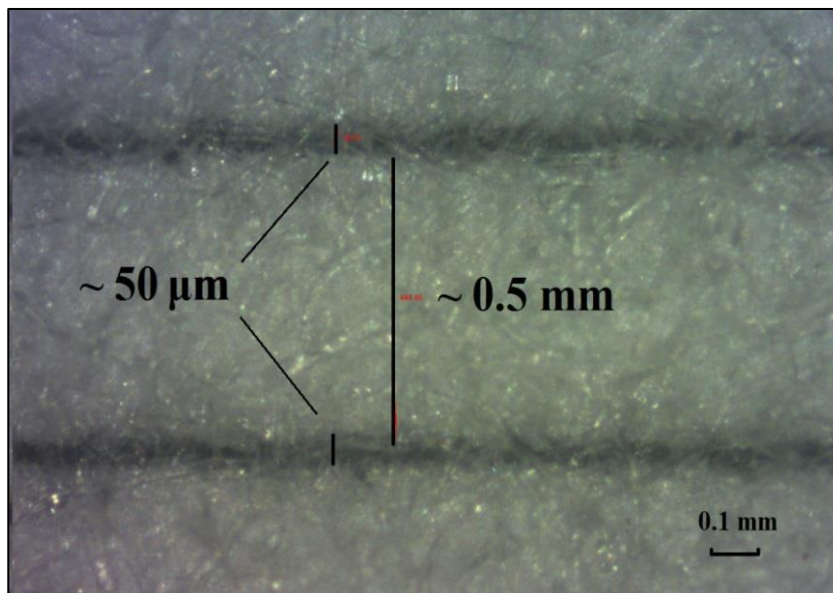


Figure 3.10 Microscope images showing two parallel lines written in SubG via LDW using a scan speed of 10 mm/s and an incident power of 10 mW at 405 nm, and having widths of $\sim 50\ \mu\text{m}$.

To further investigate the quality of the polymerised barriers, namely the ability to contain and guide the liquid, these polymerised lines were tested by introducing ink in the laser-written fluidic patterns. As shown in Figure 3.11, the squares with line-widths greater than $\sim 120\ \mu\text{m}$ and $\sim 300\ \mu\text{m}$ for Desolite® and SubG respectively were able to contain ink. The minimum line-width for a barrier wall to contain ink was found to be different for the two photopolymers.

According to the results described above, use of a c.w. laser significantly increases the writing speeds by about ~ 150 times as compared to those for a pulsed laser. This shows that the technique has one essential element needed for the stage of commercialisation and mass production.

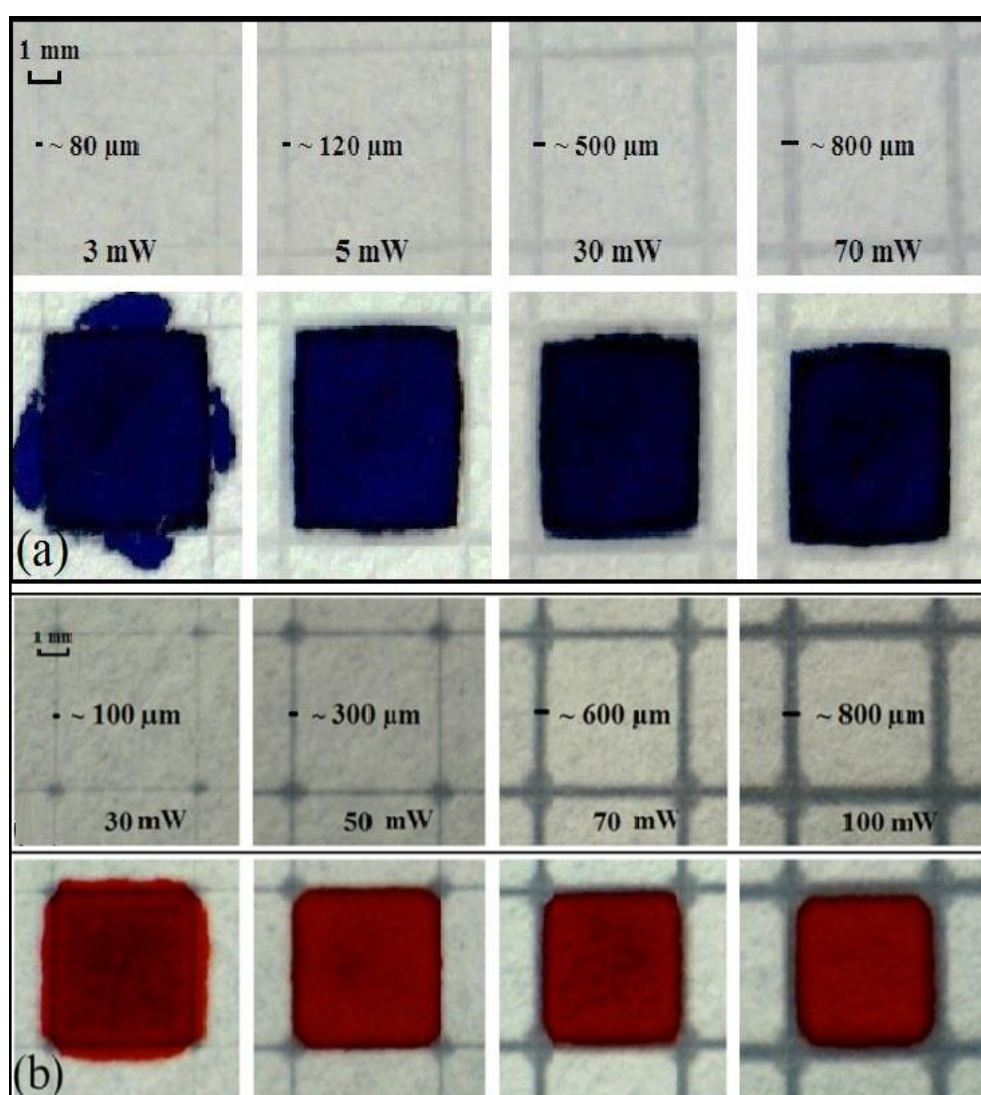


Figure 3.11 Camera images of a series of square structures before and after the introduction of ink; a) written in Desolite®; b) written in SubG.

Further experiments were done for exploring the minimum dimension that can be achieved using this technique for fabrication of a fluidic structure. Figure 3.12a shows four

fluidic channels with different channel dimensions. After the introduction of the red ink into the channel, the 80 μm channel was still able to contain and guide, which is shown in Figure 3.12b. This is the smallest fluidic structure dimension for a fluidic channel on cellulose paper reported so far and is better than the dimensions that can be achieved with the wax-printing procedure that is currently one of the most widely used for the creation of fluidic patterns in cellulose paper, and for which the dimension limitations are imposed by the undue spreading of wax during the heat-treatment/wax-penetration step. The smallest dimension for fluidic patterns reported recently on a fibre-glass substrate through the use of a simple cutting method is $\sim 137\ \mu\text{m}$ [104].

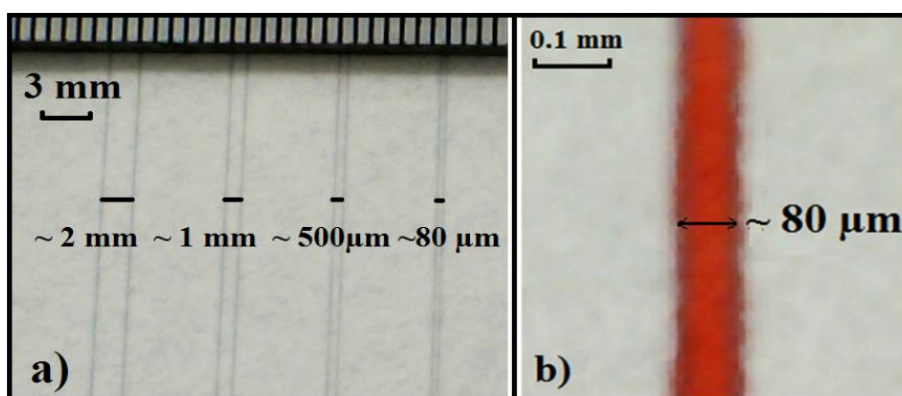


Figure 3.12 Camera images show a) four fluidic channels with different widths formed by barrier lines with a width of $\sim 120\ \mu\text{m}$, b) the $\sim 80\ \mu\text{m}$ fluidic channel in a) guiding red ink.

3.3.2 Patterning of nitrocellulose membrane

The next set of experiments was the patterning of nitrocellulose membrane. As mentioned above, the photopolymer we currently use is DeSolute® 3471-1-14, however, it is extremely viscous, having a viscosity of $\sim 10,000\ \text{mPas}$ at $25\ ^\circ\text{C}$, and so we diluted it in toluene in the ratio of 5:3 (v/v) to enable it to soak into the nitrocellulose substrates. These were then left to dry under ambient laboratory conditions, prior to the laser-patterning step.

The first structures to be investigated were simple straight-line channels which would allow determination of some of the basic parameters of laser exposure (scan speed and laser power) required. As shown in Figure 3.13a, two parallel channels were written by scanning at laser powers of 10 mW and 5 mW under the same scan speed of 10 mm/s, and the fluid containing properties of these channels was tested by flowing red ink (Parker, France) through them. As can be seen in Figure 3.13b, the scanned lines form the barrier walls that contain and guide the flow of red ink through these fluidic channels without any observed sideways leakage.

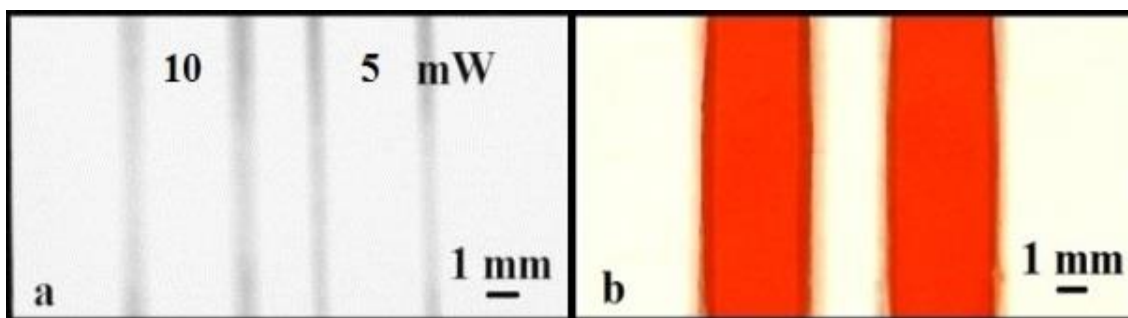


Figure 3.13 Images showing two fluidic channels formed by writing parallel lines with two different laser powers of 10 and 5 mW at a speed of 10 mm/s.

Because toluene is volatile and easily evaporates under ambient laboratory conditions, it proved difficult to uniformly soak the substrates with the photopolymer. As the width, depth and uniformity of the polymerised lines are directly dependent on the polymer concentration in the substrate, any variations would thus translate into lines having undesirable variations. To circumvent this, we chose to soak the nitrocellulose paper directly with the undiluted photopolymer. However, due to its high viscosity, it took ~ 20 seconds for the paper to fully absorb the photopolymer.

To investigate the patterning performance on nitrocellulose, the same sets of experiments were repeated as those in the case of patterning of cellulose. The relationship between the width of polymerised lines and the patterning conditions is plotted in Figure 3.14. The line widths obtained increase from $\sim 70 \mu\text{m}$ and $\sim 50 \mu\text{m}$ to $\sim 340 \mu\text{m}$ and $\sim 270 \mu\text{m}$ at scan speeds of 5 mm/s and 7 mm/s respectively for an increase in the laser power from 0.2 mW to 10 mW. Similarly, for a scan speed of 10 mm/s, the widths of the polymerised lines increase from $\sim 50 \mu\text{m}$ to $\sim 220 \mu\text{m}$ as the laser power increases from 0.3 mW to 10 mW. Overall, the width of the lines increases with the increase of the laser output power and decreases with the decrease of the laser scan speed and the minimum line width that was achieved is $\sim 50 \mu\text{m}$, which is comparable with the case of cellulose.

As our final goal was to pattern the nitrocellulose membranes for implementation of LOC fluidic devices, we then tried to identify the optimum conditions needed to form barriers that can contain and guide the fluid - as this is one of the most crucial requirements. Figure 3.15a shows a set of straight channels having a common width of 3 mm, written with a constant laser scan speed of 10 mm/s for varying laser powers ranging from 10 mW to 0.3 mW. Figure 3.15b is an image of the same set of channels after the introduction of red ink into each channel. As can be seen from this figure, the ink solution only leaks out of the channel written with the lowest laser power of 0.3 mW, and all other channels contain and guide the flow without any leakage. Using the proposed LDW photo-polymerisation technique the smallest size of barrier line that we can form in nitrocellulose and which is

able to contain and guide the flow, is $\sim 60\ \mu\text{m}$ - the smallest dimensions reported in the literature [6].

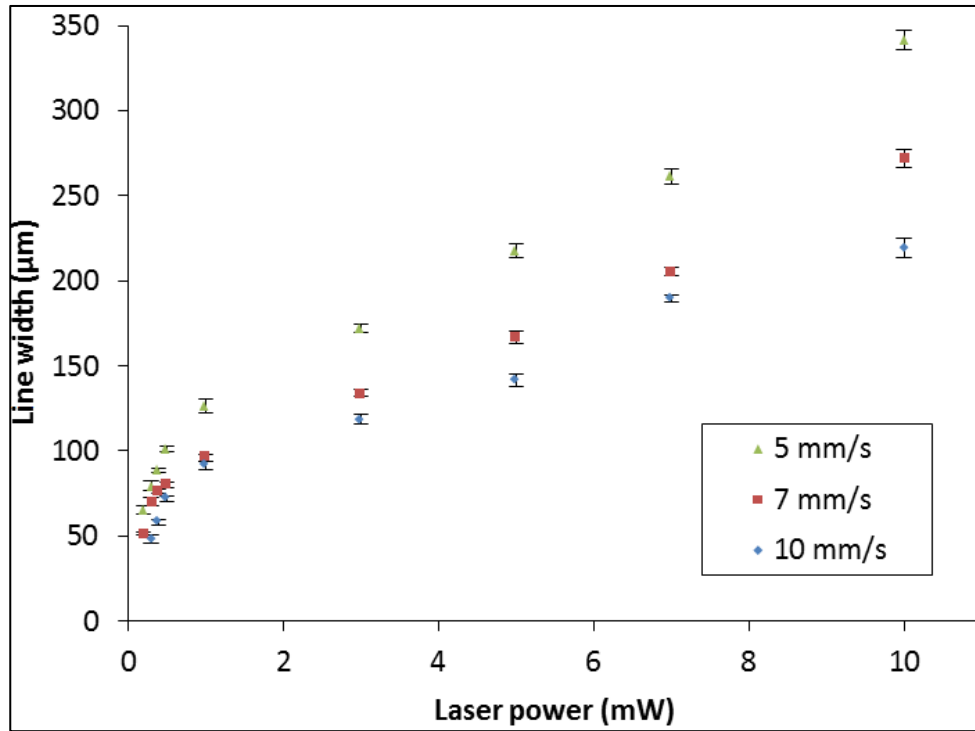


Figure 3.14 Plots showing the variations in the widths of the polymerised lines for different laser powers at three different scan speeds.

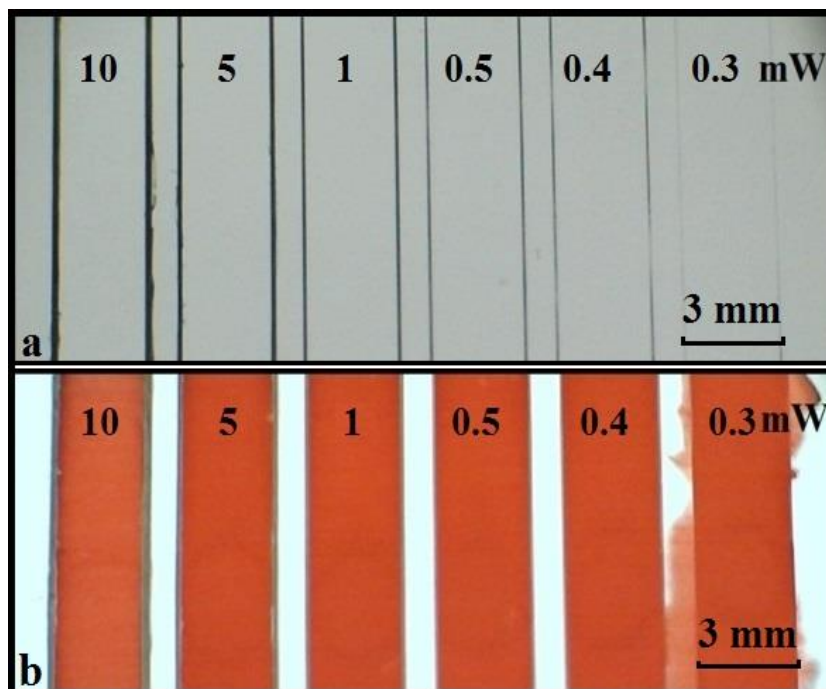


Figure 3.15 a) Image showing a set of fluidic channels formed under different patterning conditions; b) after the introduction of red ink into each channel.

In the next step, we aim to find out the minimum width for a fluidic channel that can be patterned via LDW that will successfully allow fluid flow. While the typical widths achieved with the wax printing procedure, which is currently one of the most widely implemented techniques, ranges from 0.5 mm to 4 mm [47], we anticipated that our LDW technique could produce channel widths that might be around one order of magnitude lower. To identify the smallest widths such fluidic channels can have, as shown in Figure 3.16a, we patterned several pairs of parallel lines with different channel widths which were fed by the open U-shaped structures that would form the fluid reservoirs for the ink used. All these lines were scanned at the same laser scan speed of 10 mm/s and an incident laser power of 1 mW, a condition we knew produced barrier-walls that reliably contained the fluid. As shown in Figure 3.16b, after the introduction of the ink, channels down to a width as small as $\sim 100\ \mu\text{m}$ could reliably guide the fluid. To our knowledge, this is the smallest achievable dimension reported so far for any existing paper-patterning technique, and this can be vital for reducing the footprint of such devices, which in turn can help reduce the costs of such devices because you would then need less reagents, and less of the bodily samples/fluids [6, 47].

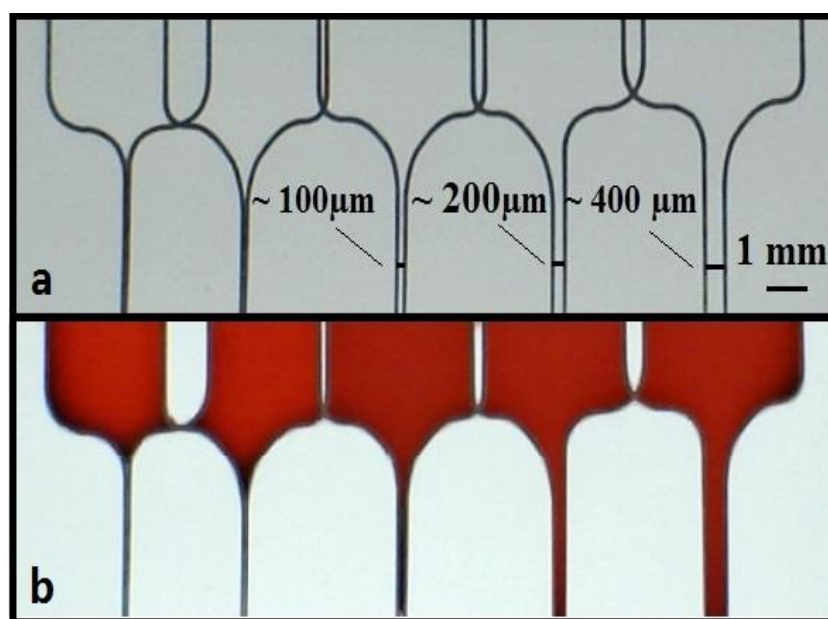


Figure 3.16 Photographic images showing a set of parallel fluidic channels having different channel widths: a) before, and b) after the introduction of red ink.

The next set of experiments relates to the writing of wells in paper, and their ability to contain fluid. Figure 3.17a shows a set of square wells with dimensions of 5 mm \times 5 mm with barrier-walls written using laser powers ranging from 0.3 mW to 10 mW at a fixed scan speed of 10 mm/s. Red ink was again introduced in a fixed volume of 3 μL that was sufficient to fill each square completely. As shown in Figure 3.17b, we similarly observed

leakage only for the wells written with a laser power of 0.3 mW, which we have determined to be the lower threshold value.

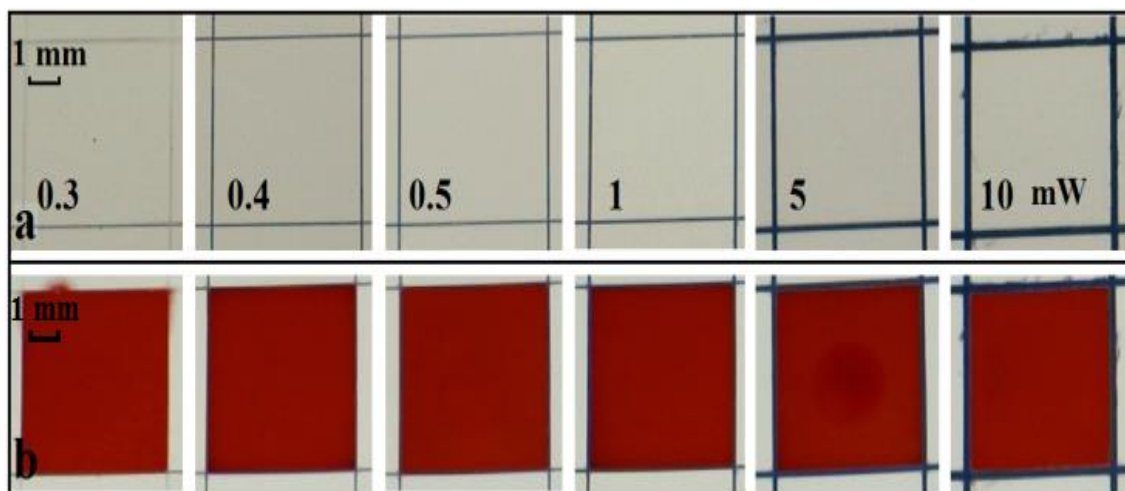


Figure 3.17 Photographic image showing a) a series of 5 mm × 5 mm square-shaped wells patterned with different laser powers of 0.3, 0.4, 0.5, 1, 5, and 10 mW at a constant scanning speed of 10 mm/s; b) after the introduction of 3 µL of red ink into each square.

The final step was to determine the maximum volume of liquid that these wells could contain without any sideways leakage, a parameter which is important when dealing with actual samples under test, where loss of potentially expensive samples of reagents outside the test area must be avoided. A similar set of squares was written (shown in Figure 3.18a) into which red ink of different volumes ranging from 1 µL to 15 µL (Figure 3.18b) was introduced. Even when the volume increased to a value of 15 µL, the wells were still able to hold the ink solutions without any overflow.

On further investigation, we observed that a surface-relief ridge was formed along, and above the patterned lines because of the polymerisation of the photopolymer that was present on the surface of the nitrocellulose membranes prior to the laser-patterning step, and has been investigated through surface-profile imaging measurements. The trace in Figure 3.18c is a surface-profile scan across a laser-polymerised line, and clearly shows the presence of a ridge (having a width of ~ 120 µm and a height of ~ 8 µm) along the polymerised line. Hence it can be concluded that the polymerised patterns defined in nitrocellulose using the LDW method not only show excellent ability in containing small liquid volumes but also show the capability to contain larger liquid volumes without any undesired spill-over, a characteristic that is of immediate interest for practical diagnostic assays.

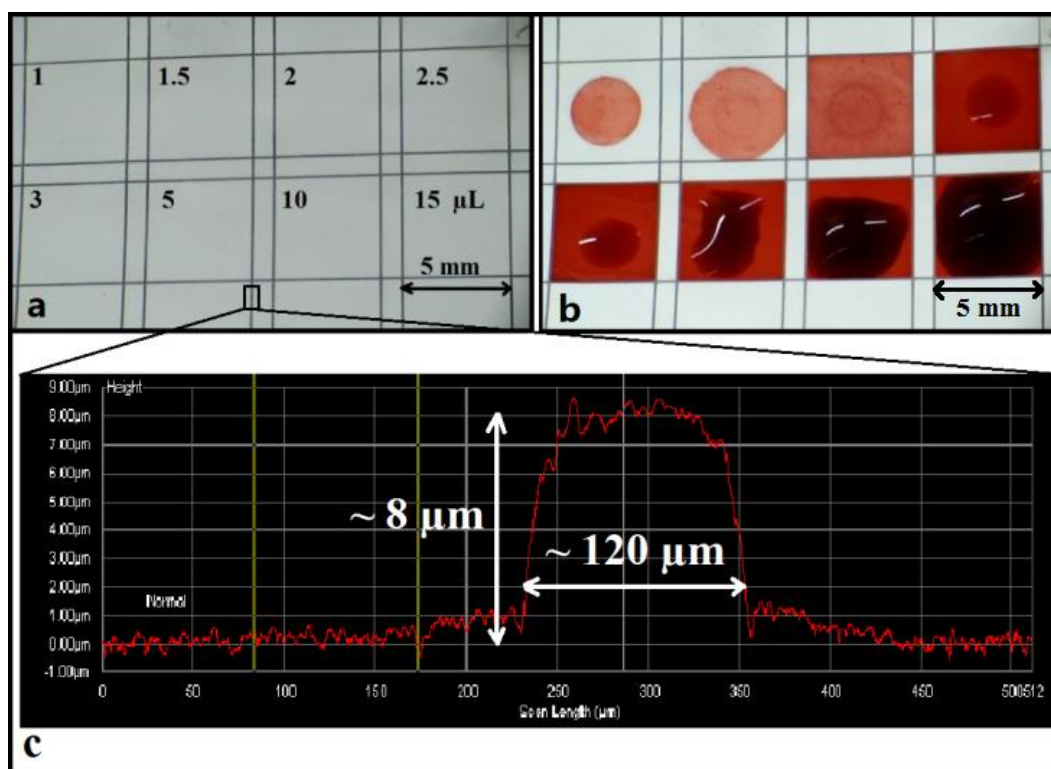


Figure 3.18 Images showing a) a series of 5 mm × 5 mm wells patterned with a laser power of 3 mW and a scan speed of 10 mm/s; b) after the introduction of red ink in different volumes of 1-15 μL into each square; c) a surface profiler scan across a polymerised barrier-wall.

3.3.3 Patterning of other porous materials

To further explore the compatibility of this technique, the next set of experiments was patterning of other porous materials. The photopolymer and solvent used here were SubG and acetone and the laser was a 405 nm c.w. laser. The results of these patterning experiments for the different materials are shown in Figure 3.19, 3.20 and 3.21.

First of all, a glass fibre filter was tested as it is one of the important component materials for a lateral flow type device. It is normally applied as the conjugate pad to hold the detector particles in a dry state and keep them functionally stable until re-hydrated by the sample [105]. As the liquid moves through the glass fibres, the detector particles previously located in the glass fibre will be released rapidly and quantitatively [106]. The result of patterning glass fibre filter is shown in Figure 19a: sets of channels were patterned in glass fibre filter with different laser incident powers at a fixed scan speed (10 mm/s), which lead to different barrier widths. After introducing red ink into each channel, all the channels were able to contain and guide the red-ink through them as shown in Figure 19b.

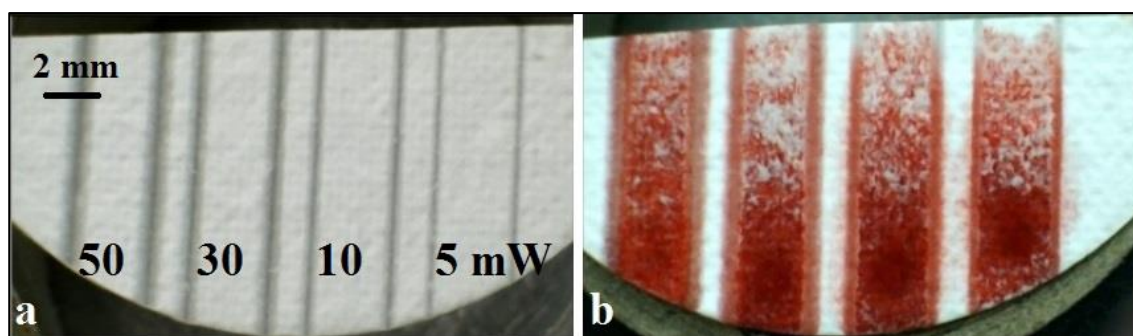


Figure 3.19 Images showing a set of parallel fluidic channels writing in glass fibre filter with different laser power at a fixed scan speed a) before, and b) after introduction of red ink.

Recently, fabric-based devices have been widely studied and regarded as an alternative to paper-based devices for low-cost POC diagnostics [107-110]. Many types of fabric have been explored for developing fabric-based microfluidic devices including nylon [108], polyester [111] and silk [109]. The advantages of using fabric as a material for fabrication of microfluidic devices include lightweight, one dimension capillary flow, flexibility, possibility of large volumetric flow, straightforwardness of chemical modification and also potential for large-scale fabrication [107, 108, 112].

To explore the effectiveness of our LDW technique for patterning fabric materials in order to fabricate fabric-based devices, we then tried to pattern a polyester wipe as a proof-of-principle demonstration. As shown in Figure 3.20, a T-shape structure was patterned in filament polyester wipe, which nicely contained and guided the fluid after the introduction of red ink from the upper end of the vertical arm of the T, which served as the sample inlet point. This shows a potential capacity of our LDW procedure as an accessible technique for making fluidic structures in fabric materials.

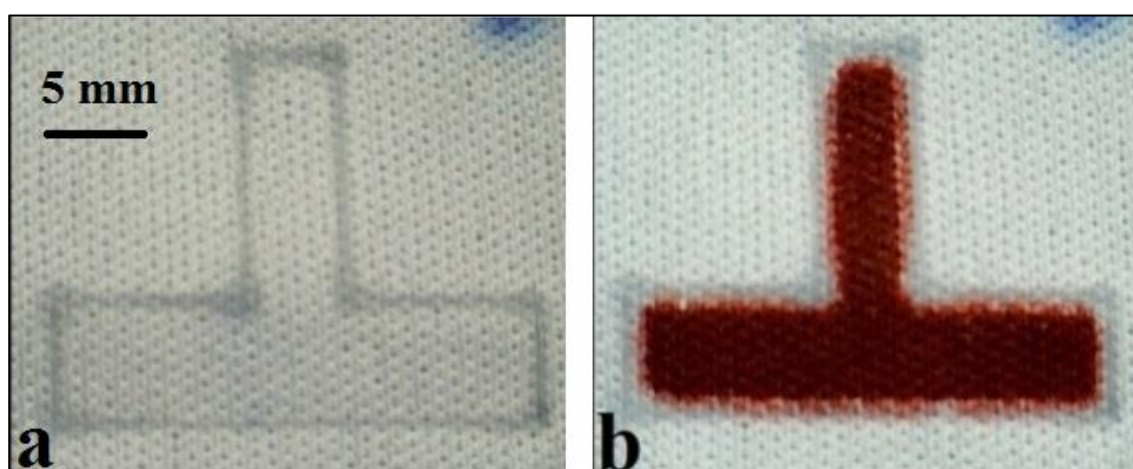


Figure 3.20 Images showing a T-shape structure patterned in filament polyester wipe a) before, and b) after the introduction of red ink.

Apart from these, we also tried to pattern a range of other porous materials, which may have further potential applications in different fields that we have not been able to explore further at the moment. As shown in Figure 3.21a and 3.21b, the patterns polymerised lines and squares in PVDF, which is a very important material in making electrical sensors and transducers due to its high piezo-, pyro- and ferroelectric properties [113-117], and printing paper respectively using our LDW technique.

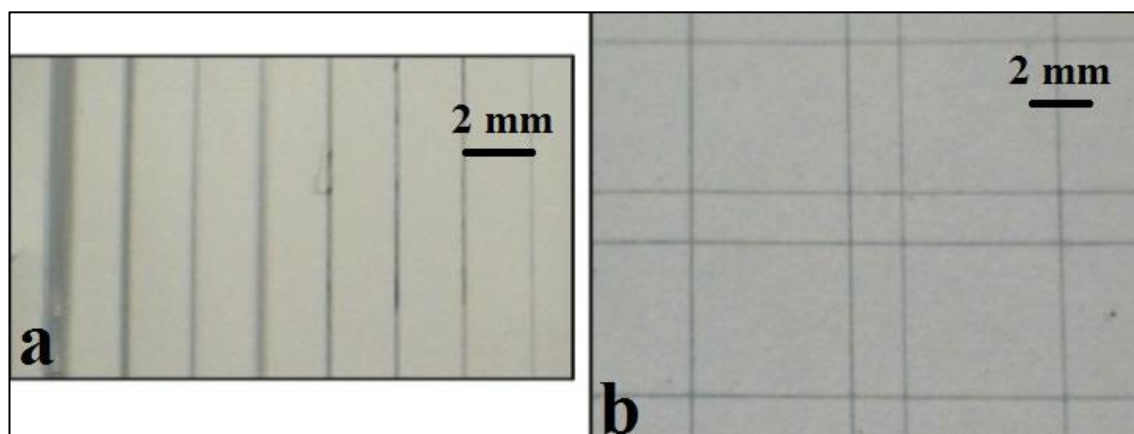


Figure 3.21 Images show the results of patterning different porous materials using LDW technique. a) PVDF and b) printing paper (photo-copy paper).

Above all, this technique can be used for patterning all kinds of substrate materials we have thought about and tried so far. These materials (glass-fibre filter, polyester and PVDF) were chosen as they are important materials used in diagnostics testing devices and protocols. Thus, we believe that in principle this method can also be suitable for patterning other kinds of porous materials having applications in diverse fields.

3.4 Performance improvement and optimisation of the LDW procedure

Above all, we have demonstrated a simple low cost LDW methodology for fabrication of paper-based devices based on simple light-induced photo-polymerisation. In contrast to the most widely used methods for patterning paper, our LDW technique is a non-contact, non-lithography and maskless procedure, which does not require cleanroom facilities and expensive equipment. However, some limitations still exist, when we consider this method as a mature technique for mass commercialised fabrication of paper-based devices. For example, the motorised stages currently used have a maximum translation range, speed and acceleration rate, and certain user interactions are required for enabling custom-designed complicated designs, such as coding and calculation etc. On the other hand, a problem has arisen during the patterning of nitrocellulose membranes that both the

photopolymer and the solvent applied during the patterning procedure alters the properties of the NC substrate to some extent, i.e. the flow rate. Although several studies have been done to identify the best photopolymer and solvent to minimize these effects, it seems to be not possible to completely eliminate this problem due to the global treatment process that is currently applied to the nitrocellulose membranes.

Therefore, to overcome these limitations and further develop our LDW technique to eventually meet all requirements for large-scale commercialized fabrication of paper-based devices, several optimisations and improvements have been explored as described in the following sections.

3.4.1 Introduction of a galvo scanner

As shown in the schematic in Figure 3.1, the basic LDW setup we first built involves linear motorised stages (DDSM100, Thorlabs, Inc.), which have a maximum translation range of 10 cm in each direction. The maximum translation speed and acceleration rate that can be achieved are 500 mm/s and 5000 mm/s² respectively. Thus the maximum patterning speed and hence the throughput is limited by the maximum achievable sample translation speed via these motorised stages. Meanwhile, as described previously, the resulting patterned polymer structures are dependent on the laser fluence, which is directly determined by the scan speed. Thus the acceleration and deceleration of the stages need to be taken into consideration and only the centre uniform speed is acceptable during the fabrication. As a result, the actual working ranges are further limited below 10 cm due to the acceleration and deceleration of the stages.

Furthermore, because of these speeding up and slowing down effects, complicated continuous designs, such as sharp corners, are not achievable with a constant speed. In order to solve this problem, a laser shutter is required to be integrated into the basic LDW setup, which only opens and lets the beam pass through when the stage has accelerated to a constant speed and closes when it starts to decelerate. As a result, complicated programs are required in order to synchronise the stages and the laser shutter for patterning of complex designs. Finally, for dual-axis applications, two linear motorised stages are bolted together in an XY configuration by using an XY adapter plate. Thus complex dual-axis structures, i.e. curves, require lots of user interactions, such as coding and calculation etc., in order to operate the movement of the stages in two directions and it is even worse if a circle or semi-circle is needed.

To overcome the above limitations, a 2D galvo scanner was introduced. These devices are used in many applications such as laser light show, laser marking, laser machining, wafer

dicing, barcode reader and laser ablation. Basically, a galvo scanner is a computer-controlled electromagnetic device that moves mirrors mounted on the end of rotary shafts. The mirrors are attached to high-speed, limited rotation direct current motors and the motion is governed by an internal position detector to allow feedback control of the motor. This is done through a signal that provides position information that is proportional to the rotation of the motor. These movable mirrors are applied to steer the laser beam to "draw" images. Galvo scanners are typically identified by their speed of operation, measured in kilo points per second (available from 8k to 60k per second). The faster the galvanometers, the smoother and more flicker-free the projected image. Each mirror inside the galvo scanner moves the beam in one plane, either the X axis or Y axis. Then the full movement of the laser beam within a defined two-dimensional square area is achieved by placing two mirrors close together at 90 degrees to each other. To realise the control of the scanning motion, scanners need a rotary encoder and control electronics that provide, for a desired angle or phase, the correct electric current to the galvanometer. A software system is usually required to control the scanning motion and collect the feedback data.

Based on the LDW setup in Figure 3.1, as shown is the schematic in Figure 3.22, a 2D galvo scanner (Laser 2000 Ltd. UK) is introduced into the optical path just after the focusing lens. The focus length of the lens is carefully selected that allows the beam to remain focused onto the substrate when passing through the galvo scanner. In this case, the substrate is immobilised during the LDW step, while the scanner projects user-defined patterns on it. The scan speed of the galvo scanner ranges from 1 mm/s to more than 100 m/s, which is more than sufficient to meet the requirement for large-scale fabrication. On the other hand, the software designed for controlling these scanners is a package similar to CAD packages made for technical drawing and optimised for laser marking. It has a quite straightforward interface that allows the user to create any complicated designs by simply drawing inside the software, which does not need additional user-involved calculations or coding.

In addition, the software also allows direct import of data/design from external sources including both vector files and raster files. For vector files, images are created using lines and curves joined at points by nodes to create an outline of a shape. This is then filled to create a solid shape if desired. The main advantages of using vectors are: firstly, this uses the same principle for drawing the image that is used for directing the beam; secondly, scalable images that can be enlarged or shrunk without the loss of any quality; finally, typically smaller file sizes than raster images. Overall, vector files are ideal for company logos and other clean-edged images, or where processing time needs to be kept to a minimum. On the other hand, for raster files, images are created using small dots or pixels

to make an image. This is the most common type of image used within computing and is ideal for displaying complex shapes or images that could not otherwise be easily simplified into vectors. The main advantages of raster images are their high level of detail and they are commonly used within computing. Therefore, raster files are ideal for marking photographs or other complex images that cannot be easily translated into lines and curves.

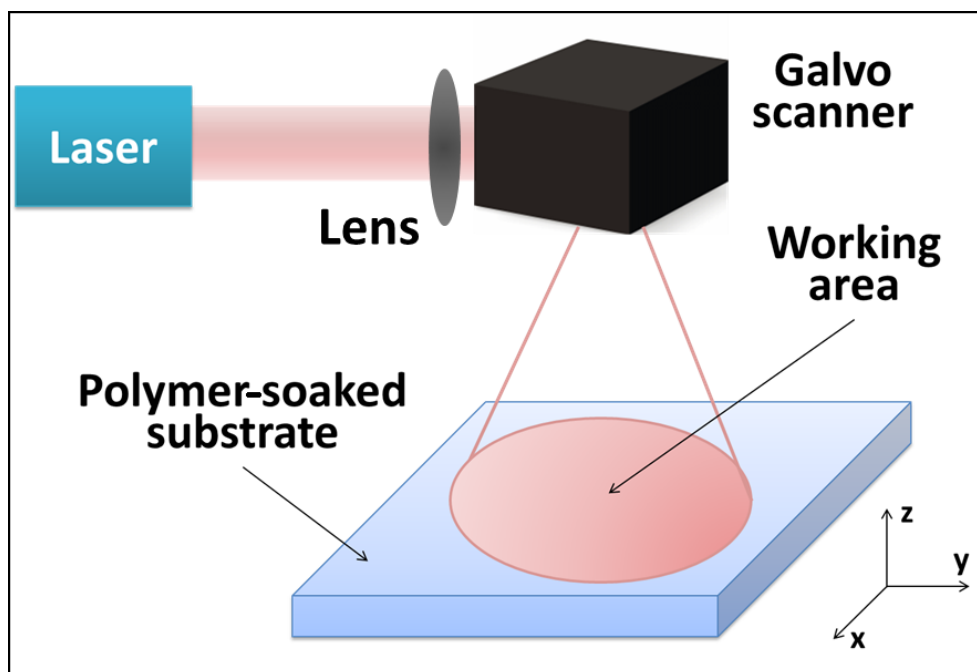


Figure 3.22 Schematic of the laser-based direct-write setup with the introduction of a galvo scanner used to form polymerised hydrophobic structures in a porous substrate.

As the first set of experiment with the implementation of the galvo scanner, a few examples of text were entered directly inside the scanner software and the patterning results are shown in the image in Figure 3.23. The polymerised polymer barriers that define the text were patterned in a cellulose filter paper using a galvo scanner with a laser output power of 30 mW at a scan speed of 50 mm/s.

Finally, more complicated structures were patterned in NC using the galvo scanner and then their performance was tested via the introduction of coloured dyes. As shown in Figure 3.24a, a triple spiral design was patterned in NC using a laser output power of 10 mW at a scan speed of 200 mm/s. Each of these three spirals has two unconnected flow paths. Figure 3.24b is an image of the bottom left spiral after the introduction of a yellow dye into one of the two flow paths from the centre of the spiral. The dye was guided and flowed along the flow path into the centre junction of three spirals without any leakage from the side of the channel. Finally, as shown in the image in Figure 3.24c, another coloured dye (red) was introduced into the second flow path in the same spiral in Figure

3.24b. As can be seen from this image, the red dye solution was contained and guided within the flow path without any leakage and contamination to the adjacent path.

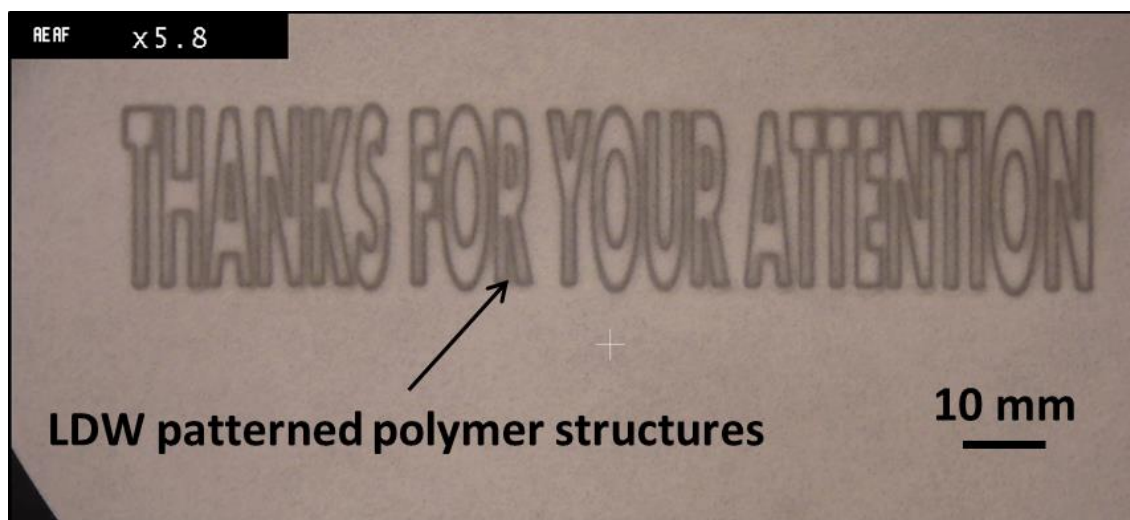


Figure 3.23 Image shows ‘THANKS FOR YOUR ATTENTION’ text that was patterned in cellulose filter paper using the galvo scanner with a laser output power of 30 mW at a scan speed of 50 mm/s.

In conclusion, with the introduction of a galvo scanner into the primary LDW setup, the fabrication speed can be significantly increased to over one meter per second at a laser power of ~50 mW. As a typical LFD device is only about few centimetres, this means that many devices can be fabricated per a second, which is sufficient for mass fabrication. On the other hand, the user friendly interface allows easy programming of the scanner with just simply drawing inside the software or importing both vector and raster files from external sources, which makes any complicated designs easily achievable, hence brings great flexibility during the fabrication procedure.

3.4.2 Introduction of local deposition procedure

It is widely known that NC is a very vital material in biological applications and is one of the most important components for LFDs, thus the patterning of NC is always regarded as one of the main purposes of introduction of our LDW technique. However, NC is also well known as a very fragile polymer-based porous material, which is extremely difficult to preserve in order to keep its original properties.

According to the experiments of patterning nitrocellulose membranes described earlier, a problem occurred in the photopolymer and the solvent applied during the patterning and development procedures alter the properties of the nitrocellulose membranes substrate. One of the main properties that can be easily observed to be altered after patterning

procedure is the flow rate, which is hugely reduced with the application of both the photopolymer and the solvent during the patterning steps, an unwanted side effect. In addition, the reduction of the flow rate seems to be increased with the increase of the time that the nitrocellulose membranes are immersed with photopolymer and the solvent. Although several different photopolymers, as well as solvents, have been tested as described previously in the materials and reagents section, it seems that these influences can only be minimised rather than completely avoided.

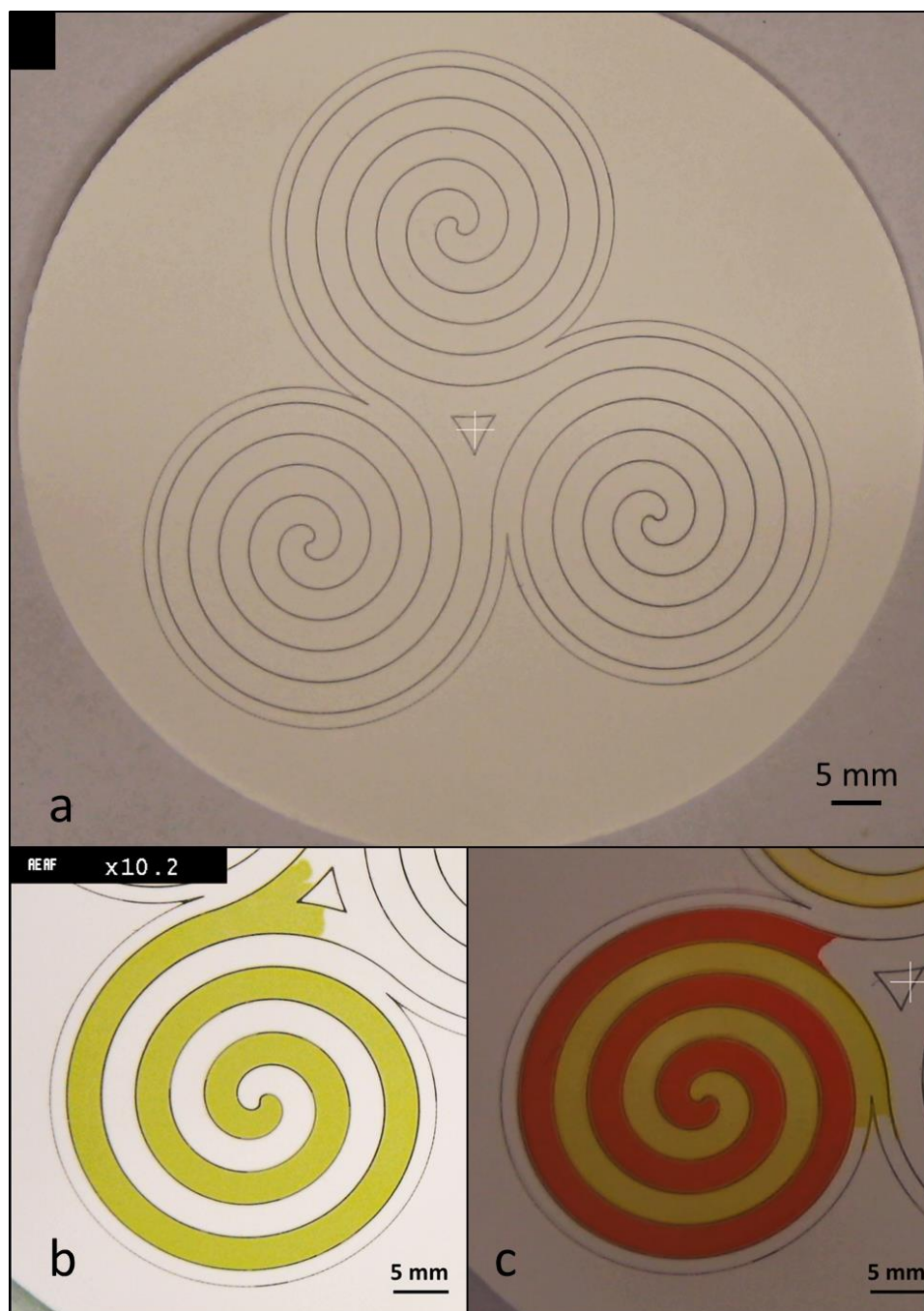


Figure 3.24 Photographic images showing a) a triple spiral design patterned in NC via a galvo scanner; b) the introduction of yellow dye into one of the spirals and c) the introduction of red dye into the same spiral, which shows no over contamination.

Apart from the flow rate, we believe that other properties might also be altered due to the contact with the photopolymer and solvent to some extent, although no clear evidence has been observed and no further studies have been done. Finally, though these effects were only observed in nitrocellulose membranes so far and have not yet been identified in other porous materials, which are much less fragile, such as cellulose filter paper, glass fibre filter etc., we believe that certain effects on the properties will still exist due to specific polymer or solvent contamination of the original substrate materials.

In order to overcome these problems, the idea of local deposition of photopolymer instead of global soaking of the substrate with the photopolymer has been proposed. The updated setup is described in the schematic in Figure 3.25: a local deposition module is introduced into the initial LDW setup shown in Figure 3.1. As shown in the schematic, the photopolymer is locally deposited onto the substrate with user-defined designs, and then a laser beam follows the deposited tracks, which induces the polymerisation of the deposited photopolymer. The fluidic structures are defined by the deposition procedure and no further development procedure is required, as there is no unwanted material (i.e. un-polymerised monomers) that needs to be removed.

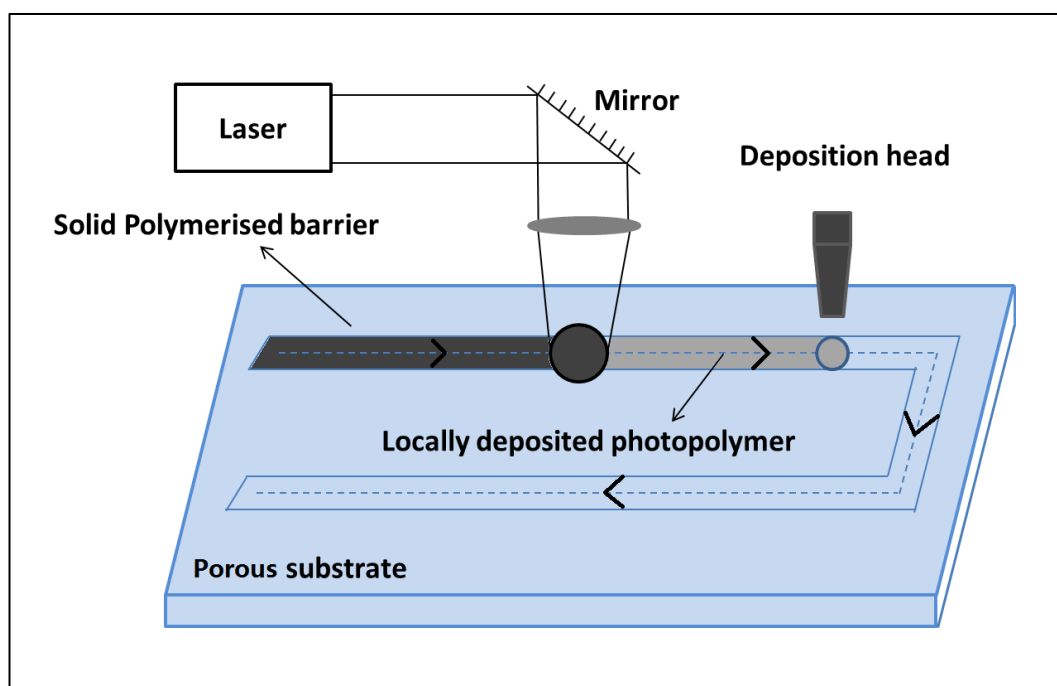


Figure 3.25 Schematic of the modified laser-based direct-write setup with the introduction of local deposition of photopolymer for creating polymerised hydrophobic structures in the porous substrate.

The whole patterning procedure is described in the step-wise schematic in Figure 3.26: two simple steps are involved, which are local deposition followed by laser polymerisation. In the first step, the photopolymer is locally deposited onto the substrate with a pre-

programmed design. The photopolymer will then extend through the thickness of the substrate below the deposited areas via the capillary force after a very short period of time (normally less than a few seconds) depending on their viscosity. For the second step, after the photopolymer has extended through the full thickness, a laser beam is applied to scan along the pre-deposited photopolymer tracks. During the second step, the dimension of the laser beam is carefully adapted in order to make sure that it is larger than the width of the deposited patterns. This is to ensure that no un-polymerised material will be left in or on the substrate after the laser scanning step, as there will be no development procedure applied afterwards.

Above all, the remainder of the substrate is not either exposed to any photopolymer or solvent due to the local application of the photopolymer and the elimination of the development procedure. As a result, the properties of the patterned substrate remain unmodified, which completely bypasses the problems that can occur during the initial LDW procedure when the global application of the photopolymer and solvent are required.

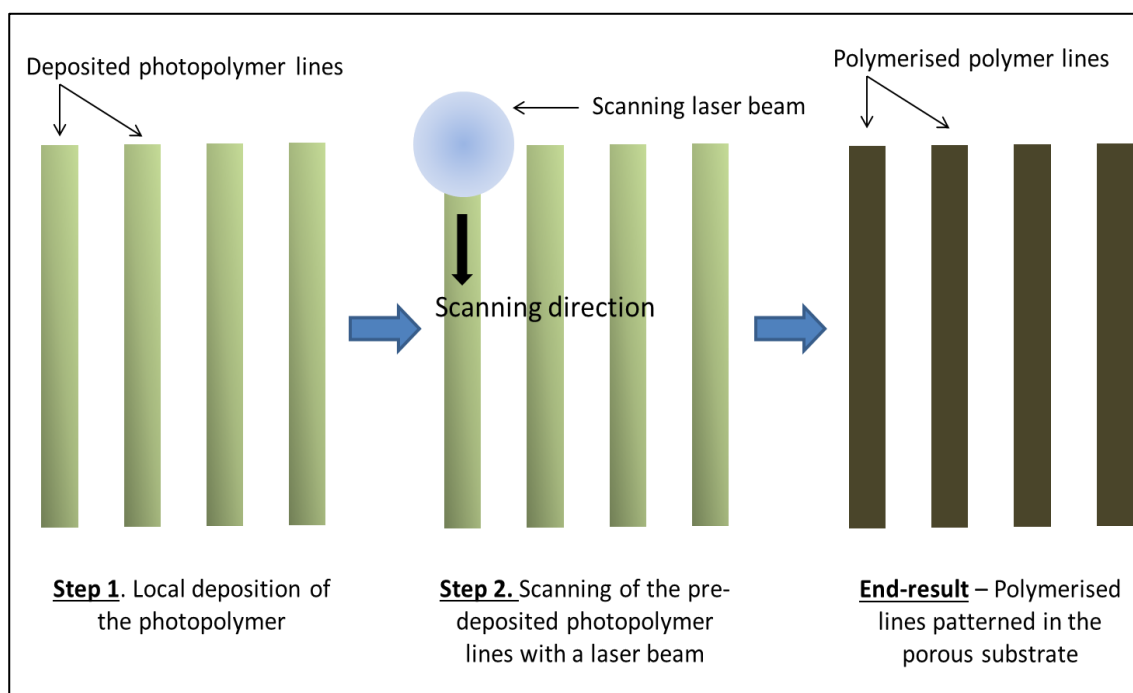


Figure 3.26 Schematic of the modified LDW paper-patterning procedure: local deposition of photopolymer followed by photo-polymerisation.

To implement the local deposition of the photopolymer, we introduced a BioDot AD3220 aspirate/dispense platform (BioDot AD3220). This platform combines three-dimensional motion control with a BioJet Plus™ non-contact nanoliter dispenser, which is a standard dispense system widely used in the LFD market for precise deposition of very small volumes of biological reagents onto various substrates. The BioJet Plus™ technology has evolved from the BioJet technology, allowing it to dispense quantitatively in a “Step-and-

Repeat” mode, as well as dispense “On-the-Fly”. The high speed, non-contact, quantitative dispensing is achieved via coupling the high-speed micro solenoid valve to a high-resolution syringe pump with synchronisation of the stage. It allows dispensable volume ranges from 1.3 nL- 2 μ L as a single drop, or more than 5 nL with “On-the-Fly” mode, which directly depends on the material properties of the dispensed fluid, especially the viscosity, surface tension etc. More details on the theory and working protocol of the BioDot aspirate/dispense platform can be found in appendix B.

As the system is designed and optimised to dispense biological reagents, which normally have viscosities close to water, it is the first time that we have tried to explore its ability for deposition of the photopolymers that usually have much higher viscosities. The main reason for choosing this platform rather than other dispense systems that are optimised for high viscosity materials is that it is popularly used in almost all of the LFD manufacture companies for deposition of bio-reagents onto their devices. Thus we aim to explore the possibility of the introduction of our laser patterned procedure with minimal change to their original production lines. Meanwhile, we are also looking forward to enabling the substrate patterning procedure (deposition of the photopolymer) and the deposition of the biological reagents ideally simultaneously via the same system with just simply using different heads.

During the dispensing, several parameters are critical, thus need to be carefully chosen in order to achieve the desired result. These parameters include drop pitch, the number of drops, drop volume and open time. Drop pitch is defined as the distance desired between each dispensed drop and number of drops is the number of dispenses needed for each row. Drop volume is the size or amount of each drop dispensed, which can be altered from the nanoliter to microliter level as required. Finally, open time is the amount of time that the solenoid valve will stay open for each dispense, which is one of the most important parameters for achieving and maintaining the steady state pressure (SSP). For a dispense system at SSP, the proper open time will result in the displaced volume equal to the dispensed volume. If the open time is too short, then over time pressure will build beyond the SSP. If the open time is too long, the SSP will be dissipated eventually resulting in drops not being ejected from the tip. As the open time is the approximate time required for the fluid to move through the valve, it increases with increasing drop size and increasing viscosity. Above all, a proper open time is extremely critical for accurate dispensing and needs to be discreetly adjusted for different fluids and drop sizes.

For the first set of experiments, two different photopolymers were dispensed onto an NC substrate using the BioDot dispense system. The photopolymer was aspirated from an external microwell plate and deposited from a height of 5 mm at room temperature. The

results are shown in Figure 3.27a: four parallel lines were deposited on NC with two different photopolymers, namely Norland 84 and SubG. All lines were dispensed at a set valve open time of 600 μ s with 40 nl drop volume, 0.5 mm drop pitch and 40 drops. It can be clearly observed in Figure 3.27 that the two photopolymers reacted very differently with the NC: Norland 84 makes grey tracks on NC, while the lines of SubG are transparent, whereas the widths of lines with both photopolymers are similar at about 1 mm. In order to test these dispensed polymer lines even without curing, red ink was introduced into channels that are formed by these parallel lines. As shown in Figure 3.27b, the dispensed lines of Norland polymer are not able to contain the red ink with serious leakages clearly observed along the lines. On the other hand, the deposited lines of SubG polymer are able to contain and guide the red ink nicely without any undesired leakage. As a result, the SubG photopolymer was chosen for the following experiments.

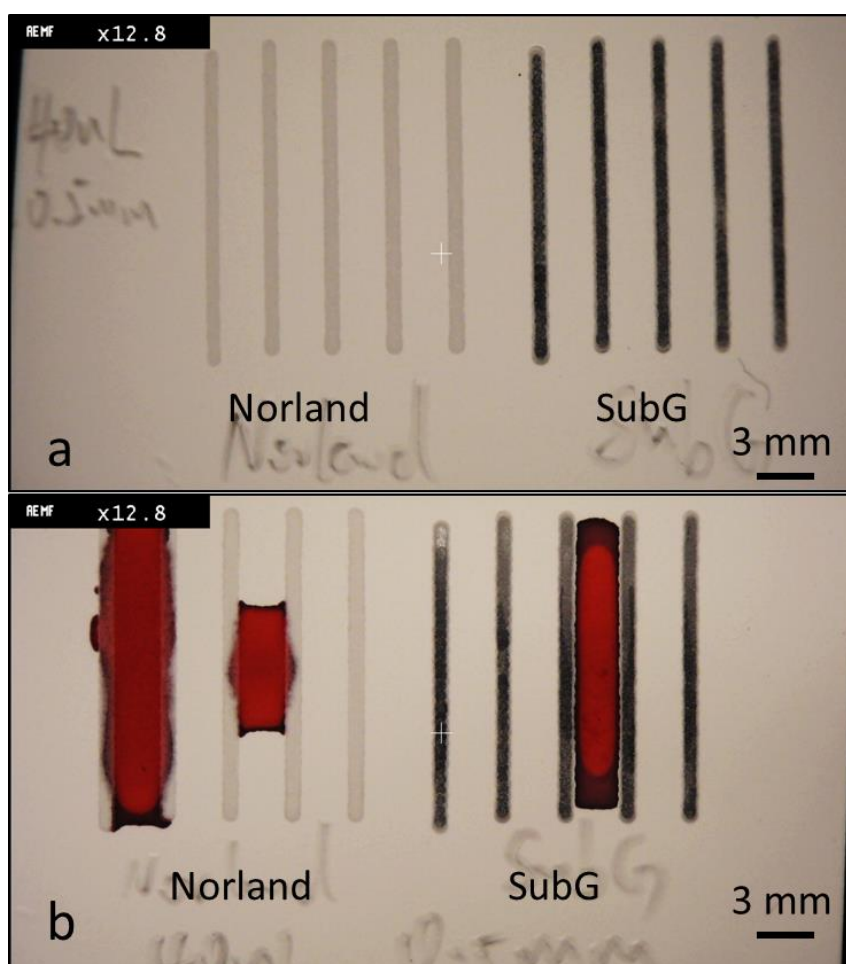


Figure 3.27 Microscope image showing two sets of parallel lines that were dispensed on NC via the BioDot dispense system with two different photopolymers with a drop volume of 40 nL at 0.5 mm pitch. a) Before and b) after the introduction of red ink into the gap between those polymer lines.

As the polymer is dispensed onto a porous substrate, it will spread both lateral and vertically over time due to the capillary force and the speed of this spread depends on the properties of the applied photopolymer, especially viscosity. On one hand, we would need a sufficient time for the polymer to spread vertically throughout the thickness of the substrate in order to achieve a complete wall; on the other hand, we also want to leave as short a time as possible before curing the polymer, as the width of the polymer line will become wider with time due to the lateral spreading of the polymer. For an NC substrate that is commercially available, the thickness is normally only about 80 μm , thus in our experiments the spread of the photopolymer from the top surface throughout to the bottom is normally accomplished within seconds. Therefore, we made an assumption that the spread of the photopolymer throughout the thickness of the NC substrate happens immediately after dispensing.

In order to study how this spreading of the photopolymer affects the width of the dispensed lines, two sets of parallel polymer lines were dispensed onto NC substrate with the same dispensing parameters, namely 40 nL drop volume, 0.5 mm drop pitch with a valve open time of 600 μs . One set of these dispensed polymer lines was cured with the 405 nm laser immediately after dispensing, while the other set was left in a black box overnight without exposure to light. The images of both samples were captured using a USB camera as shown in Figure 3.28: a) cured sample and b) non-cured sample. It can be clearly observed from the images that the lines in the non-cured sample are much wider than those in the cured sample, which is almost two to three times wider.

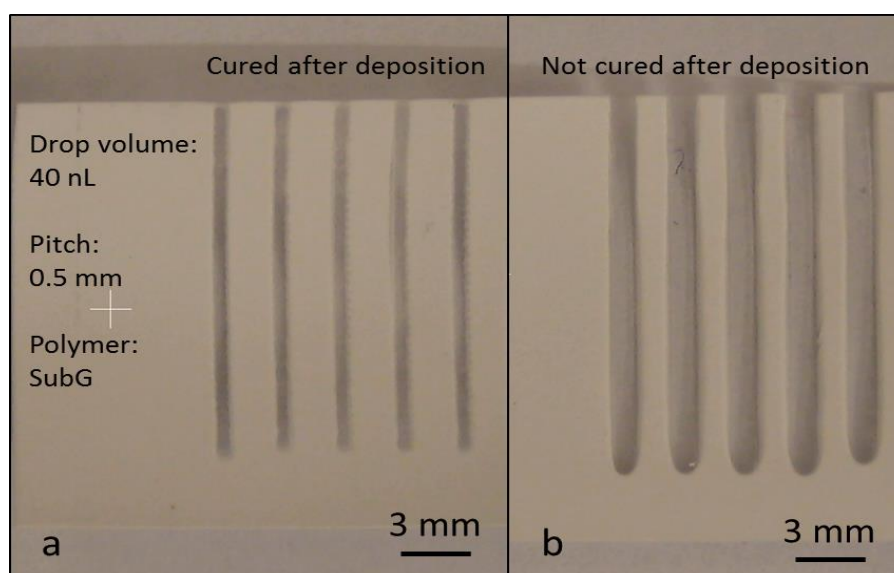


Figure 3.28 Photographic images showing sets of parallel-deposited photopolymer lines on NC via the BioDot system with a 40 nL drop volume and 0.5 mm pitch at a valve open time of 600 μs . a) Cured with laser light immediately after dispensing; b) Not cured after deposition and left in the dark overnight.

For the next step, a set of parametric studies was performed in order to further investigate the relationship between the widths of those dispensed polymer barriers and the dispensing conditions. As a few parameters can be adjusted during the dispensing that will all affect the dispensing result, as a simplification, here we only study the influence of the drop volume to the width of the dispensed line keeping all other parameters as constants.

To perform these studies, sets of parallel lines were dispensed on NC with different drop volumes ranging from 10 nL to 50 nL at a fixed 0.5 mm drop pitch. Two sets of samples were prepared: cured immediately after dispensing and dispensing without curing. For the first set of samples, the dispensed polymer lines were cured via the 405 nm laser immediately after dispensing and the image was then taken using a USB camera as shown in Figure 3.29. For the other set of samples, no laser curing procedure was performed after dispensing and the image was taken after leaving the sample in the dark overnight, which allows the un-polymerised photopolymer to spread via the capillary force. An image of these non-cured samples is shown in Figure 3.30, which clearly shows that the lines were much wider than those shown in Figure 3.29 due to the spreading of the photopolymer. It can be clearly observed in both images that the line width of the polymer line obtained is a function of the applied drop volume.

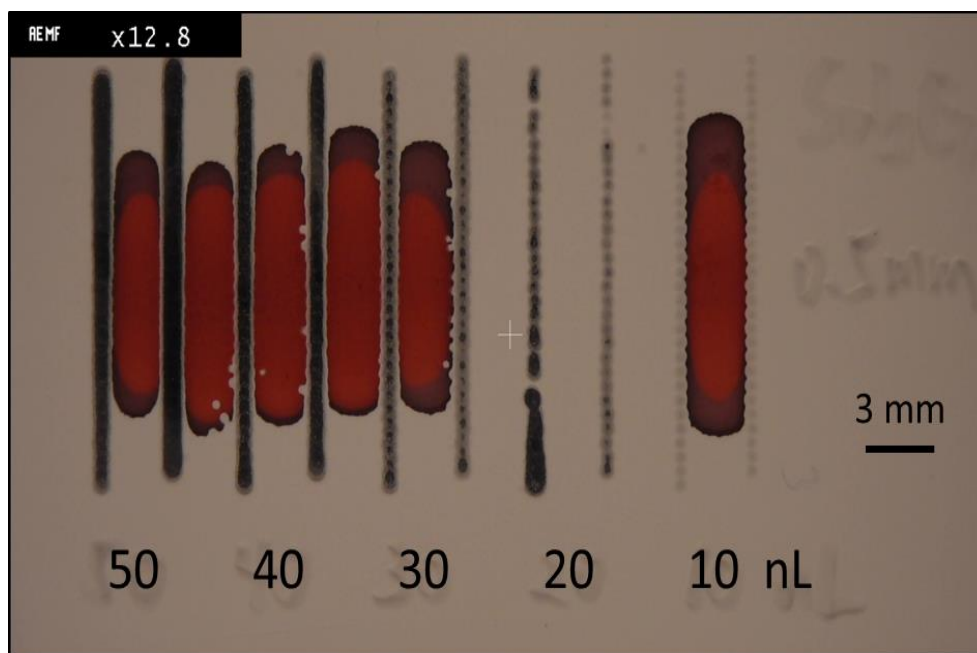


Figure 3.29 Photographic image showing a set of parallel photopolymer lines that are dispensed on NC via the BioDot system with different drop volumes ranging from 10 nL to 50 nL at a fixed pitch of 0.5 mm. The dispensed polymer lines were cured via a 405 nm laser immediately after dispensing. Red ink was introduced for testing the performance of these printed lines.

In the following step, the width of these dispensed polymer lines in both conditions was measured again using CorelDRAW based on the photographic images shown in Figure 3.29 and 3.30 respectively. The measurement is summarised as plots in Figure 3.31, which shows the relationship between the width of the polymerised lines and the drop volume. As shown in the plot, for the polymer lines that were cured immediately after dispensing, the line-widths are seen to increase from a value of $\sim 360\ \mu\text{m}$ to a value of $\sim 800\ \mu\text{m}$ with the increase of the drop volume from 10 nL to 50 nL. Similarly, as shown in Figure 3.31 again, for the polymer lines that were dispensed and left overnight in the dark without any curing procedure, the width increases with increasing drop volume from a value of $\sim 400\ \mu\text{m}$ at 10 nL to a value of $\sim 1700\ \mu\text{m}$ at 50 nL. This can be attributed to the fact that with an increase in the drop volume, a larger volume of the photopolymer is dispensed for each line, thus resulting in polymerised lines with larger widths. Additionally, it can be also observed that the width of the dispensed line increases with the spreading of the photopolymer via the capillary force over time.

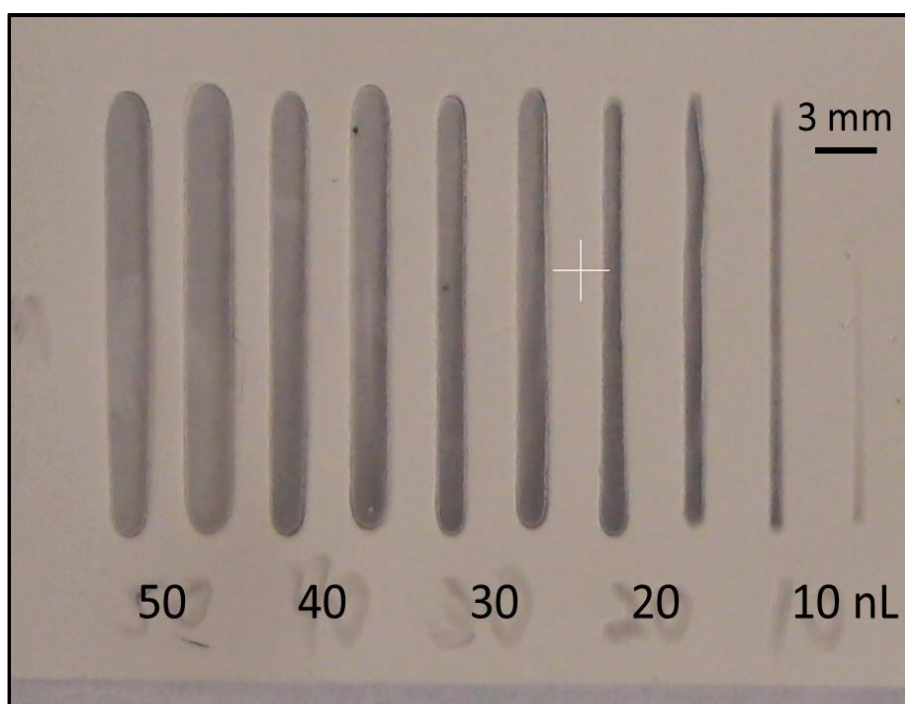


Figure 3.30 Photographic image showing a set of parallel photopolymer lines that are dispensed on NC via the BioDot system with different drop volumes ranging from 10 nL to 50 nL at a fixed pitch of 0.5 mm. No laser curing procedure was performed after dispensing and the image was taken after leaving the sample in the dark overnight.

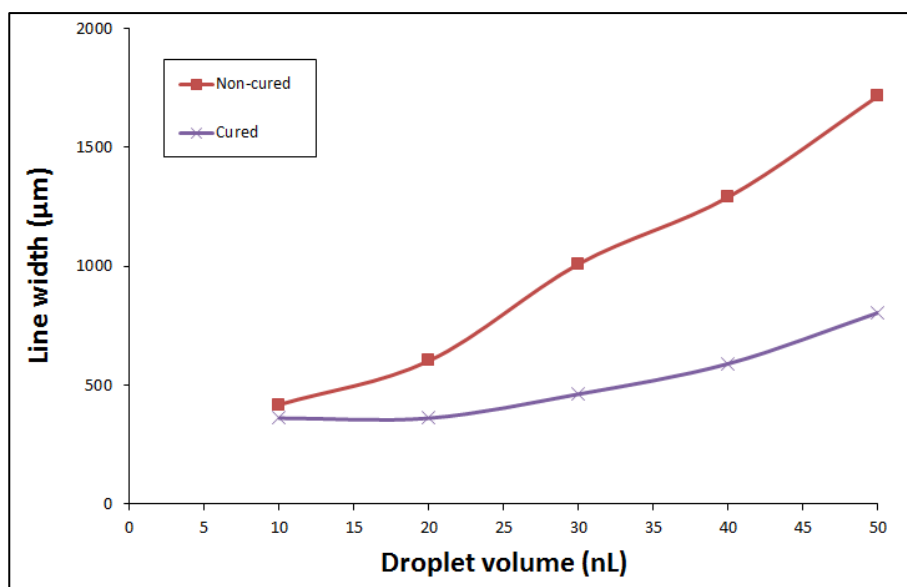


Figure 3.31 Image of plots showing the relationship between the resulting dispensed polymer line before width and the dispensed volume. Lines are a simple guide for the eye.

During the above experiments, we found that after introducing red ink into those fluidic structures, which are defined by the dispensed polymer barrier, the fluid was nicely contained and guided. However, a gap can be observed between the fluid and the dispensed polymer barrier. As shown in Figure 3.29, with the introduction of the red ink between those dispensed polymer-lines, narrow rectangular spaces ('white' areas) that lie along the polymer lines can be clearly observed. These narrow gaps isolate the fluid from the polymer barriers, and, however, have not been identified in any of the previous experiments, where the polymer barriers were produced via the most basic LDW method.

In order to further investigate this finding, these dispensed photopolymer lines were then studied using light microscopy. As shown in Figure 3.32, a microscopy image shows the junction of the dispensed polymer line (50 nL one in Figure 3.29) and the fluidic channel with red ink under higher magnification. A narrow rectangular gap with a width of ~ 60 μm can be clearly identified, which is located along the edge of the dispensed polymer line that isolates the inked channel and the polymer line. In a more extreme case, as shown in Figure 3.29, although the dispensed polymer lines with 10 nL drop volume seem discontinuous, they are still able to contain and guide after the introduction of the fluid. The microscopy image of these lines is shown in Figure 3.33: the polymer line consists of individual drops of dispensed polymer and each has an identical diameter of ~ 450 μm . As shown in the microscopy image, although the polymer dots are separated from each other, the fluid (red ink) is still nicely confined without any leakage through the gap in between and an undulating edge is presented that follows the track of these polymer dots.

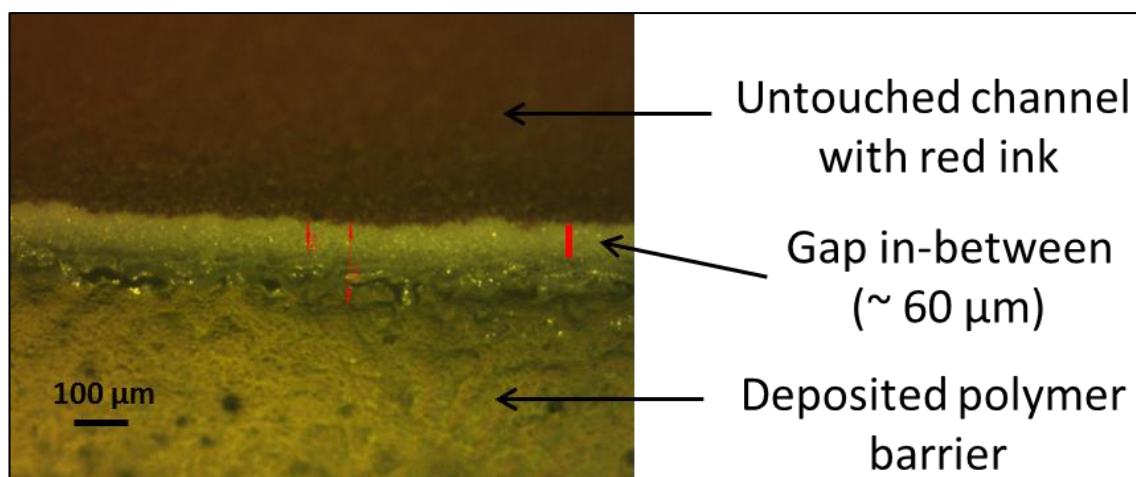


Figure 3.32 Microscope image of the dispensed polymer line in Figure 3.29 with a 50 nL drop volume shows a narrow rectangular gap that isolates the inked channel and the deposited polymer line.

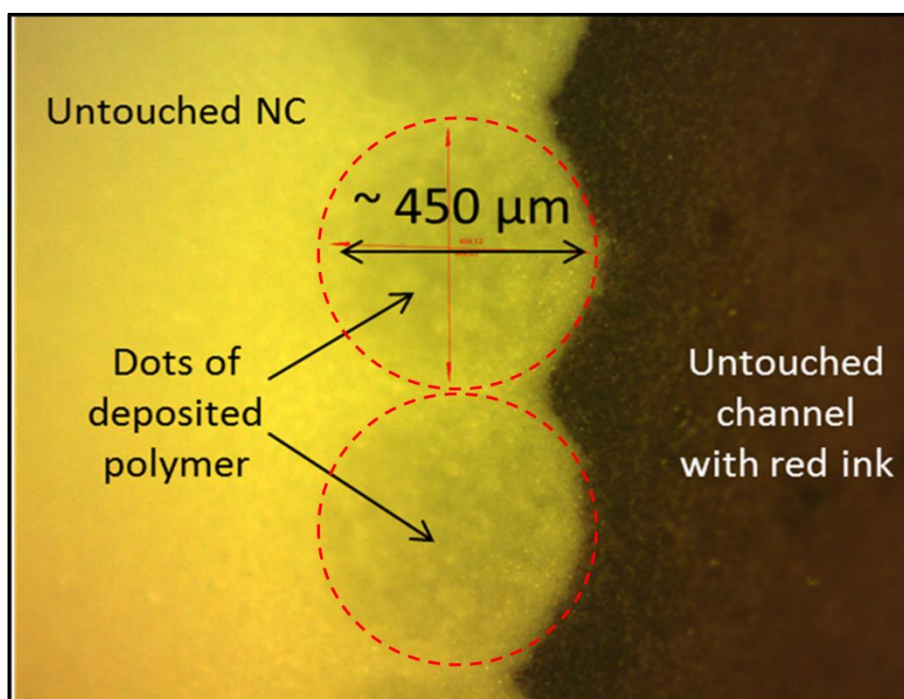


Figure 3.33 Microscope image of the dispensed polymer line with a 10 nL drop volume as shown in Figure 3.29. Red circles are a simple guide for the eye.

In our view, we believe that these isolation areas are because of the solvent in the acrylic-based photopolymer we used, which flows further than the monomer. When the photopolymer is dispensed onto the NC, both the monomer and the solvent in it start to spread via capillary action, while the solvent flows faster and further than the monomer. After the light-induced polymerisation, the monomers get cross-linked together forming the polymer barrier, which can be clearly distinguished from the substrate. According to our experiment with solvent trials performed previously, we have proved that the

nitrocellulose membrane is extremely sensitive to this type of solvent, which will destroy the nitrocellulose membrane and convert it from hydrophilic to hydrophobic. Thus, these areas also become hydrophobic due to the reaction with the solvent and hence are able to block the fluid as well.

Finally, to further investigate the performance of the patterned structures that are achieved with the introduction of this local deposition procedure to the basic LDW technique, a set of flow channels were produced in NC by dispensing of photopolymer followed by the LDW polymerisation. As shown in Figure 3.34a, three dispensing conditions were tried with different drop volumes at 40, 80 and 100 nL at a drop pitch of 0.5 mm, and for each condition, two flow channels were created that are defined by three parallel walls. All the dispensed polymer lines were cured with the 405 nm laser immediately after dispensing. To test these flow channels, two different inks, red and green, were introduced into these adjacent channels respectively. The results are shown in Figure 3.34b: for all three dispensing conditions, both inks are well-contained and guided in their respective channels without any leakage or cross-contamination.

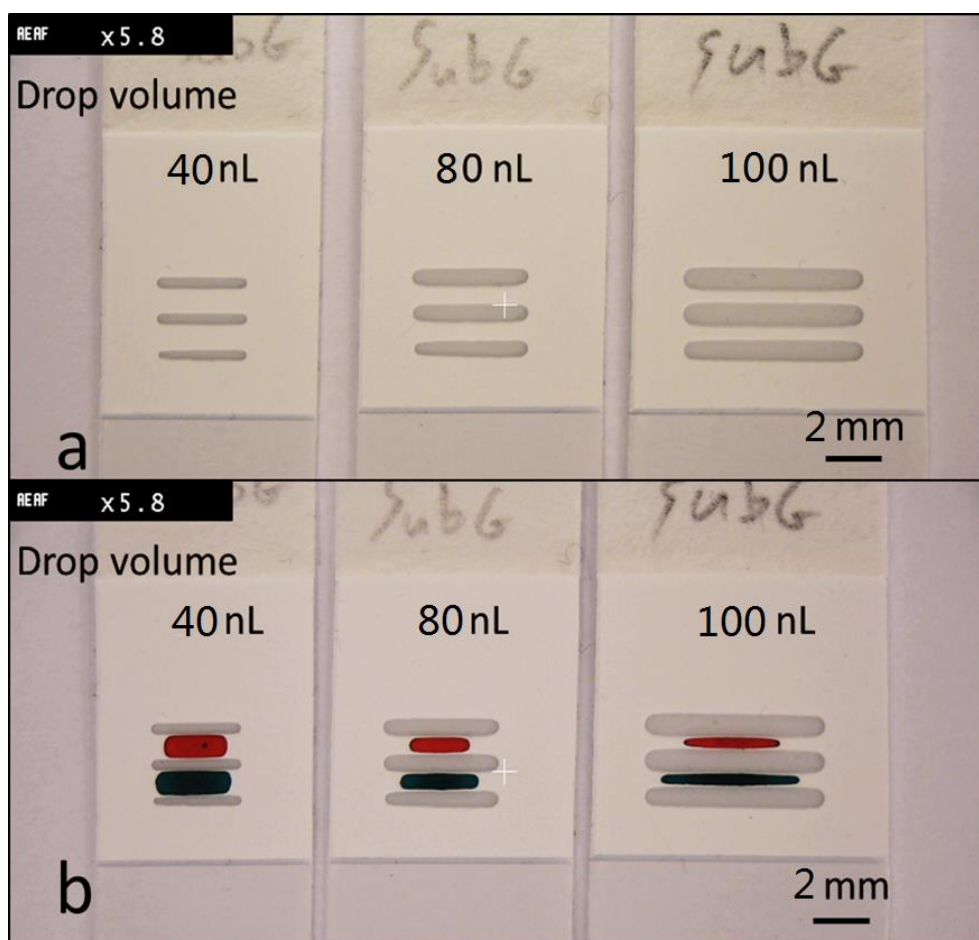


Figure 3.34 Photographic images showing the dispensed and cured photopolymer lines with three different drop volumes (40, 80 and 100 nL) at a 0.5 mm drop pitch. Before a) and after b) introduction of different colour inks.

Above all, with the introduction of a local deposition procedure, the photopolymer is only applied locally to a substrate in accordance with a desired pattern of fluid flow channels, and that pattern is then cured by localised light exposure, which does not require a subsequent solvent development procedure. The patterned design of the flow channel network is then defined predominantly by the deposition stage rather than the laser scanning step as in the previous case. Most importantly, the remainder of the substrate is not exposed to either photopolymer or development solvent at all. Thus, with this simple improvement, the problem of altering properties of the patterned substrate during the initial LDW procedure has been satisfactorily solved.

3.5 Summary

We have demonstrated that a simple, low-cost laser-based direct-write technique based on the principle of light-induced polymerisation can be used for the rapid fabrication of fluidic structures in porous materials. The laser-polymerised patterns form the hydrophobic barrier-walls of interconnected hydrophilic fluidic structures such as channels and wells. In contrast to the most widely used methods for patterning paper, our approach not only eliminates the requirements for cleanroom-based steps, expensive masks, specialist reagents, and custom-designed equipment, but is also amenable to large-scale commercialization. Since LDW is a non-contact procedure, it minimises any chance of cross-contamination, an essential criterion in the fabrication of microfluidic devices for biological and biomedical applications. Additionally, compared with other methods, the technique is also well-suited for up-scaling to mass-production.

We have shown that using this method it is possible to create microfluidic channels and barrier-walls with dimensions of $\sim 100\ \mu\text{m}$ and $\sim 60\ \mu\text{m}$, respectively, the smallest values that have been reported so far, which will allow for miniaturisation of the diagnostic sensor, and a corresponding minimal use of reagents. With our existing laser-writing set-up, it is possible to pattern samples, using a c.w. laser, at speeds of a metre per second, and accounting for the time required for the pre- and post-processing steps needed to make a complete device, our estimate is that it is possible to fabricate at least one device per second.

Finally, in order to further optimise this LDW patterning technique so that it can fully meet the requirements for mass commercialised fabrication of paper-based devices, two main improvements have been successfully introduced into the basic LDW procedure. For the first improvement, a galvo scanner is introduced, which allows further increase of the fabrication speed and more accurate control of the patterning condition. The user-friendly

interface also allows easy programming of complicated designs, which brings great flexibilities during the fabrication procedure.

For the second improvement, in order to avoid any influence of the photopolymer and the solvent to the patterned substrate, a local deposition procedure is introduced. With this local dispensing procedure, the photopolymer is only applied locally to a substrate and then cured via localised light exposure. As no redundant photopolymer is left, no subsequent solvent development procedure is required. As a result, the remainder of the substrate is not exposed to either photopolymer or solvent at all, which remains in its untouched virgin state. Thus, with this simple improvement, the problem of altering properties of the patterned substrate during the initial LDW procedure has been satisfactorily addressed.

Overall, we believe that this LDW technique could be an ideal choice for rapid fabrication of paper-based microfluidic devices that can be used for a variety of applications such as clinical diagnostics and analytical chemistry.

Chapter 4: Fluidic delay strategies in paper-based devices

4.1 Introduction

In order to implement real analytical assays using paper-based microfluidic devices, and hence bring them to market, several capabilities beyond just a simple platform for running the assay are required. An ideal paper-based microfluidic device should enable POC assays with minimal or ideally no intervention and manipulation from the user, truly realising 'sample-in-result-out' tests/devices for which all processes in between are automated. In order to work towards this goal, recent research has been focused on the development of methodologies to control the flow of fluids in paper-based devices. The introduction of control over the delivery of fluids could realise a large number of additional attributes in paper-based devices such as timers and metering [118, 119], diodes and valves [120, 121], fluidic batteries [2, 122], and fluidic dilution, separation and mixing [123-125]. Most importantly, these fluid control techniques would immediately contribute to the realisation of automated multi-step immunodiagnostic protocols such as ELISA, which are normally performed in a laboratory and require skilled personnel to perform the sequential multiple steps [126, 127].

Current methods that have already been reported for manipulating fluid flow in paper-based fluidic devices can be classified into four main categories: manually activated control [101, 121], modification of the topology and geometry [58, 126], addition of dissolvable chemicals [120, 127], and creation of physical barriers [128], and each of these procedures has its own advantages, as well as some characteristic limitations. Techniques that use manually activated control and physical barriers require additional fabrication steps, while adding dissolvable chemicals have the dual drawback of additional processing steps and the introduction of chemicals such as sugar in the flow-path which might alter or limit the intended function of the devices. Implementation of a similar flow-delay might be possible through careful considerations of the geometry of the fluidic channels. However, to introduce a flow-delay through changes to the channel geometry will require either an increase in the channel dimension or an increase of the channel length, both of which would have the undesired effect of either increasing the footprint of the device and/or increasing the volume of the reagents used. Our method instead allows the introduction of flow-delay to any pre-designed device without any change to the channel geometries, thus keeping the device compact and requiring smaller reagent volumes.

In this chapter, to control and engineer fluidic delays in paper-based devices, we report the use of a new approach that is an extension of the basic LDW technique that has been described in the previous chapter for creating fluidic patterns and devices made up of interconnected channels and reaction chambers. To produce flow-control, the approach presented here relies on the use of physical barriers that run across the flow-path (i.e. perpendicular to the fluidic channels) and hence introduce a delay in the fluid flow. As was the case for our LDW method where we demonstrated the use of laser light to form patterns in paper through light-induced photo-polymerisation, the flow delay barriers in this report are created using the same principle of light-induced photo-polymerisation. In brief, the delay mechanism is based on the use of two different kinds of delay barriers - solid barriers with variable depths and porous barriers with variable porosities, and both could be achieved during the same device fabrication step by simply adjusting the patterning parameters, such as the laser output power and scan speed. Unlike other fluid flow control methods reported for paper-based microfluidics, the approach presented here does not require any additional processing equipment or specialist materials and as described earlier uses the same fabrication approach that defines the fluidic channels themselves.

4.2 Fluidic delay strategies

As mentioned before, the introduction of control over the transport of fluid will enable greater functionalities for paper-based microfluidic devices. Here, based on our LDW technique described above, we introduced two methods for producing delay barriers to control and engineer fluidic delays in such devices. One method is based on the use of a pulsed laser (266 nm) and is described in Figure 4.1a. During our earlier studies into the fabrication of fluidic channels using pulsed laser irradiation, we observed that by controlling the scanning speed (and therefore the effective exposure) of the laser beam, we could polymerise lines of various depths inside the paper substrate as illustrated schematically in Figure 4.1a. Slower scanning speeds produced polymerisation through the full depth of the paper, while faster scanning speeds led to photo-polymerisation only in the upper portion of the paper, thus creating partial barriers that the liquid had to overcome. These fluidic 'delay barriers' can, therefore, decrease the flow by a rate that is proportional to their depth, and hence this principle can be used to impose a user-defined variable time-delay in the wicking of the liquids and test samples.

According to the discussion in Chapter 2, the polymerisation depth is determined by the light penetration depth, which can be described by the following equation:

$$z = \frac{\lambda}{4\pi k + \lambda \alpha_s} \ln\left(\frac{I_0}{I(z)}\right) \quad [7]$$

As shown in this equation, the depth is related to both the wavelength and the intensity of the light. For a fixed wavelength, the main determinant is the laser intensity that is related to the scan speed with the following equation:

$$I_0 = \frac{P}{2\pi\omega S} \quad [8]$$

where P is the output power of the laser, ω is the beam radius and S is the scan speed.

Substituting I_0 into the former equation, we are then able to obtain the following equation that describes the relationship between the polymerisation depth and the scan speed.

$$z = \frac{\lambda}{4\pi k + \lambda \alpha_s} \ln\left(\frac{P}{2\pi\omega I(z)}\right) \quad [9]$$

An alternative method, which is illustrated in Figure 4.1b, allows the writing of barriers via manipulation of the extent or degree of polymerisation using c.w. laser (405 nm) exposure. In this case, however, the barriers produced extend throughout the full paper thickness, but the degree of polymerisation can be engineered to form barriers whose porosity can be controlled by varying incident laser fluence, which is determined by the incident laser power and the laser scan speed. For these less dense, leaky barriers, the polymerised material does not completely fill the voids within the paper matrix, and instead the polymerised material simply coats, we surmise, the fibrous strands, without forming a completely impermeable barrier. Both the depth and porosity of the polymerised barriers can be controlled through the change in the fluence of the incident laser light.

The schematic in Figure 4.2 shows a simple fluidic geometry that can be used to produce delay barriers via either of these two methods, (1) by controlling the depth of solid/impermeable barriers (as shown in Figure 4.2b) that are patterned across the flow and which simply impede the fluid flow by reducing the depth of the fluidic channel or, (2) by forming porous barriers (as shown in Figure 4.2c) that allow controlled leakage of the fluids.

As described in Chapter 2, the flow of the fluid in a porous medium during wet-out follows the Washburn equation. However, in both cases here, the constant cross-sectional area assumption and the non-limiting source fluid assumption of the Washburn equation are violated.

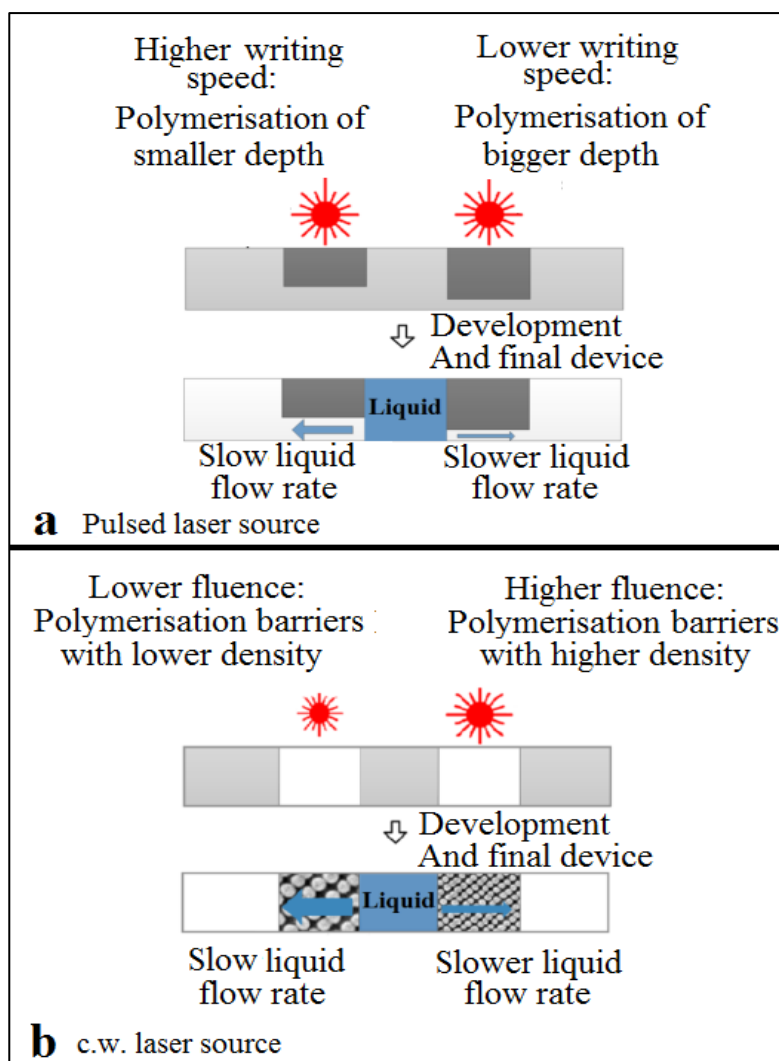


Figure 4.1 Schematic of the fabrication of polymerised barriers with: a) variable depth and b) variable porosity.

In order to study the flow, the flow channel with a delay barrier, as described above, can be treated as three individual parts: part 1 with larger depth/pore size, part 2 with smaller depth/pore size and finally part 3 with larger depth/pore size. Assume the times for fluid flow in each part are t_1 , t_2 and t_3 respectively, then the overall transport time is $t=t_1+t_2+t_3$. Part 1 of the flow path acts as a non-limiting source of fluid for part 2 with smaller depth/pore size. Hence, the individual flow in both parts follows the Washburn relation. In terms of the flow in the last part, according to the Washburn equation, the flow velocity decreases during progression through parts 1&2 of the flow channel. Assuming incompressibility of the fluid, in terms of the same distance, a greater time will be required for part 3 with a larger volume to fill. This leads to a further decrease in the velocity in part 3 with larger depth/pore size.

Overall, in this chapter, we have proposed two methods for creating flow constrictions (a solid barrier and a porous barrier) inside the flow paths, and, as described above, one or

more constriction can be designed into a flow channel in order to alter the overall transport time.

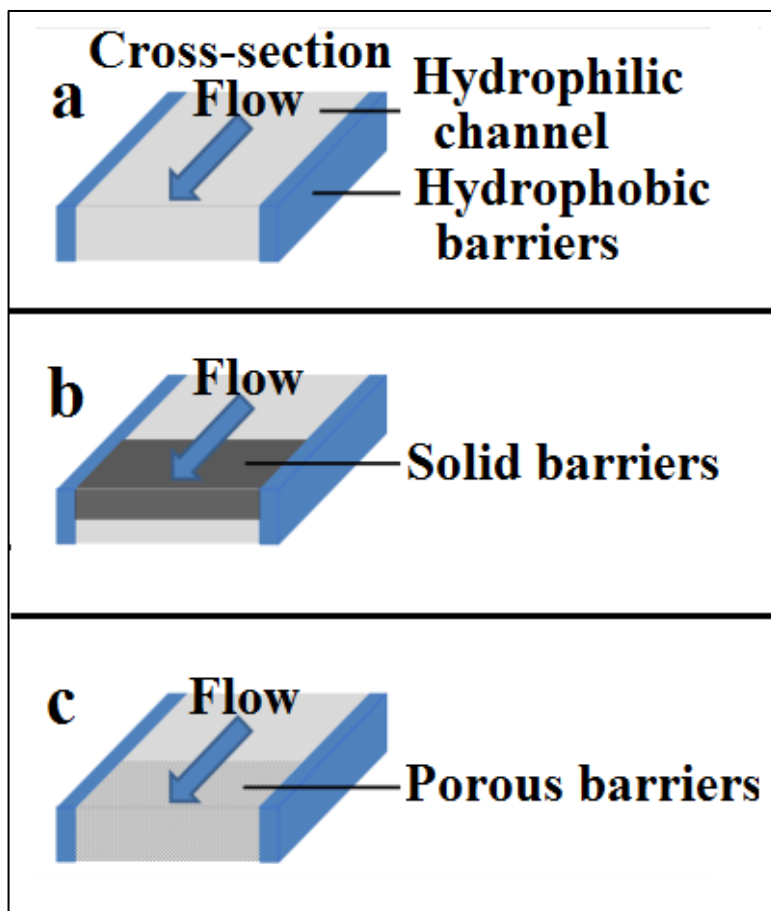


Figure 4.2 Schematic representation of: a) cross-section of a fluidic channel; b) cross-section of a fluidic channel with solid barriers; c) cross-section of a fluidic channel with porous barriers; d) layout of a pre-defined fluidic structure.

4.3 Experimental results

The basic LDW setup is the same as described previously in chapter 3, which is shown in the schematic in Figure 3.1. The lasers used for the making these delay barriers were a Q-switched Nd: YVO₄ laser (BM Industries, Thomson CSF Laser, France) operating at 266 nm, with a pulse duration of 10 ns, a maximum single pulse energy of 2 mJ, and a repetition rate of 20 Hz (for method 1 as outlined above, and shown in Figure 4.2b) and a 405 nm continuous wave (c.w.) diode laser (MLDTM 405 nm, Cobolt AB, Sweden) with a maximum output power of ~110 mW (for method 2, shown in Figure 4.2c). The paper substrates used were Whatman® No. 1 filter paper from GE Healthcare Inc. The photopolymer chosen for these experiments was Sub G, from Maker Juice, USA.

As a first demonstration, Figure 4.3 illustrates the difference between such solid and porous polymerised barriers. As shown in Figure 4.3a, the polymerised regions for solid barriers written with a pulsed laser could only be observed on the top, and not the lower face of the paper, suggesting partial polymerisation through the thickness of the paper. However, the polymerised regions for porous barriers written with a c.w. laser always extended throughout the entire paper thickness, as shown in Figure 4.3b. Blue ink was added to the sample in Figure 4.3a to enhance the contrast between the paper substrate and the lines.

As described in the following sections, we compared both of these methods for generating controllable flow delay in fluidic channels. The study was aimed at characterising the influence of the laser fluence and exposure on the depth and porosity of the barriers for both methods, including an investigation of delay as a function of positions and numbers of barriers. All the flow characterisation measurements were done under a specific arrangement as shown in Figure 4.4. And, in order to quantify the ability of the barriers to delay the fluid flow, we have introduced a normalised ‘delay factor’, which we define as the time to flow (from the starting line to the finishing line as shown in Figure 4.4) in a channel that has barriers, divided by the time to flow in a channel without barriers:

$$\text{Delay factor} = \frac{\text{Flow time for a channel with barriers}}{\text{Flow time for a channel without barriers}}$$

The flow time for a control channel with the same geometry as that in Figure 4.4 but without any barrier is approximately 2 minutes and 40 seconds.

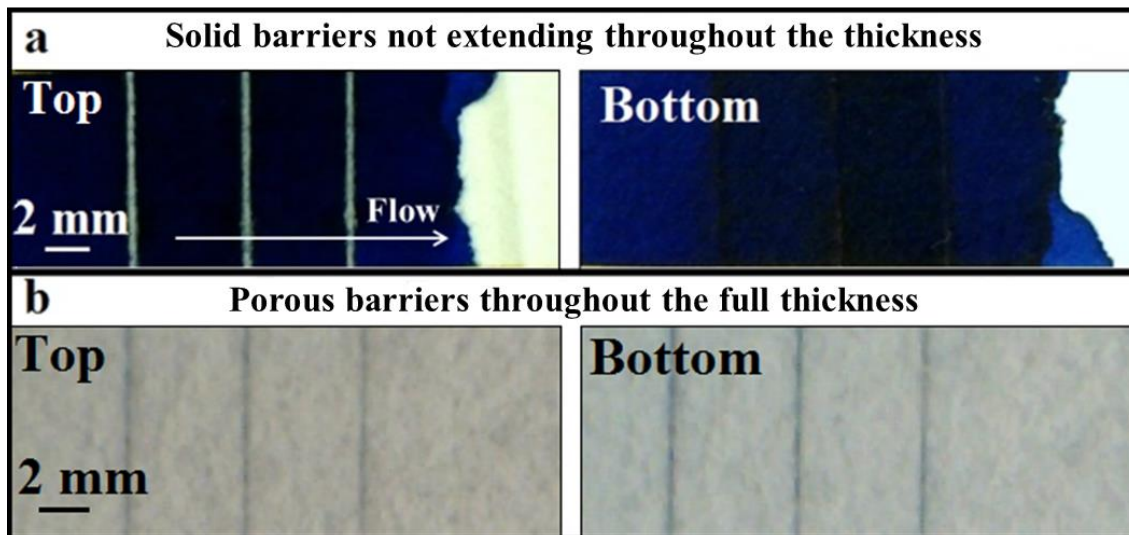


Figure 4.3 Images showing the delay barriers from both sides of the cellulose paper. a) Depth-variable solid barriers formed by pulsed laser exposure; b) porosity-variable barriers formed by c.w. laser exposure.

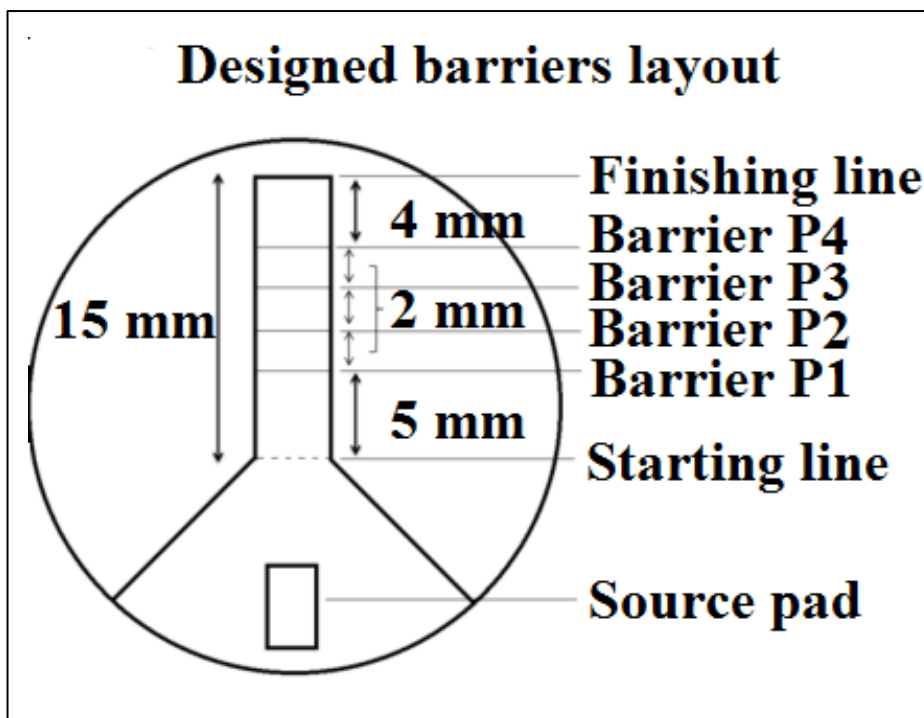


Figure 4.4 Schematic representation of the layout of the fluidic device and the position of delay barriers (P1, P2, P3 and P4) used for studying the flow delay introduced by delay barriers.

4.3.1 Delay via solid barriers created by a pulsed laser

In order to explore the relationship between the depth of the solid barriers and the incident fluence, which depends on both the laser average power and the laser scan speed, we first fabricated a set of polymerised barriers written with a fixed incident average power (7 mW) but different speeds from 0.1 mm/s to 1.5 mm/s. We then measured the depth of these barriers by cutting the paper substrates along a line that intersects the barriers and then imaged the cross-sections of the paper using an optical microscope. The relationship between the depth and the barrier writing speed is plotted in Figure 4.5, which shows that an increase in the writing speed from 0.3 mm/s to 1.5 mm/s leads to a decrease in the depth of the barrier from $\sim 82 \pm 6 \%$ to $\sim 17 \pm 6 \%$ of the thickness of the paper. The experimental results here are in agreement with the above calculation, as shown in Section 4.2.

To understand and quantify the usefulness of these solid barriers with variable depths in both delaying and even completely stopping the fluid flow, we fabricated a set of 4 channels, as shown in Figure 4.6a, and then patterned delay barriers perpendicular to the flow direction. Each of the fluidic channels was inscribed with two barriers, both of which had been written under the same writing conditions. Importantly, for each of the fluidic channels (1 - 4), these pairs of horizontal lines were written with the same incident

average power (7 mW) but different speeds namely, 1 mm/s, 0.7 mm/s, 0.5 mm/s and 0.3 mm/s, thus forming solid barriers with different depths, which can be calculated from the plot in Figure 4.5.

As shown in Figure 4.6b and 4.6c, blue coloured ink introduced from the inlet of the channels (marked in the image) experiences a flow rate that is a clear function of the presence and strength of the inscribed barriers, with channel 4 being the slowest, and channel 1 the fastest. The ink was introduced at the same time in each of the four channels. Figure 4.6b and 4.6c are images taken 2 minutes and 3 minutes after the introduction of ink, and as seen in Figure 4.6b, the ink has already flowed past the two barriers of channel 1, is leaking past the second barrier of channel 2, has just reached the second barrier in channel 3, while it has just crossed the first barrier in channel 4.

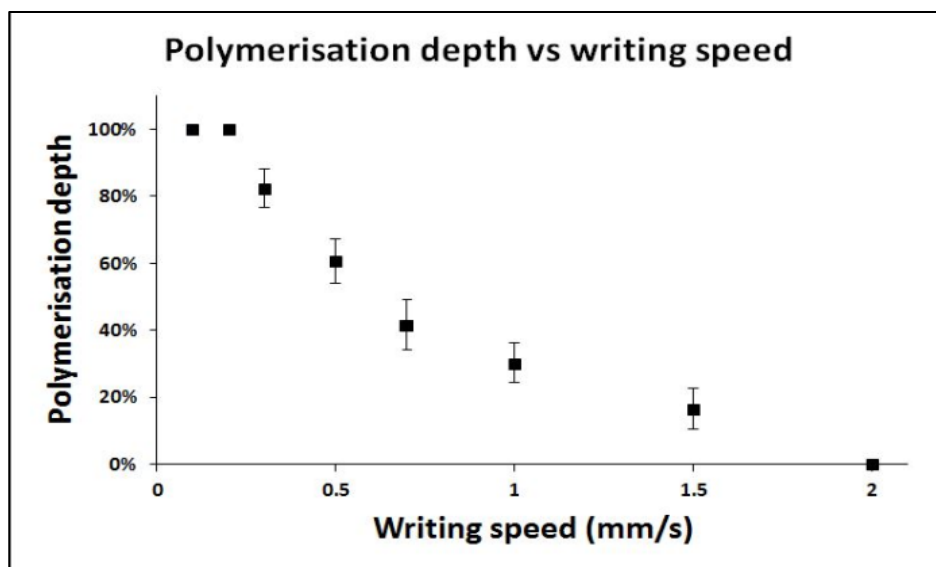


Figure 4.5 Comparison between the depth of the polymerisation in the paper and the writing speed of the delay barriers. Error bars indicate the standard deviation for 5 measurements.

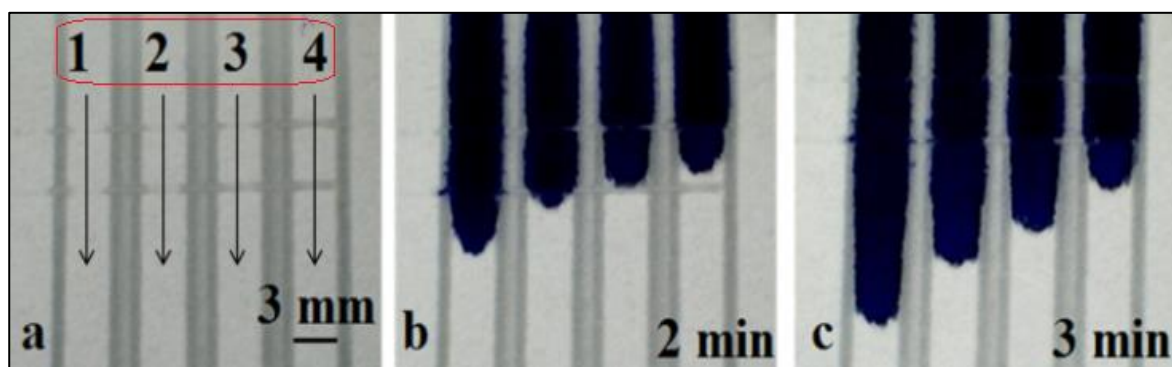


Figure 4.6 Image showing the delay of the liquid flow after the introduction of blue ink in fluidic channels with barriers created using different writing speeds.

To quantify the flow delay versus writing conditions, we used the arrangement of Figure 4.4, using tris buffered saline (TBS) (pH = 7.4), a reagent conventionally used as a buffer in bio-chemical assays, as the liquid medium. The fluid ‘delivery time’ was defined and measured as the time the TBS solution needed to travel from the starting line to the finishing line, a distance of 15 mm in total. The channel walls were written with the 405 nm c.w. laser (20 mW, 10 mm/s), whereas the barriers were written with a pulsed laser at writing speeds from 1 mm/s to 0.3 mm/s.

First, we studied the consequence of having solid barriers with different depths in the flow-path, however with only one delay barrier at position P1 (as shown in Figure 4.4) in each of the pre-defined devices. Several devices, each with one single delay barrier were written under different writing conditions, by changing the scan speed (from 1 mm/s to 0.3 mm/s) at a constant laser average power of 7 mW, which corresponded to creation of solid barriers with depths ranging from $\sim 30 \pm 6\%$ to $\sim 82 \pm 6\%$ of the thickness of the paper (as shown in Figure 4.5). The results for the delay factor are plotted in Figure 4.7 which show an increase in the delay factor from ~ 1.1 to ~ 1.6 with an increase in the barrier depth from $\sim 30 \pm 6\%$ to $\sim 82 \pm 6\%$.

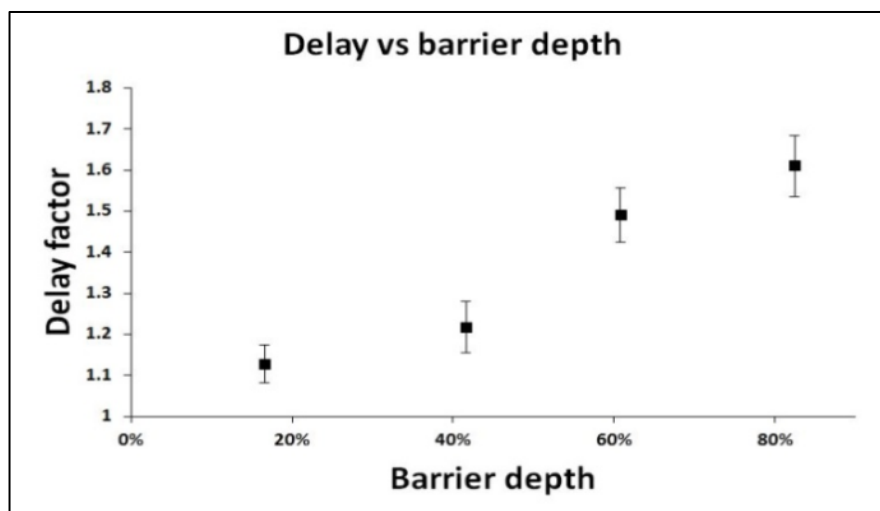


Figure 4.7 Plots showing the delay factor for devices with barriers having different depths. Barriers were written with different writing speeds at a fixed average power of 7 mW. Error bars indicate the standard deviation for 5 measurements.

While use of a pulsed laser allows fabrication of depth variable solid barriers for implementation of fluid delay in paper-based microfluidic devices, as shown in previous results, the fabrication speed of delay barriers is only sub-millimetre per second, which is too slow to meet the requirement for mass and large-scale fabrication. As a result, we then introduced porous barriers, which are created using a c.w. laser, as an alternative method

for generation of fluid delay in paper-based devices. This method will be described in detail in the following section.

4.3.2 Delay via porous barriers created by a c.w. laser

In this case, both the fluidic channels and the flow delay barriers were written with the same c.w. laser by simply changing either the laser output power or writing speed. To allow for a direct comparison with the results for the solid barriers, fluidic devices that were tested had the same design as in Figure 4.4. Four porous barriers were written across the fluidic channels, in this case, to explore the role of the writing condition, number and position of the barriers. Thus, a comprehensive study was performed to explore the flow delay induced through barriers written under a range of different writing conditions.

We first performed a comparative study of barriers patterned under different writing conditions, namely different laser powers and scan speeds. Subsequently, we then changed the number of the barriers to explore the relationship between the delay and the number of barriers in the flow path. As in Figure 4.4, a one barrier design refers to a device with a single barrier patterned at position P1 in the channel; a two barrier device refers to a channel with two barriers patterned at P1 and P2, and so on.

As shown in Figure 4.8a, for barriers written at a fixed scan speed of 100 mm/s, the fluid delay gradually increased with an increase of the laser power, and progressively decreased for barriers written with an increasing scan speed at a fixed laser output power of 20 mW, as shown in Figure 4.8b. These results show that the porosity of these barriers is a clear function of the laser fluence used and that any targeted delay (within the experimental error) can be achieved by choosing the correct fluence. Similarly, for the plots shown in both Figure 4.9a and 4.9b, which are based on the use of multiple barriers, we observe identical trends - for barriers written with the same writing conditions, as expected, the delay increases with an increase in the number of barriers.

As described above, both the flow inside the channel and through the delay barrier can be described using the Washburn equation. The time for a fluid flow in a channel without any delay barrier can be calculated from the following equation:

$$t_0 = \frac{4\mu L^2}{\gamma D_0} \quad [10]$$

where D_0 is the pore size of the paper.

On the other hand, the delay time for a fluid flow through a delay barrier can be expressed as:

$$\Delta t = \frac{4\mu L^2}{\gamma D_B} \quad [11]$$

where D_B is the pore size of the porous delay barrier, which determined by the incident laser fluence as shown in Figure 4.11.

Here we measured the delay by introduction of different numbers of porous barriers inside an identical channel with a fixed length, as shown in the schematic in Figure 4.4. As the delay barriers here are only around 100 μm each in length, we assume that they can be ignored with respect to the whole flow channel. As a result, the total time for fluid to travel from the starting line to the finishing line with delay barriers as shown in Figure 4.4 can be simply defined as:

$$t = t_0 + N \cdot \Delta t \quad [12]$$

where N is the number of delay barriers introduced into in the flow channel.

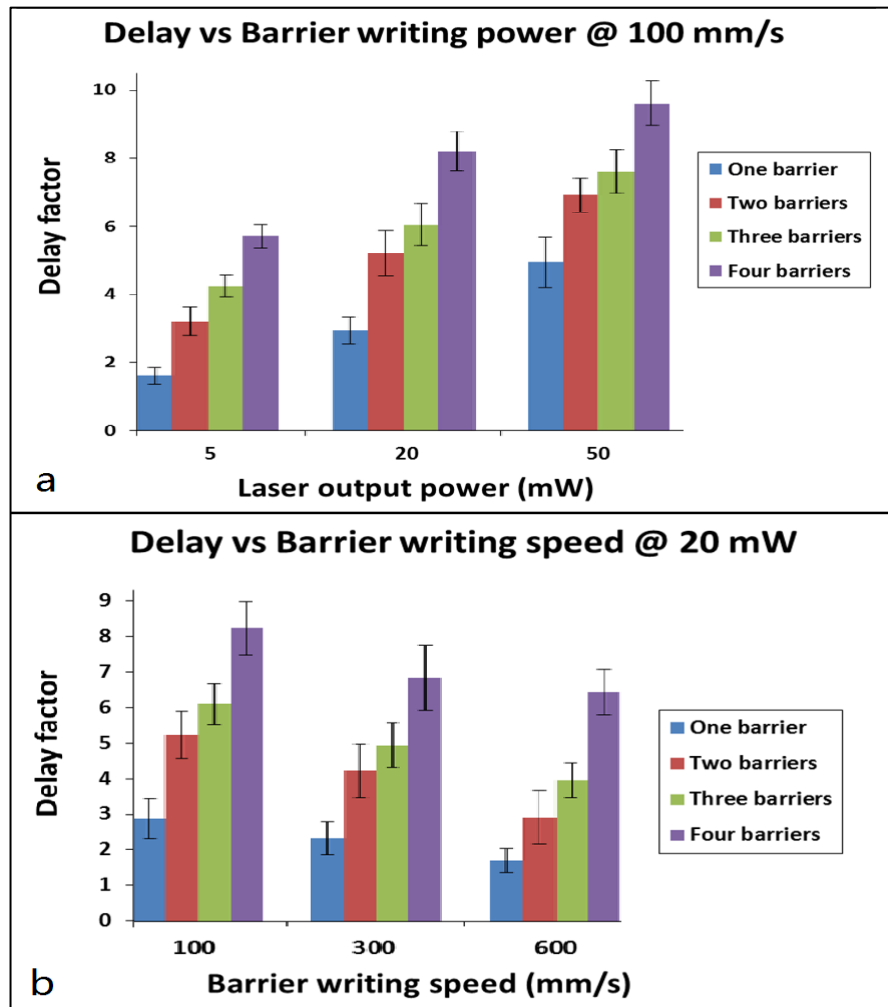


Figure 4.8 Plots showing the delay factor of delay-barrier-designed devices. a) Barriers written with different laser output powers at a fixed scan speed; b) barriers written with different scan speeds as a fixed laser output power. Error bars indicate the standard deviation for 5 measurements.

The delay factor then can be calculated as:

$$\text{Delay factor} = \frac{t}{t_0} = 1 + N \cdot \frac{\Delta t}{t_0} \quad [13]$$

The experimental results are in agreement with the above calculation, as shown in Figure 4.9. According to the above equation, the slope of the line is determined by the delay time of the individual delay barrier. As discussed above the delay time of an individual barrier is inversely proportional to the pore size, which is determined by the laser fluence. As a result, the slope is proportional to the fluence, which agrees with the experimental data in Figure 4.9 namely that the slope of each plot increases with an increase of the laser power and decrease of the scan speed.

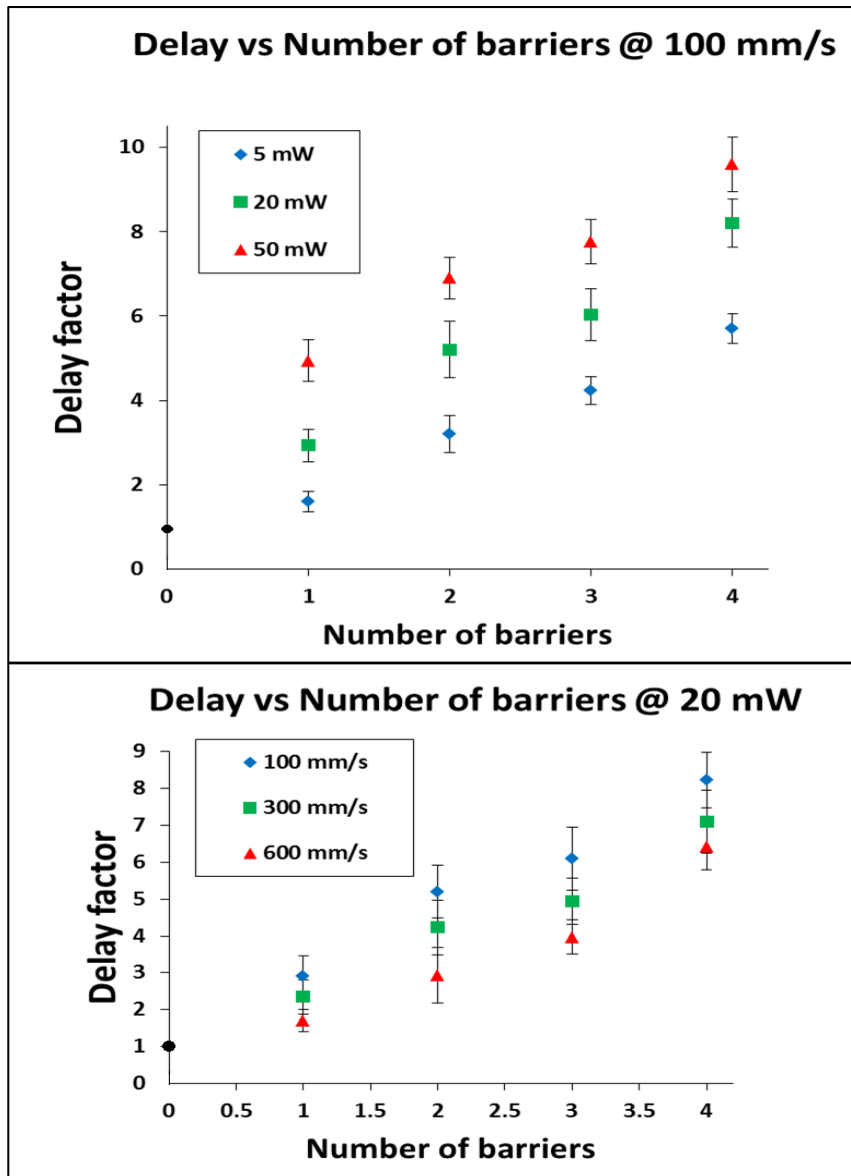


Figure 4.9 Plots showing the delay factor of delay-barrier-designed devices. Different numbers of barriers written at a) fixed scan speeds, b) fixed laser output powers. Error bars indicate the standard deviation for 5 measurements and lines are a simple guide for the eye.

In addition to this dependence on the porosity of the barriers and the number of barriers, we observed that the fluid delay also depended on the position of the porous barrier. We introduced a single porous delay barrier written under the same writing condition at different positions (P1 – P4) as shown in Figure 4.4 and then studied the fluid delay. The plot of the fluid delay versus the position of the porous barrier is shown in Figure 4.10. As the delay barrier was shifted further from the starting line towards the finishing line, the delay factor rapidly dropped from ~ 2.5 (for position P1) to ~ 1.3 (for position P4). We believe this is because of the geometry of the device since the volume of the paper that serves as the reservoir for the fluid flow changes with a shift in the position of the delay barrier. The volume before the delay barrier acts as a pump for subsequent flow, thus affecting the flow rate after the barrier.

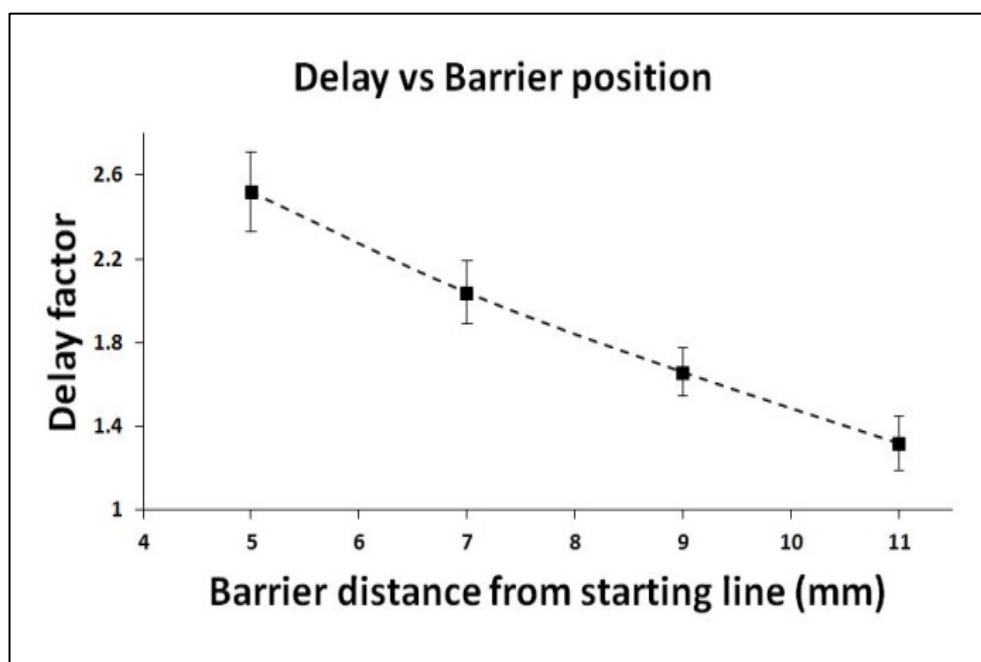


Figure 4.10 Plots showing the relationship between the fluid delay factor and the position of the delay barriers (distance to the starting line) with the same condition of 200 mm/s scan speed and 20 mW laser output power. Error bars indicate the standard deviation for 5 measurements and lines are a simple guide for the eye.

4.3.2.1 Weight measurements of porous barriers

To further understanding the porosity of the above patterned porous delay barriers, weight measurements of individual different polymer barriers were implemented. To perform the measurement, the Whatman No.1 cellulose filter papers were first cut into the same 2 cm \times 2 cm squares and the weight of individual samples was measured with an electronic laboratory balance and the numbers are shown in Table 4.1. Then the samples were soaked in the same photopolymer bath, followed with LDW of the same number (5) of lines but with different laser fluences, ranging from ~ 0.1 J/cm² to ~ 1.7 J/cm². Thus, the

resulting polymer lines in individual samples had the same length but with different widths due to the different laser fluences applied. The samples were then subjected to a sequential solvent development procedure (acetone, IPA and finally DI water) and left to completely dry in order to remove any un-polymerised polymer and remaining solvents. These samples with patterned polymer lines were then weighted again and the weights are shown in Table 4.1. The total weight of the polymer in the individual paper substrate (net weight) was then calculated via subtracting the weight of the blank substrate from the same substrate after introducing the polymer lines.

In order to calculate the density/porosity of the polymer lines, which is defined as weight per unit volume, the line width of the polymer lines patterned with different fluences was measured under light microscopy. Thus, the total volume of the polymer lines in the individual substrate can be calculated via the following equation,

$$\begin{aligned} \text{Total volume of polymer} \\ &= \text{Line width} \times \text{Line length} \times \text{thickness of the substrate} \\ &\times \text{the number of individual lines in each sample} \end{aligned}$$

The length of the polymer line is 2 cm and the number of individual lines in each sample is 5 for each substrate and the thickness of the substrate is 180 μm .

Finally, the porosity/density of the patterned porous lines can be calculated from the following equation,

$$\text{Porosity} \left(\frac{\text{mg}}{\text{mm}^3} \right) = \frac{\text{Net weight}}{\text{Total volume of polymer}}$$

The net weight is defined as the weight difference of the same sample before and after the introduction of polymer lines.

Finally, the results of these measurements and calculations are shown in Figure 4.11, which shows the correlation between the applied laser fluence and the resulting porosity/density of the polymer barrier. As shown in the plot in Figure 4.11, the porosity of the resulting polymer barriers increases from $\sim 0.3 \text{ mg/mm}^3$ to $\sim 0.7 \text{ mg/mm}^3$ with the increase of the applied laser fluence from $\sim 0.1 \text{ J/cm}^2$ to $\sim 1.7 \text{ J/cm}^2$. In conclusion, the higher the laser fluence used for the fabrication of the polymer structures, the higher the density of the polymer, and therefore the larger flow delay that can be introduced.

Laser incident power (mW)	Laser fluence (J/cm ²) @50mm/s	Weight before (mg)	Weight after (mg)	Net weight before and after (mg)
0	Blank	34.5	34.5	0
5	0.08	34.0	34.4	0.4
10	0.17	35.1	35.9	0.8
30	0.49	33.9	36.0	2.1
50	0.83	34.2	37.1	2.9
70	1.16	34.5	38.9	4.4
100	1.66	35.0	40.4	5.4

Table 4.1 Summary of the weight measurements of the paper substrate with polymer lines that were patterned with different laser incident powers at a fixed writing speed of 50 mm/s. The weight numbers in this table were the mean number of three measurements.

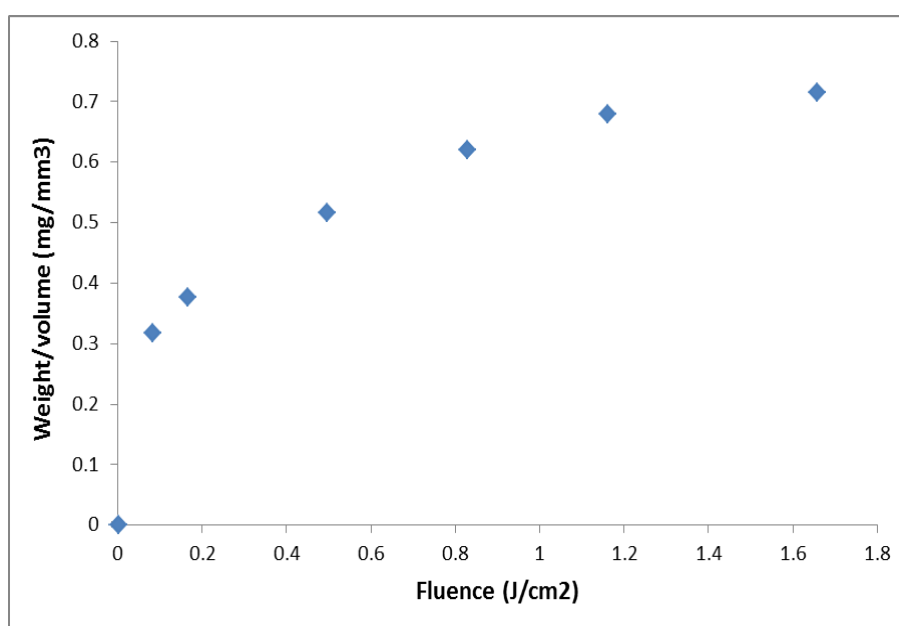


Figure 4.11 Plot showing the relationship between the laser fluence used to prepare polymer structures and their density (weight/volume).

4.3.3 Validation of delay barriers for multiple fluid delivery

Implementation of automated paper-based devices that are user-friendly and need minimal intervention from the patient or an unskilled user need strategies that allow

control over the flow of several liquids (reagents and samples) along their pathways. Such devices allow the implementation of a multi-step assay (such as an ELISA), and in this section, using fluid delay strategies effected using the flow-barriers described earlier, we demonstrate the usefulness of our method to fabricate such automated paper-based tests. Figure 4.12 shows a device that uses a network of three identical channels for sequential delivery of three fluids to a common detection or reaction point. As shown in Figure 4.12, sequential delivery of each of these fluids is made possible by introducing (a set of three identical) porous delay barriers written with a c.w. laser across the fluid channels. By changing the porosity of each set of delay barriers through simple adjustments of the laser parameters, different delays can be introduced into each channel.

To show the operation of our devices, we first introduced a source pad (a stack of 8 cellulose papers) into each channel that allows us to load a comparatively large volume of fluid ($\sim 40 \mu\text{L}$) into each channel and also serves as a continuous reservoir of liquid (Figure 4.12). We first tested the performance of our devices using TBS as the test-fluid which was introduced into the source pad in each of the three channels semiseriously. Figure 4.12 is a set of images that are snapshots taken sequentially at different times after introducing the TBS into the source pads. The fluid in channel 2 (that does not have any delay barriers) arrived at the intersection zone first (after 5 minutes) and continued to flow onwards until the fluid in channel 3 (with weaker delay barriers) arrived at the intersection (after 10 minutes). Thereafter, the fluids from these two channels mixed and flowed forward until the arrival of the fluid from the third channel (with stronger delay barriers) after 20 minutes. Finally, the mixture of three fluids then wicks through the reaction pathway in the following 10 minutes.

To further illustrate the dynamics related to the mixing of the different fluids and to make the concept of flow delay more obvious, we instead used two different coloured inks to source the three separate channels (black for channel 1 and 3 and red for channel 2). The sequential images that show the flow through the device are shown in Figure 4.13. When compared to the (blank) channel 2 that did not have any delay barriers, the fluid delivery through channel 1 and channel 3 was delayed by 15 and 5 minutes respectively. Overall, the results for both of the devices that were either tested using TBS or the coloured inks show clear evidence that our laser-patterned delayed-fluid flow strategy can be used to make paper-based automated devices.

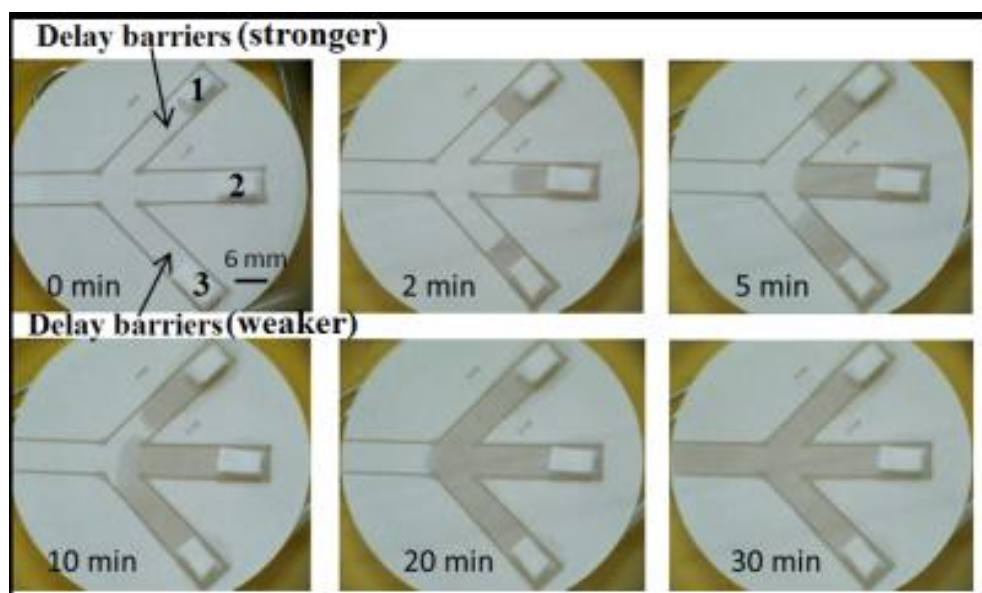


Figure 4.12 Image showing a 2D multi-channel fluidic device used for sequential delivery of three fluids (TBS). Three identical channels modified with different delay barriers (1.Stronger delay barriers; 2.blank; 3.weaker delay barriers).

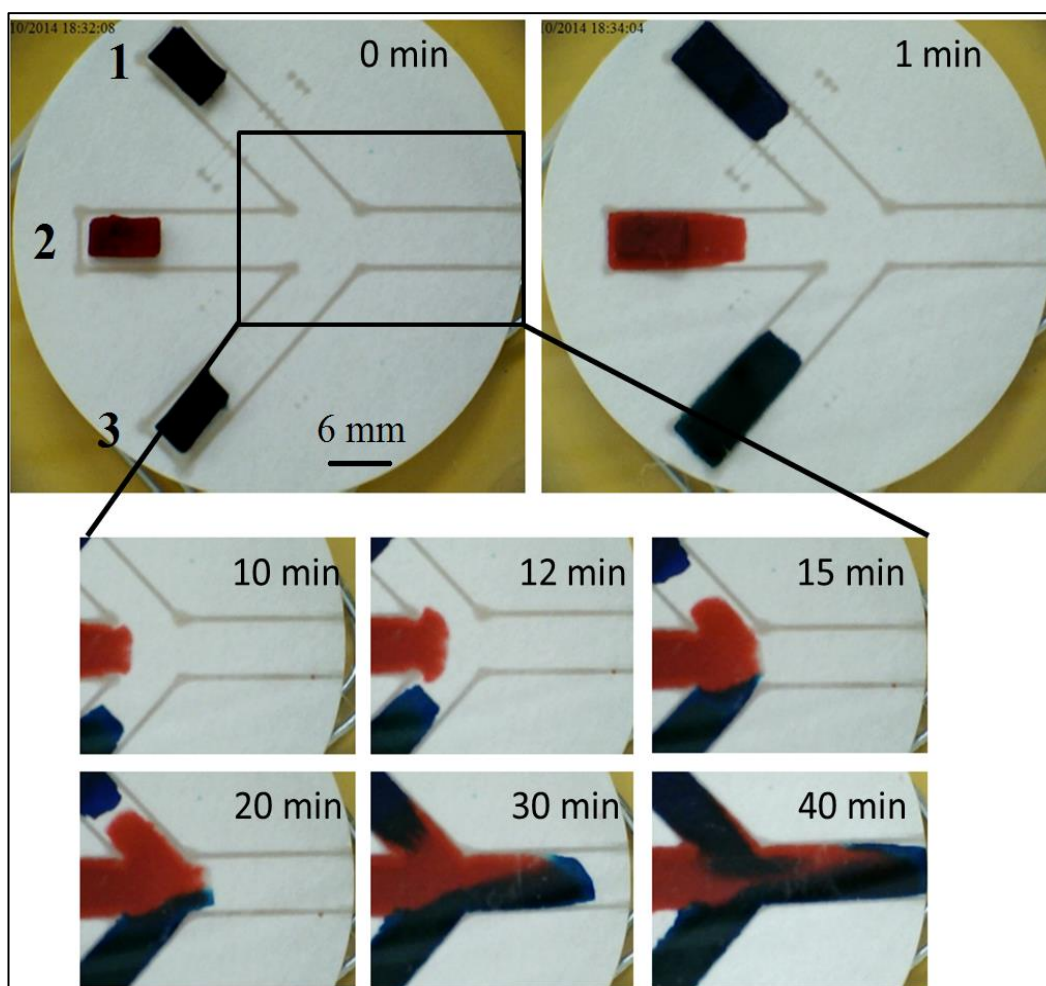


Figure 4.13 Sequential images showing the arrival and mixing of black and red inks from three separated flow channels in a 2D multi-channel device and the subsequent mixing of the inks.

4.4 Summary

In this chapter, we report a new method based on our LDW technique that allows the fabrication of pre-programmed or timed fluid delivery in paper-based fluidic devices without any additional equipment or minimal actions from the user. Two different delay mechanisms are introduced: 1) solid barriers with differing depths and 2) permeable barriers with differing porosities, and these could be fabricated by simple adjustments of the laser patterning parameters, such as the laser power and the writing speed. Both types of barriers yield similar results for control over the fluid flow. The efficiency of the delay, namely the delay factor, was seen to depend not only on the condition (porosity or depth) of the delay barriers but also on the number and the position of the barriers.

These programmable fluid delay techniques should help to further improve the functionalities of paper-based microfluidic devices as such control can be used to enable automated multi-step fluidic protocols. In contrast to other methods reported for controlling fluidic transport, our approach eliminates the requirements for cleanroom-based steps, or custom-designed equipment, or the need for long flow paths, which can then translate into requirements for larger analyte volumes. Most importantly, since the delay mechanism can be an integral part of the fabrication of the fluidic devices themselves, we believe this integrated process presents a considerable manufacturing and hence commercial advantage. Above all, we believe that this method could be an ideal choice for rapid fabrication of custom-designed paper-based microfluidic devices for realising single or multistep analytical tests.

Chapter 5: Three-dimensional structures in paper-based devices

5.1 Introduction

Paper-based microfluidic devices have been popularly studied in the last few decades, and a huge number of advantages have been explored, such as low-cost, mass production, disposability, equipment free etc. [14, 53, 124, 129]. However, some disadvantages or limitations are also apparent, such as issues with the control of flow rate, multiplexed detections/assays on the same device footprint and further reduction of size in order to achieve compact devices that require less volume of reagents with shorter distribution times [6, 130, 131]. As a result, 3D microfluidic paper analytical devices, as an alternative solution, have been proposed in recent years, which enable distribution of fluids in both lateral and vertical directions [5, 14, 132, 133].

Compared with traditional 2D devices, 3D devices introduce a number of unique characteristics which are advantageous for certain applications. First of all, 3D devices would enable multiple assays on the same device footprint as they allow fluids to flow across one another without any mixture. Furthermore, as the fluid movement is in three dimensions that flow through multiple layers of paper, they also introduce a potential capacity for implementation of multi-step assays in a compact device. Finally, because the fluids flow both laterally (in the paper plane) and vertically (through the thickness of paper), the quantity of reagents lost in wetting the paper will be minimised, hence help to further decrease the volume required for performing an assay. This will also help to hugely reduce the reagent distribution times.

One of the key challenges for fabrication of a 3D paper-based device at the moment is to ensure contact between hydrophilic features in each layer of the paper [6]. Three general solutions have been reported for avoiding this problem, which include: 1) attaching one layer of paper to another in a layer-by-layer manner with either double-sided tape or hydrophilic spray adhesive [5, 134]; 2) applying an outer adhesive, clamp, or protective coating to pre-assembled layers, which hold the layers in contact with each other [132, 135]; 3) forming hydrophobic barriers/areas partially inside the substrate forming 3D structures in a single layer of paper substrate [136].

5.2 Background

The first 3D paper-based microfluidic device was reported by Whitesides' group using a double-sided tape to physically attach individual 2D devices together, which were pre-patterned using the photolithography method [5]. Laser drilling of holes were performed in the tape at specific places, where the desired flow through is required, with back-filling with cellulose powder in order to create hydrophilic connections between adjacent layers of paper. However, this method is limited by its tedious sequential assembly process that is incompatible with mass fabrication. As an alternative technique, hydrophilic spray adhesive was also used to glue layers of pre-patterned 2D devices together, which allows rapid laboratory-based fabrication of 3D devices [134]. As this method relies on cold lamination techniques to hold layers of stacked 2D devices together and seal the devices, it is only able to achieve 3D devices with a few layers of paper, which is not feasible if assembling more layers is required [49, 137]. Following these reports, Crooks et al. reported an alternative method for creation of 3D paper-based devices based on the principle of origami, which is inspired from the traditional Japanese paper folding art [132, 135, 136]. In this approach, a 3D device is achieved by laying and folding a single piece of pre-patterned paper and then the stack is held together using a designed clamp. The origami technique during this approach allows patterning of different layers of paper in one go and additionally eliminates the alignment step. The folding design also enables opening and altering the devices during the reagent preparation step and even during the course of an assay [136, 138]. However, in terms of disadvantages, this method cause issues of reproducibility as individuals assembling the device may have different levels of experience and this interaction may also bring potential contamination. Overall, most of these methods were reported based on fabrication of 3D devices on cellulose paper. However, other porous materials, such as thread [108, 110], cloth [112] and silk fabric [109], were also explored by different groups for fabrication of 3D microfluidic devices, although the assays' reproducibility on these materials has not been verified or authenticated [6].

Unlike all the methods discussed above, in this chapter, we report a new approach for fabrication of 3D devices, which again is a simple extension of the basic LDW technique that has been described in previous chapters for both fabrication of 2D microfluidic devices and implementation of flow-control. As was the case for our LDW method where we demonstrated the use of laser light to form 2D patterns and delay barriers in paper through light-induced photo-polymerisation, the 3D structures in this report are created using the same principle of light-induced photo-polymerisation. In brief, through controlling the patterning conditions, we could produce solid hydrophobic structures

either partially inside a single layer of paper or all the way through a few layers of paper. Thus by selectively patterning from both sides of the paper we could fabricate 3D devices based on both a single layer of paper and a stack of multi-layers. Unlike other 3D device fabrication methods, the approach presented here does not require any additional processing equipment or alignment/assembling steps and as described earlier uses the same fabrication approach that produces a 2D fluidic device.

5.3 Experimental results

5.3.1 Stacking and sealing of multi-layer papers

During our earlier LDW studies for fabrication of 2D paper-based microfluidic devices, we observed that the photo-polymerization process is not only restricted to a single substrate but can also extend further into a composite formed from several layers. In order to understand and further explore this phenomenon, we prepared samples with different numbers of layers (two to five) and investigated their patterning using the same LDW method. The schematic for this is shown in Figure 5.1: firstly, different numbers of cellulose papers were stacked together and then soaked with the photopolymer. The same LDW patterning process was applied to form simple structures in these multi-layered samples. After the final development process, it was then observed that these multi-layers had been efficiently bonded together to form a single composite structure.

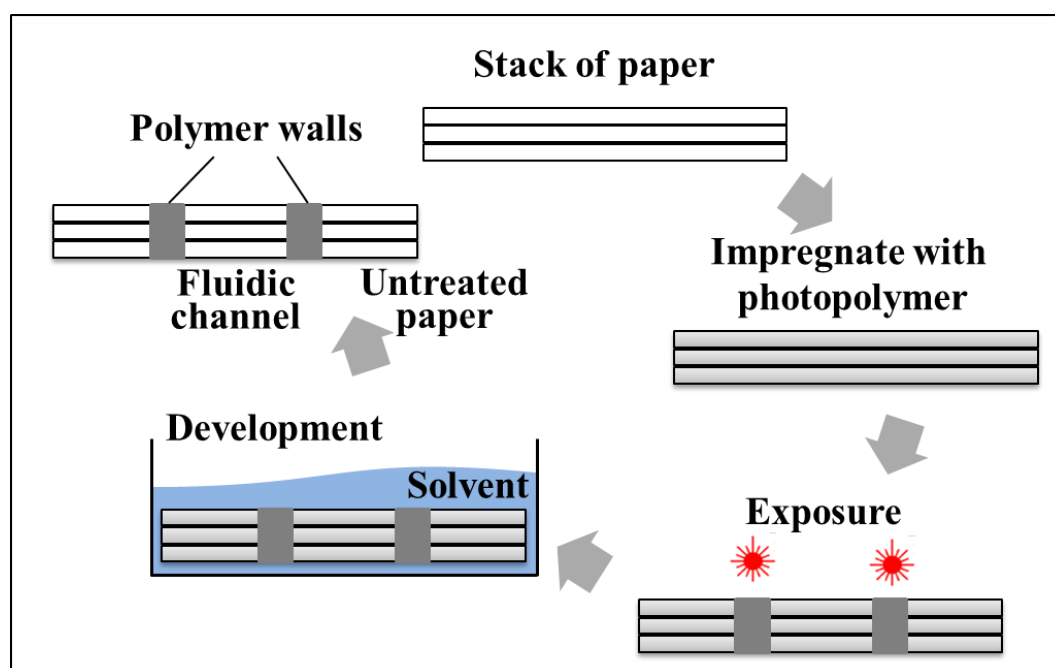


Figure 5.1 Schematic of patterning multi-layer stacks using the LDW technique.

Based on our current setup with a 405 nm c.w. laser, we found that a maximum of three layers of cellulose paper (each with a thickness of 180 μm) can be bonded together using a laser output power of 100 mW at a scan speed of 10 mm/s. The polymerised lines were evident throughout all three layers of paper and as shown in Figure 5.2a and 5.2b, can be clearly observed on both sides of the three-layer stack. We then tested these structures by applying different volumes of blue ink, from 3 μL to 7 μL , into these square wells from the top surface as shown in Figure 5.2c. The ink was well-confined within the square wells defined by the polymerised walls and flowed vertically from the upper layer to the layers underneath. The result is shown in Figure 5.2d: 3 μL of blue ink is just enough to reach the third layer, while the whole square well of all three layers get fully inked with a volume of 6 μL while 7 μL is seen to produce slight overflowing. It is clear therefore that the polymerised structures that extend from the top layer all the way to the bottom layer perform the dual function of bonding and forming walls that contain and hold the fluid without any leakage, as seen in the image using 6 μL in Figure 5.2d.

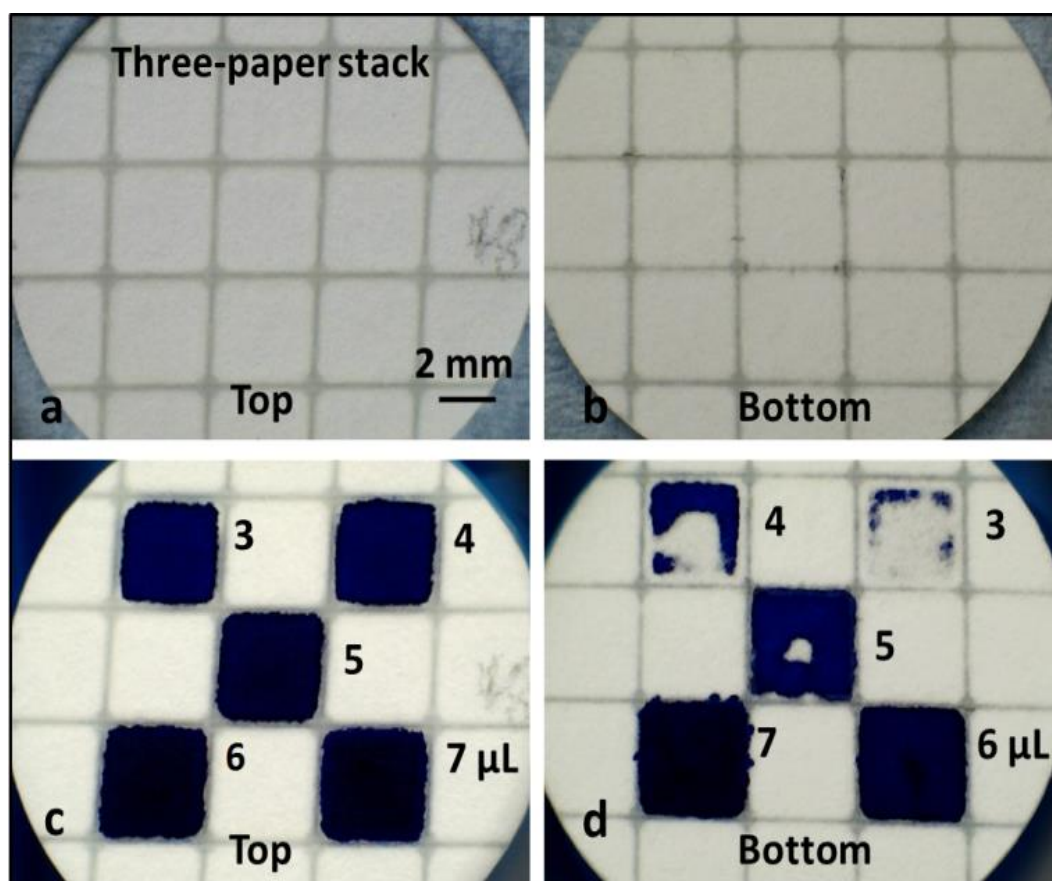


Figure 5.2 Images showing the polymerised structures from both sides a) top side, b) bottom side) of a stack with three layers of cellulose paper and images of both sides of the device c) top side, d) bottom side) after introduction of blue ink of different volumes (3-7 μL) into the designated well.

Using the same parameters, we then attempted to pattern stacks with four layers. However, although the layers were indeed bonded together, leakage was much more of an issue. So under our normal patterning process conditions, we did not pursue composites with greater than three layers. However, stacked structures with more layers would indeed be possible through choosing different patterning parameters, such as lower scan speed and higher incident power.

Following these first results we then trialled assembly of multi-layer stacks but this time composed of dissimilar substrate materials. The schematic image in Figure 5.3a shows our first realisation of a stacked structure using different materials: two layers of cellulose paper with a PVDF layer in between that have been bonded together via a common photopolymerization process. As shown in the schematic, a rectangular channel and a T-junction were patterned on the top and bottom surface respectively and four sealing points were formed throughout all three layers for bonding. To test the device, red and blue inks were separately introduced onto the top and the bottom surfaces of this stack, and as shown in Figure 5.3b and 5.3c the inks were guided in the channel and T-junction respectively. From Figure 5.3b and 5.3c, it can also be clearly observed that both inks flow only within their respective layers and did not penetrate through to the opposite layer due to the presence of the intermediate blocking layer (hydrophobic PVDF). This innovative result presents a solution for not only sealing of paper-based devices by isolating the device between dissimilar outer cladding layers but also, most importantly, permitting 3D pathways to be engineered through a judicious assembly of several layers, possibly combined with holes and voids in some layers.

Any paper-based device is normally intended for operation under ambient conditions, which can lead to a number of limitations when compared to fully enclosed microfluidic devices. Two of the main drawbacks are: a) the device is at risk of contamination during the fabrication, transportation and operation, and b) possible evaporation of the fluid in the open air which may lead to change of the sample concentration, or an altered flow rate due to change in sample viscosity [17, 139]. We believe that the results we have achieved above should contribute to a reduction of these two limitations by sandwiching a conventional paper-based microfluidic device with two outer layers of hydrophobic material. The LDW technique can be further extended to develop a new approach that helps with sealing in microfluidic paper-based analytical devices (μ PAD). Additionally, the technique could also be further employed for permitting 3D pathways through carefully designing the patterning protocol and subsequent assembly of several layers for the realisation of a practical 3D paper-based device.

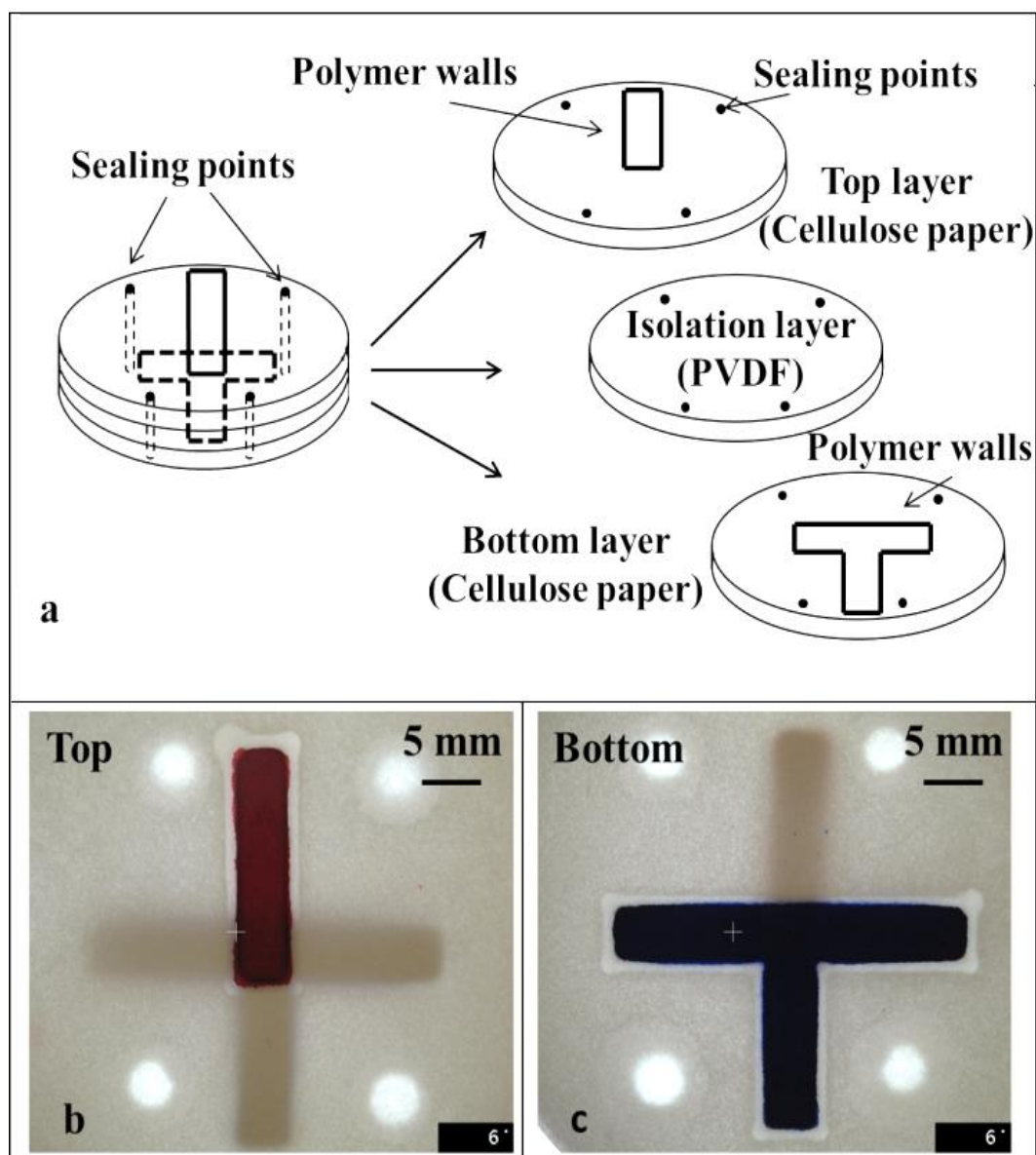


Figure 5.3 a) Schematic image showing the arrangement of a stacked device with different structures in top and bottom layers, which are isolated with a hydrophobic film in between. b) Top and c) bottom images showing the device described in a) after the introduction of different inks from top and bottom surfaces without any cross-contamination or mixing.

5.3.2 Single-sided polymerisation – for backing a paper-based device

To our knowledge, all or most of the presently reported paper-based microfluidic devices have another important limitation - operation of these unbacked devices requires that their bottom faces to remain isolated from contact with any surface to prevent fluid flow along the interface which would provide an alternative undesirable flow path. In addition to the loss of the fluid (an expensive reagent or valuable sample present in small volumes

for example), this unwanted flow can also lead to cross-contamination which in turn may produce a false result or failed test. On the other hand, as paper is normally very fragile and more so especially after getting wet, a backing support to provide mechanical strength would normally be desirable. For the case of NC membrane-based devices, the support to the membrane can be provided by an impermeable polyester layer [100]. While it is easy to procure such pre-backed NC membranes which are extensively used in LFD, it is not yet possible to source similar backed versions of paper substrates from the market. As an alternative, tape is widely used to back paper-based devices [100], but this has certain drawbacks as the adhesion becomes poor when the paper gets wet following the introduction of the sample; additionally, the adhesives in tapes can diffuse into paper over time, which can lead to contamination as well as affect the paper's hydrophilicity [17]. Another method of backing paper-based devices is based on flexography printing: a thin layer of polystyrene is printed on one side of the paper to form a hydrophobic backing [67], but this method requires additional equipment and adds cost to the final devices.

We, therefore, introduce here the use of our LDW technique as a new solution for backing paper-based devices. From the experiments we have done previously, we have observed that by controlling the patterning parameters (laser incident power and scan speed), we could alter the depth of polymerised structures inside the substrate that thereby forms a hydrophobic polymerised layer within the substrate itself, which could be used as the backing layer. Compared with the methods currently used for backing, our LDW method allows the formation of a backing structure inside the substrate during the device fabrication procedure without any need for extra materials or equipment, which would then lead to cost reduction and simplicity of fabrication. The schematic illustrating this is shown in Figure 5.4: the paper substrate is first impregnated with photopolymer, then during the exposure step, the laser parameters are selected to polymerise only to a certain depth inside the substrate. After the final development process, the un-polymerised material is washed away, leaving behind a polymer layer with a specified depth inside the substrate, which thereby serves as the required backing.

We, therefore, performed a parametric study to understand the influence of different patterning parameters, which also included a number of repetitive scans. The basic LDW setup is the same as described previously and the paper substrates used were Ahlstrom® Grade 320 chromatography paper with a thickness of 2.48 mm. As a proof-of-principle, in order to form a backing structure, we scanned the laser beam across the substrate in a line-by-line manner with a centre-to-centre separation of 1 mm (as shown in Figure 5.5a), which was appropriate for the lines to just touch each other without any significant

overlap or gaps. By forming adjacent polymerised lines under the same writing conditions, it was possible to create a 2D polymerised layer inside the substrate.

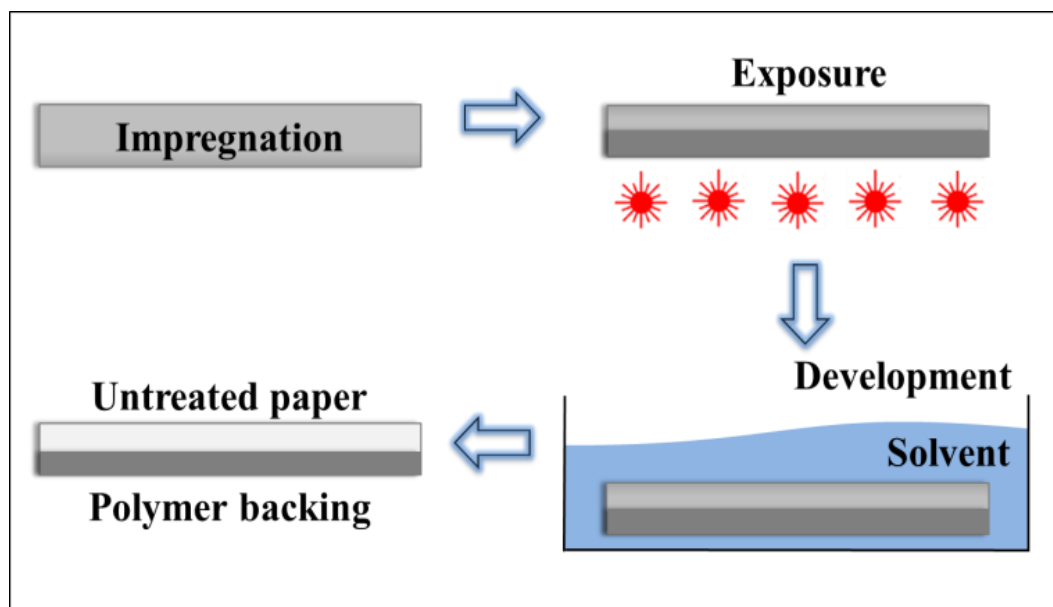


Figure 5.4 Schematic of patterning a backing layer inside the paper substrate using the LDW technique.

The cross-sectional images in Figure 5.5b and 5.5c show examples of a patterned paper with different thicknesses of polymerised layers formed at the bottom of the substrate that was achieved by simply altering the patterning parameters. As shown in Figure 5.5b and 5.5c, after introducing red ink from the un-polymerised side, we could clearly identify the polymerised layers (the white regions). As seen in the images: the thickness of the polymerised structures increases from $\sim 700\ \mu\text{m}$ to $\sim 1\ \text{mm}$ with an increase of laser output power from 30 mW to 70 mW at a fixed scan speed of 5 mm/s. As shown in both images, the polymerised layer, although written in a line-by-line manner was continuous and uniformly thick, and the demarcating interface between the un-polymerised and polymerised section is clearly defined.

To further study the depth of the polymerised layers as a function of the patterning parameters, we performed a study with the results shown in Figure 5.6. For a fixed scan speed, as expected, the depth of the polymerised layer increases with an increase of the incident laser power. For example, at a fixed scan speed of 10 mm/s, the depth of the polymerised layer increases from $\sim 400\ \mu\text{m}$ to $\sim 950\ \mu\text{m}$ with an increase of laser output power from 10 mW to 100 mW. Similar behaviour was observed with a layer depth increase from $\sim 450\ \mu\text{m}$ to $\sim 1050\ \mu\text{m}$ and $\sim 1200\ \mu\text{m}$ to $\sim 2050\ \mu\text{m}$ at a fixed scan speed of 5 mm/s and 1 mm/s respectively for incident laser power ranging from 10 mW to 100 mW. As expected, we can also observe from the same plots that the depth of the polymerised layers increases with the decrease of the scan speed at fixed laser powers.

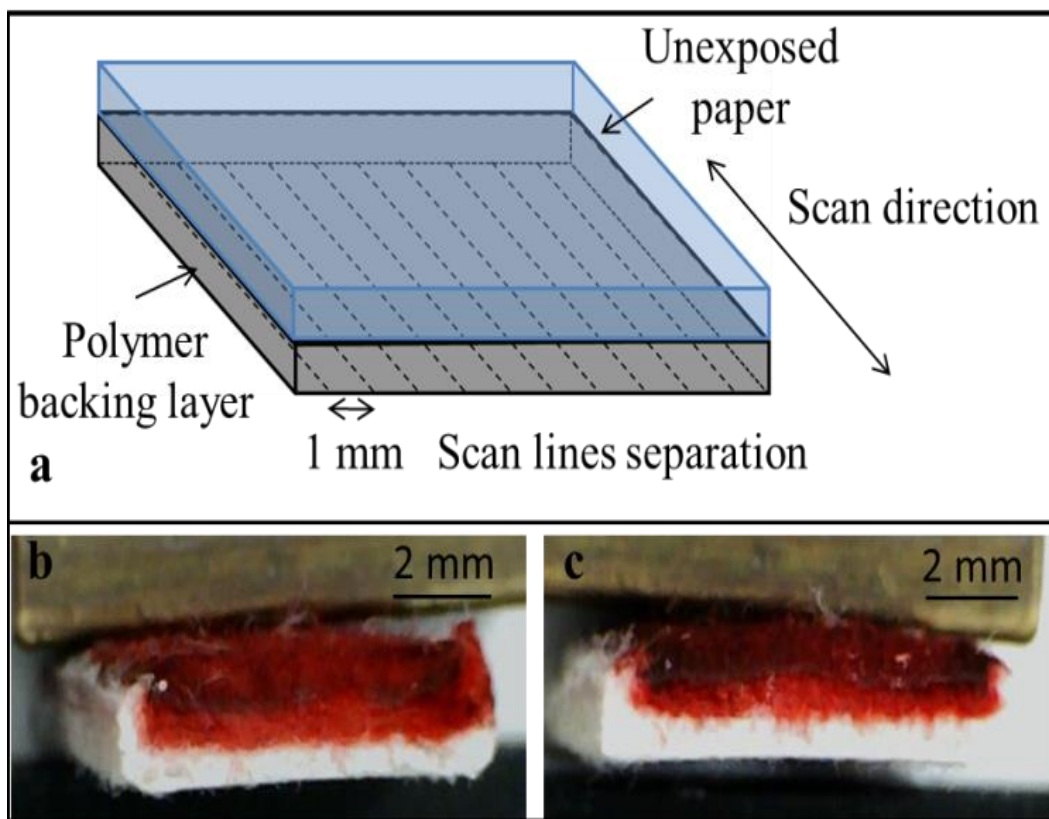


Figure 5.5 a) Schematic of patterning a backing structure by scanning the laser beam across the substrate in a line-by-line manner with a separation of 1 mm. Cross-sectional images showing polymerised layers (un-inked white layers) on one side of thick cotton fibre filter paper with different thicknesses of: b) $\sim 700\ \mu\text{m}$ and c) $\sim 1\ \text{mm}$, after the introduction of red ink from the other side.

Additionally, we observed that the depth of a single polymerised line also depends on the number of scans performed under the same writing conditions, which thereby alters the resulting thickness of the polymerised backing layers. In order to study how the number of scans affects the polymerised depth, we scanned the beam once, twice and three times respectively under the same writing conditions. The histogram in Figure 5.7 shows that the depth of the polymerised layer increases monotonically with an increasing number of repeat scans. As shown in the plots, the depth of the polymerised layer increases from $\sim 400\ \mu\text{m}$ to $\sim 800\ \mu\text{m}$ with an increase of the number of scans from one to three at a patterning condition of 10 mW of incident power at 10 mm/s scan speed. Similar trends were observed for all laser powers used (30, 50, 70 and 100 mW) for the same scan speed of 10 mm/s.

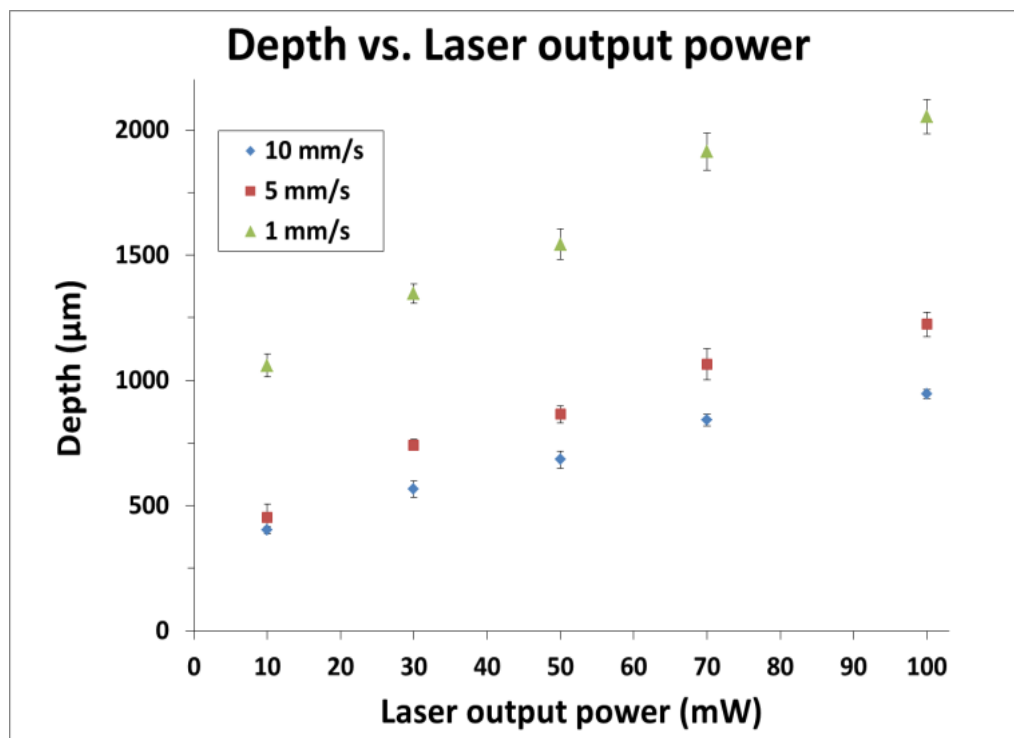


Figure 5.6 Plots showing the variation in the depth of the polymerised layers for different laser powers at three different scan speeds. Error bars indicate the standard deviation for 5 measurements.

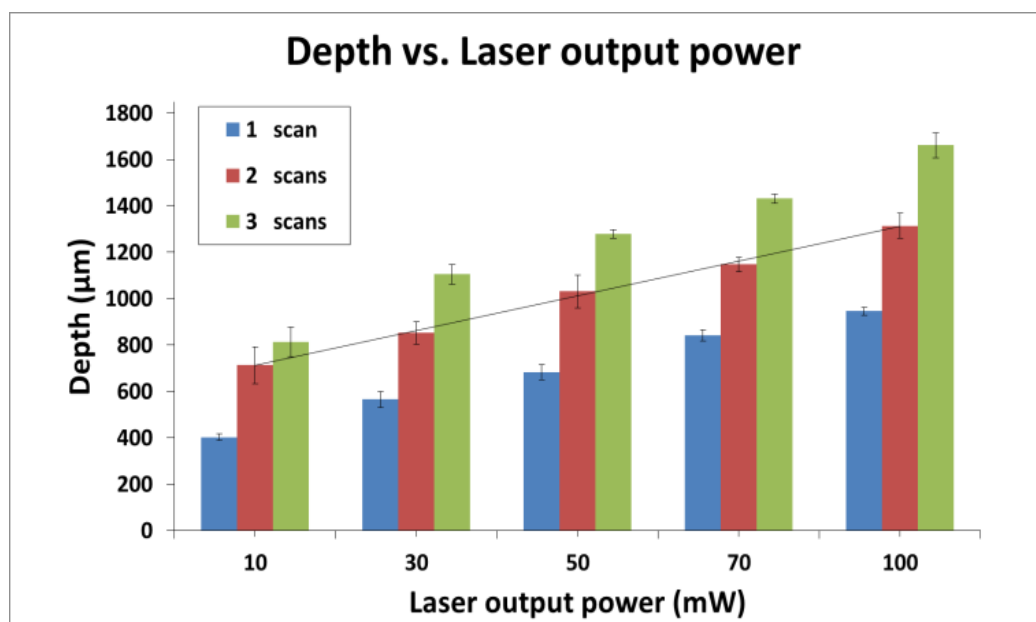


Figure 5.7 Plots showing the variations in the depths of the polymerised layers for different laser powers at a fixed scan speed of 10 mm/s for three different numbers of scans. Error bars indicate the standard deviation for 5 measurements and the straight line for the case of 2 scans is a simple guide for the eye.

5.3.3 Single-sided polymerisation – for reduction in the dead-volume of a paper-based device

An additional benefit of this technique lies in the reduction of the active paper volume that can be produced routinely for all such test substrates, which leads to a corresponding reduction of reagent/sample volume required. Due to the opacity of the substrate, the observable signals (the colour change) that provide the test results originate only from the top region or plane of the substrate (which for a nitrocellulose membrane extends below the surface to a depth of $\sim 10\ \mu\text{m}$), and any colour change from deeper regions (the so-called dead volume) makes a negligible contribution to the observable signal, and is, therefore, redundant [140]. Reduction of the thickness of the substrate at the detection area will therefore not only help with the saving of reagents/samples but will also help increase the limit of detection. Because the amount of the sample which previously would have soaked the entire volume of the substrate will now instead fill up a comparatively smaller volume of the substrate, the sample concentration will be relatively higher and thus will lead to an improved limit of detection.

To test this hypothesis, as shown in Figure 5.8a, a simple proof-of-principle experiment was performed by introducing different volumes (1, 2 and 3 μL) of red ink into $4 \times 5\ \text{mm}$ well structures patterned on samples 1 and 2, which were backed with layers that had different thickness of $\sim 400\ \mu\text{m}$ and $\sim 600\ \mu\text{m}$, using the LDW method. The paper substrates used for both samples were Ahlstrom® Grade 222 chromatography paper with a thickness of 0.83 mm. As shown in Figure 5.8a, the colour intensities change in each well with different ink volumes and also differ between the two samples with different thickness of backing for the same volume.

The images were then processed with the ImageJ software (National Institutes of Health, USA) to extract the respective grayscale colour intensities of the red colour produced within the central area of each well and the results are plotted in Figure 5.8b. The conclusion here is that the detected colour intensity increases with an increase of the ink volume, but more importantly, also increases with an increase of the backing thickness, i.e. the signal is enhanced with a reduction of the dead volume. We, therefore, believe that by designing and choosing the appropriate thickness of the backing, we should be able to control the volume of the substrate and hence reduce the dead volume thereby increasing the limit of detection and saving on sample or reagent needed.

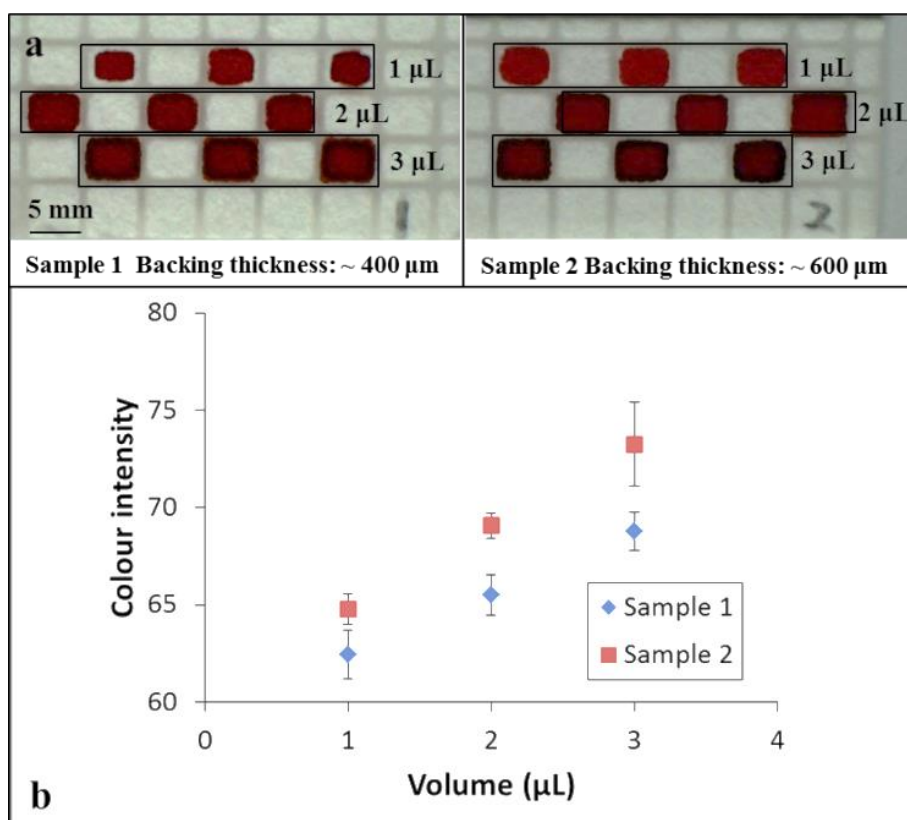


Figure 5.8 (a) Images showing the results of the introduction of different volumes of red ink into $4 \times 5\text{mm}$ well structures patterned in two samples with different backing thickness. (b) Plots constructed using the grayscale intensity values taken from the images shown in (a). Error bars indicate the standard deviation for 3 measurements.

In summary, we have proved that by simply changing the patterning parameters, we can polymerise lines with different depths in the substrate, and therefore, by scanning lines in a line-by-line manner we could form polymerised layers with the desired depths, and these can be used either as backing for paper-based devices or to alter the volume of the paper-based fluidic devices. Here, for our first simple proof-of-principle experiment, we have used an un-optimised line-by-line scanning procedure in order to cover a large area. Alternatively, instead of repetitive multiple scanning protocols, a single-step process that uses a cylindrical lens could also be employed. In this case, the lens focuses the beam only in one direction and leaves the other direction wide enough to cover an extended lateral region and this is an intended future approach.

5.3.4 Dual-sided polymerisation – for fabrication of a 3D paper-based device

In order to exploit fully the true potential of this approach, we have explored the possibility of creating such polymerised patterns through exposure from either side of a

single substrate. The objective here was to use this dual-sided polymerisation protocol to fabricate a 3D device in a single paper substrate. The concept is explained through the schematic depicted in Figure 5.9a. As shown in this figure, by patterning via exposure from both the top and bottom faces of a single paper substrate it should be possible to create polymerised blocks that extend partially from both faces of the substrate and define an enclosed flow-path that is embedded within the substrate. By selectively positioning and connecting such polymerised areas, we can then construct arbitrarily-shaped connected 3D flow paths that guide the fluid both in the horizontal and vertical directions. The schematic in Figure 5.9b shows an example of such 3D paper-based devices created in a single substrate with several fully enclosed and interconnected channels. As shown in the cross-section schematic, solid polymerised barriers were formed from both top and bottom, leaving gaps in both vertical and horizontal directions. The gaps in the vertical direction form three open windows A, B and C, where the reagent/sample will appear after passing through the enclosed channels between the two inlets (①②). The enclosed channels that connect the inlets and three open windows are defined by gaps between the solid barriers in the horizontal direction. Photographic images of the top and bottom views of a real device with the illustrated arrangement are shown in Figure 5.9c: the white areas are bare/un-polymerised sections of the paper and the pale yellow areas are the hydrophobic polymerised regions.

In order to test these 3D structures, we first introduced red ink from the inlet ① of the device described in Figure 5.9b. The sequential images in Figure 5.10 show the flow of red ink, which were taken from both top and bottom faces of the device. After the introduction of the ink, it flowed into the first enclosed channel between inlet ① and the open window A. The red shaded areas were observed from both sides of the device and illustrate the ink flow inside the channel. After a short period of time, the ink flowed through the first section of the enclosed channel and reached the open area A: as shown in the images the red ink has filled in area A and is visible from both top and bottom.

We have also introduced red ink from the inlet ② and the result is shown in Figure 5.11. The ink again flowed through the enclosed channel between the inlet and the open area C and finally reached the open window C and hence appeared on the top side. The difference of the structures in the right and the left sections of the device is that the polymerised structures at the bottom cover the whole area without having an open window. It can be regarded as a 3D device with an enclosed channel and an open window just on the top plus a backing structure underneath, which helps to provide support to the device.

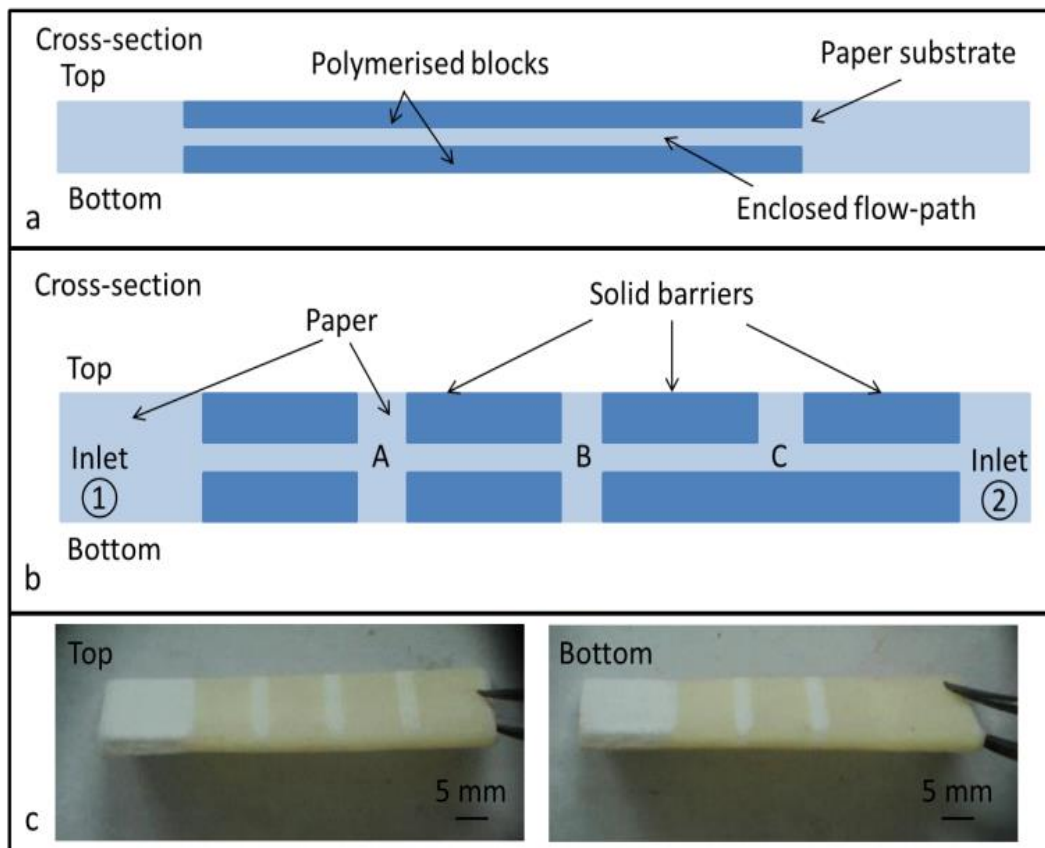


Figure 5.9 a) Schematic showing an enclosed flow-path formed by creating polymerised blocks from both faces of a single paper substrate. b) Schematic representation of the cross-section of a 3D fluidic device with two inlets (①②) from either end. c) Photographic images taken from the top and bottom of the device described in b).

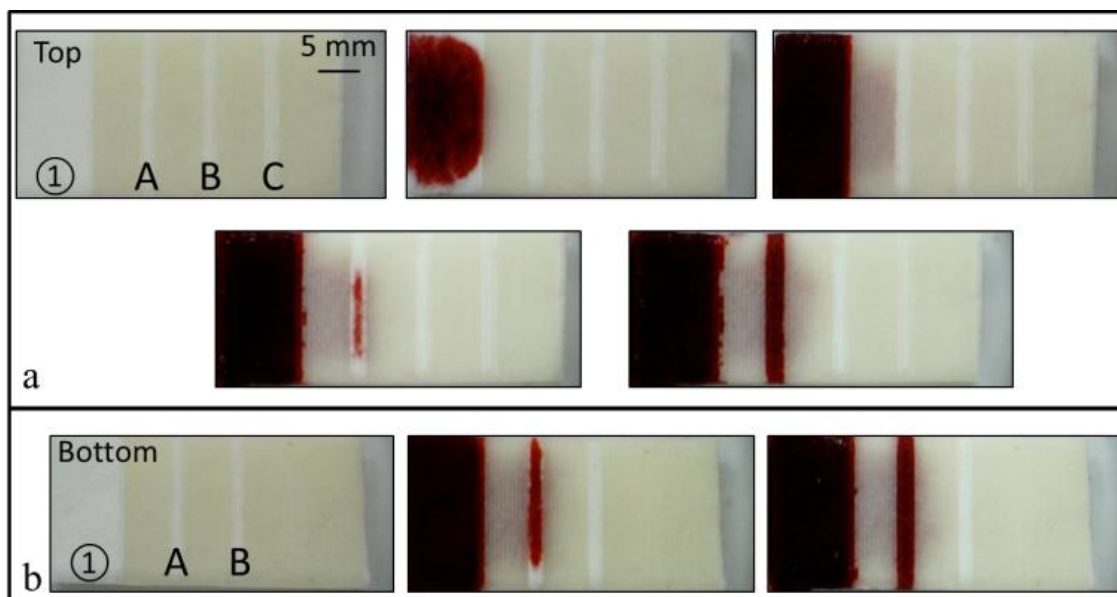


Figure 5.10 Sequential images taken from the a) top and b) bottom showing the device described in Figure 5.9b after the introduction of red ink from the inlet ①.

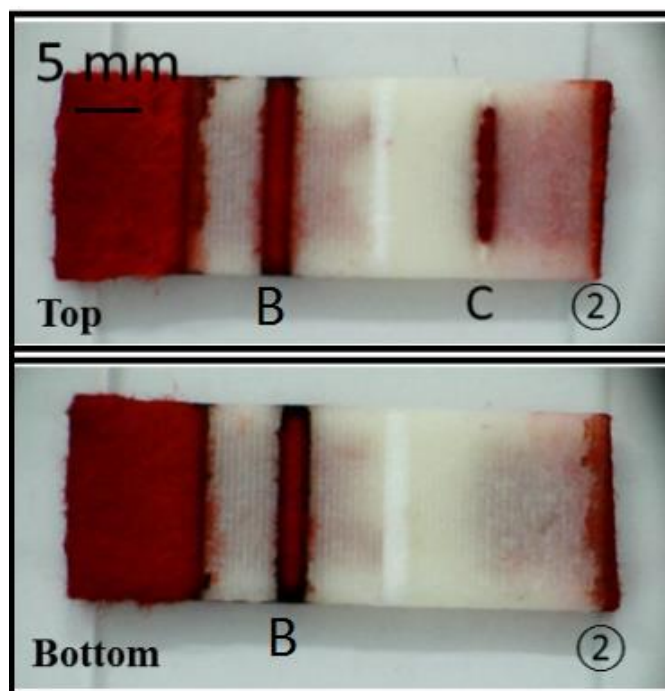


Figure 5.11 Photographic images showing the top and bottom of the device described in Figure 5.9b after the introduction of red ink from the inlet ②.

Finally, the cross-section image in Figure 5.12 illustrates the flow process of the red ink inside this 3D device. The narrow red lines inside the substrate, which connect the inlets and open areas, show the flow of the red ink inside the enclosed channels. The ink from inlet ① flowed and filled up the open area A, which allows the ink to be seen from both top and bottom, through an enclosed channel in between and then kept flowing towards the open area B along another enclosed channel. Similarly, the ink filled in the open area C and shows up only from the top with the source from the inlet ② again through an enclosed channel inside the substrate that was formed with solid blocks on both sides. Such fully enclosed channels can be achieved easily with our LDW method, which prevents liquid exchange between the exterior and the interior of the channel.

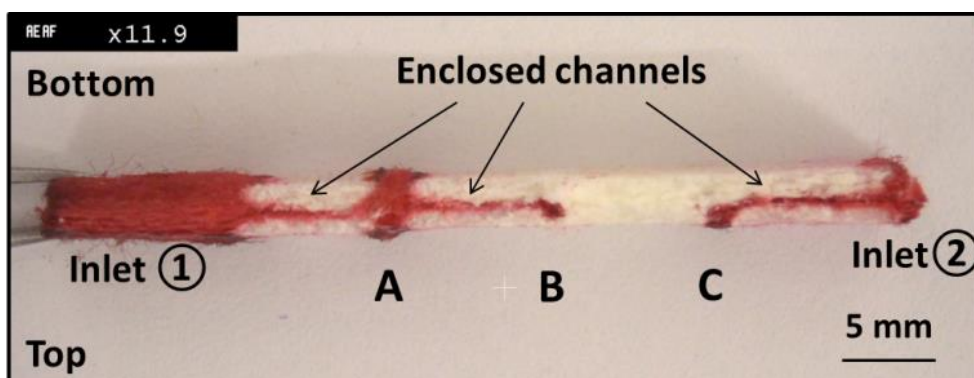


Figure 5.12 Cross-section image showing the enclosed channels and flow of the red ink in the device described in Figure 5.9b after the introduction of ink from both inlets.

Above all, the approach reported here for fabrication of 3D paper-based devices is a simple extension of the basic LDW technique that has been used for fabrication of 2D microfluidic devices [141, 142]. Through selectively designing and patterning polymerised structures from both sides of the substrate, we could fabricate 3D structures inside a single substrate. Unlike other 3D device fabrication methods, the approach presented here does not require any additional processing equipment or alignment/assembling steps and uses the same fabrication approach described earlier for producing a 2D fluidic device.

5.4 Summary

In this chapter, we tried to explore and extend our LDW approach further for applications beyond fabrication of simple 2D microfluidic paper-based devices and implementation of programmable flow delay. These aims were to maximise the capacity of our technique. First of all, we found that by altering the patterning parameters, the polymerization process can extend through a few layers of substrates that are stacked together. This can be used for sealing the devices in order to solve potential evaporation and contamination problems. We believe that through carefully designing the patterning strategy or judicious assembly of several layers, it could also be further developed for permitting 3D pathways for the realisation of a 3D paper-based device.

Following these, we then explored the possibility of using this approach for fabrication of backing structures inside the substrate itself instead of an additional polyester film, which is normally used to laminate the device afterwards. We found that by simply changing the patterning parameters, we could polymerise lines with different depths in the substrate; hence by scanning lines in a line-by-line manner we could form polymerised layers with different depths, which can be used as backing for paper-based devices. We then performed a parametric study to identify the relationship between the depth of the polymerised layer and several patterning parameters, such as laser output power, laser scan speed and number of repeat scans. Ideally, a cylindrical lens would be applied in future, which focuses the beam only in one direction at leaves the other direction wide enough to cover the whole device, in order to avoid sequential line-by-line scanning. In addition, we realized that this polymerised layer with different controllable depth can be also used to control the paper volume, which will help to reduce the required reagent volume and most importantly, with our hypothesis, can be used for enhancing the assay sensitivity and detection limit.

Finally, by combining all our previous achievements, we then showed the possibility of fabrication of 3D devices using our LDW technique. The polymerized layer can be formed inside the substrate at different depths, as discussed in the previous parametric study,

through selectively designing and patterning some of these polymerised structures from both sides of the substrate, we could fabricate 3D structures inside a single layer of substrate. Unlike other 3D device fabrication methods, our LDW approach does not require any additional processing equipment or alignment/assembling step and uses the same fabrication approach that is described earlier for producing a 2D fluidic device by simply altering the patterning parameter.

Chapter 6: Triggerable fluidic gates in paper-based devices

6.1 Introduction

To date, a number of methods have been reported and applied for producing hydrophobic structures inside the paper substrate for confining fluids in designated channels and subsequently delivering them to desired zones for specifically intended reactions. However, in order to perform more challenging analyses on a paper-based platform, a few limitations still exist, and improvements need to be made for more user-friendly operation and implementation. One such limitation is the absence of a switchable fluid flow manipulation method or procedure that facilitates the possibility of user-determined ‘flow-on-demand’ controls within a fluidic device, and such a mechanism is urgently needed so that the sample under test can be, for example, inserted into a reader or other associated equipment and the test performed at a time chosen and determined by the user.

Tools and mechanisms that provide for fluid manipulation and gated or user-triggerable flow are hence urgently needed. To date, although several methods have been reported that enable the control of the fluid flow, i.e. controllable fluid delay via altering either the fluid flow rate or the physical length of the flow path, approaches that achieve on/off triggerable fluidic switching are also equally important, and so far practical and user-implemented solutions for the latter have not been widely explored. These mechanisms play an important role in multi-step protocols such as multi-step assays and signal amplification [6].

In this chapter, we introduce a method that would enable large-scale commercial production, at reduced costs, of fluidic gates in paper-based microfluidic sensors via the use of printed wax barriers. This methodology we have proposed can be used for fabrication of fluidic gates in paper or any other porous substrates that are frequently employed to fabricate microfluidic devices. The method is based on the use of a barrier of wax (in this prototype first demonstration) that is printed across the fluidic flow path, which can be triggered by local melting leading to the leakage of fluids across the gate. Unlike other reported fabrication methods, our approach allows fabrication of fluidic gates with an extremely simple and cheap printing procedure without the need for additional expensive equipment and complicated procedures. Moreover, as materials such as wax can be bio-compatible and the switching of the gates is realised by local heating of the barrier via a non-contact approach, this approach does not introduce any contamination

into the flow path of the fluidic devices. Finally, these gates are highly controllable by application of variable intensity or strength heat sources.

6.2 Background

To date, several methods have been reported in the literature to control fluid flow and thus enable fluidic switching in paper-based microfluidic devices. For all of these reports, fluid gating in paper-based devices has been demonstrated either by user-involved physical connection of separate channels, i.e. manually connecting or disconnecting the hydrophilic pathway [101, 121], or via insertion of dissolvable barriers across the flow path [143].

The first example of a paper-based microfluidic switch was built to control capillary wicking in fluid channels by manually connecting or disconnecting the hydrophilic pathway. This was accomplished by cutting a channel into two pieces and manually separating the channels to allow or inhibit the capillary flow [101]. However, this method requires additional effort from the user to ensure the alignment and contact of the separated channels without leakage, and so lacks reproducibility and is not very practical.

An alternative technique was reported by Martinez et al. for use in three-dimensional flow paths. The mechanism of this gating valve is based on closing the gap between two vertically aligned fluidic channels by applying pressure [121]. Closing the gap allow fluids to wick along the connected channels. The single-use 'ON' button was activated using a ballpoint pen (pin pressure). However, such designs require the additional use of cellulose powder and custom-made tapes to enable the vertical flow paths through the multiple layers. In addition, it also suffers from complex fabrication procedures that arise from the need for alignment of the flow paths within the multiple layers.

Subsequent work by Lutz et al. reported an alternative method for creation of the paper-based valves and this is based on dissolvable fluidic time delays [143]. Feasibility studies demonstrated the impregnation of sucrose in the flow path to create time delays that spanned seconds to hours. However, this mechanism is extremely sensitive to the specific properties of the fluids and is also influenced by the fluid evaporation rate, and hence the ambient environment. In addition, the impregnated sucrose, which is pre-dispensed in the substrate, needs to be compatible with the analytes that are intended for measurement.

Recently, another method was reported by Salentijn et al. to enable valves via the use of an ink-jet printed AKD gate [144]. As the AKD is impermeable to most aqueous solutions and only permeable with some solvents, i.e. alcohols, these AKD barriers can be switched on and off by changing the solvent –thereby stopping or allowing the flow of fluids through

the gate. However, this method requires complicated multiple fabrication procedures and needs additional solvents to enable the switch, which runs the risk of contamination. Other potential mechanisms, such as dissolvable fluidic time delays and modification of the paper volume [127, 128], have also been proposed, however, they are technically based on altering the fluidic distribution rate (slow release of fluids), which basically cannot enable real-time on-demand absolute on/off switching (i.e. gating) of fluids.

6.3 Fluidic gate strategy

Wax printing is one of the most commonly used methods for fabrication of paper-based devices. A commercially available office wax printer is used to print wax onto the paper surface with any user-defined designs within seconds, and subsequently, the wax printed paper is heated to allow the wax to melt and penetrate through the paper. On removal of the external heat source, the melted wax re-solidifies and produces a solid hydrophobic barrier that confines the fluid flow [65, 97]. Here, we are using the same approach to create a wax gate or valve in a similar porous substrate. A commercially available wax printer (Xerox ColorQube 8580) was used to print wax onto the surface of the substrate at the desired position, and then the wax was melted by either putting the whole device onto a hot plate or by locally heating the wax via a resistive element or light source. This wax barrier then acts as a triggerable fluidic gate, which can be switched via the application of local heating.

To enable such on/off triggerable switching in fluidic devices, we propose a methodology, which is based on a triggerable wax gate inside the porous paper substrate within the fluidic channel. In brief, the switching of a flow inside a fluidic channel is achieved by insertion of a triggerable hydrophobic wax barrier across the flow path. In the absence of an external trigger, the barrier acts as a closed gate that blocks the fluid flow and the gate can thus be thought of as being in an 'OFF' state. In order to trigger the switchable gate, the wax barrier is locally heated at a specific location, to just above its melting point, inducing a leakage of the fluid through the formerly impenetrable barrier, and this enables the fluid to flow further along its path, to its intended destination where the test or other functions are implemented. In this state, the gate can thus be thought of as being in an 'ON' state. Thus, these triggerable barriers act as controllable on/off gates that either impede or allow the flow of fluids on demand in fluidic devices.

With the introduction of our fluidic gate strategy, a number of advantages have been established. Unlike these other fabrication methods, our approach does not require additional materials, solvents and user interactions in order to enable the switching, and the fabrication procedure is easily implemented. The fluidic gating, in our case, is based on

the use of only a highly bio-compatible material with no additional solvents. Since the switching of the gate is realised by a non-contact mechanism, such as local heating of the gate barrier material, this avoids any contamination of the device. Most importantly, our gating principle is highly controllable as this can be achieved by simply applying the triggering source locally as desired.

6.4 Experimental results

6.4.1 Triggering via global heating by a hot plate

For a proof-of-principle, as shown in Figure 6.1a, a wax line was printed using a wax printer across the fluid flow path created in a nitrocellulose membrane that had been cut to the shape of a single rectangular strip. Then the NC was left on a hot plate at 100 °C for 30 seconds to allow the wax to fully penetrate throughout the membrane. In the next step, the device was removed from the hot plate and left at room temperature for at least 10 minutes for the wax to fully re-solidify. After it solidified, this wax line was ready for use as a barrier or gate that blocked the fluid flow in the NC.

To test this wax barrier, a cellulose pad, which performs the function of a fluid source pad, was positioned at one end on top of the NC as shown in Figure 6.1a. On introduction of 50 µL of red ink into the source pad, as shown in Figure 6.1b, the ink flowed from the source pad into the NC and was then stopped by the solid wax barrier, which impeded its flow path. To enable the flow, the device was then moved into a covered petri dish (for minimising the evaporate) onto a hot plate at a temperature of 100 °C in order to melt the wax barrier, and this allowed the ink to leak through the barrier and continued to flow further along the strip. As shown in Figure 6.1c and 6.1d, once the wax barrier was melted, the wax gate was opened and let the ink flow through continuously.

In these first proof-of-principle experiments, because of the high melting point of the wax we have used, a high temperature of ~100 °C was needed to trigger the gate. However, gates with much lower trigger temperatures can be easily manufactured by choosing other commercially available low melting point waxes. For example, a variety of paraffin waxes are available with melting temperatures ranging from ~50 °C to ~80 °C, where most of the biological assays can normally perform without temperature-dependent degradation.

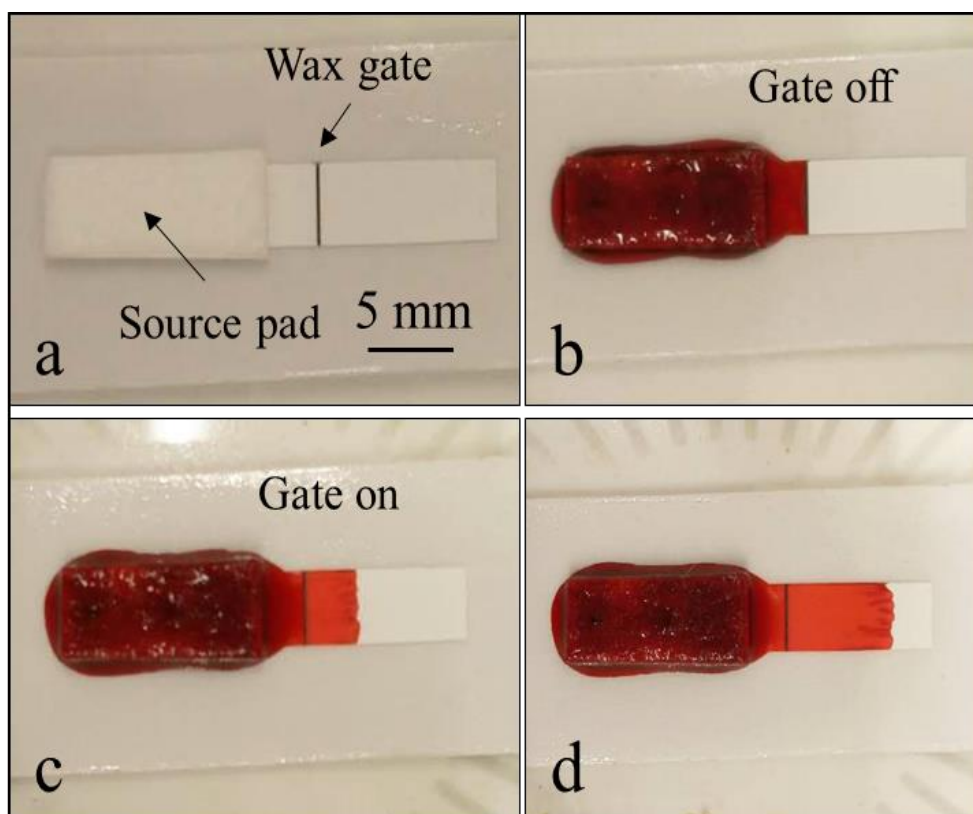


Figure 6.1 Sequential photographic images showing the flow of red ink on a NC strip with a triggerable wax gate in the middle of the flow path. The gate was triggered globally via a hot plate.

6.4.2 Triggering via localised heating by a wax pen

Although no major problem has been raised due to above non-localised global heating, two localised heating mechanisms have also been proposed. The first localised heating was realised using a wax pen (known as lightweight wax-carving tools that offer instant heat widely used for wax and candle making or jewellery design and repair). It has a compact pointed heating element (few millimetres in size) driven by a battery that operates with fingertip control. The maximum temperature that the heating tip can reach is about 800 °C, which is high enough to melt the wax locally by simply positioning the tip close to the wax barrier in a non-contact manner.

The sequential images in Figure 6.2 show an example of enabling a wax gate via localised heating using a wax pen. As shown in Figure 6.2a, wax barriers, with a thickness of ~ 5 mm, were created across the fluid flow path in a single rectangular cellulose strip. On introduction of 10 μ L of yellow dye into the inlet, as shown in Figure 6.2a, the ink flowed along the flow path then stopped at the solid wax barrier. To enable the flow, the wax pen was carefully positioned close to the heating point without contact, as shown in Figure 6.2b, which melted the wax only in that desired area and allowed the dye to leak through.

To test the barrier after removing the heating source, as shown in Figure 6.2c and 6.2d, another green dye was introduced into the same inlet and it flowed through the wax barrier via the same tunnel formed at the heating point. Overall, the wax gate here can be locally triggered via a locally applied heating and once the wax gate is opened the fluid will carry on flowing through and the heating source is no longer needed.

For the next step, in order to further understand the working mechanism behind these triggerable wax gates, these wax gates were then studied under light microscopy. First of all, a device with the same arrangement as shown in Figure 6.2 was prepared and then PBS solution instead of coloured dyes was introduced into the device. The reason for using PBS instead of coloured dyes is because it is colourless and will not be observed after evaporation. Then the gate was enabled by locally melting the wax using a wax pen. A large volume of PBS was supplied to ensure that enough fluid flowed through the gate. Finally, the device was left to dry at room temperature before being analysed via light microscopy.

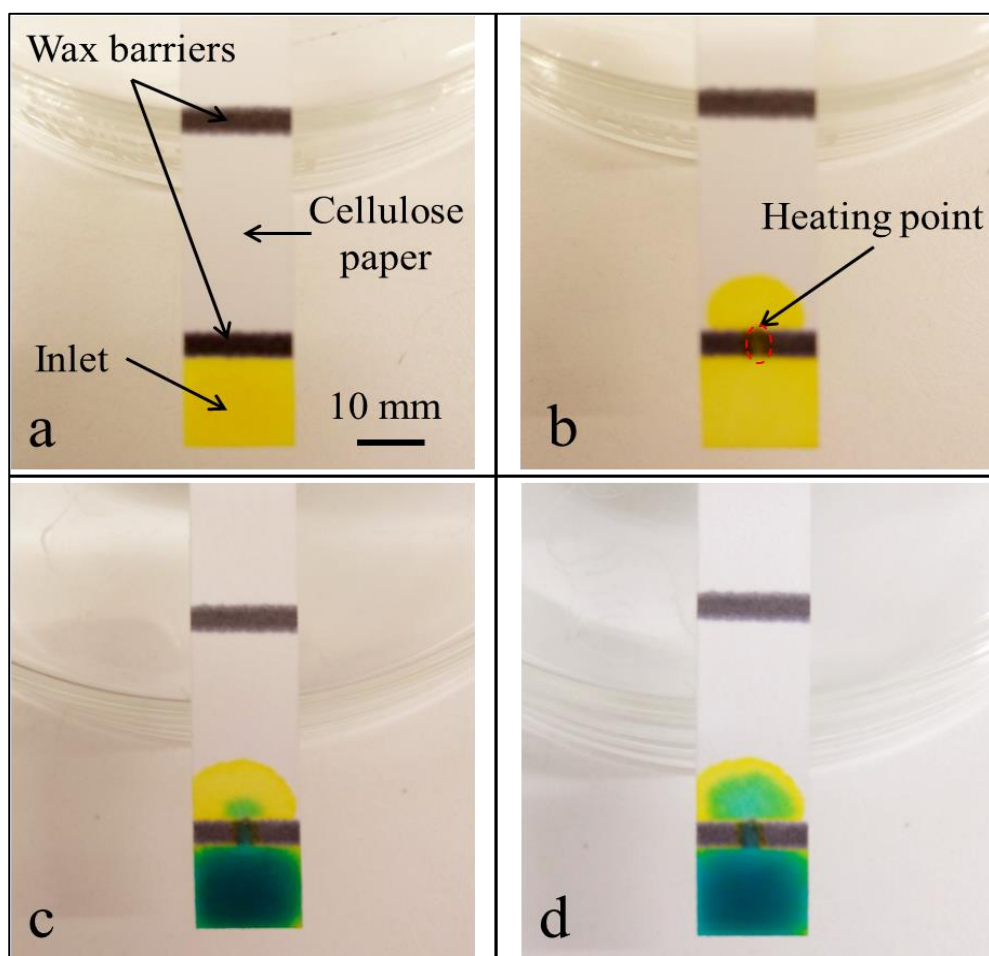


Figure 6.2 Sequential photographic images showing the flow of yellow dye followed with green dye on a cellulose paper strip with a triggerable wax gate in the middle of the flow path. The gate was triggered locally via a wax pen.

The images in Figure 6.3a and 6.3b show an unheated area of the wax gate, which remains as a solid barrier, with 10 x and 20 x magnifications respectively. In both images, it can be clearly observed that both the cellulose fibrous strands and the voids were fully coated and filled with the wax, which appears as a black band. However, the images in Figure 6.3c and 6.3d show the area of the wax gate, where the heating was applied and then the fluid flowed through, again with two different magnifications of 10 x and 20 x. Compared with the area shown in Figure 6.3a and 6.3b, this area was much more 'clean' with only a few small black areas visible, which means only a residual amount of wax remained in this area, thus the fluid was able to flow in this area via capillary action.

We assume that this is due to the wax in this area being melted and subsequent removal away by the flow (some being pushed to the side and some carried with the flow). Therefore, the heating source is only needed for a very short period of time at the beginning in order to trigger the gate and once the gate is on, the heating source is no longer needed.

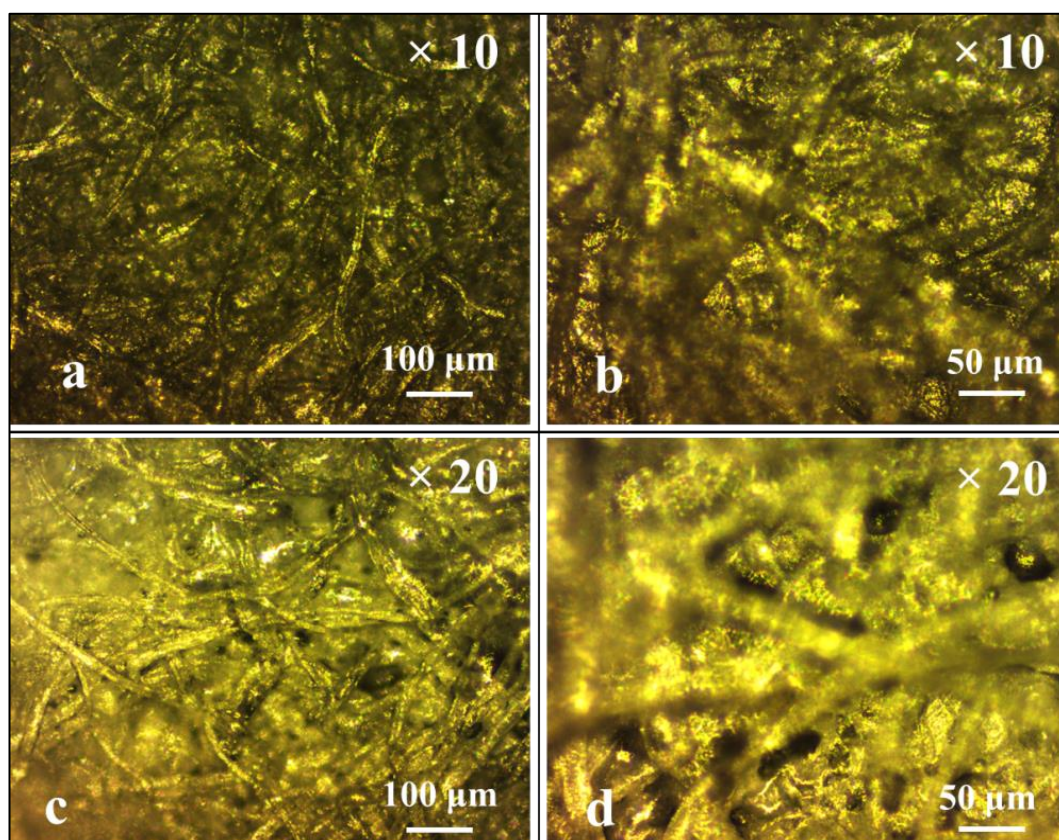


Figure 6.3 Microscopy images of a wax gate at different positions with different magnifications: a) and c) 10 x; d) and d) 20 x. a) and b) show the unheated area, which remains as a solid barrier, and c) and d) show the heated area, where the fluid (PBS) flowed through.

6.4.3 Triggering via localised heating by a c.w. laser

A final option is to use another localised heating mechanism, which is based on locally applying a c.w. laser beam. The energy of the laser beam is absorbed and melts the wax only in the exposed area, and hence enables the flow.

For this experiment, as described above, we first used the same wax printing procedure to create a device with a grid-like structure in a NC substrate (Figure 6.4). To start the experiment, 5 μ L of red ink was first pipetted into the central well, as shown in Figure 6.4a the ink remains fully contained inside the square well defined by the wax barrier walls. Then a 405 nm c.w. laser beam with an output power of 5mW was focussed onto one of these wax walls as shown in Figure 6.4b. The local melting of the wax at the exposure point resulted in an immediate leakage of the previously contained ink from the central well into the adjoining left well. The subsequent image in Figure 6.4c shows the flow of the ink from the central inlet well into the adjacent well through the opening formed by local melting of the wax barrier.

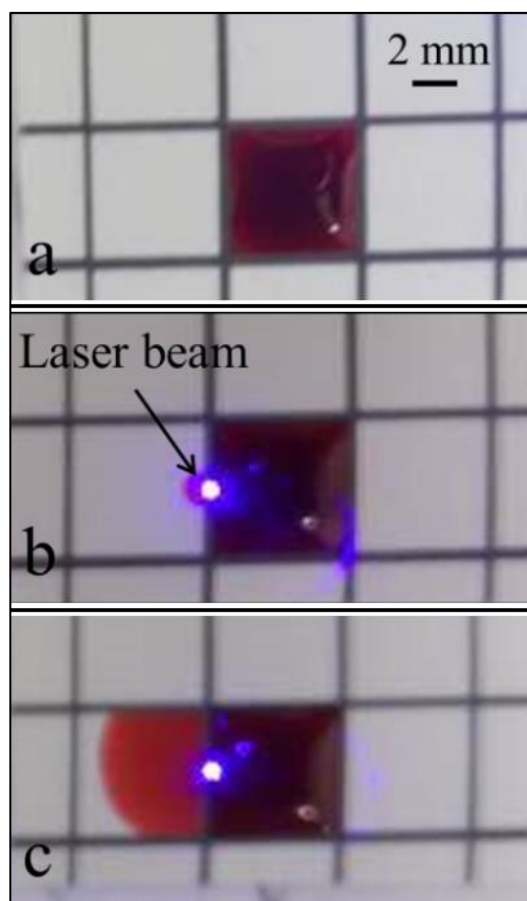


Figure 6.4 Sequential photographic images show triggering of the wax gate using a locally applied laser light source.

6.4.4 Validation of fluidic gates for implementation of assays

Finally, to validate the effectiveness of these wax barriers as fluidic gates, we have successfully implemented a few assays on such paper-based devices with the use of these wax-patterned gates. Figure 6.5 shows the detection of nitrite, which is regarded as a considerable health concern due to the contamination of water sources from fertilisers, animal waste and sewage. The detection assay was a Griess reaction, which is the most commonly used colorimetric reaction for the detection of nitrite, and details of this assay are described in Appendix C2. To perform the detection, a NC device with pre-patterned structures was prepared and Griess reagent (2 μ l) was selectively pipetted into four square-wells labelled A, B, C and D on the grid-like structure (as shown in Figure 6.5a). The device was then left to dry at room temperature for at least 1 h before use. The grid pattern that formed the square-well structures was patterned via a wax printing approach described earlier. Water-based samples of sodium nitrite were prepared on the day of testing at dilutions of 10 mM. As shown in Figure 6.5b, the sample (10 μ l) was pipetted into the central sample inlet square-well and remained confined inside the square by the wax walls. To start the assay, the device was positioned onto a hot plate with a temperature of 100 $^{\circ}$ C, and as the wax barriers become permeable due to the melting of the wax, the sample is released into the detection zones A, B, C and D, which produced pinkish-red colour changes that reveal the presence of the nitrite in the measured sample. The sequential images in Figure 6.5c – 6.5f show the flow of the samples from the inlet well into the detection wells and the process of the detection after triggering the wax gates via a hot plate.

In addition to the above simple one-step detection, a more complex LFD that implements a sandwich ELISA for detection of CRP has also been successfully demonstrated using a similarly designed wax gate. The arrangement of the four constituent substrates that form the lateral-flow strip is shown in Figure 6.6a and consists of a sample pad and a wicking pad that are made of cellulose paper, a conjugate pad that is made of glass fibre filter and has been pre-soaked with horseradish peroxidase (HRP) conjugate detection antibody and a reaction pad that is made of NC. The principle of this assay is as follows: the sample introduced into the source pad which is at one end of the strip device, flows laterally towards the wicking pad which is positioned at the other end of the strip. As the sample migrates through the conjugate pad the target analyte in the sample will bind to the enzyme-conjugated antibody (in the conjugate pad) and then this reaction matrix migrates into the next section of the strip, the NC membrane, where the analyte will then bind to the capture antibody that is pre-immobilized in the reaction zone and the excess reagent/sample then wicks further and finally gets collected by the wicking pad. A

colorimetric substrate is then added to the reaction pad, which reacts with the enzyme to produce a specific blue colour change that demonstrates the presence of the target analyte in the sample.

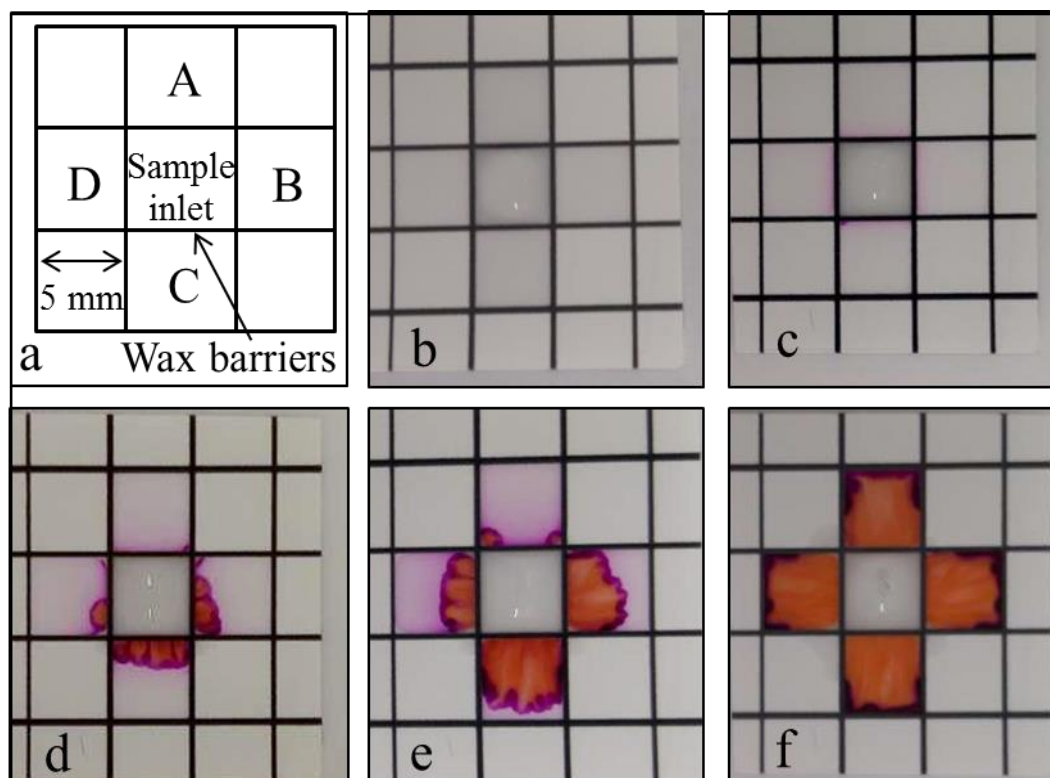


Figure 6.5 a) Schematic image shows the arrangement of the device. b) Image shows the introduction of the sample into the inlet well and its containment inside the well. c) – f) Sequential images showing the process of the detection after triggering the wax gates.

As shown in Figure 6.6a, a wax gate was produced across the flow path in the reaction pad. The capture antibody was also pipetted on the reaction pad after the fabrication of the wax gate and left to immobilise at room temperature for 1 hour. To perform the assay, 50 μL of CRP sample with a concentration of 1 $\mu\text{g}/\text{mL}$ was introduced onto the sample pad. The sample flowed from the sample pad onto the conjugate pad and was captured by the detection antibody. This matrix then continuous to flow forward onto the NC until it encounters the wax gate where the flow is stopped. To enable the flow further past this gate to affect the assay, the wax gate has to be switched on, and this was done by positioning the strip-device onto a hot plate at 100 $^{\circ}\text{C}$. The sample-conjugate matrix which has flowed past the gate then gets captured by the capture antibody pre-localised on the NC. The conjugate capture at the site of the capture antibody is revealed by the subsequent addition of the chromogenic reagent that was added onto the detection zone. As shown in Figure 6.6b, the result is the appearance of a blue spot at a specific location (the site where the capture antibody is localised) on the NC, confirming the presence of CRP in the tested sample.

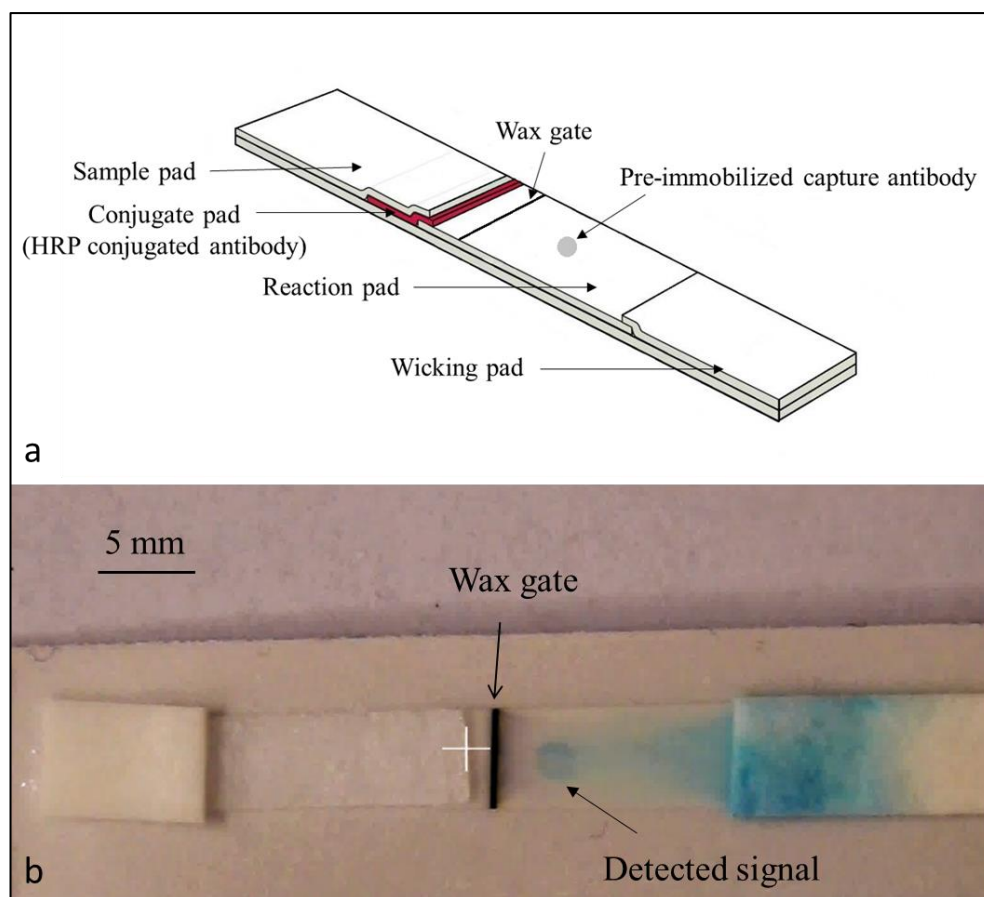


Figure 6.6 a) Schematic image show the arrangement of a designed lateral-flow strip with a wax gate. b) Image shows the result of implementing a sandwich CRP ELISA on the lateral-flow strip described in a).

6.5 Summary

The approach we have demonstrated here for fabrication of fluidic gates or valves in porous material based fluidic devices is based on simple wax barriers printed using a cheap office wax printer. These wax gates can be switched from their impregnable state with the application of a heat source. In more detail, the wax in the heated area is melted and then pushed away by the flow, which hence results in a clean permanent flow path that allows fluid to flow through continuously once the gate is opened.

To trigger the gate, a heating source is only needed for a very short period of time, when the gate is opened the heating source is then no longer needed and the gate will stay in the 'ON' state forever. For these first proof-of-principle experiments, a hot plate, a wax pen and a c.w. laser were applied to show the triggered gate via both non-localised and localised heating.

Finally, in order to prove the effectiveness of the idea of using printed wax barriers as fluidic gates, both a simple single step assay for detection of nitrite and a complicated multistep sandwich ELISA for detection of CRP have been successfully implemented.

In conclusion, the approach reported here allows fabrication of triggerable fluidic gates with an extremely simple and cheap procedure without the need for additional expensive equipment and complicated procedures. In addition, as the wax is known to be bio-compatible and the switching of the gate can be realised by non-contact local heating approaches, i.e. resistive heating or a laser source, no contamination will be introduced to the device during the triggering of the gate. Finally, these wax gates are highly controllable as desired by precise application of the heat source. Overall, we believe that this idea of using the heat triggerable wax-barrier could be ideal for implementation of fluidic gates in paper-based microfluidic devices.

Chapter 7: Implementation of assays on paper-based devices

7.1 Introduction

Paper-based microfluidic devices have been proposed as a low-cost POC platform for rapid diagnostics test since their origins in 2007 [4]. However, dipsticks, as early paper-based assay formats, were first proposed in the 1950s to quantify glucose detection in urine [145]. Following this, they were further developed by comparing the results to a colour-coded chart, which then improve of them to the level of a semi-quantitative tool that allows determination of the glucose concentration. Currently, a large number of commercial urinalysis dipsticks already exist in the market for detection of a wide range of analytes such as hCG (human chorionic gonadotropin), ketone, protein, nitrite etc. [6]. Parallel to the dipstick tests, the invention of the lateral flow test as an established assay format for POC diagnostics dates back to the 1950s with the first emergence of latex agglutination assays and radio-immunoassays [146, 147]. After about two decades, nitrocellulose membranes have been developed as a substrate for lateral flow molecular detection in the 1970s [148], which then prompted the birth of the early serological lateral flow test for detection of hCG- β via radioimmunoassay [149, 150], which is a major biomarker for a human pregnancy test. Since then, rapid lateral flow tests have been popularly researched and developed for not only clinical diagnostics [49, 93, 151], but also other fields such as food safety [76, 152, 153], drug abuse [71], and environmental monitoring [68, 79, 154-157].

To date, a wide range of detection mechanisms have been proposed for paper-based microfluidic devices. The sensing mechanisms include colorimetric detection [4, 53], electrochemical sensing [68, 158], nanoparticle-based detection [159, 160], electrochemiluminescence [155, 161], chemiluminescence [162, 163], fluorescence [164, 165], and hybrid sensing [166]. Among these diagnostic techniques, colorimetric detection is regarded as the simplest and most commonly used mechanism for commercial paper-based devices although they are struggling to achieve high detection sensitivity and quantitative analysis. For a typical colorimetric detection, either an enzymatic or a chemical reaction will happen, when the target analyte in the sample meets the reaction reagent, which then produces a visible colour change. The reaction reagent can be enzymes, dyes or acid-based indicators. Early examples of paper-based microfluidic devices based on colorimetric detection were performed as a detection of pH, glucose and

protein in artificial urine [4, 53]. With further development of the technique, it was found that semi-quantitative readouts can be achieved by comparing with a premade calibration chart. However, paper-based microfluidic devices based on colorimetric detection still have a few disadvantages. As the result is based on the identification of the colour distribution, it is a challenge to the naked eye, and thus specialised readers may sometimes be needed [53]. Additionally, the signal can be easily compromised by the background noise from the paper, which is a highly scattering and non-uniform material.

In order to perform the validation of our paper-based microfluidic devices, which are fabricated using the LDW technique, we have tried to implement a number of colorimetric assays with different assay protocols including glucose oxidase (for detection of glucose), tetrabromophenol blue binding (for detection of bovine serum albumin (BSA)), Griess reaction (for detection of nitrite) and ELISA (for detection of various biomarkers). The detail of the implementation of those assays onto our pre-patterned paper-based devices and the achieving results will be described in this chapter.

7.2 Enzyme-linked immunosorbent assay (ELISA)

ELISA is one of the most commonly used assays for biochemical detection, which provides a high sensitivity through enzymatic signal amplification [167, 168]. It is a form of biochemical assay that uses antibodies and colour change to detect the presence of antigens such as antibodies and viruses [168, 169].

It is a useful technique for determining either the presence or the concentration of antibodies, which has resulted in wide application in clinical diagnosis for detection of various diseases, such as HIV, tuberculosis, malaria, cancer etc. [170-174]. They can provide relatively fast, highly specific, highly sensitive, and very robust detection through enzymatic signal amplification [167]. In addition, it is also popularly used in the food industry for monitoring of food allergens [175-178], and toxicology for screening certain classes of drugs [179-181].

Basically, it is one of the most commonly used immunoassays that typically employs Immunoglobulin G (IgG) antibodies that are directed against a wide range of proteins for different diseases, conditions and allergens. These antibodies can be either monoclonal (only bind to a very specific binding site of antigens) or polyclonal (binding to multiple sites of antigens). The binding of the antigen and antibody is then detected using an enzyme-linked to a secondary antibody (another IgG antibody), which turns the antigen-antibody complex into a coloured product when a chromogenic enzyme substrate is added. Enzymes are one of the most popular labels for immunoassays and they include HRP,

alkaline phosphatase (ALP) or glucose oxidase. In some cases, these enzymes are exposed to reagents that cause them to produce light or chemiluminescence instead of a colouration of the solution.

For a standard ELISA, antigens are first attached to a surface, and then a specific antibody, which is linked to an enzyme, is applied that will bind to the antigen. Washing steps are applied between each step using detergent solution in order to remove any antibody and protein with non-specific binding. Finally, a colorimetric substrate is added, which will react with the enzyme to produce a visible colour change.

Four types of ELISA are commonly used namely direct ELISA, indirect ELISA, sandwich ELISA and competitive ELISA. Direct ELISAs involve binding of the antigen to the substrate followed by an enzyme-labelled antibody as shown in Figure 7.1a. For indirect ELISAs, as shown in Figure 7.1b, the antigen again is first attached to the substrate followed by a primary antibody, which is unlabelled this time. After that, an enzyme-conjugated secondary antibody is added, which will specifically bind to the unlabelled primary antibody.

As a more complicated version, sandwich ELISAs involve the specific binding of an antigen from the sample to the capture antibody, which is pre-attached to the substrate. Then an enzyme-labelled detection antibody, which is specific to the antigen, is added that will bind to the antigen hence form a 'sandwich' arrangement. A representative image of the sandwich ELISA is shown in Figure 7.1c. Finally, the last type of ELISA: competitive ELISA (Figure 7.1d), which involves the simultaneous addition of 'competing' antibodies or proteins and the antigen to the pre-immobilized antigen standard. Then only unoccupied antibodies will bind the antigen standard on the substrate. As a result, a larger quantity of analyte in a sample results in fewer free antibodies in the solution that means a smaller number of labelled antibodies can be bound to the antigen standard on the substrate thus resulting in a less intense signal.

Paper-based ELISA, which was first developed by the Whitesides' group using a piece of cellulose paper [182], has been rapidly developed in recent years as it allows minimal reagent volumes and simple equipment and materials, and allows cheap, quick and reliable diagnosis [182-184]. It has been proven to be much cheaper, faster and easier to operate than a conventional ELISA that is performed on a microtiter plate, while conveying a similar level of specificity and sensitivity.[184]

In this report, we replaced the microtiter plate with our patterned paper-based microfluidic devices which are based on cellulose filter paper and nitrocellulose

membranes to implement both single step direct ELISAs and more complicated multistep sandwich ELISAs for detection of a range of biomarkers including TNF- α , CRP etc.

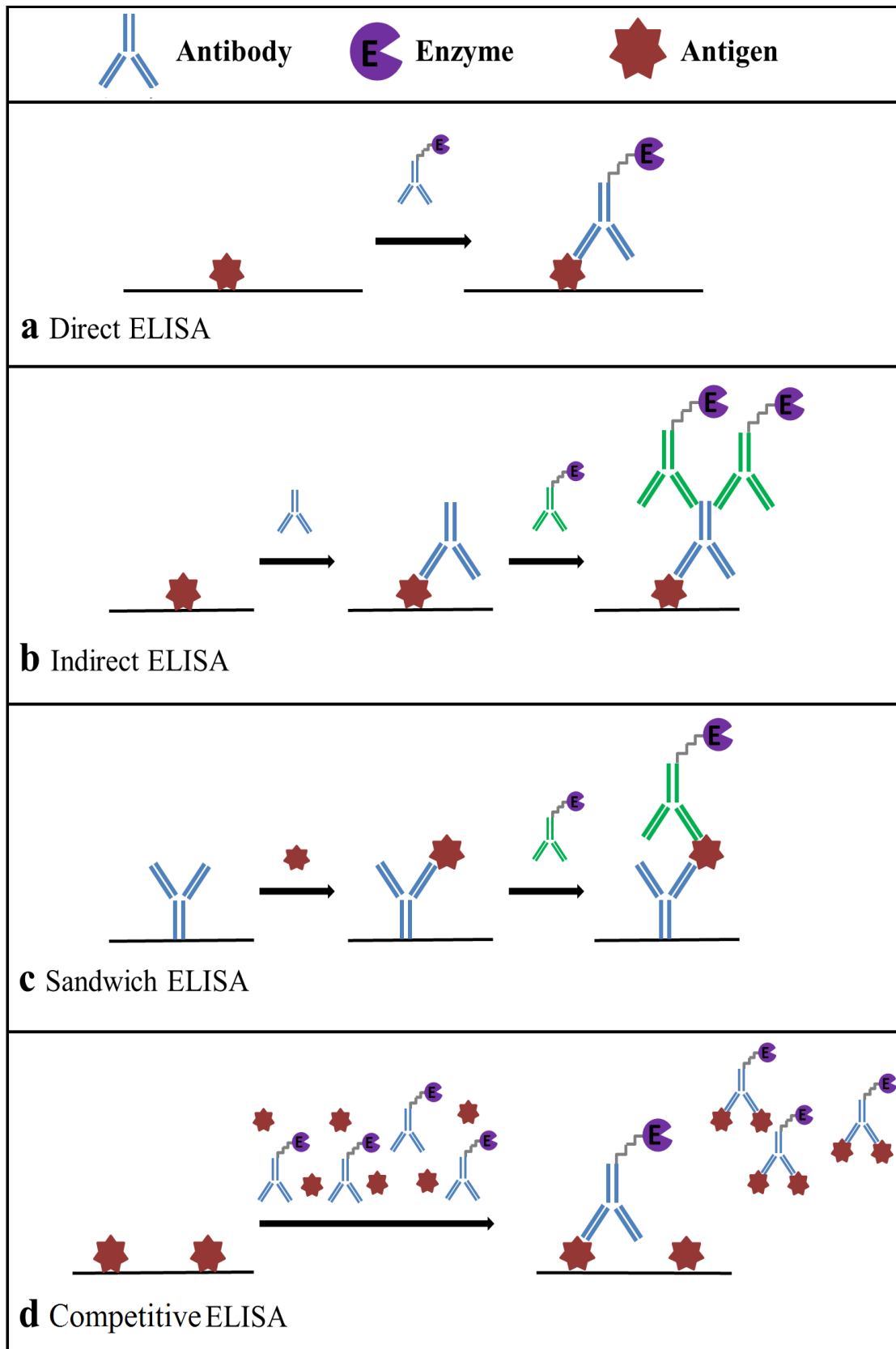


Figure 7.1 Representative images of the different formats of ELISA. a) Direct ELISA, b) indirect ELISA, c) sandwich ELISA and d) competitive ELISA.

7.2.1 Limit of detection

In analytical chemistry, one of the most important parameters during the assay validation is the limit of detection (LOD), which is defined as the lowest quantity of a substance that can be distinguished from the absence of that substance (a blank value) within a stated confidence limit (generally 1%) [185]. Several approaches for determining the detection limit are possible, including visual evaluation, a signal-to-noise approach and standard deviation estimation [186].

For visual evaluation, the detection limit is determined by the analysis of samples with known concentrations of analyte and by establishing the minimum level at which the analyte can be reliably detected.

On the other hand, for the signal-to-noise approach, the detection limit is determined by comparing measured signals from samples with known low concentrations of analyte with those of blank samples and by establishing the minimum concentration at which the analyte can be reliably detected. In this case, the detection limit is estimated from the mean of the blank, the standard deviation of the blank and some confidence factor.

The limit of blank (LOB) is another important parameter which determines the LOD of an assay. LOB describes the highest measurement result that is likely to be observed (with a stated probability) for a blank or negative sample. The assumption in the determination of the LOB is that values exceeding the 95th percentile of the distribution of values on truly blank or negative samples deviate significantly from blank or negative measurements. When a sample produces an observed value that exceeds this limit, it may be declared to contain an amount of analyte that exceeds zero [187]. Given a Gaussian distribution of blank or negative values, this limit corresponds to:

$$\text{LOB} = \mu_B + 1.645SD_B \quad [14]$$

where μ_B and SD_B are the mean and standard deviation of the blank or negative measurements, respectively.

LOD is the lowest analyte concentration likely to be reliably distinguished from the LOB and at which detection is feasible. Experimentally, in order to calculate the LOD, a minimum of 10 individual samples with concentrations ranging from the LOB to approximately 4xLOB shall be tested at least 10 times by at least two technicians in a minimum of two days or runs. A pooled estimated standard deviation of the sample distribution at a low level (SD_s) can be derived from repeated measurements with the set

of samples (a minimum of 10 measurements of at least 10 samples). Finally, an estimated LOD is then obtained as:

$$\text{LOD} = \text{LOB} + 1.645SD_S \quad [15]$$

Finally, LOC can also be determined based on the standard deviation of the response and the slope. The detection limit (DL) may be expressed as:

$$\text{LOD} = 3.3 \frac{\sigma}{S} \quad [16]$$

where σ is the standard deviation of the response and S is the slope of a linear calibration curve. The above definition is only restricted within the cases of linear calibration ($S=\text{constant}$), however, for most of the competitive immunoassays, the calibration curves are curvilinear ($S=\text{variable}$) and the LOD cannot be estimated simply from this equation.

In this report, we have simply estimated the LOD of our implemented assays based on the visual evaluation. The LOD of the CRP based on ELISA by using our laser-patterned devices is about 1ng/mL, which is comparable to the LOD that can be achieved using commercially available ELISA kits.

7.3 Experimental results

7.3.1 Implementation of one step colorimetric assays

In order to show the feasibility of this procedure in producing fluidic-based diagnostic devices, we first started with the implementation of simpler single step colorimetric detection on our patterned paper substrates. We first patterned the paper substrate with a crosshatch grid pattern that resembled a conventional microtiter plate. These fluidic structures were patterned into both cellulose filter paper (Whatman Grade 1) and nitrocellulose membranes (Whatman BA85) using the 405 nm laser with the photopolymer SubG and DeSolute® 3471-3-14 respectively. The fluidic structures in cellulose paper were created with a laser power of 70 mW and a writing speed of 10 mm/s, while the patterns in nitrocellulose membranes were achieved with a laser output power of 1 mW at a writing speed of 10 mm/s.

First of all, we tested the use of the grid-like fluidic pattern of square wells in nitrocellulose membranes by implementing the detection of nitrite in water. The detection of nitrite is based on the Griess reaction, which is a chemical reaction that detects the presence of organic nitrite compounds [188]. During the Griess reaction, nitrite ions react with a primary aromatic amine under acidic conditions forming a diazonium salt which

further reacts with an aromatic compound to form a coloured azo dye. It is the most commonly used colorimetric reaction for the detection of nitrite. To perform the assay, the prepared Griess reagent (2 μ l) was first pipetted into each square-well of the grid-like structure (as shown in Figure 7.2a) in the nitrocellulose paper, which was then left to dry at room temperature for at least 1 h before use. Samples of sodium nitrite were prepared on the day of testing at dilutions of 10 mM, 2.5 mM, 1.25 mM, 625 μ M, 500 μ M, 312 μ M, 250 μ M and 156 μ M as labelled in Figure 7.2a. The samples (2 μ l) were pipetted on individual squares, and the colour change produced was imaged by taking a photograph of the paper-device after 1 min with a USB camera as seen in Figure 7.2a. This image was then processed with the ImageJ software to extract the respective colour intensities of the purple colour produced within the square well detection zones. The average grayscale intensities of each detection zone and of the background of the image were measured, and the background intensity was subtracted from the intensity of each detection zone to obtain the actual colour intensity of each spot to eliminate the influence of the background. By measuring the colour intensities of the known concentrations, we were then able to plot the curve (as seen in Figure 7.2b), which then can be used for calibration. Hence, by comparing the colour change observed for an unknown concentration with a known calibration curve would then allow determination of the concentration for that unknown sample. Ideally, using such test patterns with nine wells, it should be possible to quantify nine unknown samples illustrating the utility and simplicity of using such low-cost paper-patterns to perform multiplexed quantitative analysis.

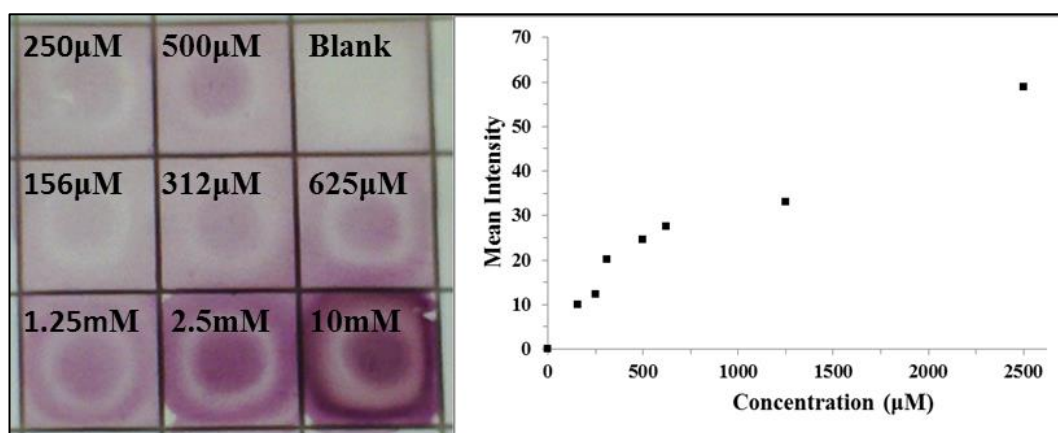


Figure 7.2 (a) 5×5 mm wells patterned with a laser power of 1 mW and a scan speed of 10 mm/s and prepared for the detection of nitrite by the Griess reagent, after the introduction of the sodium nitrite samples. (b) Calibration curve constructed using the grayscale intensity values taken from the image shown in (a).

Following the successful operation of nitrite detection on our patterned devices, we then tried to implement the detection of BSA and glucose on our fabricated paper-based

devices. Again we used the same grid-like fluidic pattern of square wells, which, however, were patterned in cellulose paper this time.

The detection of BSA is based on the colour change of tetrabromophenol blue (TBPB) when it ionises and binds to proteins resulting in a colour change from yellow to blue [189]. To perform the BSA test, we pipetted 3 μ l of a 250 mM citrate buffer solution at pH 1.8 in each square well (5 mm \times 5 mm) of the test-pattern. The test paper was then allowed to dry for 1 hour before 3 μ l of a 3.3 mM solution of the second reagent, TBPB in 95% ethanol, was added into each well. After further drying at room temperature for 1 hour, the test-pattern was ready for use in the detection of BSA via the addition of sample solutions into the respective square wells of the test-pattern. We pipetted sample solutions made up in de-ionised (DI) water, with BSA concentrations ranging from 0.25 to 50 mg/ml into each well as labelled in Figure 7.3a. The introduction of the sample solutions resulted in a colour change in each well showing different concentration-dependent shades of blue colour (as seen in Figure 7.3a), which were fully developed after 10 minutes.

The glucose assay is based on the enzymatic oxidation/pre-oxidation of iodide to iodine associated with the presence of glucose, which results in a colour change from clear to brown [190]. To perform the detection of glucose, we again used the same square-well patterned device (cellulose filter paper). First, 3 μ l of glucose oxidase/ peroxidase reagent were pipetted into each well. As with the BSA test, the reagents were left to dry at room temperature for 1 hour before further use. The test was then executed by the addition of sample solutions with different concentrations of glucose into each well of the test-pattern and the concentration of glucose in each sample is labelled in Figure 7.3b. The concentration of glucose in the artificial solutions made up in DI water ranged from 15.6 to 1000 μ g/ml. The introduction of the sample solutions into the wells resulted in a change of colour from white to different shades of brown (Figure 7.3b). The colours were fully developed after 10 minutes.

Normally, quantification of the results is very important for medical diagnostic tests, as in most cases, a 'yes/no' answer would not be sufficient. Therefore a way of obtaining the concentration of the analyte from the captured photos was necessary, and we have used the same method reported above for the quantification of the nitrite detection. The images were processed with the ImageJ software to extract the respective colour intensities of the blue and brown colour produced within the detection zones for the BSA and glucose respectively. By measuring the colour intensities of the known concentrations, we were then able to plot the calibration curves as seen in Figure 7.4 and Figure 7.5. Using the same procedure as above, we can determine the concentration values of BSA and glucose of

unknown samples by measuring their colour intensities and comparing them to the calibration curves.

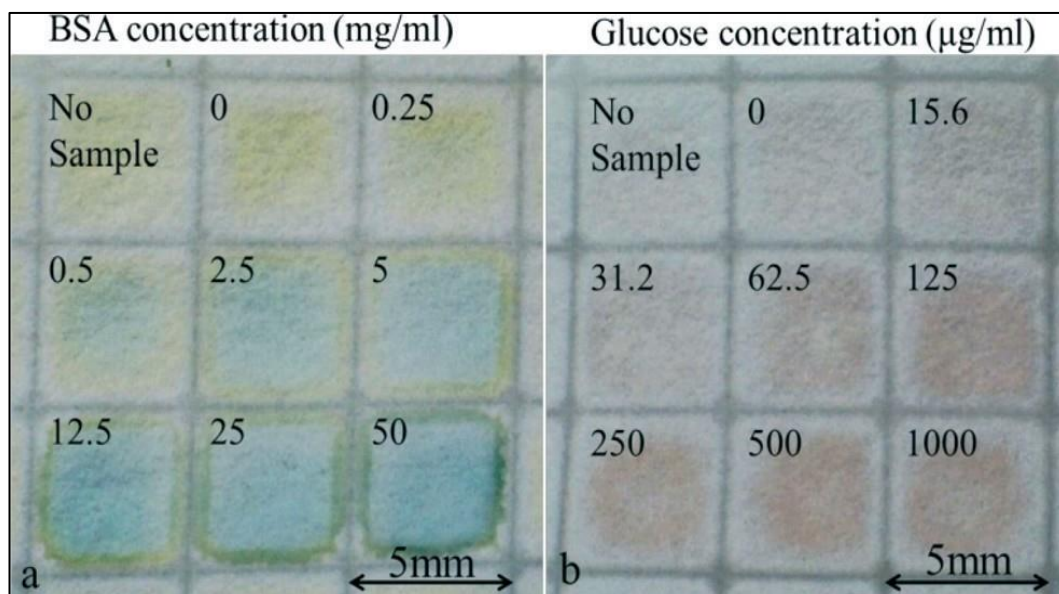


Figure 7.3 Patterned cellulose paper after completion of a) the BSA detection assay showing different shades of the blue-green colour, corresponding to the different concentrations of BSA pipetted in each well and b) the glucose assay showing different shades of the pink-brown colour, corresponding to the different concentrations of glucose in each well.

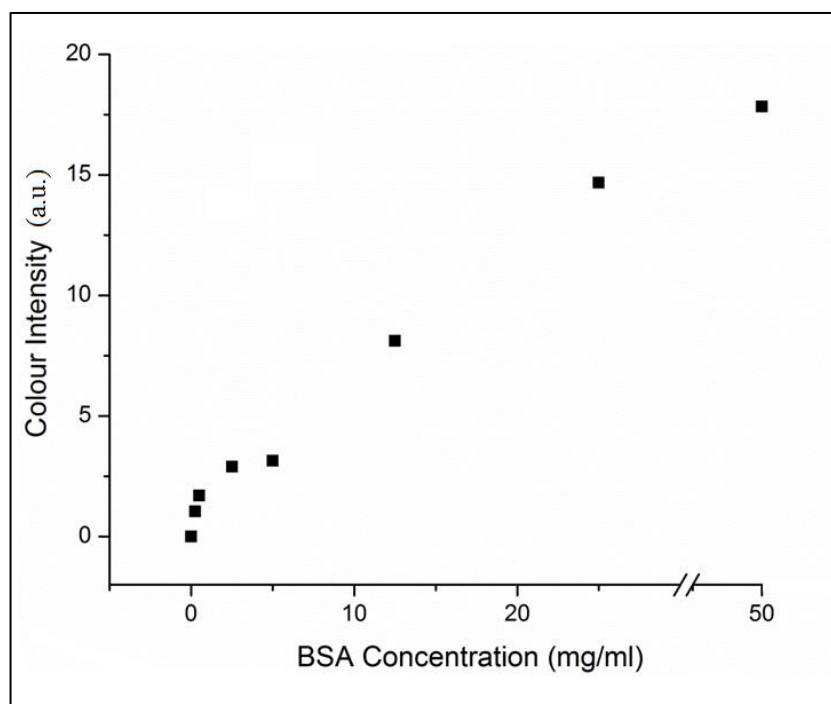


Figure 7.4 Calibration curve for the detection of BSA constructed using the grayscale intensity values taken from the image shown in Figure 7.3a.

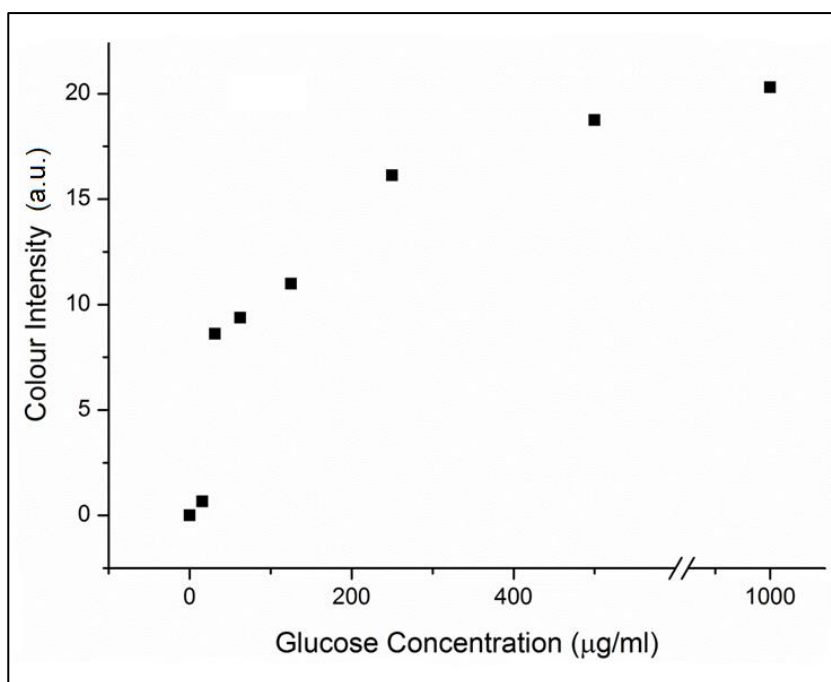


Figure 7.5 Calibration curve for the detection of glucose constructed using the grayscale intensity values taken from the image shown in Figure 7.3b.

The next part of our experimental validation involved the use of a fluidic device shaped as a T-junction, for the simultaneous multiplex detection of BSA and glucose in the same sample solution, as shown in Figure 7.6. These T shape fluidic structures were patterned into the cellulose paper substrates using the 405 nm laser and the photopolymer SubG, at a power of 70 mW and a writing speed of 10 mm/s.

As shown in Figure 7.6a, the lower end of the vertical arm of the T served as the sample inlet point, and the two ends of the horizontal arm of the T served as the test zones. The reagents required for the assays were first pipetted at these two test zones and were allowed to dry. A sample solution (15 µl) containing both BSA and glucose (in concentrations of 50 mg/ml and 1000 µg/ml respectively in de-ionised water), when pipetted at the inlet of the device, flowed towards the test areas, and produced a colour change (blue) for BSA and (brown) for glucose with the level of colour change depending on the concentrations of the biomolecules in the sample solution at the respective specified test zones. The dark area, circled in red, (Figure 7.6a) in the initial section of the vertical arm of the T is the trace produced by the introduction of the fluidic sample solution, and the pale yellow colour of the right end of the horizontal arm of the T is from the dried reagents pipetted into the test zones. Figure 7.6b is an image of the T after completion of the detection assay. For an unknown sample, the concentration of the BSA and glucose in the sample solution can be evaluated by capturing a picture of the T-sensor with a camera, then measuring the intensities of the RGB colours at the test zones and comparing these to a pre-defined calibration curve.

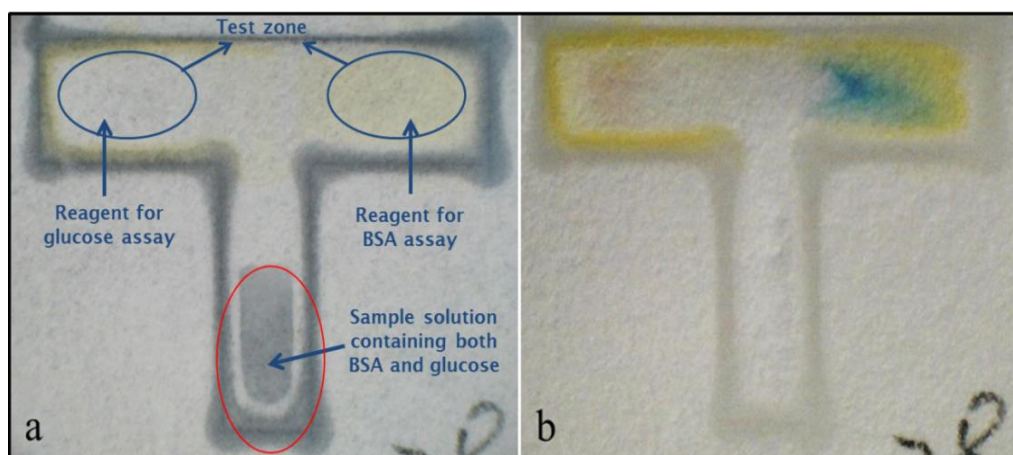


Figure 7.6 Camera images of the patterned device, designed for the simultaneous detection of glucose and BSA, a) at the time of introduction of the sample solution and b) after detection was completed and measurements were taken.

7.3.2 Implementation of multi-step sandwich ELISA

The following sets of experiments describe the implementation of multi-step ELISA on cellulose paper, nitrocellulose membranes and also pre-patterned paper-based microfluidic devices fabricated using our LDW technique discussed above.

First of all, we started from the simplest type of ELISA (one step ELISA) based on two specific antibodies without any antigen involved and the schematic diagram in Figure 7.7 describes the assay step-by-step. An untagged primary antibody is first pipetted onto the paper substrate and left for immobilization overnight, and then the whole substrate is blocked by blocking solution for a minimum of an hour to prevent non-specific binding during the subsequent step. Afterwards, a HRP-tagged secondary antibody that is specific to the primary antibody is added and left for incubation for an hour. Then the substrate is washed with a washing solution to remove any unbound secondary antibody. Finally, the colorimetric substrate tetramethylbenzidine (TMB) is introduced, which will react with the enzyme to produce a visible colour change that illustrates the presence of the primary antibody.

The untagged primary antibody used in the present experiments was purified mouse IgG2a (BD Biosciences, UK) and the enzyme-conjugated antibodies were goat anti-mouse IgG (H + L) (Life Technologies, UK) tagged with the enzyme HRP. Both antibodies were diluted to working concentrations using 1% BSA in PBS as a reagent dilution. The chromogenic substrate used was 3,30,5,50-TMB (Sigma-Aldrich, T0440), which will be catalysed to oxidise by enzyme HRP that yields a characteristic blue colour change that is visible to naked eye. The blocking solution was 5% BSA (Sigma-Aldrich) in PBS (PAA

Laboratories, UK) and the washing solution was PBS. The image was captured using a USB camera 5 minutes after adding TMB. The result for implementation of this one step ELISA is shown in Figure 7.8. Specific blue spots were observed on both cellulose paper (Figure 7.8a) and nitrocellulose membranes (Figure 7.8b), which illustrated the presence of untagged target antibody.

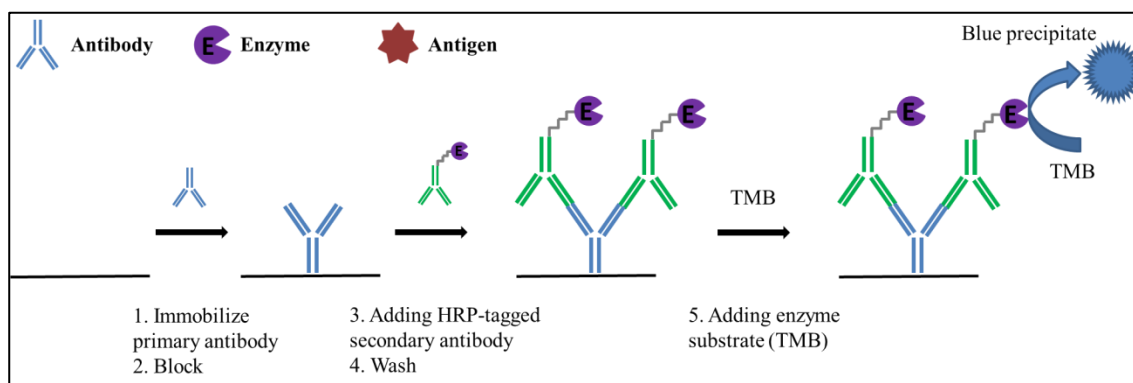


Figure 7.7 Schematic diagram showing the logic sequence for performing direct one-step ELISA on a paper-based device.

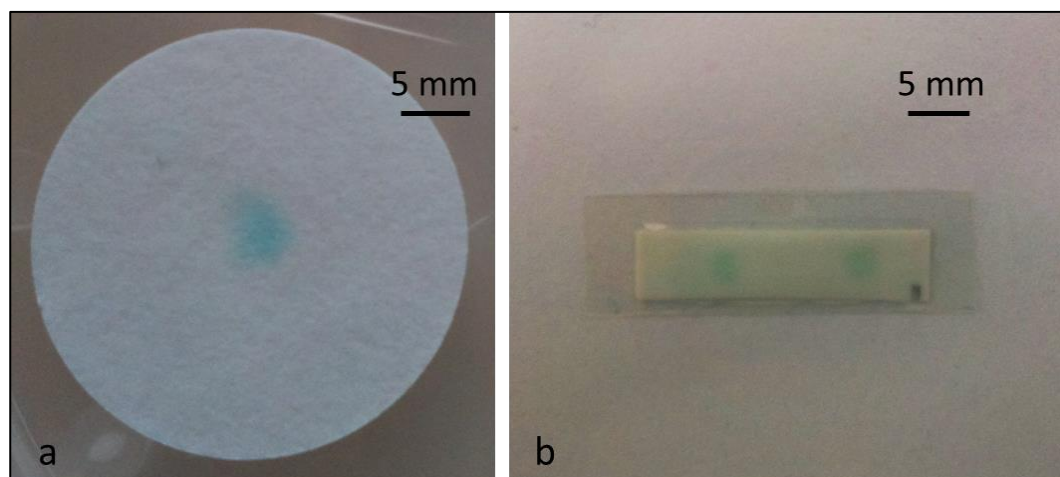


Figure 7.8 Image showing the result of the implementation of one-step ELISA on a) cellulose filter paper and b) nitrocellulose membrane.

After successful implementation of the above simple single step ELISA, we then tried a more complicated and most commonly used method for diagnostics in the market – sandwich ELISA. As shown in the schematic diagram in Figure 7.9, unlike the one-step ELISA described previously, a target antigen is introduced in this approach. The main purpose of this assay is to detect the presence of the target antigen in the sample by detecting the tagged antibody that is specifically bound to the antigen. To perform the assay, as shown in Figure 7.9, an untagged capture antibody is first pipetted onto the paper substrate and left for immobilisation overnight, and then the whole substrate is blocked by blocking solution for a minimum of an hour to prevent non-specific binding

during the subsequent step. After this, a sample with the target antigen is added and left for incubation for 1 hour. During this period, the target antigen will bind to the immobilised capture antibody through specific binding. Then a washing step is applied in order to remove any unbound sample and antigen. After the washing, an HRP-tagged secondary antibody that is specific to the antigen is added and left for incubation again for an hour. During this incubation, the detection antibody will bind specifically to the antigen, which is captured by the capture antibody in the previous step, to form a 'sandwich' arrangement. After an additional washing process, the substrate is washed with a washing solution to remove any unbound secondary antibody. Finally, the colorimetric substrate TMB is introduced, which will react with the enzyme to produce a visible colour change that illustrates the presence of the target antigen.

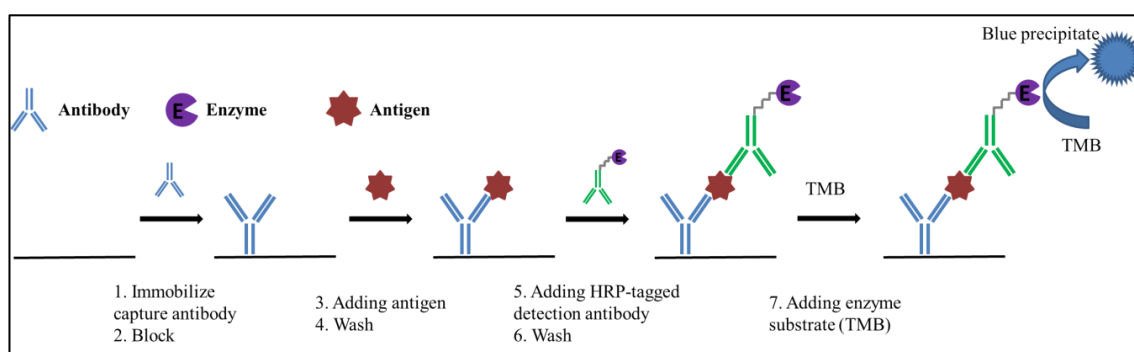


Figure 7.9 Schematic diagram showing the logic sequence for performing a sandwich ELISA on a paper-based device.

We first started with a sandwich ELISA for detection of TNF- α on un-patterned nitrocellulose membranes. The ELISA kit used in the implementation of the TNF- α detection (DuoSet® Human TNF- α) was purchased from R&D Systems, Inc. (UK). All the antibodies and antigens used were from this kit and were diluted to the working concentrations of 4 $\mu\text{g/mL}$, 500 ng/mL and 370 ng/mL for the capture antibody, conjugated detection antibody and TNF- α standard respectively using a 1% BSA in PBS solution. The blocking solution and washing solution used were the same as describe above in operation of the one-step ELISA.

The result for implementation of this sandwich TNF- α ELISA on nitrocellulose paper is shown in Figure 7.10; the specific blue spots illustrate the presence of TNF- α in the tested 'sample'. However, our tested device only worked for the detection of TNF- α at a very high concentration of 370 ng/mL in the tested sample. This is far from the sensitivity that can be achieved with commercial ELISA tests performed on a different platform (microtiter plates), which are normally able to detect TNF- α in the range of pg/mL . As a result, our next goal is to increase the limit of detection in order to meet the standard requirement by

either developing the assay procedures or carefully designing and modifying the patterned devices.

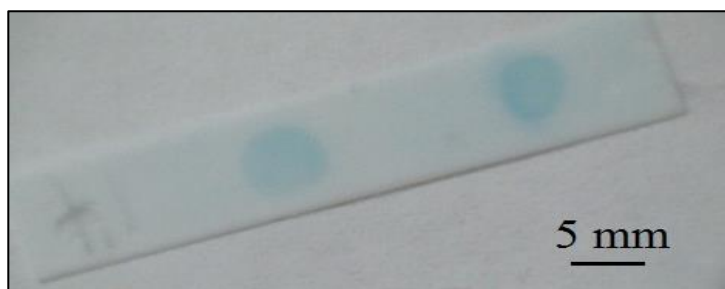


Figure 7.10 Image showing the result of the implementation of sandwich TNF- α ELISA on nitrocellulose membrane with a sample concentration of 370 ng/mL.

As the detection of TNF- α is normally required in the pg/mL range, which is extremely low and thus requires very high sensitivity that increases the difficulty in implementation on a paper platform. As a result, we then changed our target to another biomarker – CRP, which requires a much higher detection level in the ng/mL range that makes it easier to handle. CRP is a ring-shaped protein found in blood plasma and the levels of which respond to inflammation, so it is widely used as a marker for inflammation and also one of the most important biomarkers used in POC diagnostics [188, 191]. The CRP detection we implemented is based on the same protocol as described in Figure 7.9. The ELISA kit used was DuoSet® Human CRP purchased from R&D Systems, Inc. (UK). All the antibodies and antigens used were from this kit and were diluted to the working concentrations of 2 μ g/mL, 22.5 μ g/mL and 90 ng/mL for the capture antibody, conjugated detection antibody and CRP standard respectively. The result is shown in Figure 7.11: two specific blue spots illustrate the presence of CRP in the tested ‘sample’.



Figure 7.11 Image showing the result of the implementation of sandwich CRP ELISA on nitrocellulose membrane with a sample concentration of 90 ng/mL.

After successful implementation of sandwich ELISAs on the paper substrate, we then tried to perform the ELISA on our LDW patterned paper-based platform. As shown in Figure 7.12a, a square-well patterned device was applied for detection of CRP with different concentrations via the same sandwich ELISA as describe above. The grid pattern was

formed using our LDW technique with a laser power of 1 mW and a scan speed of 10 mm/s. The solution of mouse IgG capture antibody (2 μ L at 2 μ g/mL) was first pipetted into each square-well of the grid-like structure (as shown in Figure 7.12a), and then the device was then left to dry at room temperature for at least 1 hour. The whole paper-device was blocked using a blocking solution of 5% BSA in PBS for a minimum of 1 hour. Following this, the device was washed 3 times with PBS. Sample solutions of CRP were prepared at dilutions of 1 ng/ml, 10 ng/ml, 100 ng/ml, 1000 ng/ml, 10 000 ng/ml, and 100 000 ng/ml. The samples (2 μ L) were then pipetted on individual squares and were incubated for 1 h. Then, the device was washed again for 3 times with PBS and a solution of anti-human CRP antibody (2 μ L at 22.5 μ g/ml) was pipetted into each square-well. The whole device was again left for 1 h for incubation and this was followed by washing 3 times with PBS. In the next step, the HRP conjugated streptavidin was added into each well and the device was left in the dark for 20 min of incubation and then washed again using PBS. Finally, the chromogenic reagent TMB was pipetted on the whole device and the colour change produced was imaged by taking a photograph (as seen in Figure 7.12a) of the paper-device after 2 minutes with a USB camera. The image was then processed with the ImageJ software to extract the respective colour intensities of the blue colour produced within the square well detection zones. By measuring the colour intensities of the known concentrations, we were then able to plot the curve (as seen in Figure 7.12b) that again can then be used for calibration.

Importantly, according to the result, we achieved in Figure 7.12, we were able to detect CRP using our pre-patterned devices with concentrations of ~ 1 ng/mL, which we believe is close to the limit of detection and can be comparable with the commercialised ELISA kits performed on micro titer plates in the laboratory.

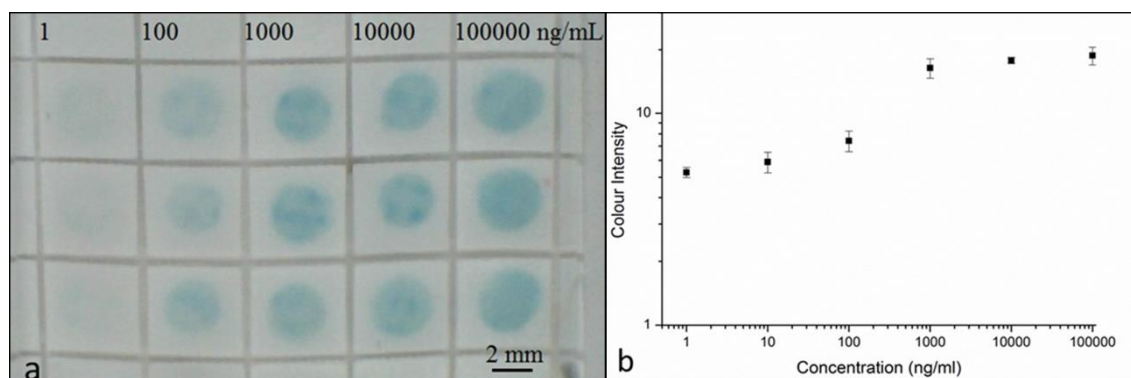


Figure 7.12 (a) Selected area of 5 \times 5mm well structure patterned with a laser power of 1 mW and a scan speed of 10 mm/s and results for the detection of CRP by the sandwich ELISA. (b) Calibration curve constructed using the grayscale intensity values taken from the image shown in (a). Error bars indicate the standard deviation for 4 individual measurements.

Above all, we have successfully implemented the complicated sandwich ELISA protocol on both untreated cellulose paper and nitrocellulose membranes and the LDW patterned paper-based devices. For the next step, in order to bring the technique more close to the market, we then decided to try the most commonly used protocol in the market (lateral flow test) for the paper-based device. The lateral flow test also called a lateral flow immunochromatographic assay is a type of rapid device for detection of various analytes with a simple strip arrangement device without the need for specialised and expensive equipment [192-194]. These lateral flow type devices are typically applied for medical diagnostics including home testing, POC testing and also for laboratory use. The home pregnancy test is one of the most well-known examples.

Typically, a lateral flow type device consists of several zones made from different materials with different functionalities as shown in Figure 7.13. Basically, a normal lateral flow strip consists of four parts: a sample pad, a conjugate pad, a reaction pad and finally an absorbent pad. The sample is added on the stripe from the sample pad, which is normally a cellulose filter that can hold a large volume of sample, then the sample flow to the conjugate pad, which is normally made from glass fibre filter. At the conjugate pad, the target analyte in the sample will bind with the specific conjugate, which is usually biomolecules that are conjugated with colloidal gold or coloured micro-particles. These specific conjugates have normally been immobilised during the manufacture of the strip and because of the property of the material used for this pad they can be easily released after having been rehydrated. After the conjugate pad, the mixture then migrates to the next section of the stripe, which is the reaction zone that has the test and control lines. The test line is composed of an antibody that is specific to the target analyte, thus the complex analyte-conjugate will bind to the test line only if the analyte is present in the sample, which then produces a colorimetric change at the test line indicating the presence of the analyte. On the other hand, the control line is composed of an antibody that binds to the conjugated biomolecule, which will always produce a colorimetric change regardless of the presence of target analyte and indicates the correct implementation of the assay.

For the implementation of a lateral flow type assay on our paper-based devices, the assay protocol we used was the sandwich ELISA for detection of CRP, which has been successfully implemented in previous experiments as describe above. All the reagents and antibodies were from the same commercialised ELISA kit as for the previous experiments. Although a typical later flow strip consists of a few different materials as described above, from the start, we simplify this arrangement by trying to use just a single material, which is either cellulose filter paper or nitrocellulose membrane.

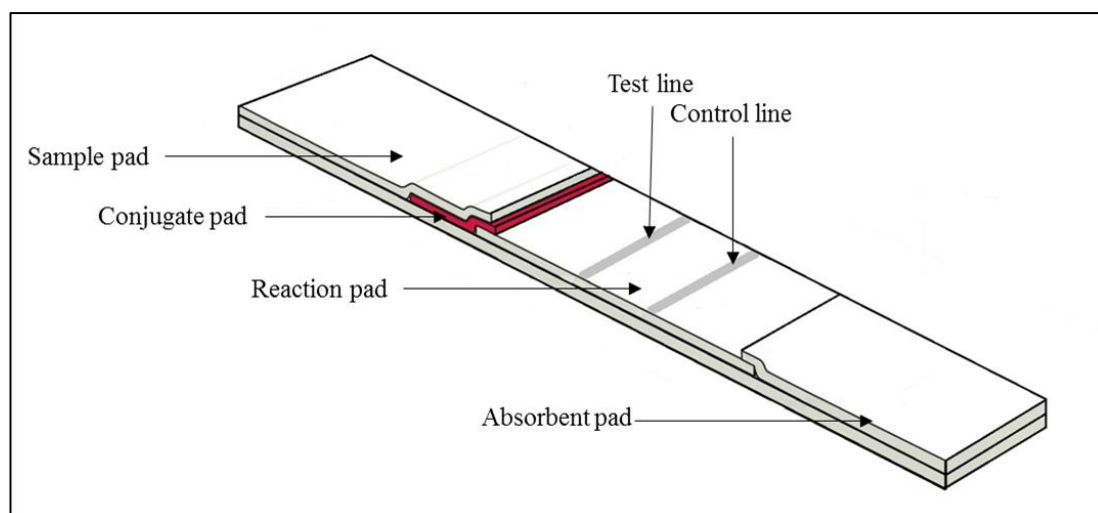


Figure 7.13 Schematic of a lateral flow-type biosensor that consists of four components: sample pad, conjugated pad, reaction pad and absorbent pad.

A schematic of a lateral flow strip we first used for implementation of assays is shown in Figure 7.14a: it is a single piece of nitrocellulose membrane with a cellulose pad at the end to act as an absorption/waste pad. To operate the assay, the capture antibody is first pipetted onto the testing zone and left overnight for immobilisation. Then the whole device is blocked using blocking solution for one hour to avoid any unspecific binding of antibodies and analytes to the paper substrate in the following processes. After the blocking, the whole strip is washed three times using washing solution and then the detection antibody is added in the conjugate zone and left to dry for one hour. After drying, the device is then ready to use. To perform the test, the sample solution with target analyte (CRP) is added to the sample adding zone, which will flow pass the conjugate zone and rehydrate the detection antibody, and then the mixture will flow forward to the testing zone and finally any excess reagent is absorbed by the absorption pad at the end. Finally, the TMB is added in the testing zone, which will react with the HRP-tagged detection antibody that is locked to the immobilised capture antibody through the target analyte to produce a colour change.

The result of the implementation of CRP detection based on sandwich ELISA using a lateral flow strip with an arrangement demonstrated in Figure 7.14a is shown in Figure 7.14c. Compared with the arrangement of the preparation of capture antibody shown in Figure 7.14b, the results marked in the black frame in Figure 7.14c match this arrangement, which illustrates the successful operation of the assay although it is a very weak signal with some background noise. Further optimisation work, such as alternating the antibodies' concentrations, improving the blocking efficiency and selection of better substrate materials, are still needed in order to get a clear and visible signal with less background noise.

For the next step, we then tried to perform the same ELISA for detection of CRP in an LFD that has a standard arrangement as shown in the schematic image in Figure 7.13 with all four different components present. An image of these devices is shown in Figure 7.15: a paper strip that is 5 mm wide and 5.5 cm long with four different materials sequentially positioned. All the reagents and antibodies were from the same ELISA kit as used in the previous experiments.

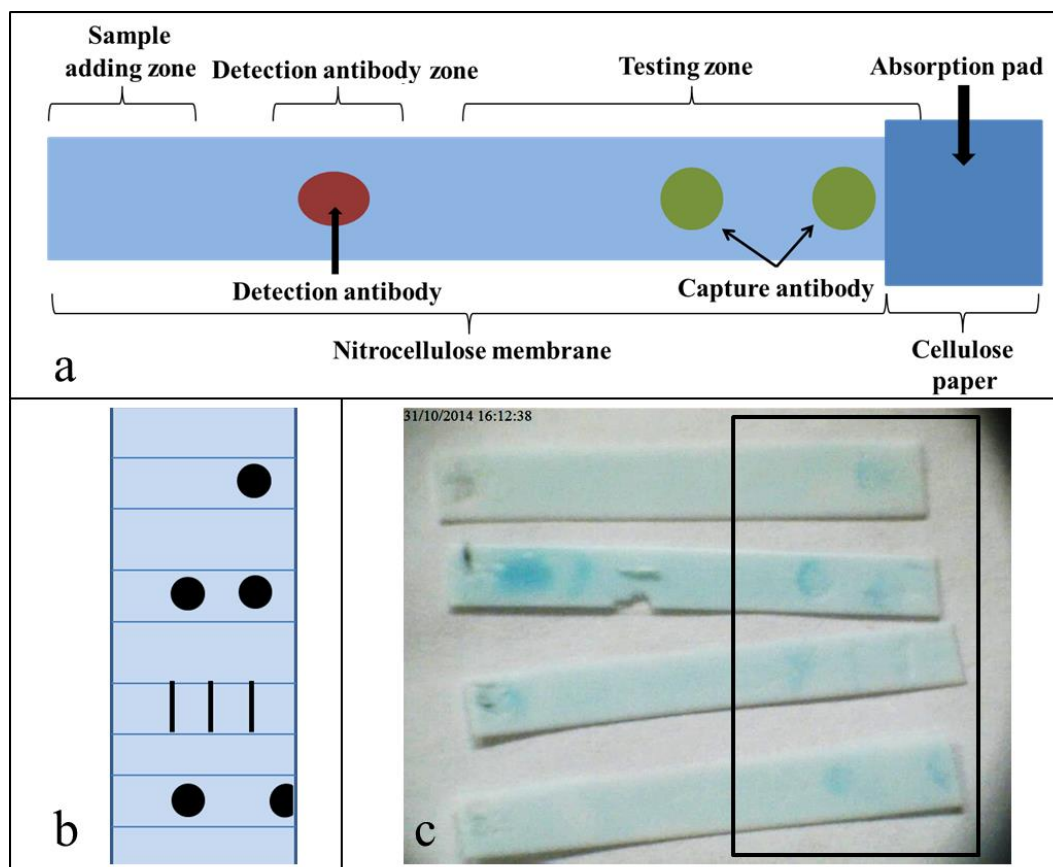


Figure 7.14 a) Schematics showing the arrangement of a lateral flow paper strip for implementation of CRP detection. b) Schematic indicates the method of preparation of the capture antibody. c) Image showing the result of lateral flow detection of CRP on a device as described in a) based on a sandwich ELISA.

To operate the assay, the capture antibody again is first pipetted onto the reaction pad and left overnight for immobilisation. Meanwhile, the HRP-tagged detection antibody is added to the conjugate pad and left to dry overnight. Then the reaction pad is blocked using blocking solution for one hour to avoid any unspecific binding. After the blocking, all four components are then assembled together onto a sticky backing card with the arrangement shown in Figure 7.13. The device is then ready to use. To perform the test, the sample solution with the target analyte (CRP) is added to the sample pad and the result is shown in Figure 7.16: two specific blue spots represent the presence of CRP in the sample. Compared with the results in Figure 7.14, the signal on these devices with the standard

arrangement (all four components) is better than that on a device consisting of only NC, with less background noise. However, a certain level of background can still be observed.

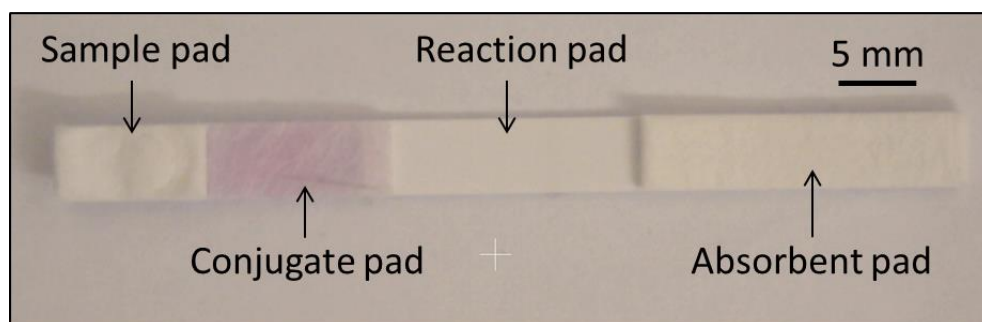


Figure 7.15 Image of a real device showing the arrangement of a lateral flow paper strip for implementation of CRP detection.

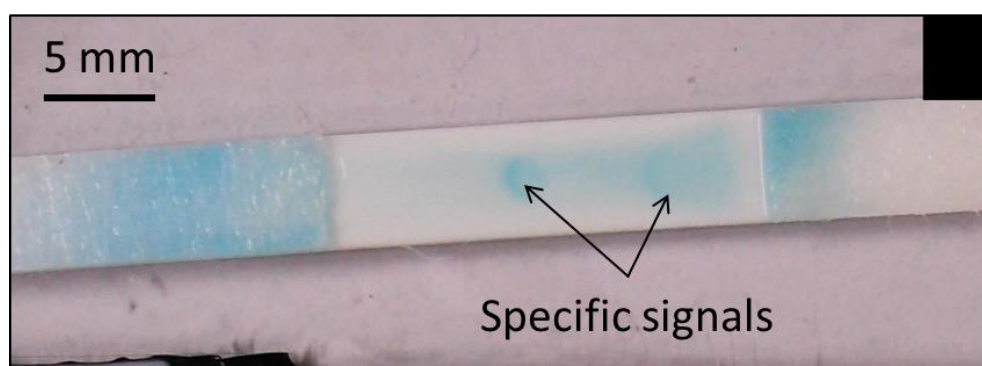


Figure 7.16 Image showing the result of the implementation of an enzyme-based sandwich ELISA for detection of CRP on a paper strip shown in Figure 7.15 with a sample concentration of 90 ng/mL.

Up to now, all ELISAs we have performed are based on an enzymatic reaction, more specifically the colour reaction between enzyme HRP and colorimetric substrate TMB. Because of this, an additional step of adding the substrate is always needed in order to perform the colour change. However, this step can be avoided via tagging the detection antibody with nanoparticles instead of an enzyme. In this case, the detectable colour signal will automatically appear with the accumulation of nanoparticles without the need for applying an additional substrate. As the detection antibody we used is already bound to biotin and streptavidin-conjugated gold nanoparticles are commercially available, the easiest way to tag this detection antibody with nanoparticles is via a commonly used streptavidin biotin binding. It is well known that streptavidin has an extraordinarily high affinity for biotin and the binding of biotin to streptavidin is one of the strongest non-covalent interactions known in nature [195]. In these experiments, the Streptavidin-Au with 20 nm particle size were purchased from Sigma-Aldrich (UK). The Au-tagged detection antibodies were prepared by simply mixing the solution of the streptavidin-Au

and the detection antibody then left for 10 minutes at room temperature for incubation before use.

Following the same assay protocol as described above with the Au-tagged detection antibody replacing the HRP tagged detection antibody, the result is shown in Figure 7.17: two clear red spots show the detection of CRP in the sample. Compared with the results in both Figures 7.14 and 7.16, the signal here is much clearer with no visible background noise.

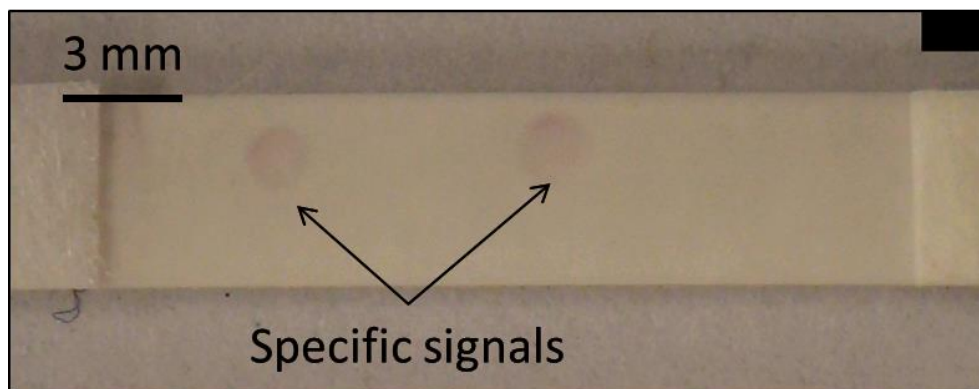


Figure 7.17 Image showing the result of the implementation of an Au nanoparticle-based sandwich ELISA for detection of CRP on a paper strip shown in Figure 7.15 with the sample concentration of 90 ng/mL.

7.3.3 Implementation of automatic multi-step assays

The final goal is to develop automated paper-based microfluidic devices that are user-friendly needing minimal intervention from the patient or an unskilled user need strategies that allow control over the flow of several liquids (reagents and sample) along their pathways. Such devices allow the implementation of a multi-step assay (such as an ELISA) automatically that do not need any human intervention. In the following experiments, we then tried to fabricate such automated paper-based devices using fluid delay strategies as described in chapter 4 and then validating the devices by implementing a multi-step ELISA for detection of CRP.

Firstly, we used the device with the same arrangement as shown in Figure 4.12 and 4.13 as described in chapter 4: a network of three identical channels for sequential delivery of three fluids to a common detection or reaction point. The sequential delivery of each fluid is made possible by introducing (a set of three identical) porous barriers written with a c.w. laser across the fluid channels with different porosity through simple adjustments of the laser parameters, which then introduce different delays to each channel. In the following experiment, we demonstrate the use of this device to implement automatic

multi-step ELISA for CRP detection. All the antibodies and reagents used were from the ELISA kit and were diluted to the working concentrations of 3.6 $\mu\text{g/mL}$ and 162 ng/mL for capture antibody and conjugated antibody respectively and the streptavidin HRP was diluted in PBS with a ratio of 1:200. The CRP human standard (C1617) was purchased from Sigma-Aldrich (UK) and diluted to different working concentrations using calibrator diluent (1% BSA in PBS).

To prepare the device for implementation of an assay, the capture antibody was first pipetted at four distinct spots (1 μL per spot) within the detection zone as shown in Figure 7.18a and then left to dry for one hour at room temperature. The whole device was then immersed in a blocking solution (5 % BSA in PBS) for one hour at room temperature, followed by three sequential washing steps using PBS. Finally, after subsequent drying, the device was ready to use.

To perform the assay, 40 μL of each reagent was sequentially pipetted onto the source pads within a period of a few seconds in each channel and the device was left in a covered petri dish at room temperature to allow for the timed, sequential delivery of the individual solutions along each channel, into the detection zone for reaction with the capture antibodies immobilized therein. The devices were held along their edges by a specially designed holder that suspended them in the air thus eliminating any contact with the petri dish surface underneath which otherwise would have altered the flow of the reagents. After 30 minutes, the whole device was washed three times using PBS for five minutes each. Finally, 10 μL of the colorimetric substrate TMB (Tetramethylbenzidine) was added at the detection zone and the result was read after 20 minutes.

Ideally, such a device should also enable the sequential delivery of TMB to the detection zone via another fluid flow channel, and that would then be a true example of a sample-in-result-out type device, however, for this initial proof-of-principle experiment where we intend to show the usefulness of delays, we have not yet manufactured such a test. In the case of several routinely employed assays, the detection antibodies are tagged either with a gold nanoparticle or coloured beads, and if we choose to use detection antibodies labelled in this fashion, then there would not be the need to have this additional delivery path. Figures 7.18b, 7.18c and 7.18d show the results for the detection of different concentrations of CRP, and the clearly visible and distinct four blue spots that appear in the detection zone (with minimal background colour ‘noise’) confirm the presence of CRP in the sample. Figure 7.18d shows the result for a control device tested with a sample solution that did not have CRP. As shown in the figure, for this negative result, we do not observe any specific blue spots in the detection zone. The colour intensity of the spots in Figure 7.18b is greater than that in Figure 7.18c, which is greater than that in Figure 7.18d,

and this relates to the higher concentration of CRP in the corresponding samples that were used in the three different cases. For some of the spots, their non-symmetric circular shape is as a result of the spotting of the capture antibodies more towards one edge of the channel walls, resulting in a clipping of their circular shape. The images in Figure 7.18b and 7.18c clearly demonstrate the successful detection of CRP on our laser-patterned paper-based device with incorporated fluid delay mechanisms. In addition, as shown in Figure 7.18d, using our devices, we were also able to detect CRP with concentrations of less than ~ 10 ng/mL, which we believe is close to the limit of detection.

This device is an example of a semi-automatic type test that still requires intervention from a user, but we are planning on developing this concept further in the immediate future to enable a fully-automated device which would then be a true example of a sample-in-result-out type device.

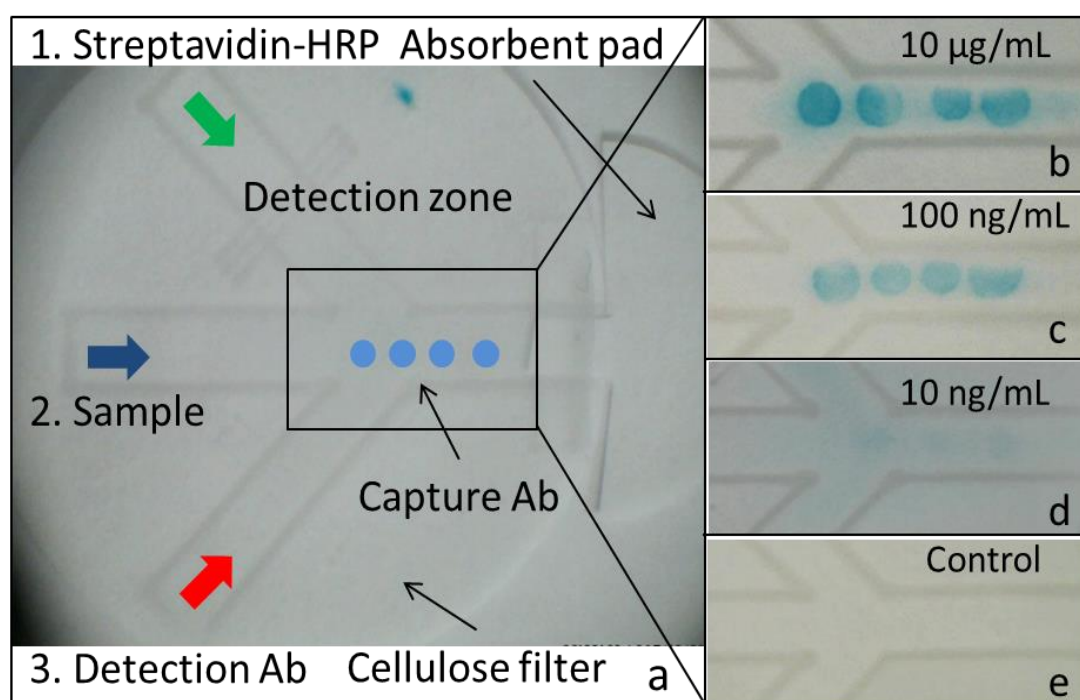


Figure 7.18 Automated multi-step ELISA for CRP detection in a 2D multi-channel fluidic device. a) Image of a device showing its design and indicating reagent locations for the assay. Four blue spots, shown schematically in a), represent the position of immobilised capture antibody in the detection zone. b), c), d) and e) are photos of the CRP ELISA result on the device for different sample concentrations of 10 μ g/mL, 100 ng/mL, 10 ng/mL and no sample respectively.

After successful implementation of the multi-step ELISA on a cellulose paper-based device, we then focus on the nitrocellulose membranes, which are a more commonly and popularly used material in POC diagnostics. For the operation of an automated multi-step CRP detection, we first fabricated a 2D multi-channel fluidic device on nitrocellulose

membranes, which is shown in Figure 7.19, using our LDW technique with a similar three channel arrangement as described previously. It is a three channel design with different delays in two of the channels, which then allow sequential delivery of reagent from each channel to the reaction zone. After the device was fabricated, it was then prepared before operating the test with immobilisation of capture antibody and blocking. After those preparations, for implementation of the assay, the sample, detection antibody and HRP were added sequentially within a few seconds into the channel without delay, the channel with weaker delay and the channel with stronger delay respectively. Finally, after washing, the TMB was added into the detection zone and the result is shown in Figure 7.19f: four specific blue spots illustrate the presence of the target analyte in the sample.

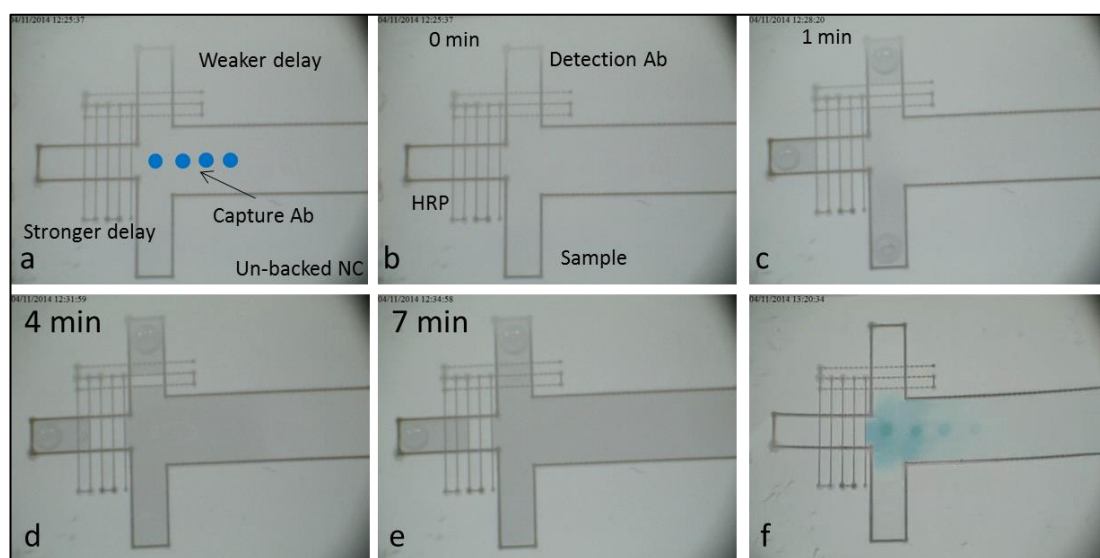


Figure 7.19 Automated multi-step ELISA for CRP detection in a 2D multi-channel fluidic device. a) Image of a device showing its design and indicating reagent locations for the assay. Four blue spots, shown schematically in a), represent the position of immobilised capture antibody in the detection zone. b), c), d) and e) are sequential photos of the device after different times of adding the reagents, and f) is a photo shows the result.

7.3.4 Detection of CRP in real human bodily fluids

In the previous sections of this chapter, a number of both simple one-step and complicated multi-step assays have been successfully performed in our patterned paper diagnostic devices. In this section, for the purpose of proving that these devices can also be used in a real setup, the performance of these paper-based devices was then tested by diagnosing analytes in real human bodily fluids including human urine and human blood plasma. Again, the analyte of interest was CRP, as the protocol was known and well-developed in this format as described in previous sections.

The healthy urine samples were obtained from hospital and were spiked with known concentrations of CRP. These spiked samples were then tested using an NC device with grid-like structures patterned via our LDW approach as shown in Figure 7.20. The diagnosis was performed via a sandwich ELISA with the same protocol as described in the previous section. As a comparison, samples of PBS with spiked known concentrations of CRP were also tested on the same device. The results of these tests can be seen in Figure 7.20 with blue spots in individual wells representing the presence of CRP in those spiked samples. These confirm that these laser-patterned devices can be used for the detection of CRP in human urine samples.





Spiked urine samples 500, 250, 125, 62.5, 31.25 $\mu\text{g/mL}$	
Spiked urine samples 16, 8, 4 $\mu\text{g/mL}$, 9 ng/mL	
Spiked PBS samples 500, 250, 125, 62.5, 31.25 $\mu\text{g/mL}$	
Spiked PBS samples 16, 8, 4 $\mu\text{g/mL}$, 9 ng/mL	

Figure 7.20 Detection of CRP in human urine on LDW patterned NC device. The first two rows show detection of various concentrations of CRP in spiked healthy human urine, and the two last rows show detection of the same concentrations of CRP in spiked PBS.

Following the successful implementation of detection using human urine samples, in the next set of experiments, another important bodily fluid, human blood plasma, was tested. The human samples were obtained from our collaborators at Southampton University General Hospital. These plasma samples were from patients that had conditions such as heart attacks and therefore had high CRP levels, and had been measured at the hospital by traditional microtiter plate-based ELISA. Therefore, a direct comparison is made between our technique and the routinely used method. Furthermore, healthy samples were also applied and used as the negative control for these tests. In addition, the healthy samples with spiked CRP at different concentrations were also tested on the same device. The results of the tests using human blood samples are shown in Figure 7.21: all infected clinical samples produced a consistent signal at the different wells that contain the same sample. Moreover, there is a distinct degradation of the colour intensity of the spiked healthy samples as the concentration of the CRP decreases, and finally, the non-spiked healthy samples show a very low signal, which was the negative control.


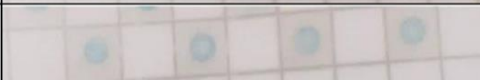


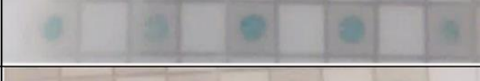
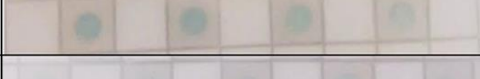

Unknown clinical sample SK001	
Unknown clinical sample SK005	
Unknown clinical sample SK006	
Unknown clinical sample SK015	
Healthy spiked 500, 250, 125, 62.5, 31.25 µg/mL	
Healthy spiked 16, 8, 4, 2 µg/mL	
Healthy not spiked	

Figure 7.21 Detection of CRP in blood plasma on laser-patterned nitrocellulose. Both infected clinical samples and healthy samples were tested.

Overall, we have successfully demonstrated that our LDW fabricated devices can be used for medical diagnosis with real human bodily fluid samples, which further validates the effectiveness of these patterned paper-based devices as a clinical diagnostic tool.

7.4 Summary

In order to validate the effectiveness of our LDW technique for fabrication of paper-based microfluidic devices, in this chapter we implemented and tested a range of colorimetric biochemical analyses and also clinical diagnostic assays on both un-patterned and patterned cellulose paper as well as nitrocellulose membranes.

We started with simple one-step assays for detection of glucose, BSA and nitrite in water. We successfully achieved both multiplex analyses for the single analyte with different concentrations, and simultaneous detection of two different analytes. Subsequently, by plotting a calibration curve from the sample with known concentrations, we are then able to measure the concentration of unknown samples by measuring their colour intensities and comparing them to the calibration curve, which provides a semi-quantitative analysis on these paper-based devices.

After successfully implemented those simple one step colorimetric assays, we then focussed on more complicated multi-step diagnostic protocols: ELISA, for detection of TNF- α and CRP. For CRP ELISA, we were able to detect CRP with a concentration of about 1 ng/mL, which is close to the limit of detection and can be comparable with the commercialised ELISA kits performed on a microtiter plate in the laboratory. Following these, we also successfully implemented lateral flow protocols on our paper-based devices

and then designed an automated paper-based microfluidic device that allows control over the flow of several fluids along their pathways for operating a multi-step ELISA automatically. All the reagents needed are added to the device at the same time, and then the delay strategies in each channel allow control and sequential delivery of these reagents to a reaction zone after different periods of time as required, in order to perform multi-step analyses. Finally and most importantly, we have also successfully demonstrated that these devices can be used for the detection of CRP in real human bodily fluid samples, including urine and blood plasma, which further confirm and validate the effectiveness of these LDW patterned paper-based devices.

Finally, a number of advantages of using a laser-patterned paper-based device for these assays were demonstrated in this chapter. First of all, the reagents and sample volumes used are hugely reduced to only 2 μl per square well from 100-200 μl usually required in a standard ELISA test. As reagents are typically extremely expensive and samples are usually precious, this helps to cut down the cost of the assay considerably. Another significant advantage is the reduction of the time required to perform this assay. After the incubation of the capture antibody on the paper device, the assays performed on a paper-based device require only about 5 to 15 minutes in total to complete, compared to 6 or more hours required for a standard ELISA test. Additionally, the cost of the paper device is much smaller (~ 0.05 GBP per device) compared to the cost of the plastic multi-well plate (~ 1 GBP) commonly used in ELISA tests. Finally, the whole footprint of the device is greatly reduced, allowing for easier and cheaper transportation. Overall, we believe that these LDW patterned paper-based devices could be an ideal alternative choice for medical diagnostics, which are much faster, cheaper and easier to use than currently used laboratory-based analyses.

Chapter 8: Conclusions and future work

8.1 Conclusions

This chapter provides a summary of all the results described in this thesis concerning about development of a novel laser-based direct write approach not only for fabrication of paper-based medical diagnostic sensors but which also allows the introduction of a wide range of additional functionalities and the validation of these LDW-fabricated devices for implementation of various detection tests.

8.1.1 LDW patterning for fabrication of paper-based devices

In Chapter 3, we have demonstrated a simple, low-cost laser-based direct-write technique for the rapid patterning of fluidic structures in various porous materials for fabrication of paper-based microfluidic devices. The main substrates that have been explored to test the applicability of this technique are cellulose paper and nitrocellulose membranes, both of which are very important materials used for fabricating paper-based microfluidic devices. Compared with other techniques previously reported for fabrication of such devices, this LDW procedure is mask-less, non-contact and non-lithographic, which helps to avoid any cross-contamination during the fabrication process. Additionally, the approach also eliminates the requirement for expensive masks, cleanroom-based steps, specialist reagents and custom-designed equipment, which make it well-suited for up-scaling to mass-production.

The results discussed above show that this method is able to create polymerised barriers on both cellulose paper and nitrocellulose membranes with dimensions of only $\sim 120\ \mu\text{m}$ and $\sim 60\ \mu\text{m}$, respectively, and the minimum dimensions needed for making microfluidic channels that can contain and guide liquids are $\sim 80\ \mu\text{m}$ and $\sim 100\ \mu\text{m}$ respectively. All these values mentioned here are the smallest that have been reported so far, which would help towards further miniaturisation of such paper-based microfluidic devices. In addition, with our existing laser-writing set-up, we have proved that it is possible to achieve mass production with a speed of at least one device per second.

Finally, in order to further optimise this LDW patterning technique, two main improvements have been successfully introduced into the basic LDW procedure. For the first improvement, a galvo scanner is introduced, which allows a further increase of the fabrication speed and more accurate control of the patterning condition, which brings great flexibility during the fabrication procedure. In addition to this, a local deposition

procedure is introduced, which satisfactorily solves the problem of altering properties of the patterned substrate during the initial LDW procedure and additionally eliminates the undesirable solvent development procedure.

8.1.2 Introduction of fluidic delays via LDW approach

In Chapter 4, two delay mechanisms (depth-variable barriers and porosity-variable barriers) were introduced based on the same LDW technique that allows the fabrication of pre-programmed or timed fluid delivery in paper-based fluidic devices without any additional equipment or minimal actions from the user.

The results show that through adjustment of the laser writing parameters such as the laser power and scan speed we can control the depth and/or the porosity of these delay barriers which, when fabricated in the fluid path, produce controllable fluid delay. We have demonstrated that the efficiency of the introduced delay, namely the delay factor, depended not only on the condition (porosity or depth) of the delay barriers but also on the number and the position of the barriers. Using this delay patterning protocol, we generated flow delays spanning a few minutes to over an hour.

The introduction of these programmable fluid delays would then help to add further functionalities to paper-based microfluidic devices, particularly for applications such as automated multi-step fluidic protocols. In contrast to other methods reported for controlling fluidic delivery, this approach eliminates the requirements for cleanroom-based steps, or custom-designed equipment, or the need for long flow paths. Most importantly, with our existing LDW set-up, the delay mechanism can be an integral part of the fabrication of the fluidic devices themselves, and this is a distinct improvement over other methods that require additional procedures for introduction of fluidic control.

8.1.3 Fabrication of 3D paper-based device via LDW approach

Compared with simple 2D paper-based devices, 3D devices introduce a number of unique characteristics which are advantageous for certain applications and thus have been studied in recent years. In Chapter 5, we then further extended our LDW approach for application beyond fabrication of simple 2D microfluidic paper-based devices. During the previous experiments, we found that the depth of the polymerised structures in the substrate can be controlled during the patterning procedure.

Firstly, with the fabrication of these polymerised structures extending through a few layers of substrate, 2D devices can be stacked and sealed, which hence solves potential

evaporation and contamination problems. In addition, through carefully designing the patterning strategy or judicious assembly of several layers, it allows 3D pathways for the realisation of a 3D paper-based device. Secondly, with the fabrication of these polymerised structures in a single substrate that extends to different depths, backing structures can be achieved inside the substrate itself. In addition, these polymerised structures with different controllable depth can be also used to control the effective paper volume, which will help to reduce the required reagent volume and most importantly, with our hypothesis, can be used for enhancing the assay sensitivity and limit of detection. Finally, by carefully designing and positioning of these depth-variable polymerised structures in a single substrate, 3D flow paths can be constructed for the realisation of a 3D paper-based device based on a single layer of the substrate.

Overall, unlike other 3D device fabrication methods, our LDW approach does not require any additional processing equipment or alignment/assembling step and uses the same fabrication approach that is described earlier for producing a 2D fluidic device by simply altering the patterning parameter.

8.1.4 Enabling triggerable fluidic gates in paper-based devices

To add further functionalities to paper-based devices, in Chapter 6, we have demonstrated a new approach for fabrication of fluidic gates or valves based on simple wax barriers printed using a cheap office wax printer. These wax gates can be triggered by the application of a heat source. In more detail, the wax in the heated area is melted and then pushed away by the flow, which hence results in a clean permanent flow path that allows fluid to flow through. Thus, these triggerable barriers act as controllable on/off gates that either impede or allow the flow of fluids on demand in fluidic devices.

To enable the switching action, we have successfully demonstrated both non-localised heating using a hot plate and localised heating using a wax pen or a laser. Furthermore, in order to prove the effectiveness of this idea of using printed wax barriers as fluidic gates, both a simple single step assay for detection of nitrite and a complicated multistep sandwich ELISA for detection of CRP have been successfully implemented.

Overall, the approach reported here allows fabrication of triggerable fluidic gates with an extremely simple and cheap procedure without the need for additional expensive equipment and complicated procedures. In addition, these wax gates are highly controllable as desired by precise application of the heat source. Therefore, we believe that this approach could be an ideal choice for implementation of fluidic gates in paper-based microfluidic devices.

8.1.5 Validation of the fabricated paper-based devices

In Chapter 7, a range of biochemical analyses and also clinical diagnostic assays have been successfully implemented on these LDW patterned devices in order to validate the LDW technique for fabrication of paper-based devices.

For simple one-step analyses, detection of glucose, BSA and nitrite in water have been successfully implemented in both multiplex analyses for a single analyte with different concentrations and simultaneous detection of multiple analytes. In addition to these, more complicated multi-step ELISAs for detection of TNF- α and CRP were also tested in our patterned devices. For CRP, we were able to detect concentrations of about 1 ng/mL, which is close to the limit of detection and can be comparable with commercialised ELISA kits. Additionally, for all the above tests, semi-quantitative analyses were also accomplished by comparing the colour intensities to a calibration curves. Following these, based on the delay strategies we introduced in Chapter 4, we also successfully developed an automated paper-based microfluidic device that allows control over the flow of several liquids along their separate pathways for operating a detection of CRP in an automatic manner. Finally and most importantly, we have also confirmed and validated the effectiveness of these LDW patterned paper-based devices using real human bodily fluid samples, including urine and blood plasma.

In addition, a number of advantages of using a laser-patterned paper-based device for these assays were also demonstrated in Chapter 7, which includes reduced sample and reagent volumes required, shorter assay performing time and finally much lower cost. Overall, we believe that these LDW patterned paper-based devices could be an ideal choice for both chemistry analysis and clinical diagnostics, which are much faster, cheaper and easier to use than currently used laboratory-based approaches.

8.2 Future work

We believe that the LDW technology described in the previous chapters has great potential in the manufacturing of low-cost POC medical diagnostic devices. Although much has been done in developing, optimising and testing of this LDW approach and the fabricated devices as described in this thesis, there is still enormous room for improvements and innovations in this field. Therefore, we have already identified several key areas that we believe further studies are necessary in order to further explore and expand the potential of our manufacturing technique.

As future work, one of the immediate goals would be to continuously investigate and explore new materials, include both photopolymer and the solvent used, in order to further optimise the patterning procedure, and which might also result in easier, faster and more cost-effective manufacturing. In addition, a range of different lasers are also worth trying that would result in optimised patterning performance.

Secondly, we have shown that our devices have great potential in improving the sensitivity of detection, which is currently regarded as one of the greatest challenges for transferring paper-based diagnostic devices from their research phase towards real world application. This work will involve the further investigation of functional structures that are introduced in paper-based devices via our LDW approach for increasing the sensitivity and also limit of detection.

Thirdly, the next big revolution in paper-based devices is the ability for implementation of multiplexed diagnostics. Most of the detection protocols in real world scenarios are much more complicated and many require multi-analyte diagnoses in order to diagnostic a single condition. Multiplexed quantitative detections for a single analyte are also equally important, as for most conditions, more information instead of just a yes/no answer is required in order to make a diagnosis. With our LDW approach, we have proved the ability to pattern multiple flow channels in a single device potentially for achieving the multiplexed detection of either multiple conditions or a single condition with different levels. Hence, we believe that our laser-based techniques could produce devices that allow multiplexed detection, which helps to achieve fast, accurate and quantitative diagnoses.

Fourthly, our final goal would be to demonstrate fully automated paper-based biosensors that allow real clinical diagnosis and do not require any additional handling from the user apart from the introduction of the sample. This work will involve the use of the best-identified laser-patterning protocol for the fabrication of a simple fluid-flow-based prototype test/sensor that can be applied for pre-clinical trials in the detection of diseases and diagnosis. As a platform technology, it is expected that once the first prototype is developed, it will be easier and faster to develop biosensors for detecting other diseases.

Finally, there are several innovative ideas that have been proposed during this work, and further exploration is required. These tasks will involve investigating areas that are more speculative and lie outside the fundamental laser-based paper structuring for POC applications. Firstly, the introduction of optical functionality into paper-based devices: this task involves the injection of light into the LDW patterned polymer tracks in order to form waveguides either in or on the paper substrate. As a result, this optical functionality may offer a route to implement more complicated tests that involve light as a diagnostic media

in paper-based devices beyond currently available detections. Secondly, LDW patterning of fabrics: this could be applied as a method for fabrication of 'smart plasters' or wearable monitoring and diagnostic devices, which enable novel POC diagnostics. Finally, investigation of 'smart' polymers: this task involves exploring functional photopolymers that can be sensitive to a number of different stimuli, i.e. temperature, intensity of light, pH, electrical or magnetic fields, and can respond in different ways. With the introduction of such materials to paper-based devices, it would allow for novel analyte detection techniques and manipulation of solutions within the device.

Appendix A Laser Fluence Calculation

During the LDW procedure, a laser beam is focused onto the substrate through a lens, which then induces cross-linking of the photopolymer that is pre-permeated in the substrate. In order to understand and optimise this polymerisation procedure, it is important to know the actual fluence in the exposed area, which causes the photopolymerisation.

Commonly, the laser fluence is used to describe the energy delivered per unit area from a pulse laser. It is normally defined in units of J/cm². The following equation is normally used to calculate the laser fluence of a laser pulse:

$$\text{Fluence} \left[\frac{\text{Joules}}{\text{cm}^2} \right] = \frac{\text{Laser pulse energy [J]}}{\text{Exposure area [cm}^2\text{]}} \quad (1)$$

In the case of a c.w. laser, the output is normally defined by power rather than pulse energy as for a pulsed laser. As a result, to define the laser fluence for a c.w. laser, a slight modification to the above equation will be needed. The equation below is then used to calculate the fluence for a c.w. laser:

$$\text{Fluence} \left[\frac{\text{Joules}}{\text{cm}^2} \right] = \frac{\text{Delivered energy [J]}}{\text{Exposure area [cm}^2\text{]}} \quad (2)$$

For a c.w. laser, the output is usually defined in power with units of watts. Hence, to calculate the delivered energy from a c.w. laser, a time factor needs to be introduced and the calculation can be done using the following equation:

$$\text{Delivered energy [Joules]} = \text{Laser power [W]} \times \text{Scan time [s]} \quad (3)$$

However, for our LDW approach, the focused beam scans along the surface of the substrate at specific scan speeds, thus the exposed area can be then roughly defined as a rectangular area with the length of scanned distance and width of the laser spot at the substrate surface. The length of the scanned distance can be simply calculated according to the chosen scan speed and the scan time. An assumption is made here that the exposure area is a rectangular shape that ignores the start and the end of the scanned area, which should be semi-circular because the beam itself is circular. These areas of the two semi-circles at the start and end of the scan are negligible compared with the total exposure area. Therefore, the following equation is used to define the exposure area.

$$\begin{aligned}
 \text{Exposure area [cm}^2\text{]} &= \text{Laser spot diameter [cm]} \times \text{Scanned distance [cm]} \\
 &= \text{Laser spot diameter [cm]} \times \text{Laser scan speed } \left[\frac{\text{cm}}{\text{s}} \right] \\
 &\quad \times \text{Scan time [s]}
 \end{aligned} \tag{4}$$

Finally, substitute equations (3) and (4) into (2), we are then able to obtain the equation for calculation of fluence for a c.w. laser as follows:

$$\begin{aligned}
 \text{Fluence } \left[\frac{\text{Joules}}{\text{cm}^2} \right] &= \frac{\text{Delivered energy [J]}}{\text{Exposure area [cm}^2\text{]}} \\
 &= \frac{\text{Laser power [W]} \times \text{Scan time [s]}}{\text{Laser spot diameter [cm]} \times \text{Laser scan speed } \left[\frac{\text{cm}}{\text{s}} \right] \times \text{Scan time [s]}} \\
 &= \frac{\text{Laser power [W]}}{\text{Laser spot diameter [cm]} \times \text{Laser scan speed } \left[\frac{\text{cm}}{\text{s}} \right]}
 \end{aligned} \tag{5}$$

Appendix B BioDot dispensing system

In this appendix, the background, theories and calculations of the BioDot Aspirate/Dispense system are described in detail.

The BioJet Plus™ technology is a hydraulically driven system that combines the high-resolution displacement capabilities of a syringe pump with a high-speed BioJet valve. This combination permits the non-contact dispensing of nanoliter volumes. As described in schematic in Figure B1, the dispensing system mainly consists of a syringe pump module that is connected to the backside of the dispense valve. For continuous dispensing, the reagent or solvent is pulled from a reservoir into the syringe and then dispensed through the micro-solenoid valve.

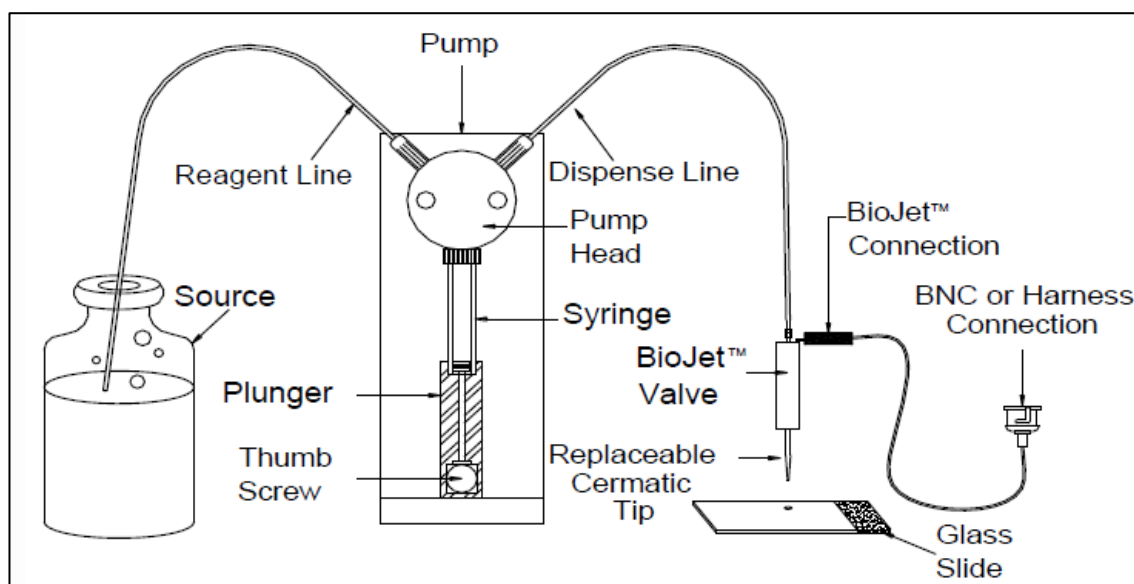


Figure B 1 Schematic of the BioDot AD3220 dispense/aspirate system with a BioJet™ non-contact nanoliter dispenser head [196].

Two modes of liquid handling are possible, which are continuous (bulk) dispensing and aspirate/dispense. Continuous dispensing involves pulling reagent or solvent from a reservoir into the syringe and then dispensing it through the micro-solenoid valve. Aspirate/dispense is accomplished by filling the system with backing fluid, dipping the tip of the valve into a sample, withdrawing the syringe to aspirate the sample, and then dispensing the aspirated sample. For all trials of local deposition of both photopolymer and biological reagent described in this thesis, we chose to use the second mode (aspirate/dispense) due to the smaller volume required and easy switching of the source.

In order to accomplish the dispense function, this hydraulically driven dispensing system requires a fluid medium to be present from the syringe to the micro-solenoid BioJet Plus

valve. Four main steps are involved in a typical dispensing process. For the first step, the syringe is displaced a given amount. At the second step, the valve is opened for a short period of time (normally milliseconds). Then, during the third step, fluid is released from the valve and travels to the tip. Finally, for the last step, the fluid increases its linear velocity as it passes through the tip orifice and is ejected as either a drop or a stream (if the amount of the fluid is large) onto the substrate. One valve actuation results in one drop.

The steady state pressure (SSP) in the dispensing system is the key to BioJet Plus™ in order to dispense the proper volume. This pressure is achieved by the displacement of fluid by the syringe pump and is proportional to the displacement (drop size). The SSP is determined by the system compliance, which is dominated by entrapped air bubbles. Once the SSP is established, the amount of fluid displaced by the syringe pump will equal the amount that is dispensed.

The plot in Figure B2 shows schematically how the pressure changes in the system according to the SSP during a normal prime/aspirate/dispense cycle. The prime is used to initialize and fill the syringe pumps, micro-solenoid BioJet Plus™ valves of the dispense head, and connecting tubing with fluid from the reservoir. The reservoir fluid can be either system fluid for an aspirate/dispense step of the reagent or sample fluid for continuous (line or dot) dispensing. When the dispense system is primed, several hundred micro liters of fluid are dispensed as a stream. The resistance to flow caused by the valve and tip orifice causes the pressure within the system to become higher than desired for SSP as shown in Figure B2. To achieve SSP, you must first vent the valves, which involves opening the valves without displacing fluid. This brings the system to ambient (zero) pressure and from this point the SSP can be achieved.

For the next step, the aspirate function draws the sample from a reservoir, usually a micro-well plate, into the tip of the dispenser. As shown in the plot in Figure B2, during the normal aspiration process, a slight negative pressure is produced. This negative pressure is relieved by performing a vent, which opens the micro-solenoid valve without displacing any fluid. When the sample is aspirated, the syringe pump draws fluid through the tip orifice. The resistance to flow from the tip and valve creates a negative pressure, which must first be overcome to achieve a steady state pressure. As with priming, venting the system can bring the system to a zero/ambient pressure, from which the SSP can be applied.

Finally, before the real dispensing can proceed, pre-pressurization and pre-dispense procedures are required in order to bring the pressure in the system from the zero pressure back to the SSP, which then allows accurate and stable dispensing of the

programmed volume. For the pre-pressurization procedure, the syringe pump is displaced without opening the BioJet Plus™ valve, which raises the pressure in the system very close to the desired SSP. After pre-pressurization, several pre-dispenses at the programmed volume should be performed for fine-tuning the SSP that brings the pressure to the appropriate level for the programmed volume. Finally, the dispensing happens under the SSP, where the syringe pump to displace fluid and the BioJet Plus™ valve opens resulting in a drop or series of drops of the programmed volume.

Priming, aspiration, pre-pressurization and pre-dispense are the four main procedures that influence the achievement and maintenance of the SSP and thus influence the dispense volume. Apart from these factors, the SSP is also affected by a number of other factors such as gas bubbles, tip effects, syringe speed and valve open time.

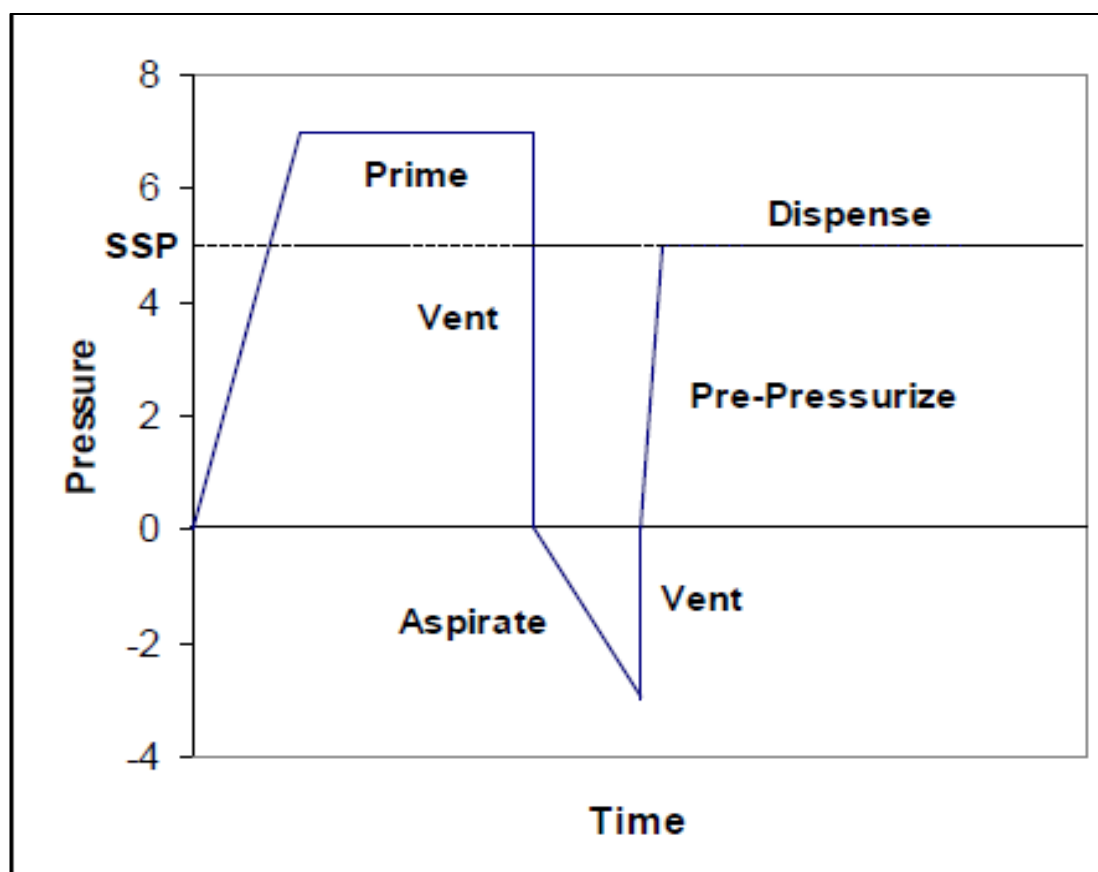


Figure B 2 Schematic figure shows the variation of the pressure during a prime, aspirate, and dispense cycle [196].

The flow chart in Figure B3 describes the logic sequence of the AxSys™ software program, which is a bespoke software package for the operation of the BioDot dispensing system. For the first step, the software requires the user to choose the dispense mode from either dot dispense or line dispense. Then a set of dispensing parameters is required for either mode that has been decided. In the next step, the user again needs to decide the

liquid handling mode, which can be either continuous (bulk) dispensing or aspirate/dispense. If an aspirate/dispense mode is chosen, further actions are required including the confirmation of the coordinates for the aspiration source and then aspiration of the target fluid from the reservoir. For continuous dispensing mode, the source is automatically selected and no any further interactions are required. In the following step, a series of pre-dispense preparation procedures are required before actual dispensing can be accurately performed, which include pre-dispense, pre-pressurization and cleaning of the dispensing tip. After the above pre-dispense preparations, the system will then start its actual dispense process according to the required design that is pre-programmed by the user. Finally, the whole dispensing procedure ends with cleaning and parking of the dispensing head.

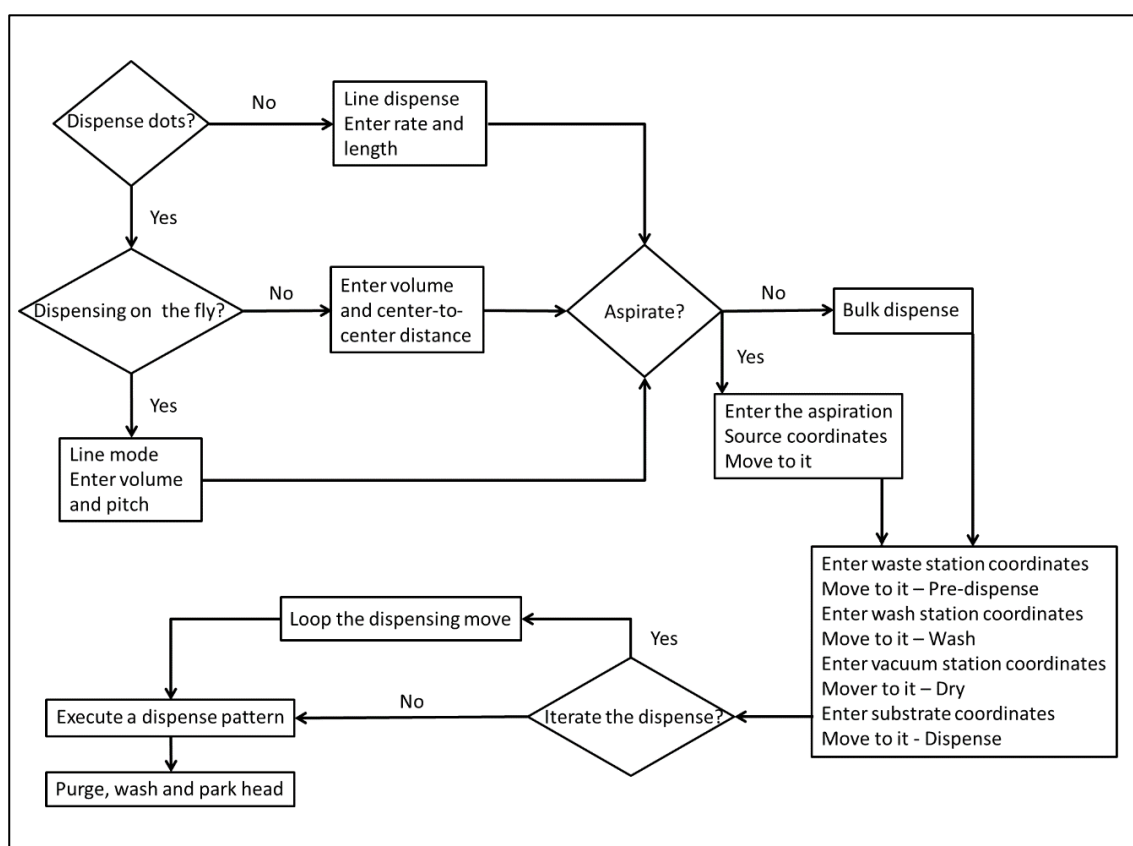


Figure B 3 Flow chart showing the logic sequence of the AxSys™ software program for operation of the BioDot dispensing system.

The step-wise schematic in Figure B4 shows the working protocol for the AD3220 BioDot aspirate/dispense system. The dispensing starts with the homing of the platform followed with prime and vent of the system. The prime is used to initialize and connect the syringe pumps and the valves to the reservoir. After priming, the valve is vented in order to bring the pressure in the system from ambient pressure to above SSP. In the next step, a tip cleaning procedure occurs, which includes wash, vacuum and drying of the tip. Following

the cleaning procedure, two dispensing modes, namely continuous dispensing mode and aspirate/dispense mode, can be chosen according to different requirements and applications. For all the dispensing experiments described in this thesis, the aspirate/dispense mode is selected due to the smaller fluid volume required and easy switching of the source. In terms of the aspirate/dispense mode, an additional aspiration step is included in order to aspirate the sample from an external reservoir into the tip of the dispenser, which is followed again by cleaning of the tip. For the next step, a series of pre-dispense procedures are performed, which include pre-dispense, pre-pressurisation and tip cleaning, in order to get the system ready for an accurate and stable dispensing, mainly stabilising the system at the desired SSP. The actual dispensing is then performed under the desired SSP, which allows accurate and stable dispensing of the programmed volume. For the last step, the dispensing ends with homing of the system.

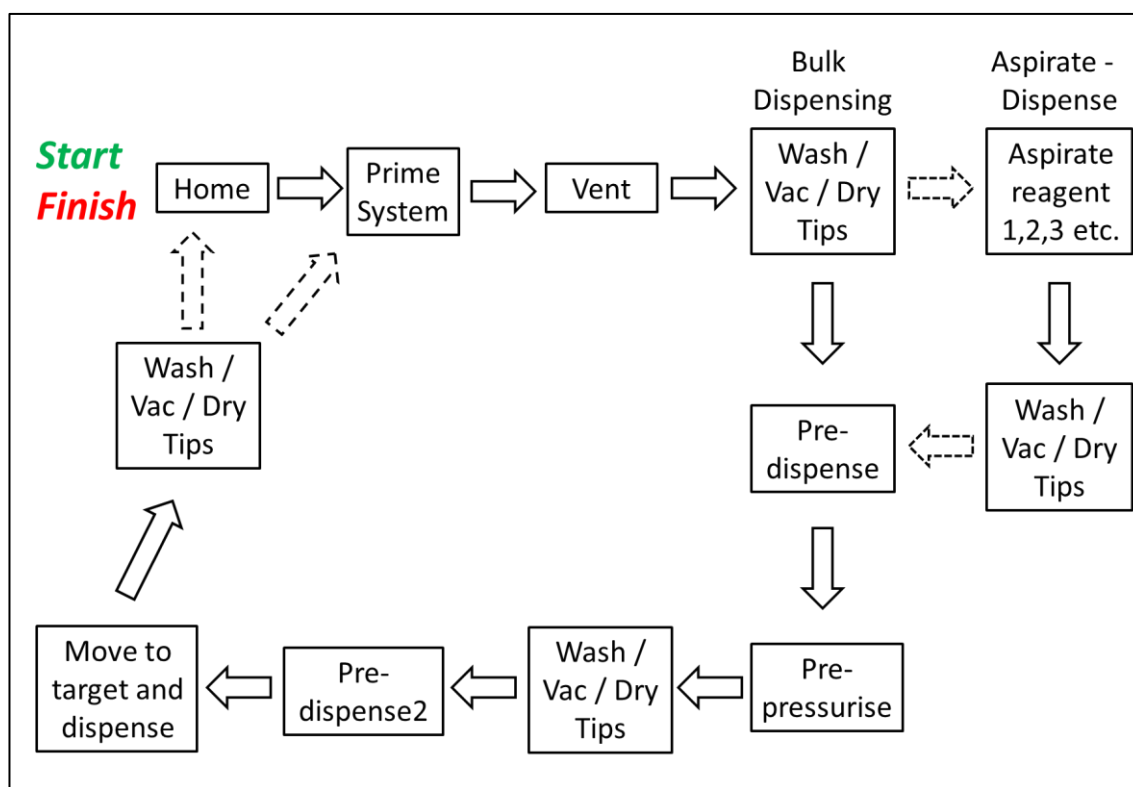


Figure B 4 Step-wise schematic describing a general working protocol for the BioDot aspirate/dispense system, which involves several basic steps in a logic sequence.

Appendix C Assay protocols

C.1 Assay for the detection of BSA

1. Add 250 mM citrate buffer at pH 1.8 to the detection zone and leave the device to dry at room temperature for at least 1 hour.
2. Add 3.3 mM TBPB in 95% ethanol solution into the same detection zone and allow the device to dry at room temperature for at least 1 hour.
3. Add solutions of BSA sample and incubate for 10 minutes at room temperature.
4. Capture photographs of the test.
5. Compare the colour intensity to the calibration curve to determine the concentration of BSA.

C.2 Assay for the detection of glucose

The detection of glucose is based on an enzymatic reaction: the horseradish peroxidase/glucose oxidase reaction, which then produces a product that can be detected.

1. Add the glucose oxidase/peroxidase solution (5:1 ratio and 15 units of protein per ml of solution) to the detection zone and leave the device to dry at room temperature for at least 1 hour.
2. Add solutions of D-glucose sample in DI water in various concentrations and incubate for 10 minutes at room temperature.
3. Capture photographs of the test.
4. Compare the colour intensity to the calibration curve to determine the concentration of glucose.

C.3 Assay for the detection of nitrite

The detection of nitrite is achieved via the Griess reaction, which is the most common colorimetric reaction used for the detection of nitrite, in which nitrite ions react with a primary aromatic amine under acidic conditions forming a diazonium salt which further reacts with an aromatic compound to form a coloured azo dye.

1. Preparation of Griess reagent: dissolving 50 mM sulfanilamide, 330 mM of citric acid and 10 mM of N-(1-naphthyl)-ethylenediamine dihydrochloride in DI water.
2. Add the prepared Griess reagent to the detection zone and allow the device to dry at room temperature for at least 1 hour.
3. Prepare the stock solution of 10 mM sodium nitrite.

4. Dilute the stock sodium nitrite solution in DI water and add onto the device then allow incubating for 10 minutes at room temperature.
5. Capture photographs of the test.
6. Compare the colour intensity to the calibration curve to determine the concentration of nitrite.

C.4 Assay for the detection of TNF- α

The detection of TNF- α is based on a sandwich ELISA.

1. Add capture antibodies onto the device and leave overnight at room temperature for immobilisation.
2. Block any areas of the device that do not have bound capture antibodies by submerging the device in a blocking solution. The blocking solution is 5% BSA in PBS. Incubate for at least 1 hour in room temperature.
3. Add the standard or diluted sample onto the device at the required concentrations. Incubate at room temperature for 1 hour.
4. Wash 3 times for 5 minutes each in 0.05% Tween20 in PBS wash buffer.
5. Add biotinylated detection antibodies on the paper at their working concentration. Incubate at room temperature for 1 hour.
6. Wash again as step 4.
7. Add streptavidin-HRP at working concentration and incubate for 30 minutes in the dark.
8. Wash again as step 4.
9. Add colorimetric substrate TMB to induce a colour change.
10. Capture photographs of the test.
11. Compare the colour intensity to the calibration curve to determine the concentration of TNF α .

C.5 Assay for the detection of CRP

The detection of TNF- α is based on a sandwich ELISA.

1. Add capture antibodies onto the device and leave overnight at room temperature for immobilisation.
2. Block any areas of the device that do not have bound capture antibodies by submerging the device in a blocking solution. The blocking solution is 5% BSA in PBS. Incubate for at least 1 hour at room temperature.
3. Add the standard or diluted sample onto the device at the required concentrations. Incubate at room temperature for 1 hour.

4. Wash 3 times for 5 minutes each in 0.05% Tween20 in PBS wash buffer.
5. Add biotinylated detection antibodies on the paper at their working concentration. Incubate at room temperature for 1 hour.
6. Wash again as step 4.
7. Add streptavidin-HRP at working concentration and incubate for 30 minutes in the dark.
8. Wash again as step 4.
9. Add colorimetric substrate TMB to induce a colour change.
10. Capture photographs of the test.
11. Compare the colour intensity to the calibration curve to determine the concentration of CRP.

Appendix D Publications

D.1 Journal Publications

- P. J. W. He, I. N. Katis, R. W. Eason and C. L. Sones, “Laser direct-write for fabrication of three-dimensional paper-based devices”, *Lab on a Chip*, vol. 16, pp. 3296-3303, 2016.
- P. J. W. He, I. N. Katis, R. W. Eason and C. L. Sones, “Engineering fluidic delays in paper-based devices using laser direct writing”, *Lab on a Chip*, vol. 15, pp. 4054-4061, 2015.
- P. J. W. He, I. N. Katis, R. W. Eason and C. L. Sones, “Laser-based patterning for fluidic devices in nitrocellulose”, *Biomicrofluidics* 9, 026503, 2015.
- C. L. Sones, I. N. Katis, P. J. W. He, B. Mills, M. F. Namiq, P. Shardlow, M. Ibsen and R. W. Eason, “Laser-induced photo-polymerisation for creation of paper-based fluidic devices”, *Lab on a Chip*, vol. 14, pp. 4567-4574, 2014.

D.2 Conference Contributions

- (oral) C. L. Sones, P. J. W. He, I. N. Katis and R. W. Eason, “Flow Control In Laser-patterned Paper-Based Point-of-care (POC) Diagnostic Devices”, Conference on Lasers and Electro-Optics – Pacific Rim, Opto-Electronics and Communications conference, Singapore 31 Jul-4 Aug 2017.
- (oral) I. N. Katis, P. J. W. He, S. Sherwin, B. Keevil, R. W. Eason and C. L. Sones, “Bacterial pathogen detection using laser-structured paper-based diagnostic sensors”, European Materials Research Society Spring Meeting and Exhibit, Strasbourg 22-26 May 2017.
- (oral) C. L. Sones, P. J. W. He, I. N. Katis and R. W. Eason, “Laser Engineering of Three-dimensional Structures in Paper-Based Microfluidic Devices”, European Conference on Lasers and Electro-Optics and the European Quantum Electronics Conference, Munich 25-29 Jun 2017.

Appendix D

- (invited) C. L. Sones, P. J. W. He, I. N. Katis and R. W. Eason, “Laser-based methodologies for point-of-care diagnostics devices on paper”, The 18th International Symposium on Laser Precision Microfabrication (LPM), Toyama, 5-8 Jun 2017.
- (invited) I. N. Katis, P. J. W. He, C. L. Sones and R. W. Eason, “Towards AMR testing using paper-based diagnostic sensors”, SfAM Antimicrobial Resistance Meeting London 24 Nov 2016.
- (invited) R. W. Eason, I. N. Katis, P. J. W. He and C. L. Sones, “Laser-printed fluidic channels for the manufacture of multiplexed paper-based diagnostic sensors”, IOP meeting on Advances in Printed Sensors, London 8 Nov 2016.
- (invited) C. L. Sones, P. J. W. He, I. N. Katis and R. W. Eason, “Laser-direct-write (LDW) fabrication of paper-based diagnostic sensors”, QuantiScientifics workshop, Orange, 10-11 Oct 2016.
- (oral) P. J. W. He, I. N. Katis, R. W. Eason, and C. L. Sones, “Programmable delay in paper-based devices using laser direct writing”, International Conference of Microfluidics, Nanofluidics and Lab-on-a-Chip, Dalian, 10-12 Jun 2016.
- (oral) P. J. W. He, I. N. Katis, R. W. Eason, and C. L. Sones, “Laser direct writing of programmable delays for fabrication of paper-based sensors that allow CRP detection”, Biosensors 2016, Gothenburg, 25-27 May 2016.
- (invited) C. L. Sones, I. N. Katis, P. J. W. He and R. W. Eason, “Laser-direct-write (LDW) methods for fabrication of paper-based medical diagnostic sensors”, BioDot workshop: Lateral Flow: Practicalities of Developing & Manufacturing Quantitative Assays, Zaragoza 10-12 May 2016.
- (poster) P. J. W. He, I. N. Katis, R. W. Eason, and C. L. Sones, “Laser-direct-write technique for rapid prototyping of multiplexed paper-based diagnostic sensors”, Global Engage’s Microfluidics Congress, London 19-20 Oct 2015.
- (poster) P. J. W. He, I. N. Katis, R. W. Eason and C. L. Sones, “Laser engineering of various porous materials for fabrication of paper-based microfluidic devices”,

European Conference on Lasers and Electro-Optics and the European Quantum Electronics Conference, Munich 21-25 Jun 2015.

- (oral) I. N. Katis, P. J. W. He, R. W. Eason and C. L. Sones, “Laser manufacturing for multi-analyte paper-based diagnostic sensors”, European Conference on Lasers and Electro-Optics and the European Quantum Electronics Conference, Munich 21-25 Jun 2015.
- (oral) R. W. Eason, I. N. Katis, P. J. W. He and C. L. Sones, “Laser-polymerised fluidic channels for the manufacture of multiplexed paper-based diagnostic sensors”, PR15 conference Villars, Switzerland 16-19 Jun 2015.
- (oral) P. J. W. He, I. N. Katis, R. W. Eason and C. L. Sones, “Rapid prototyping of microfluidic channels in nitrocellulose using laser-direct-write patterning”, SPIE Photonics West - Microfluidics, BioMEMS, and Medical Microsystems XIII 2015, San Francisco California United States, 7 - 12 Feb 2015.
- (oral) I. N. Katis, P. J. W. He, R. W. Eason and C. L. Sones, “Direct-write laser techniques for the manufacture of multiplexed paper-based diagnostic sensors”, SPIE Photonics West - Microfluidics, BioMEMS, and Medical Microsystems XIII 2015, San Francisco California United States, 7 - 12 Feb 2015.
- (invited) C. L. Sones, I. N. Katis, P. J. W. He and R. W. Eason, “Laser-direct-write methods for fabrication of paper-based medical diagnostic sensors”, Photonics 2014: 12th International Conference on Fiber Optics and Photonics Kharagpur, India 13-16 Dec 2014.
- (invited) C. L. Sones, I. N. Katis, P. J. W. He, B. Mills, A. Mosayyebi, J. Butement, M. Feinäugle, and R. W. Eason, “Laser-based printing and patterning for biological applications” International Workshop on the Fabrication and Application of Microstructured Optical Devices, Yokohama, Japan, 27 - 28 Feb 2014.

D.3 Other Publications

- (invited) C. L. Sones, I. N. Katis, P. J. W. He, B. Mills, M. F. Namiq, P. Shardlow, M. Ibsen and R. W. Eason, “A laser application for paper-based fluidic devices” The Laser User Magazine, Issue 077, pp. 24-26, Summer 2015.

Bibliography

- [1] G. M. Whitesides, "The origins and the future of microfluidics," *Nature*, vol. 442, pp. 368-373, Jul 2006.
- [2] H. Liu and R. M. Crooks, "Paper-Based Electrochemical Sensing Platform with Integral Battery and Electrochromic Read-Out," *Analytical Chemistry*, vol. 84, pp. 2528-2532, Mar 2012.
- [3] G. M. Whitesides, "Cool, or simple and cheap? Why not both?," *Lab on a Chip*, vol. 13, pp. 11-13, 2013.
- [4] A. W. Martinez, S. T. Phillips, M. J. Butte, and G. M. Whitesides, "Patterned paper as a platform for inexpensive, low-volume, portable bioassays," *Angewandte Chemie-International Edition*, vol. 46, pp. 1318-1320, 2007.
- [5] A. W. Martinez, S. T. Phillips, and G. M. Whitesides, "Three-dimensional microfluidic devices fabricated in layered paper and tape," *Proceedings of the National Academy of Sciences of the United States of America*, vol. 105, pp. 19606-19611, Dec 2008.
- [6] A. K. Yetisen, M. S. Akram, and C. R. Lowe, "Paper-based microfluidic point-of-care diagnostic devices," *Lab on a Chip*, vol. 13, pp. 2210-2251, 2013.
- [7] D. Tobjörk and R. Österbacka, "Paper electronics," *Advanced Materials*, vol. 23, pp. 1935-1961, 2011.
- [8] T. H. Nguyen, A. Fraiwan, and S. Choi, "Paper-based batteries: A review," *Biosensors and Bioelectronics*, vol. 54, pp. 640-649, 2014.
- [9] W. K. T. Coltro, D. P. de Jesus, J. A. F. da Silva, C. L. do Lago, and E. Carrilho, "Toner and paper-based fabrication techniques for microfluidic applications," *Electrophoresis*, vol. 31, pp. 2487-2498, 2010.
- [10] D. R. Ballerini, X. Li, and W. Shen, "Patterned paper and alternative materials as substrates for low-cost microfluidic diagnostics," *Microfluidics and Nanofluidics*, vol. 13, pp. 769-787, Nov 2012.
- [11] D. D. Liana, B. Raguse, J. J. Gooding, and E. Chow, "Recent advances in paper-based sensors," *Sensors*, vol. 12, pp. 11505-11526, 2012.

Bibliography

- [12] J. Hu, S. Wang, L. Wang, F. Li, B. Pingguan-Murphy, T. J. Lu, *et al.*, "Advances in paper-based point-of-care diagnostics," *Biosensors and Bioelectronics*, vol. 54, pp. 585-597, 2014.
- [13] W.-J. Zhu, D.-Q. Feng, M. Chen, Z.-D. Chen, R. Zhu, H.-L. Fang *et al.*, "Bienzyme colorimetric detection of glucose with self-calibration based on tree-shaped paper strip," *Sensors and Actuators B: Chemical*, vol. 190, pp. 414-418, 2014.
- [14] D. Sechi, B. Greer, J. Johnson, and N. Hashemi, "Three-Dimensional Paper-Based Microfluidic Device for Assays of Protein and Glucose in Urine," *Analytical Chemistry*, vol. 85, pp. 10733-10737, Nov 2013.
- [15] N. R. Pollock, J. P. Rolland, S. Kumar, P. D. Beattie, S. Jain, F. Noubary, *et al.*, "A paper-based multiplexed transaminase test for low-cost, point-of-care liver function testing," *Science translational medicine*, vol. 4, pp. 152ra129-152ra129, 2012.
- [16] X. Chen, J. Chen, F. Wang, X. Xiang, M. Luo, X. Ji, *et al.*, "Determination of glucose and uric acid with bienzyme colorimetry on microfluidic paper-based analysis devices," *Biosensors and Bioelectronics*, vol. 35, pp. 363-368, 2012.
- [17] K. M. Schilling, A. L. Lepore, J. A. Kurian, and A. W. Martinez, "Fully enclosed microfluidic paper-based analytical devices," *Analytical chemistry*, vol. 84, pp. 1579-1585, 2012.
- [18] M. Zhou, M. Yang, and F. Zhou, "Paper based colorimetric biosensing platform utilizing cross-linked siloxane as probe," *Biosensors and Bioelectronics*, vol. 55, pp. 39-43, 2014.
- [19] S. Bagherbaigi, E. P. C rcoles, and D. H. Wicaksono, "Cotton fabric as an immobilization matrix for low-cost and quick colorimetric enzyme-linked immunosorbent assay (ELISA)," *Analytical Methods*, vol. 6, pp. 7175-7180, 2014.
- [20] L. Guan, R. Cao, J. Tian, H. McLiesh, G. Garnier, and W. Shen, "A preliminary study on the stabilization of blood typing antibodies sorbed into paper," *Cellulose*, vol. 21, pp. 717-727, 2014.
- [21] T. Valta, "Spectrally Tuned Lanthanide Photoluminescence for Point-of-Care Testing," 2015.

- [22] T.-T. Tsai, S.-W. Shen, C.-M. Cheng, and C.-F. Chen, "Paper-based tuberculosis diagnostic devices with colorimetric gold nanoparticles," *Science and technology of advanced materials*, 2016.
- [23] W. Liu, H. Yang, Y. Ding, S. Ge, J. Yu, M. Yan, *et al.*, "Paper-based colorimetric immunosensor for visual detection of carcinoembryonic antigen based on the high peroxidase-like catalytic performance of ZnFe₂O₄-multiwalled carbon nanotubes," *Analyst*, vol. 139, pp. 251-258, 2014.
- [24] L. Ge, S. Wang, J. Yu, N. Li, S. Ge, and M. Yan, "Molecularly Imprinted Polymer Grafted Porous Au-Paper Electrode for an Microfluidic Electro-Analytical Origami Device," *Advanced Functional Materials*, vol. 23, pp. 3115-3123, 2013.
- [25] J. L. Tonkinson and B. A. Stillman, "Nitrocellulose: A tried and true polymer finds utility as a post-genomic substrate," *Frontiers in Bioscience*, vol. 7, pp. C1-C12, Jan 2002.
- [26] K. K. B. Hon, L. Li, and I. M. Hutchings, "Direct writing technology-Advances and developments," *Cirp Annals-Manufacturing Technology*, vol. 57, pp. 601-620, 2008.
- [27] C. B. Arnold and A. Piqu  , "Laser Direct-Write Processing," *MRS Bulletin*, vol. 32, pp. 9-15, 2007.
- [28] G. Kopitkovas, T. Lippert, C. David, A. Wokaun, and J. Gobrecht, "Fabrication of micro-optical elements in quartz by laser induced backside wet etching," *Microelectronic Engineering*, vol. 67-8, pp. 438-444, Jun 2003.
- [29] I. N. Katis, J. A. Holloway, J. Madsen, S. N. Faust, S. D. Garbis, P. J. S. Smith, *et al.*, "Paper-based colorimetric enzyme linked immunosorbent assay fabricated by laser induced forward transfer," *Biomicrofluidics*, vol. 8, p. 9, May 2014.
- [30] J. Bohandy, B. F. Kim, and F. J. Adrian, "METAL-DEPOSITION FROM A SUPPORTED METAL-FILM USING AN EXCIMER LASER," *Journal of Applied Physics*, vol. 60, pp. 1538-1539, Aug 1986.
- [31] E. N. Glezer, M. Milosavljevic, L. Huang, R. J. Finlay, T. H. Her, J. P. Callan, *et al.*, "Three-dimensional optical storage inside transparent materials," *Optics Letters*, vol. 21, pp. 2023-2025, Dec 1996.
- [32] Q. F. Xu, V. R. Almeida, R. R. Panepucci, and M. Lipson, "Experimental demonstration of guiding and confining light in nanometer-size low-refractive-index material," *Optics Letters*, vol. 29, pp. 1626-1628, Jul 2004.

Bibliography

- [33] A. D. Jenkins, P. Kratochvil, R. F. T. Stepto, and U. W. Suter, "Glossary of basic terms in polymer science," *Pure and Applied Chemistry*, vol. 68, pp. 2287-2311, Dec 1996.
- [34] J. V. Crivello and E. Reichmanis, "Photopolymer Materials and Processes for Advanced Technologies," *Chemistry of Materials*, vol. 26, pp. 533-548, Jan 2014.
- [35] R. Phillips, "PHOTOPOLYMERIZATION," *Journal of Photochemistry*, vol. 25, pp. 79-82, 1984.
- [36] J. P. Fouassier and J. Lalevée, "Basic Principles and Applications of Photopolymerization Reactions," in *Photoinitiators for Polymer Synthesis*, ed: Wiley-VCH Verlag GmbH & Co. KGaA, 2012.
- [37] B. Baroli, "Photopolymerization of biomaterials: issues and potentialities in drug delivery, tissue engineering, and cell encapsulation applications," *Journal of Chemical Technology and Biotechnology*, vol. 81, pp. 491-499, Apr 2006.
- [38] J. R. Howell, M. P. Menguc, and R. Siegel, *Thermal radiation heat transfer*: CRC press, 2010.
- [39] P. Yager, T. Edwards, E. Fu, K. Helton, K. Nelson, M. R. Tam, *et al.*, "Microfluidic diagnostic technologies for global public health," *Nature*, vol. 442, pp. 412-418, Jul 2006.
- [40] T. Sakuta, M. Ishihara, K. Miyazawa, M. Tazunoki, H. Iwai, H. Nakamura, *et al.*, "Semiconductor integrated circuit device having a plurality of memory blocks and a lead on chip (LOC) arrangement," ed: Google Patents, 1993.
- [41] K. Sahara, K. Otsuka, and H. Ishida, "Semiconductor device and process for producing the same," ed: Google Patents, 1988.
- [42] F. Lapierre, G. Piret, H. Drobecq, O. Melnyk, Y. Coffinier, V. Thomy, *et al.*, "High sensitive matrix-free mass spectrometry analysis of peptides using silicon nanowires-based digital microfluidic device," *Lab on a Chip*, vol. 11, pp. 1620-1628, 2011.
- [43] A. A. S. Bhagat, P. Jothimuthu, and I. Papautsky, "Photodefinable polydimethylsiloxane (PDMS) for rapid lab-on-a-chip prototyping," *Lab on a Chip*, vol. 7, pp. 1192-1197, 2007.
- [44] G. Comina, A. Suska, and D. Filippini, "PDMS lab-on-a-chip fabrication using 3D printed templates," *Lab on a Chip*, vol. 14, pp. 424-430, 2014.

- [45] Y. Hongbin, Z. Guangya, C. F. Siong, W. Shouhua, and L. Feiwen, "Novel polydimethylsiloxane (PDMS) based microchannel fabrication method for lab-on-a-chip application," *Sensors and Actuators B: Chemical*, vol. 137, pp. 754-761, 2009.
- [46] M. Abdelgawad, C. Wu, W.-Y. Chien, W. R. Geddie, M. A. Jewett, and Y. Sun, "A fast and simple method to fabricate circular microchannels in polydimethylsiloxane (PDMS)," *Lab on a Chip*, vol. 11, pp. 545-551, 2011.
- [47] X. Li, D. R. Ballerini, and W. Shen, "A perspective on paper-based microfluidics: Current status and future trends," *Biomicrofluidics*, vol. 6, p. 13, Mar 2012.
- [48] R. Pelton, "Bioactive paper provides a low-cost platform for diagnostics," *Trends in Analytical Chemistry*, vol. 28, pp. 925-942, Sep 2009.
- [49] S. J. Vella, P. Beattie, R. Cademartiri, A. Laromaine, A. W. Martinez, S. T. Phillips, *et al.*, "Measuring Markers of Liver Function Using a Micropatterned Paper Device Designed for Blood from a Fingertstick," *Analytical Chemistry*, vol. 84, pp. 2883-2891, Mar 2012.
- [50] A. W. Martinez, S. T. Phillips, G. M. Whitesides, and E. Carrilho, "Diagnostics for the Developing World: Microfluidic Paper-Based Analytical Devices," *Analytical Chemistry*, vol. 82, pp. 3-10, Jan 2010.
- [51] A. W. Martinez, S. T. Phillips, E. Carrilho, S. W. Thomas III, H. Sindi, and G. M. Whitesides, "Simple telemedicine for developing regions: camera phones and paper-based microfluidic devices for real-time, off-site diagnosis," *Analytical chemistry*, vol. 80, pp. 3699-3707, 2008.
- [52] E. W. Nery and L. T. Kubota, "Sensing approaches on paper-based devices: a review," *Analytical and Bioanalytical Chemistry*, vol. 405, pp. 7573-7595, Sep 2013.
- [53] K. Abe, K. Suzuki, and D. Citterio, "Inkjet-printed microfluidic multianalyte chemical sensing paper," *Analytical Chemistry*, vol. 80, pp. 6928-6934, Sep 2008.
- [54] T. Songjaroen, W. Dungchai, O. Chailapakul, C. S. Henry, and W. Laiwattanapaisal, "Blood separation on microfluidic paper-based analytical devices," *Lab on a Chip*, vol. 12, pp. 3392-3398, 2012.
- [55] W. Dungchai, O. Chailapakul, and C. S. Henry, "A low-cost, simple, and rapid fabrication method for paper-based microfluidics using wax screen-printing," *Analyst*, vol. 136, pp. 77-82, 2011.

Bibliography

- [56] S. S. Sibbett and G. P. Lopez, "Multiplex lateral flow devices and methods," ed: Google Patents, 2008.
- [57] E. M. Fenton, M. R. Mascarenas, G. P. López, and S. S. Sibbett, "Multiplex lateral-flow test strips fabricated by two-dimensional shaping," *ACS applied materials & interfaces*, vol. 1, pp. 124-129, 2008.
- [58] E. Fu, B. Lutz, P. Kauffman, and P. Yager, "Controlled reagent transport in disposable 2D paper networks," *Lab on a Chip*, vol. 10, pp. 918-920, 2010.
- [59] E. Fu, P. Kauffman, B. Lutz, and P. Yager, "Chemical signal amplification in two-dimensional paper networks," *Sensors and Actuators B: Chemical*, vol. 149, pp. 325-328, 2010.
- [60] A. W. Martinez, S. T. Phillips, M. J. Butte, and G. M. Whitesides, "Patterned paper as a platform for inexpensive, low-volume, portable bioassays," *Angewandte Chemie International Edition*, vol. 46, pp. 1318-1320, 2007.
- [61] A. W. Martinez, S. T. Phillips, B. J. Wiley, M. Gupta, and G. M. Whitesides, "FLASH: a rapid method for prototyping paper-based microfluidic devices," *Lab on a Chip*, vol. 8, pp. 2146-2150, 2008.
- [62] D. A. Bruzewicz, M. Reches, and G. M. Whitesides, "Low-cost printing of poly (dimethylsiloxane) barriers to define microchannels in paper," *Analytical chemistry*, vol. 80, pp. 3387-3392, 2008.
- [63] K. Abe, K. Kotera, K. Suzuki, and D. Citterio, "Inkjet-printed paperfluidic immuno-chemical sensing device," *Analytical and bioanalytical chemistry*, vol. 398, pp. 885-893, 2010.
- [64] Y. Lu, W. Shi, L. Jiang, J. Qin, and B. Lin, "Rapid prototyping of paper-based microfluidics with wax for low-cost, portable bioassay," *Electrophoresis*, vol. 30, pp. 1497-1500, 2009.
- [65] E. Carrilho, A. W. Martinez, and G. M. Whitesides, "Understanding wax printing: a simple micropatterning process for paper-based microfluidics," *Analytical chemistry*, vol. 81, pp. 7091-7095, 2009.
- [66] X. Li, J. Tian, G. Garnier, and W. Shen, "Fabrication of paper-based microfluidic sensors by printing," *Colloids and surfaces B: Biointerfaces*, vol. 76, pp. 564-570, 2010.

- [67] J. Olkkonen, K. Lehtinen, and T. Erho, "Flexographically Printed Fluidic Structures in Paper," *Analytical Chemistry*, vol. 82, pp. 10246-10250, Dec 2010.
- [68] W. Dungchai, O. Chailapakul, and C. S. Henry, "Electrochemical detection for paper-based microfluidics," *Analytical chemistry*, vol. 81, pp. 5821-5826, 2009.
- [69] Z. Nie, F. Deiss, X. Liu, O. Akbulut, and G. M. Whitesides, "Integration of paper-based microfluidic devices with commercial electrochemical readers," *Lab on a Chip*, vol. 10, pp. 3163-3169, 2010.
- [70] S. Ge, L. Ge, M. Yan, X. Song, J. Yu, and J. Huang, "A disposable paper-based electrochemical sensor with an addressable electrode array for cancer screening," *Chemical Communications*, vol. 48, pp. 9397-9399, 2012.
- [71] L. Y. Shiroma, M. Santhiago, A. L. Gobbi, and L. T. Kubota, "Separation and electrochemical detection of paracetamol and 4-aminophenol in a paper-based microfluidic device," *Analytica chimica acta*, vol. 725, pp. 44-50, 2012.
- [72] N. Dossi, R. Toniolo, A. Pizzariello, E. Carrilho, E. Piccin, S. Battiston, *et al.*, "An electrochemical gas sensor based on paper supported room temperature ionic liquids," *Lab on a Chip*, vol. 12, pp. 153-158, 2012.
- [73] W. Zhao, M. M. Ali, S. D. Aguirre, M. A. Brook, and Y. Li, "Paper-based bioassays using gold nanoparticle colorimetric probes," *Analytical chemistry*, vol. 80, pp. 8431-8437, 2008.
- [74] E. Fu, T. Liang, P. Spicar-Mihalic, J. Houghtaling, S. Ramachandran, and P. Yager, "Two-dimensional paper network format that enables simple multistep assays for use in low-resource settings in the context of malaria antigen detection," *Analytical chemistry*, vol. 84, pp. 4574-4579, 2012.
- [75] S. Z. Hossain, R. E. Luckham, A. M. Smith, J. M. Lebert, L. M. Davies, R. H. Pelton, *et al.*, "Development of a bioactive paper sensor for detection of neurotoxins using piezoelectric inkjet printing of sol- gel-derived bioinks," *Analytical chemistry*, vol. 81, pp. 5474-5483, 2009.
- [76] J. C. Jokerst, J. A. Adkins, B. Bisha, M. M. Mentele, L. D. Goodridge, and C. S. Henry, "Development of a paper-based analytical device for colorimetric detection of select foodborne pathogens," *Analytical chemistry*, vol. 84, pp. 2900-2907, 2012.
- [77] A.-l. Zhang and Y. Zha, "Fabrication of paper-based microfluidic device using printed circuit technology," *Aip Advances*, vol. 2, p. 022171, 2012.

Bibliography

- [78] S. Kim, E. Jung, M. J. Kim, A. Pyo, T. Palani, M. S. Eom, *et al.*, "A simple, fast, and easy assay for transition metal-catalyzed coupling reactions using a paper-based colorimetric iodide sensor," *Chemical Communications*, vol. 48, pp. 8751-8753, 2012.
- [79] M. M. Mentele, J. Cunningham, K. Koehler, J. Volckens, and C. S. Henry, "Microfluidic paper-based analytical device for particulate metals," *Analytical chemistry*, vol. 84, pp. 4474-4480, 2012.
- [80] R. F. Carvalhal, M. Simão Kfour, M. H. de Oliveira Piazzetta, A. L. Gobbi, and L. T. Kubota, "Electrochemical detection in a paper-based separation device," *Analytical chemistry*, vol. 82, pp. 1162-1165, 2010.
- [81] M. Ornatska, E. Sharpe, D. Andreescu, and S. Andreescu, "Paper bioassay based on ceria nanoparticles as colorimetric probes," *Analytical chemistry*, vol. 83, pp. 4273-4280, 2011.
- [82] J. Liang, Y. Wang, and B. Liu, "Paper-based fluoroimmunoassay for rapid and sensitive detection of antigen," *RSC Advances*, vol. 2, pp. 3878-3884, 2012.
- [83] E. Carrilho, S. T. Phillips, S. J. Vella, A. W. Martinez, and G. M. Whitesides, "Paper microzone plates," *Analytical chemistry*, vol. 81, pp. 5990-5998, 2009.
- [84] M. M. Ali, S. D. Aguirre, Y. Xu, C. D. Filipe, R. Pelton, and Y. Li, "Detection of DNA using bioactive paper strips," *Chemical Communications*, pp. 6640-6642, 2009.
- [85] P. B. Allen, S. A. Arshad, B. Li, X. Chen, and A. D. Ellington, "DNA circuits as amplifiers for the detection of nucleic acids on a paperfluidic platform," *Lab on a Chip*, vol. 12, pp. 2951-2958, 2012.
- [86] J. Yan, L. Ge, X. Song, M. Yan, S. Ge, and J. Yu, "Paper-Based Electrochemiluminescent 3D Immunodevice for Lab-on-Paper, Specific, and Sensitive Point-of-Care Testing," *Chemistry—A European Journal*, vol. 18, pp. 4938-4945, 2012.
- [87] W. Li, M. Li, S. Ge, M. Yan, J. Huang, and J. Yu, "Battery-triggered ultrasensitive electrochemiluminescence detection on microfluidic paper-based immunodevice based on dual-signal amplification strategy," *Analytica chimica acta*, vol. 767, pp. 66-74, 2013.

- [88] S. Wang, L. Ge, Y. Zhang, X. Song, N. Li, S. Ge, *et al.*, "Battery-triggered microfluidic paper-based multiplex electrochemiluminescence immunodevice based on potential-resolution strategy," *Lab on a Chip*, vol. 12, pp. 4489-4498, 2012.
- [89] L. A. Richards, "Capillary conduction of liquids through porous mediums," *Physics*, vol. 1, pp. 318-333, 1931.
- [90] E. W. Washburn, "The dynamics of capillary flow," *Physical review*, vol. 17, p. 273, 1921.
- [91] R. Peek Jr and D. McLean, "Capillary penetration of fibrous materials," *Industrial & Engineering Chemistry Analytical Edition*, vol. 6, pp. 85-90, 1934.
- [92] E. Fu, S. A. Ramsey, P. Kauffman, B. Lutz, and P. Yager, "Transport in two-dimensional paper networks," *Microfluidics and nanofluidics*, vol. 10, pp. 29-35, 2011.
- [93] S. A. Klasner, A. K. Price, K. W. Hoeman, R. S. Wilson, K. J. Bell, and C. T. Culbertson, "Paper-based microfluidic devices for analysis of clinically relevant analytes present in urine and saliva," *Analytical and Bioanalytical Chemistry*, vol. 397, pp. 1821-1829, Jul 2010.
- [94] X. Li, J. F. Tian, G. Garnier, and W. Shen, "Fabrication of paper-based microfluidic sensors by printing," *Colloids and Surfaces B-Biointerfaces*, vol. 76, pp. 564-570, Apr 2010.
- [95] X. Li, J. F. Tian, and W. Shen, "Progress in patterned paper sizing for fabrication of paper-based microfluidic sensors," *Cellulose*, vol. 17, pp. 649-659, Jun 2010.
- [96] J. L. Delaney, C. F. Hogan, J. F. Tian, and W. Shen, "Electrogenerated Chemiluminescence Detection in Paper-Based Microfluidic Sensors," *Analytical Chemistry*, vol. 83, pp. 1300-1306, Feb 2011.
- [97] Y. Lu, W. W. Shi, L. Jiang, J. H. Qin, and B. C. Lin, "Rapid prototyping of paper-based microfluidics with wax for low-cost, portable bioassay," *Electrophoresis*, vol. 30, pp. 1497-1500, May 2009.
- [98] V. Leung, A. A. M. Shehata, C. D. M. Filipe, and R. Pelton, "Streaming potential sensing in paper-based microfluidic channels," *Colloids and Surfaces a-Physicochemical and Engineering Aspects*, vol. 364, pp. 16-18, Jul 2010.

Bibliography

- [99] D. A. Bruzewicz, M. Reches, and G. M. Whitesides, "Low-cost printing of poly(dimethylsiloxane) barriers to define microchannels in paper," *Analytical Chemistry*, vol. 80, pp. 3387-3392, May 2008.
- [100] E. M. Fenton, M. R. Mascarenas, G. P. Lopez, and S. S. Sibbett, "Multiplex Lateral-Flow Test Strips Fabricated by Two-Dimensional Shaping," *Acs Applied Materials & Interfaces*, vol. 1, pp. 124-129, Jan 2009.
- [101] X. Li, J. F. Tian, T. Nguyen, and W. Shen, "Paper-Based Microfluidic Devices by Plasma Treatment," *Analytical Chemistry*, vol. 80, pp. 9131-9134, Dec 2008.
- [102] C. D. Souza, O. C. Braga, I. C. Vieira, and A. Spinelli, "Electroanalytical determination of sulfadiazine and sulfamethoxazole in pharmaceuticals using a boron-doped diamond electrode," *Sensors and Actuators B-Chemical*, vol. 135, pp. 66-73, Dec 2008.
- [103] E. Fu, P. Kauffman, B. Lutz, and P. Yager, "Chemical signal amplification in two-dimensional paper networks," *Sensors and Actuators B-Chemical*, vol. 149, pp. 325-328, Aug 2010.
- [104] F. Xueen, W. Shasha, and K. Jilie, "Paper-based microfluidics with high resolution, cut on a glass fiber membrane for bioassays," *Lab on a Chip*, vol. 14, pp. 911-915, 7 2014.
- [105] "Rapid Lateral Flow Test Strips: Considerations for Product Development," *Millipore Inc.*, 2006.
- [106] Raphael Wong and H. Tse, "Lateral Flow Immunoassay," *Humana Press*, 2009.
- [107] T. L. Owens, J. Leisen, H. W. Beckham, and V. Breedveld, "Control of Microfluidic Flow in Amphiphilic Fabrics," *Acs Applied Materials & Interfaces*, vol. 3, pp. 3796-3803, Oct 2011.
- [108] M. Reches, K. A. Mirica, R. Dasgupta, M. D. Dickey, M. J. Butte, and G. M. Whitesides, "Thread as a Matrix for Biomedical Assays," *Acs Applied Materials & Interfaces*, vol. 2, pp. 1722-1728, Jun 2010.
- [109] P. Bhandari, T. Narahari, and D. Dendukuri, "'Fab-Chips': a versatile, fabric-based platform for low-cost, rapid and multiplexed diagnostics," *Lab on a Chip*, vol. 11, pp. 2493-2499, 2011.

- [110] X. Li, J. F. Tian, and W. Shen, "Thread as a Versatile Material for Low-Cost Microfluidic Diagnostics," *Acs Applied Materials & Interfaces*, vol. 2, pp. 1-6, Jan 2010.
- [111] D. R. Ballerini, X. Li, and W. Shen, "Flow control concepts for thread-based microfluidic devices," *Biomicrofluidics*, vol. 5, p. 13, Mar 2011.
- [112] A. Nilghaz, D. H. B. Wicaksono, D. Gustiono, F. A. A. Majid, E. Supriyanto, and M. R. A. Kadir, "Flexible microfluidic cloth-based analytical devices using a low-cost wax patterning technique," *Lab on a Chip*, vol. 12, pp. 209-218, 2012.
- [113] Y. R. Wang, J. M. Zheng, G. Y. Ren, P. H. Zhang, and C. Xu, "A flexible piezoelectric force sensor based on PVDF fabrics," *Smart Materials & Structures*, vol. 20, p. 7, Apr 2011.
- [114] F. Xia, Y. K. Wang, H. Li, C. Huang, Y. Ma, Q. M. Zhang, *et al.*, "Influence of the annealing conditions on the polarization and electromechanical response of high-energy-electron-irradiated poly(vinylidene fluoride trifluoroethylene) copolymer," *Journal of Polymer Science Part B: Polymer Physics*, vol. 41, pp. 797-806, 2003.
- [115] A. V. Shirinov and W. K. Schomburg, "Pressure sensor from a PVDF film," *Sensors and Actuators a-Physical*, vol. 142, pp. 48-55, Mar 2008.
- [116] J. Zheng, C. Xu, and T. Hirai, "Electromechanical nonionic gels," *New Journal of Physics*, vol. 10, p. 9, Feb 2008.
- [117] J. Wang, C. Y. Xu, M. Taya, and Y. Kuga, "Mechanical stability optimization of Flemion-based composite artificial muscles by use of proper solvent," *Journal of Materials Research*, vol. 21, pp. 2018-2022, Aug 2006.
- [118] H. Noh and S. T. Phillips, "Fluidic Timers for Time-Dependent, Point-of-Care Assays on Paper," *Analytical Chemistry*, vol. 82, pp. 8071-8078, Oct 2010.
- [119] H. Noh and S. T. Phillips, "Metering the capillary-driven flow of fluids in paper-based microfluidic devices," *Analytical chemistry*, vol. 82, pp. 4181-7, 2010 May 2010.
- [120] H. Chen, J. Cogswell, C. Anagnostopoulos, and M. Faghri, "A fluidic diode, valves, and a sequential-loading circuit fabricated on layered paper," *Lab on a Chip*, vol. 12, pp. 2909-2913, 2012.

Bibliography

- [121] A. W. Martinez, S. T. Phillips, Z. H. Nie, C. M. Cheng, E. Carrilho, B. J. Wiley, *et al.*, "Programmable diagnostic devices made from paper and tape," *Lab on a Chip*, vol. 10, pp. 2499-2504, 2010.
- [122] N. K. Thom, K. Yeung, M. B. Pillion, and S. T. Phillips, "'Fluidic batteries' as low-cost sources of power in paper-based microfluidic devices," *Lab on a Chip*, vol. 12, pp. 1768-1770, 2012.
- [123] K. Yeung, K. M. Schmid, and S. T. Phillips, "A thermally-stable enzyme detection assay that amplifies signal autonomously in water without assistance from biological reagents," *Chemical Communications*, vol. 49, pp. 394-396, 2013.
- [124] J. L. Osborn, B. Lutz, E. Fu, P. Kauffman, D. Y. Stevens, and P. Yager, "Microfluidics without pumps: reinventing the T-sensor and H-filter in paper networks," *Lab on a Chip*, vol. 10, pp. 2659-2665, 2010.
- [125] E. L. Fu, S. Ramsey, P. Kauffman, B. Lutz, and P. Yager, "Transport in two-dimensional paper networks," *Microfluidics and Nanofluidics*, vol. 10, pp. 29-35, Jan 2011.
- [126] A. Apilux, Y. Ukita, M. Chikae, O. Chailapakul, and Y. Takamura, "Development of automated paper-based devices for sequential multistep sandwich enzyme-linked immunosorbent assays using inkjet printing," *Lab on a Chip*, vol. 13, pp. 126-135, 2013.
- [127] B. Lutz, T. Liang, E. Fu, S. Ramachandran, P. Kauffman, and P. Yager, "Dissolvable fluidic time delays for programming multi-step assays in instrument-free paper diagnostics," *Lab on a Chip*, vol. 13, pp. 2840-2847, 2013.
- [128] D. L. Giokas, G. Z. Tsogas, and A. G. Vlessidis, "Programming Fluid Transport in Paper-Based Microfluidic Devices Using Razor-Crafted Open Channels," *Analytical Chemistry*, vol. 86, pp. 6202-6207, Jul 2014.
- [129] A. C. Siegel, S. T. Phillips, M. D. Dickey, N. S. Lu, Z. G. Suo, and G. M. Whitesides, "Foldable Printed Circuit Boards on Paper Substrates," *Advanced Functional Materials*, vol. 20, pp. 28-35, Jan 2010.
- [130] N. Hashemi, J. S. Erickson, J. P. Golden, and F. S. Ligler, "Optofluidic characterization of marine algae using a microflow cytometer," *Biomicrofluidics*, vol. 5, p. 9, Sep 2011.

- [131] N. Hashemi, J. S. Erickson, J. P. Golden, K. M. Jackson, and F. S. Ligler, "Microflow Cytometer for optical analysis of phytoplankton," *Biosensors & Bioelectronics*, vol. 26, pp. 4263-4269, Jul 2011.
- [132] H. Liu and R. M. Crooks, "Three-Dimensional Paper Microfluidic Devices Assembled Using the Principles of Origami," *Journal of the American Chemical Society*, vol. 133, pp. 17564-17566, Nov 2011.
- [133] L. Ge, J. X. Yan, X. R. Song, M. Yan, S. G. Ge, and J. H. Yu, "Three-dimensional paper-based electrochemiluminescence immunodevice for multiplexed measurement of biomarkers and point-of-care testing," *Biomaterials*, vol. 33, pp. 1024-1031, Feb 2012.
- [134] G. G. Lewis, M. J. DiTucci, M. S. Baker, and S. T. Phillips, "High throughput method for prototyping three-dimensional, paper-based microfluidic devices," *Lab on a Chip*, vol. 12, pp. 2630-2633, 2012.
- [135] H. Liu, Y. Xiang, Y. Lu, and R. M. Crooks, "Aptamer-Based Origami Paper Analytical Device for Electrochemical Detection of Adenosine," *Angewandte Chemie-International Edition*, vol. 51, pp. 6925-6928, 2012.
- [136] C. Renault, J. Koehne, A. J. Ricco, and R. M. Crooks, "Three-Dimensional Wax Patterning of Paper Fluidic Devices," *Langmuir*, vol. 30, pp. 7030-7036, Jun 2014.
- [137] N. R. Pollock, J. P. Rolland, S. Kumar, P. D. Beattie, S. Jain, F. Noubary, *et al.*, "A Paper-Based Multiplexed Transaminase Test for Low-Cost, Point-of-Care Liver Function Testing," *Science Translational Medicine*, vol. 4, p. 10, Sep 2012.
- [138] A. V. Govindarajan, S. Ramachandran, G. D. Vigil, P. Yager, and K. F. Bohringer, "A low cost point-of-care viscous sample preparation device for molecular diagnosis in the developing world; an example of microfluidic origami," *Lab on a Chip*, vol. 12, pp. 174-181, 2012.
- [139] E. da Silva, M. Santhiago, F. R. de Souza, W. K. T. Coltro, and L. T. Kubota, "Triboelectric effect as a new strategy for sealing and controlling the flow in paper-based devices," *Lab on a Chip*, vol. 15, pp. 1651-1655, 2015.
- [140] R. L. F. S.-c. f. p. development, "Rapid Lateral Flow Test Strips - considerations for product development," *Millipore Corporation, Billerica, MA*, pp. 9-10.

Bibliography

- [141] C. L. Sones, I. N. Katis, P. J. W. He, B. Mills, M. F. Namiq, P. Shardlow, *et al.*, "Laser-induced photo-polymerisation for creation of paper-based fluidic devices," *Lab on a Chip*, vol. 14, pp. 4567-4574, 2014.
- [142] P. J. W. He, I. N. Katis, R. W. Eason, and C. L. Sones, "Laser-based patterning for fluidic devices in nitrocellulose," *Biomicrofluidics*, vol. 9, p. 10, Mar 2015.
- [143] B. Lutz, T. Liang, E. Fu, S. Ramachandran, P. Kauffman, and P. Yager, *MicroTAS*, pp. Okinawa, Japan, 2012.
- [144] G. I. Salentijn, N. N. Hamidon, and E. Verpoorte, "Solvent-dependent on/off valving using selectively permeable barriers in paper microfluidics," *Lab on a Chip*, 2016.
- [145] A. H. Free, E. C. Adams, M. L. Kercher, H. M. Free, and M. H. Cook, "Simple specific test for urine glucose," *Clinical chemistry*, vol. 3, pp. 163-8, 1957 1957.
- [146] J. C. Sternberg, "RATE NEPHELOMETER FOR MEASURING SPECIFIC PROTEINS BY IMMUNOPRECIPITIN REACTIONS," *Clinical Chemistry*, vol. 23, pp. 1456-1464, 1977.
- [147] S. A. Berson and R. S. Yalow, "Species-specificity of human anti-beef, pork insulin serum," *Jour Clin Invest*, vol. 38, pp. 2017-2025, 1959.
- [148] R. Hawkes, E. Niday, and J. Gordon, "A DOT-IMMUNOBINDING ASSAY FOR MONOCLONAL AND OTHER ANTIBODIES," *Analytical Biochemistry*, vol. 119, pp. 142-147, 1982.
- [149] J. L. Vaitukaitis, "Development of the home pregnancy test," in *Understanding and Optimizing Human Development:: From Cells to Patients to Populations*. vol. 1038, S. G. Kaler and O. M. Rennert, Eds., ed New York: New York Acad Sciences, 2004, pp. 220-222.
- [150] Vaitukai.Jl, G. T. Ross, and Braunste.Gd, "RADIOIMMUNOASSAY WHICH SPECIFICALLY MEASURES HUMAN CHORIONIC GONADOTROPIN IN PRESENCE OF HUMAN LUTEINIZING-HORMONE," *American Journal of Obstetrics and Gynecology*, vol. 113, pp. 751-&, 1972.
- [151] M. Funes-Huacca, A. Wu, E. Szepesvari, P. Rajendran, N. Kwan-Wong, A. Razgulin, *et al.*, "Portable self-contained cultures for phage and bacteria made of paper and tape," *Lab on a Chip*, vol. 12, pp. 4269-4278, 2012.
- [152] S. M. Z. Hossain, R. E. Luckham, A. M. Smith, J. M. Lebert, L. M. Davies, R. H. Pelton, *et al.*, "Development of a Bioactive Paper Sensor for Detection of Neurotoxins Using

- Piezoelectric Inkjet Printing of Sol-Gel-Derived Bioinks," *Analytical Chemistry*, vol. 81, pp. 5474-5483, Jul 2009.
- [153] S. M. Z. Hossain, R. E. Luckham, M. J. McFadden, and J. D. Brennan, "Reagentless Bidirectional Lateral Flow Bioactive Paper Sensors for Detection of Pesticides in Beverage and Food Samples," *Analytical Chemistry*, vol. 81, pp. 9055-9064, Nov 2009.
- [154] Z. H. Nie, C. A. Nijhuis, J. L. Gong, X. Chen, A. Kumachev, A. W. Martinez, *et al.*, "Electrochemical sensing in paper-based microfluidic devices," *Lab on a Chip*, vol. 10, pp. 477-483, 2010.
- [155] J. J. Shi, F. Tang, H. L. Xing, H. X. Zheng, L. H. Bi, and W. Wang, "Electrochemical Detection of Pb and Cd in Paper-Based Microfluidic Devices," *Journal of the Brazilian Chemical Society*, vol. 23, pp. 1124-1130, Jun 2012.
- [156] T. Eaidkong, R. Mungkarndee, C. Phollookin, G. Tumcharern, M. Sukwattanasinitt, and S. Wacharasindhu, "Polydiacetylene paper-based colorimetric sensor array for vapor phase detection and identification of volatile organic compounds," *Journal of Materials Chemistry*, vol. 22, pp. 5970-5977, 2012.
- [157] S. M. Z. Hossain and J. D. Brennan, "beta-Galactosidase-Based Colorimetric Paper Sensor for Determination of Heavy Metals," *Analytical Chemistry*, vol. 83, pp. 8772-8778, Nov 2011.
- [158] S. G. Ge, L. Ge, M. Yan, X. R. Song, J. H. Yu, and J. D. Huang, "A disposable paper-based electrochemical sensor with an addressable electrode array for cancer screening," *Chemical Communications*, vol. 48, pp. 9397-9399, 2012.
- [159] E. Fu, T. Liang, J. Houghtaling, S. Ramachandran, S. A. Ramsey, B. Lutz, *et al.*, "Enhanced Sensitivity of Lateral Flow Tests Using a Two-Dimensional Paper Network Format," *Analytical Chemistry*, vol. 83, pp. 7941-7946, Oct 2011.
- [160] C. Z. Li, K. Vandenberg, S. Prabhulkar, X. N. Zhu, L. Schneper, K. Methee, *et al.*, "Paper based point-of-care testing disc for multiplex whole cell bacteria analysis," *Biosensors & Bioelectronics*, vol. 26, pp. 4342-4348, Jul 2011.
- [161] M. Zhang, L. Ge, S. G. Ge, M. Yan, J. H. Yu, J. D. Huang, *et al.*, "Three-dimensional paper-based electrochemiluminescence device for simultaneous detection of Pb²⁺ and Hg²⁺ based on potential-control technique," *Biosensors & Bioelectronics*, vol. 41, pp. 544-550, Mar 2013.

Bibliography

- [162] J. H. Yu, L. Ge, J. D. Huang, S. M. Wang, and S. G. Ge, "Microfluidic paper-based chemiluminescence biosensor for simultaneous determination of glucose and uric acid," *Lab on a Chip*, vol. 11, pp. 1286-1291, 2011.
- [163] J. H. Yu, S. M. Wang, L. Ge, and S. G. Ge, "A novel chemiluminescence paper microfluidic biosensor based on enzymatic reaction for uric acid determination," *Biosensors & Bioelectronics*, vol. 26, pp. 3284-3289, Mar 2011.
- [164] M. M. Ali, S. D. Aguirre, Y. Q. Xu, C. D. M. Filipe, R. Pelton, and Y. F. Li, "Detection of DNA using bioactive paper strips," *Chemical Communications*, pp. 6640-6642, 2009.
- [165] P. B. Allen, S. A. Arshad, B. L. Li, X. Chen, and A. D. Ellington, "DNA circuits as amplifiers for the detection of nucleic acids on a paperfluidic platform," *Lab on a Chip*, vol. 12, pp. 2951-2958, 2012.
- [166] A. Apilux, W. Dungchai, W. Siangproh, N. Praphairaksit, C. S. Henry, and O. Chailapakul, "Lab-on-Paper with Dual Electrochemical/Colorimetric Detection for Simultaneous Determination of Gold and Iron," *Analytical Chemistry*, vol. 82, pp. 1727-1732, Mar 2010.
- [167] T. T. Ngo and H. M. Lenhoff, "ENZYMES AS VERSATILE LABELS AND SIGNAL AMPLIFIERS FOR MONITORING IMMUNOCHEMICAL REACTIONS," *Molecular and Cellular Biochemistry*, vol. 44, pp. 3-12, 1982.
- [168] E. Engvall and P. Perlmann, "Enzyme-linked immunosorbent assay (ELISA) quantitative assay of immunoglobulin G," *Immunochemistry*, vol. 8, pp. 871-874, 1971.
- [169] S. Paulie and H. Perlmann, "Enzyme-Linked Immunosorbent Assay," *eLS*, 2003.
- [170] G. R. Pape, M. Troye, B. Axelsson, and P. Perlmann, "SIMULTANEOUS OCCURRENCE OF IMMUNOGLOBULIN-DEPENDENT AND IMMUNOGLOBULIN-INDEPENDENT MECHANISMS IN NATURAL CYTOTOXICITY OF HUMAN-LYMPHOCYTES," *Journal of Immunology*, vol. 122, pp. 2251-2260, 1979.
- [171] P. Perlmann, K. Berzins, H. Perlmann, M. Troyeblomberg, M. Wahlgren, and B. Wahlin, "MALARIA VACCINES - IMMUNOGEN SELECTION AND EPITOPE MAPPING," *Vaccine*, vol. 6, pp. 183-187, Apr 1988.
- [172] Ljungstr.I, E. Engvall, and Ruitenbe.Ej, "ELISA, ENZYME LINKED IMMUNOSORBENT ASSAY - NEW TECHNIQUE FOR SERO-DIAGNOSIS OF TRICHINOSIS," *Parasitology*, vol. 69, pp. R24-R24, 1974.

- [173] M. Seppala, E. M. Rutanen, M. Heikinheimo, H. Jalanko, and E. Engvall, "DETECTION OF TROPHOBLASTIC TUMOR ACTIVITY BY PREGNANCY-SPECIFIC BETA-1-GLYCOPROTEIN," *International Journal of Cancer*, vol. 21, pp. 265-267, 1978.
- [174] P. Sipponen, E. Ruoslahti, M. Vuento, E. Engvall, U. Stenman, T. Ihamaki, *et al.*, "CEA AND CEA-LIKE ACTIVITY IN GASTRIC CANCER," *Acta Hepato-Gastroenterologica*, vol. 23, pp. 276-279, 1976.
- [175] O. Stephan, N. Weisz, S. Vieths, T. Weiser, B. Rabe, and W. Vatterott, "Protein quantification, sandwich ELISA, and real-time PCR used to monitor industrial cleaning procedures for contamination with peanut and celery allergens," *Journal of Aoac International*, vol. 87, pp. 1448-1457, Nov-Dec 2004.
- [176] O. Stephan and S. Vieths, "Development of a real-time PCR and a sandwich ELISA for detection of potentially allergenic trace amounts of peanut (*Arachis hypogaea*) in processed foods," *Journal of Agricultural and Food Chemistry*, vol. 52, pp. 3754-3760, Jun 2004.
- [177] R. Meyer, F. Chardonens, P. Hubner, and J. Luthy, "Polymerase chain reaction (PCR) in the quality and safety assurance of food: Detection of soya in processed meat products," *Zeitschrift Fur Lebensmittel-Untersuchung Und-Forschung*, vol. 203, pp. 339-344, 1996.
- [178] A. J. van Hengel, "Food allergen detection methods and the challenge to protect food-allergic consumers," *Analytical and Bioanalytical Chemistry*, vol. 389, pp. 111-118, Sep 2007.
- [179] O. S. Frankfurt and A. Krishan, "Enzyme-linked immunosorbent assay (ELISA) for the specific detection of apoptotic cells and its application to rapid drug screening," *Journal of Immunological Methods*, vol. 253, pp. 133-144, Jul 2001.
- [180] N. F. Carter, C. J. Hammond, M. J. Green, P. I. Hilditch, and S. C. Williams, "Disposable, for ELISA; pollution control for food, drink and drugs," ed: Google Patents, 1992.
- [181] M. Ashby and J. Rine, "Methods for drug screening," ed: Google Patents, 1996.
- [182] C. M. Cheng, A. W. Martinez, J. L. Gong, C. R. Mace, S. T. Phillips, E. Carrilho, *et al.*, "Paper-Based ELISA," *Angewandte Chemie-International Edition*, vol. 49, pp. 4771-4774, 2010.

Bibliography

- [183] C. K. Hsu, H. Y. Huang, W. R. Chen, W. Nishie, H. Ujiie, K. Natsuga, *et al.*, "Paper-Based ELISA for the Detection of Autoimmune Antibodies in Body Fluid-The Case of Bullous Pemphigoid," *Analytical Chemistry*, vol. 86, pp. 4605-4610, May 2014.
- [184] C. M. Cheng, A. W. Martinez, J. Gong, C. R. Mace, S. T. Phillips, E. Carrilho, *et al.*, "Paper-Based ELISA," *Angewandte Chemie International Edition*, vol. 49, pp. 4771-4774, 2010.
- [185] D. MacDougall and W. B. Crummett, "Guidelines for data acquisition and data quality evaluation in environmental chemistry," *Analytical Chemistry*, vol. 52, pp. 2242-2249, 1980/12/01 1980.
- [186] I. H. T. Guideline, "Validation of analytical procedures: text and methodology," *Q2 (R1)*, vol. 1, 2005.
- [187] D. A. Armbruster and T. Pry, "Limit of blank, limit of detection and limit of quantitation," *Clin Biochem Rev*, vol. 29, pp. S49-52, 2008.
- [188] I. Guevara, J. Iwanejko, A. Dembińska-Kieć, J. Pankiewicz, A. Wanat, P. Anna, *et al.*, "Determination of nitrite/nitrate in human biological material by the simple Griess reaction," *Clinica Chimica Acta*, vol. 274, pp. 177-188, 1998.
- [189] M. J. Pugia, J. A. Lott, J. A. Profitt, and T. K. Cast, "High-sensitivity dye binding assay for albumin in urine," *Journal of Clinical Laboratory Analysis*, vol. 13, pp. 180-187, 1999.
- [190] J. D. Peele, R. H. Gadsden, and R. Crews, "SEMIAUTOMATED VS VISUAL READING OF URINALYSIS DIPSTICKS," *Clinical Chemistry*, vol. 23, pp. 2242-2246, 1977.
- [191] P. Libby, P. M. Ridker, and A. Maseri, "Inflammation and atherosclerosis," *Circulation*, vol. 105, pp. 1135-1143, 2002.
- [192] C. Fernandez-Sanchez, C. J. McNeil, K. Rawson, O. Nilsson, H. Y. Leung, and V. Gnanapragasam, "One-step immunostrip test for the simultaneous detection of free and total prostate specific antigen in serum," *Journal of Immunological Methods*, vol. 307, pp. 1-12, Dec 2005.
- [193] V. Gubala, L. F. Harris, A. J. Ricco, M. X. Tan, and D. E. Williams, "Point of Care Diagnostics: Status and Future," *Analytical Chemistry*, vol. 84, pp. 487-515, Jan 2012.

- [194] X. Mao, Y. Q. Ma, A. G. Zhang, L. R. Zhang, L. W. Zeng, and G. D. Liu, "Disposable Nucleic Acid Biosensors Based on Gold Nanoparticle Probes and Lateral Flow Strip," *Analytical Chemistry*, vol. 81, pp. 1660-1668, Feb 2009.
- [195] N. M. Green, "Avidin," *Advances in protein chemistry*, vol. 29, pp. 85-133, 1975.
- [196] "AD Systems Reference Manual," *BioDot, Inc.*, Part number 0005-0052, 2008.



Cite this: *Lab Chip*, 2014, **14**, 4567

Laser-induced photo-polymerisation for creation of paper-based fluidic devices

C. L. Sones,* I. N. Katis, P. J. W. He, B. Mills, M. F. Namiq, P. Shardlow, M. Ibsen and R. W. Eason

Paper-based microfluidics is a rapidly progressing inter-disciplinary technology driven by the need for low-cost alternatives to conventional point-of-care diagnostic tools. For transport of reagents/analytes, such devices often consist of interconnected hydrophilic fluid-flow channels that are demarcated by hydrophobic barrier walls that extend through the thickness of the paper. Here, we present a laser-based fabrication procedure that uses polymerisation of a photopolymer to produce the required fluidic channels in paper. Experimental results showed that the structures successfully guide the flow of fluids and allow containment of fluids in wells, and hence the technique is suitable for fabrication of paper-based microfluidic devices. The minimum width for the hydrophobic barriers that successfully prevented fluid leakage was $\sim 120\ \mu\text{m}$ and the minimum width for the fluidic channels that can be formed was $\sim 80\ \mu\text{m}$, the smallest reported so far for paper-based fluidic patterns.

Received 21st July 2014,
 Accepted 29th September 2014

DOI: 10.1039/c4lc00850b

www.rsc.org/loc

1. Introduction

Point-of-care (POC) testing plays a vital role for early stage non-invasive clinical detection and diagnosis. One of the principal reasons for its widespread uptake is because it provides an effective and rapid *modus-operandi* that either excludes or minimises unnecessary delay by providing a prompt exchange of vital information between the clinical care team and the patient undergoing tests. This is achieved through diagnostic testing conducted at the POC – at a patient's bedside, either in the comfort of their home, at their general practitioner's clinic, or in a hospital emergency unit.

Such POC testing is facilitated through the use of uncomplicated, user-friendly and portable testing devices and much effort has been directed towards producing diagnostic test-kits that are not only smaller, faster and smarter, but also satisfy the elusive goal of being cost-effective – a vital requirement that ensures economic viability, since such POC test procedures may need to be performed repeatedly over potentially very large sample groups, that could even extend to an entire nation in the case of a pandemic.

It has been recognised that microfluidic-based lab-on-chip (LOC) technology has considerable potential, and hence sustained efforts have been directed towards developing LOC-type fluidic systems for medical diagnostic devices.¹ The prime reason for this enthusiasm lies in the obvious advantages presented by these compact LOC devices such as the use of smaller reagent volumes, faster reaction times and

portability arising from the device sizes, as well as ease of manufacture and distribution.

Compact LOC devices have primarily been developed on platform substrates such as silicon and glass, using cleanroom-based fabrication processes adapted from the semiconductor processing industry. In an attempt to further reduce the manufacturing costs, a low-cost polymer, polydimethylsiloxane (PDMS), which can be used in a rapid prototyping environment, was considered as a better choice for implementation of microfluidic-based LOC devices. This material still presents certain limitations and comparatively high fabrication costs however, which has led to a subsequent search for other alternatives, which now include paper, and thread.²

In particular, paper, with its varied characteristics, is now considered as a highly suitable alternative for fabrication of LOC-type devices, and many labs have focused their attention in this direction.^{3–5} Of particular importance is the relatively low-tech nature of paper, which has almost all of the attributes that would help realise low-cost POC diagnostic tests, particularly in the context of poorly resourced locations and environments that exist today within developing countries.

2. Paper for POC diagnostics

As a substrate material, paper is inexpensive, abundantly available in a range of different engineered forms and properties, can be stored and easily transported, modified in terms of its liquid transport properties, and can be readily disposed of after use *via* incineration. Additionally, paper-based fabrication procedures can be intrinsically cheap, and

Optoelectronics Research Centre, University of Southampton, Highfield, Southampton, UK SO17 1BJ. E-mail: cls@orc.soton.ac.uk; Tel: +44(0) 2380 597719

paper as a platform technology is mature and well-established, lending itself to routine low-cost volume production procedures. Finally, delivery of paper-based items is routinely available to everyone world-wide that has access to a postal service.

Paper is currently used for analytical and clinical chemistry, and chromatographic tests are routinely performed in commercial analytical laboratories for the detection of different chemical species. Two of the most commonly known paper-based chromatographic clinical tests are the pregnancy test and the lateral flow-based urine dipsticks that can simultaneously detect sugar, pH, ketone *etc.*^{6–10} However, clinical tests that can yield quantitative information of a multiplexed nature (*i.e.* can perform a series of parallel tests) using a single test strip are clearly the way forward, and recent reports of microfluidic paper-based analytical devices (μ PADs) suggest that these may be the ideal platform for performing such tests.¹¹

As their name suggests, paper-based microfluidic devices have either a single or multiple flow channels that are designed to guide and transport an analyte fluid, from a point of entry on the device to a reaction zone that has been pre-treated with specific reagents. Unlike glass, silicon or polymer substrates, where the fluidic channels are surface-relief structures that have been inscribed in these substrates, for paper-based devices the fluidic channels are formed inside and extend throughout the full thickness of the paper. The walls that are required to delineate the separate fluidic channels to contain and guide the flow of liquids have been successfully demonstrated using hydrophobic materials such as SU8, PDMS, polystyrene (PS), alkyl ketene dimer (AKD) and wax.³

The earliest approach presented by the Whitesides' group,¹² relied on a cleanroom-based lithographic technique that involved exposure of a UV-sensitive polymer (SU8) impregnated in a paper, through a custom-designed mask, to cross-link it and form the required barriers for the intended fluidic channels. In order to reduce the costs associated with such a conventional lithographic procedure, a subsequent approach they presented involved the use of a modified desktop plotter that dispensed an ink composed of the low-cost elastomeric polymer PDMS.¹³ Several other groups have also proposed and demonstrated the usefulness of other paper-patterning approaches such as inkjet printer-based etching of paper impregnated with PS,¹⁴ plasma-treatment through a metal mask of a paper impregnated with hydrophobic AKD,¹⁵ paper-cutting using a computer-controlled X–Y knife plotter,¹⁶ printing of wax,^{17,18} inkjet-printing,^{19,20} flexographic printing,²¹ wax-screen printing,²² and laser-ablative treatment of a paper with a hydrophobic coating.²³

Each of these procedures has its own advantages, as well as some characteristic drawbacks. Techniques such as UV-lithography and plasma-treatment require the use of expensive and fixed-pattern masks as well as dedicated equipment and controlled conditions in labs. The knife-plotting technique requires specialised or custom-modified patterning equipment whereas other techniques sometimes require undesirable post-processing procedures. Another important

issue is the limitation on achievable feature size resulting from the lateral spreading of the hydrophobic material (for example with wax printing), and finally the need for specialised chemicals or inks (for ink-jet printing) or the use of harsh chemical etchants.

In this work, we present the use of a laser-based procedure to create the fluidic patterns in a paper substrate that has been previously impregnated with a hydrophobic material. This laser-based direct-write (LDW) approach is non-contact in nature, and this is advantageous when fabricating such biological or biomedical devices as this helps avoid cross-contamination that can arise from contact of the deposition tool with the substrate. It is also a mask-less, non-lithographic procedure, and hence is ideally suited for use in the preliminary trial fabrication stage as well as final device and mass-production stages. As with any laser-based procedure, the technique also offers the possibility to control the patterning process through choice of the laser parameters such as wavelength, pulse duration and repetition rate. More importantly, if desired, it is routinely possible to reduce the dimensions of the patterned features down to a value of 50 μm , or even below, and our current results show that fluidic channels with barrier wall width as small as $\sim 100\ \mu\text{m}$ can be fabricated. Finally, this LDW process can also be scaled up for mass-production, possibly on a roll-to-roll scale. After initial set-up costs required for the laser and other equipment required for pattern definition, production costs for individual tests could be acceptably low.

3. Experiments and results

3a. Outline of experimental procedure

As described earlier, the inscription of the fluidic patterns in paper is achieved *via* a LDW procedure that uses the principle of light-induced photo-polymerisation, where the laser beam is scanned over the paper, and/or the paper is moved beneath the laser spot. Before this patterning step, the paper is briefly soaked in the light-sensitive polymer which has been diluted in an appropriate solvent (isopropanol), and then left to dry under ambient laboratory conditions.

The schematic of the experimental setup employed for this LDW procedure is shown in Fig. 1, where the UV laser beam is directed towards the polymer-impregnated paper which was mounted on a xyz-translational stage. A cylindrical lens (either $f = 36\ \text{mm}$, or $f = 25\ \text{mm}$) focused the laser beam onto the paper surface, and translation in the two planes (x and y) perpendicular to the propagation direction of the incident laser beam allowed inscription of (2D) user-defined patterns on the paper surface. Translation along the third (z) axis of the stages was used to ensure optimum positioning with respect to the focal plane of the lens.

Laser illumination of the impregnated paper induces polymerisation only within the exposed regions through initiation of light-induced cross-linking of the polymer. By varying the exposure parameters of laser energy density (for pulsed laser sources), or laser power (for continuous wave (c. w.) lasers),

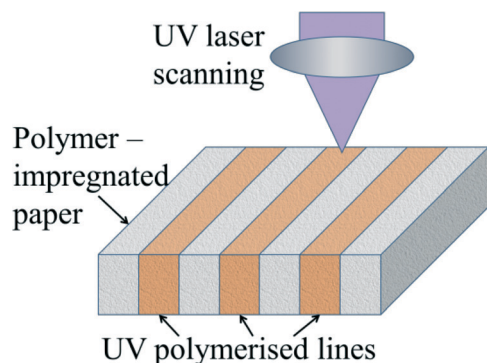


Fig. 1 Schematic showing the laser-patterning of fluidic channels throughout the entire thickness of the paper.

and speed of translation of the paper, the extent of this local polymerisation can be precisely controlled. These parameters clearly play a crucial role in determining both the widths and depths of the regions polymerised, and through variations in the incident laser exposure it is possible to produce polymerised structures that extend throughout the desired thickness of the paper substrate. The final step in the fabrication procedure involves washing away the un-polymerised material from the paper substrate by immersing the paper in isopropanol.

The procedure described here results in a paper substrate with user-defined regions that have been selectively polymerised through the direct-write step. Fig. 2 shows a step-wise schematic depicting the sequential processing steps involved in the creation of these fluidic channels – laser scanning of parallel lines along the surface of the paper substrate

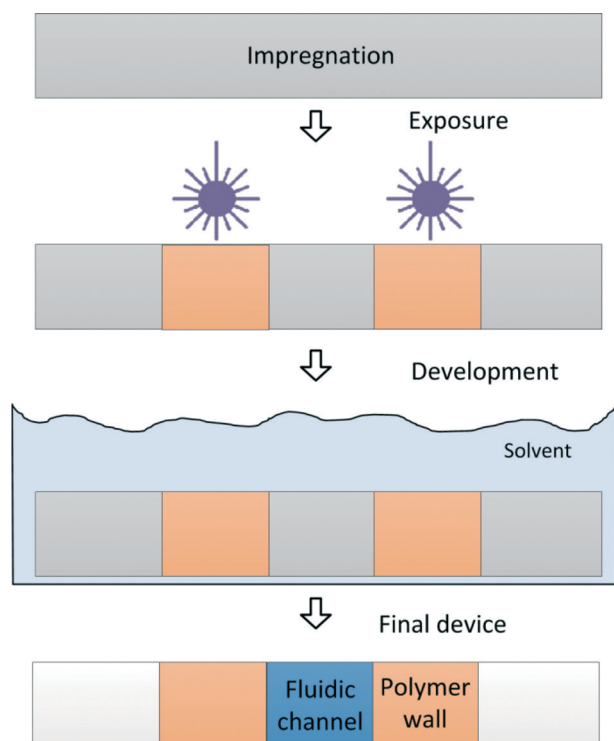


Fig. 2 Schematic of the paper-patterning procedure.

under the correct conditions creates photo-polymerisation-induced hydrophobic barrier walls that define a fluidic channel.

The choice of laser used dictates several important parameters of the photo-polymerisation process such as the optical penetration depth in the paper, writing speeds for the barriers and finally the width of both the barriers and the fluidic channels, due to scattering of the incident laser light within the paper matrix, which can lead to photo-polymerisation occurring beyond the width of the focused laser spot. The first laser used for the direct-write pattern definition step was an Nd: YVO₄ laser (B M Industries, Thomson CSF Laser, France) operating at 266 nm, with a pulse duration of 10 ns, a maximum single pulse energy of 2 mJ, and a repetition rate of 20 Hz. Subsequently, we explored the use of cheaper and smaller c. w. diode-lasers, namely Omicron (Laserage, Germany), operating at 375 nm with a maximum output of 70 mW, and Cobolt MLD (Cobolt AB, Sweden), operating at 405 nm and delivering a maximum output power of ~110 mW. We also explored two different photopolymers, namely DeSolite® 3471-3-14 from DSM Desotech Inc., and Substance G (SubG) from Maker Juice, USA. A range of trial experiments was then performed to investigate and optimise the exposure parameters and photo-polymerisation characteristics which involved these three laser sources, pulsed and c. w., and two different photopolymers, under varying parameters such as laser pulse energy/power, sample translation speed, and focal spot size for each combination.

For experiments with the pulsed 266 nm laser, the range of translational speeds was varied from 0.05 mm s⁻¹ to 0.5 mm s⁻¹, together with a variation of incident average powers ranging from ~7 mW to ~10 mW (corresponding to energies of ~0.35 mJ to ~0.5 mJ per pulse). The paper was positioned at a distance of 10 mm away from the focal point of the cylindrical lens ($f = 36$ mm), and the corresponding dimension of the laser spot (on the paper substrate) was ~0.3 mm × 1 mm. The corresponding incident fluence hence ranged from 4.6 J cm⁻² to 66 J cm⁻².

For experiments with the c. w. 375 nm laser, the range of translational speeds was varied from 4 mm s⁻¹ to 6.7 mm s⁻¹, with corresponding variation of incident power ranging from 1 mW through to 50 mW. The paper was positioned at the focal point of the cylindrical lens ($f = 25$ mm), and the corresponding incident fluence ranged from ~1.9 J cm⁻² to ~156 J cm⁻².

For experiments with the c. w. 405 nm laser, the range of translational speeds was varied from 4 mm s⁻¹ to 10 mm s⁻¹, with a corresponding variation of incident power ranging from 1 mW through to 100 mW. The paper was positioned at the focal point of the cylindrical lens ($f = 25$ mm), and the corresponding incident fluence ranged from ~1.25 J cm⁻² to ~312.5 J cm⁻².

3b. Results and discussion for patterning with 266 nm pulsed laser

Fig. 3 shows three sets of parallel lines that have been inscribed using the 266 nm pulsed laser source, at translation

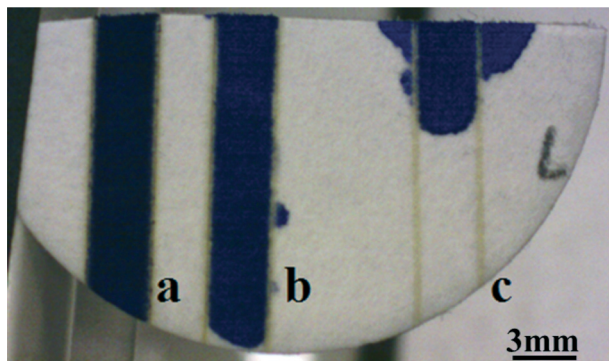


Fig. 3 Three sets of parallel lines that have been polymerised while being translated at three different speeds, namely, a) 0.06 mm s^{-1} , b) 0.07 mm s^{-1} and c) 0.09 mm s^{-1} .

speeds of 0.06 mm s^{-1} , 0.07 mm s^{-1} and 0.09 mm s^{-1} with an incident average laser power of 7 mW. The photopolymer used for this was DeSolite®. A blue ink solution was subsequently pipetted into the channels, to test the ability of the structures to contain and wick liquids along the channel. The ink was pipetted from one side of the channel (the top side in the figure shown) in $3 \mu\text{L}$ droplets, until the channel was filled or a leak was observed.

It was found that the polymerisation depths of the barrier walls for channel (c) was only about 60% of the thickness of the paper, whereas for channel (b) this depth was about 75% of the paper thickness. For channel (a) however, the barrier walls extended throughout the full thickness of the paper, enabling leak-free transport of the ink on introduction at one end of the fluidic channel. In contrast, for channels (b) and (c), whose barrier walls do not extend throughout the entire paper thickness, undesirable and irregular leakage of the ink was seen from either side of the channel walls. For speeds slower than 0.06 mm s^{-1} , for this pulsed laser source, ablation along a central section of the barrier wall was observed as the local fluence had exceeded the paper ablation threshold at the peak of the Gaussian laser profile.

Subsequent experiments were performed with the paper held at a distance of 1 mm from the focal point. Translation speeds were trialed ranging from 0.06 to 0.5 mm s^{-1} , and for speeds greater than 0.35 mm s^{-1} the photo-polymerised structures did not extend throughout the paper, while for speeds slower than 0.25 mm s^{-1} ablation occurred along the central region of the scanned lines. For speeds lower than 0.2 mm s^{-1} the paper was physically cut through along the length of the scanned line.

From the above results, the correlation between spot size of the incident laser source and resultant size of the polymerised regions is easily determined, and hence for a specific choice of laser and photopolymer it is then possible to deduce the correct exposure regime that will produce any desired line-width. However, for our demonstrations it is important to note that the smallest barrier widths that are able to contain and guide the fluid flow are of order $100 \mu\text{m}$. Since there is a minimum fluence requirement for

photo-polymerisation at any specific translational speed, this fluence then determines the maximum translational speed (and hence device fabrication) speed. However, the above demonstration clearly shows the ability to build compact fluidic flow-based devices which encompass the basic needs for smaller volumes of expensive reagents in the fabrication of low-cost LOC-type medical diagnostic devices.

3c. Results and discussion for patterning with c. w. lasers at 375 nm and 405 nm

In order to explore the possibility of using of our paper-patterning procedure with different laser parameters, we then tried other lasers which operated continuously (c. w. mode), at wavelengths of either 375 nm or 405 nm instead of 266 nm. One of the primary reasons for choosing c. w. operation was that it would allow us to circumvent the deleterious ablative effects that we observe when scanning with the pulsed laser at higher peak powers. Additionally, operation at these longer wavelengths would translate into greater absorption depths for the incident light, hence allowing much higher writing speeds than those used with the pulsed 266 nm source.

Fig. 4 shows a set of lines polymerised with the 375 nm laser, where the line-widths obtained are shown as a function of incident laser power and paper translation speed. Fig. 4a shows results for a fixed incident laser power of 1 mW, and the line-widths are seen to increase from a value of $\sim 130 \mu\text{m}$ at 6.7 mm s^{-1} to a value of $\sim 320 \mu\text{m}$ at 4 mm s^{-1} . Similarly, as shown in Fig. 4b, for a fixed scan speed of 6.7 mm s^{-1} , the width of the polymerised lines increases with increasing incident laser powers from a value of $\sim 500 \mu\text{m}$ at 5 mW, to a value of $\sim 1200 \mu\text{m}$ at 50 mW. This can be attributed to the fact that with an increase in the incident laser power, a larger fraction of the incident Gaussian intensity laser profile would be above the polymerisation threshold, thus resulting in polymerised lines with larger widths.

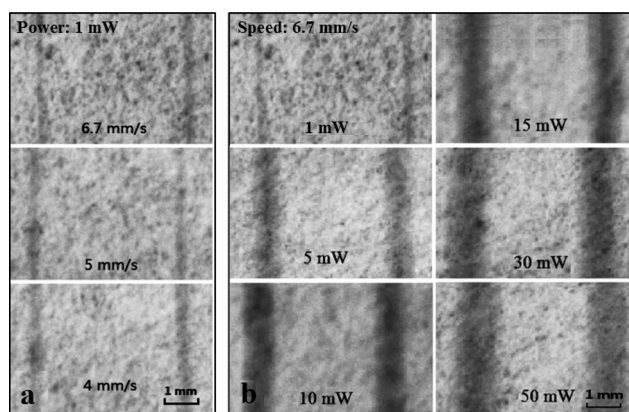


Fig. 4 Images of sets of parallel lines that have been photo-polymerised using a 375 nm c. w. laser under different writing conditions: (a) fixed laser power, variable translation speed, and (b) fixed translation speed, variable laser power. Photopolymer used was DeSolite®.

The graph in Fig. 5 summarises the above observations, and presents the relationship between the line-widths of the polymerised regions for different scan speeds and different laser powers. The data presented in Fig. 5 show that, for a fixed laser power of 10 mW, the widths of the polymerised lines increased from $\sim 680 \mu\text{m}$ to $\sim 1000 \mu\text{m}$ with decreasing scan speeds, and for a fixed scan speed of 6.7 mm s^{-1} , the widths of the lines increased from $\sim 130 \mu\text{m}$ to $\sim 1200 \mu\text{m}$ with increasing laser powers.

We observed a similar effect for the 405 nm laser, and the relationship between the widths of the lines for different scan speeds and different laser powers is shown in Fig. 6. For a fixed laser power of 10 mW, the widths of the polymerised lines increase from $\sim 220 \mu\text{m}$ to $\sim 330 \mu\text{m}$ with decreasing scan speeds, and for a fixed scan speed of 6.7 mm s^{-1} , the widths of the lines increase from $\sim 80 \mu\text{m}$ to $\sim 800 \mu\text{m}$ with increasing

laser powers. The smaller line-widths for the irradiation at a wavelength of 405 nm, are a direct consequence of the better beam quality of the 405 nm laser compared to the 375 nm laser and the absence of parasitic lobes in the spatial intensity profile that we saw with the 375 nm source which, though of low intensity, does induce additional photo-polymerisation and therefore produce a broadened line-width compared to the theoretical limit for a perfect single mode laser source. Table 1 shows a summary of the resulting line-widths for the lines polymerised with the two c. w. wavelengths under different laser writing conditions.

The immediate observation using c. w. laser sources is the considerable increase in writing speeds possible compared to the pulsed laser source. As an example, to polymerise a line which was 2 cm in length at an incident fluence of 9.3 J cm^{-2} , the scan speeds for the pulsed laser was $\sim 0.25 \text{ mm s}^{-1}$, whereas for the c. w. laser the scan speed was ~ 40 times faster at $\sim 10 \text{ mm s}^{-1}$ – these comparatively faster speeds are a very positive attribute that has immediate benefits for increased rate of production if this technology reaches the stage of commercialisation.

All of the experiments described so far were performed using the DeSolute® photopolymer. However, to make a useful comparison, we repeated our experiments with another photopolymer, SubG. Due to the extremely low viscosity (12 cP @ 25°C) of SubG, we soaked the paper directly with the photopolymer solution without the need for any solvent-based dilution, unlike the case for DeSolute®, which had to be diluted in a solution of isopropanol prior to impregnation into the paper substrates. Fig. 7 shows a series of parallel lines that were patterned with the same laser-patterning conditions using two different photopolymers. As can be seen, the lines that were formed with SubG were narrower, and had edges that were more sharply-defined when compared with those written with DeSolute®. Fig. 8 shows the variations in width of the lines patterned with the 405 nm laser for the two different photopolymers at different incident laser powers but the same scan speeds of 10 mm s^{-1} . As can be seen from both Fig. 7 and 8 the widths of lines polymerised using SubG is consistently narrower.

An important advantage offered by LOC-type fluidic devices is their cost-effectiveness, which is a consequence of their much reduced sizes, so an important requirement is to implement the entire device with the smallest possible footprint. Using our LDW procedure for making such compact

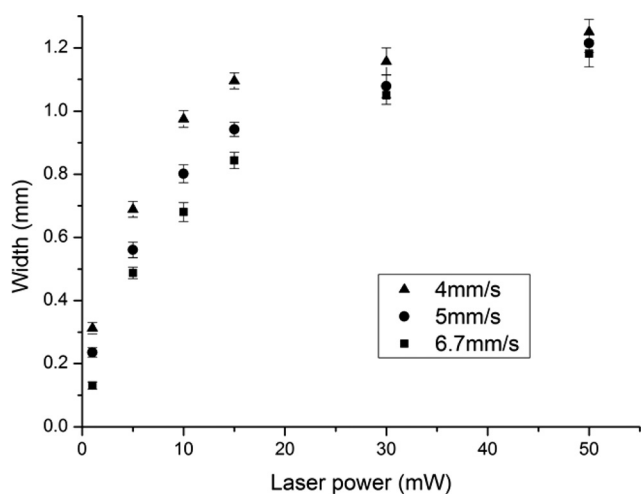


Fig. 5 Graph showing the widths of the laser-patterned lines for different incident laser powers from the 375 nm source at different scan speeds. Error bars indicate the standard deviation for 5 measurements along each line.

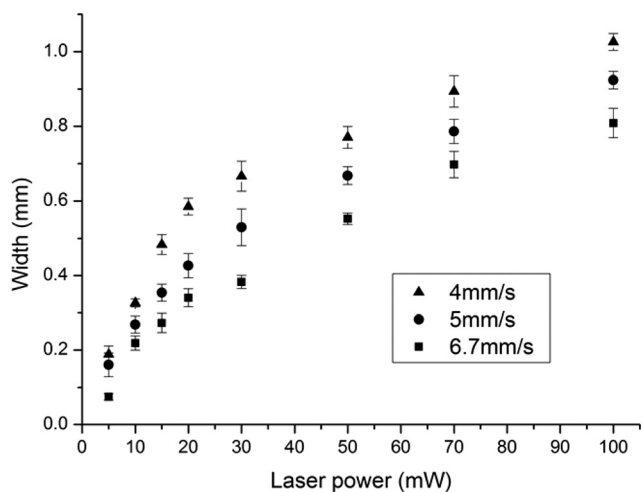


Fig. 6 Plots showing the widths of the laser-patterned lines for different incident laser powers at 405 nm at different scan speeds.

Table 1 Summary of the line-widths for writing wavelengths of 375 nm and 405 nm, at different incident powers up to a maximum value of 50 mW, but a common writing speed of 6.7 mm s^{-1}

Laser power (mW)	Line-widths (μm) for 375 nm at 6.7 mm s^{-1}	Line-widths (μm) for 405 nm at 6.7 mm s^{-1}
5	$\sim 480 \pm 15$	$\sim 80 \pm 10$
10	$\sim 680 \pm 30$	$\sim 220 \pm 20$
15	$\sim 850 \pm 30$	$\sim 270 \pm 30$
30	$\sim 1050 \pm 30$	$\sim 380 \pm 20$
50	$\sim 1180 \pm 40$	$\sim 550 \pm 20$

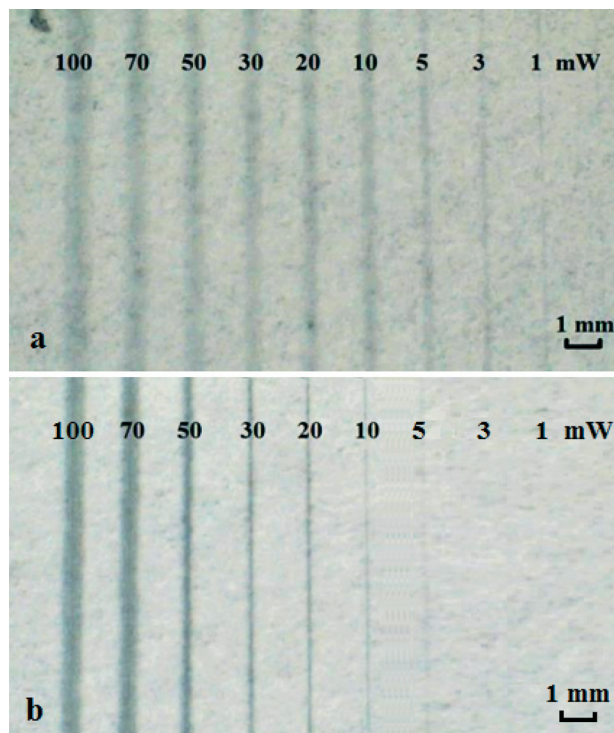


Fig. 7 Sets of parallel lines that were polymerised using a 405 nm c. w. laser with a scan speed of 10 mm s^{-1} and different incident power (100 to 1 mW) using two different photopolymers, a) DeSolite®, and b) SubG.

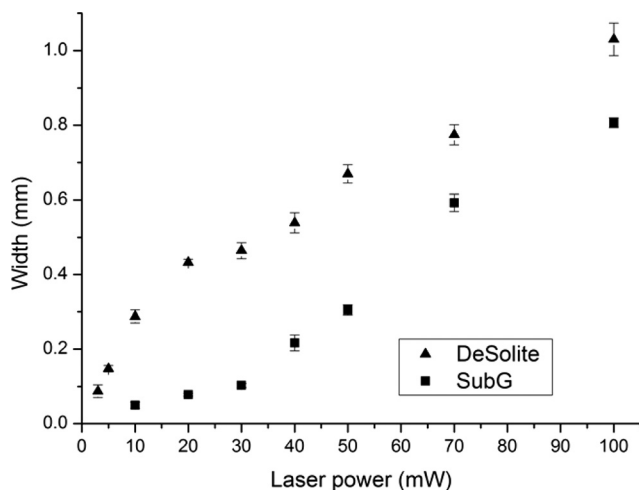


Fig. 8 Graph showing the widths of the laser-patterned lines for different incident laser powers and a scan speed of 10 mm s^{-1} . The lines were patterned with a c. w. 405 nm laser and the photopolymers used were DeSolite® and SubG. Error bars indicate the standard deviation for 5 measurements along each line.

devices would require finding the smallest dimensions not only for the fluidic barrier walls but also for the fluidic channels. To this effect, we initially investigated the minimum barrier wall widths that could be created with our procedure using a c. w. 405 nm laser. As shown in Fig. 9a, under the appropriate writing conditions (scan speed of 10 mm s^{-1} ,

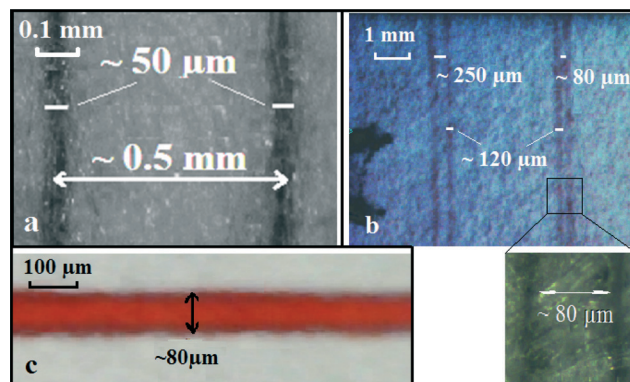


Fig. 9 a) Microscope images showing two parallel lines written in DeSolite® via LDW using a scan speed of 10 mm s^{-1} and an incident power of 10 mW at 405 nm, and having widths of $\sim 50 \mu\text{m}$, b) camera image shows two fluidic channels with widths of $\sim 250 \mu\text{m}$ and $\sim 80 \mu\text{m}$ and identical barrier wall widths of $\sim 120 \mu\text{m}$; inset shows a magnified image of the channel having a width of $\sim 80 \mu\text{m}$, c) camera image shows the $\sim 80 \mu\text{m}$ fluidic channel guiding red ink.

incident power of 10 mW and corresponding incident fluence of $\sim 125 \text{ J cm}^{-2}$), we could polymerise lines with widths of $\sim 50 \mu\text{m}$, which is smaller than the dimensions we could achieve using the pulsed laser, and to our knowledge, is also the smallest line-width reported so far for barrier-walls in paper-based devices. Although such feature dimensions would have been possible through lithographic procedures,¹⁰ our LDW method presents a far less complicated approach as it does not require lithographic masks or cleanroom-intensive processing. However, fluidic channels formed with barrier-walls that had such narrow line-widths were found to be unable to contain and guide fluids, and instead a minimum line-width of $\sim 120 \mu\text{m}$ was required.

For this barrier wall width, we then investigated the minimum widths a fluidic channel can have and still guide fluids. Fig. 9b shows two fluidic channels, which were fabricated to have identical barrier wall widths of $\sim 120 \mu\text{m}$, but two different channel widths of $\sim 250 \mu\text{m}$ and $\sim 80 \mu\text{m}$. The inset of Fig. 9b shows a magnified microscope image showing the $80 \mu\text{m}$ channel. We observed that the fluidic channel with a width of $\sim 80 \mu\text{m}$ was able to contain and guide the flow of ink. Fig. 9c shows such a channel having a width of $\sim 80 \mu\text{m}$, and barriers with widths of $\sim 120 \mu\text{m}$, guiding red ink through it. To our knowledge this is the smallest dimension for a fluidic channel on cellulose paper, and is better than the dimensions that can be achieved with the wax-printing procedure that is currently one of the most widely used for the creation of fluidic patterns in cellulose paper, and for which the dimension limitations are imposed by the undue spreading of wax during the heat-treatment/wax-penetration step. The smallest dimension for fluidic patterns reported recently on a fibre-glass substrate through use of a simple cutting method is $\sim 137 \mu\text{m}$.²⁴

As described above, a minimum line-width is necessary for a barrier wall to contain fluids, and this was found to be different for the two photopolymers. Fig. 10 shows a set of square

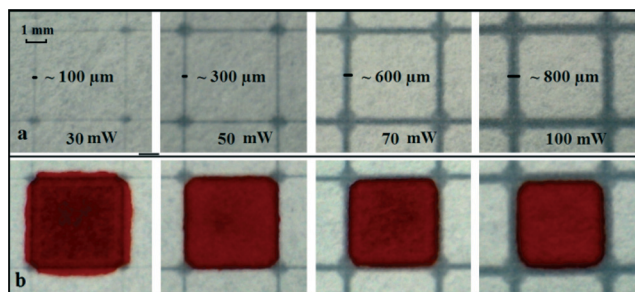


Fig. 10 Camera images a) of a series of 5×5 mm square patterns written in SubG with a 405 nm laser and different output powers (30, 50, 70, 100 mW) at the scanning speed of 10 mm s^{-1} , b) and showing the introduction of $2.5 \mu\text{L}$ of red ink to each square.

patterns each with identical dimensions of $5 \text{ mm} \times 5 \text{ mm}$, but with barrier walls that have different line-widths ranging from $\sim 100 \mu\text{m}$ to $\sim 800 \mu\text{m}$. These patterns have been written with the same laser (405 nm) but were created using the photopolymer SubG. As seen in Fig. 10, squares with line-widths greater than $\sim 300 \mu\text{m}$ were able to contain $\sim 2.5 \mu\text{L}$ of ink solution.

3d. Structuring of fluidic channels for protein and glucose detection

As our end-goal was to show the feasibility of this procedure in producing fluidics-based diagnostic devices, we patterned paper substrates with two different designs, namely a cross-hatch grid pattern that resembled a conventional micro-titer plate, and a T-junction. These fluidic tests were patterned into the paper substrates using the 405 nm laser and the photopolymer SubG, at a power of 70 mW and a writing speed of 10 mm s^{-1} .

First, we tested the use of the grid-like fluidic pattern of square wells (Fig. 11) by implementing the detection of Bovine Serum Albumin (BSA) and glucose. For the BSA test,

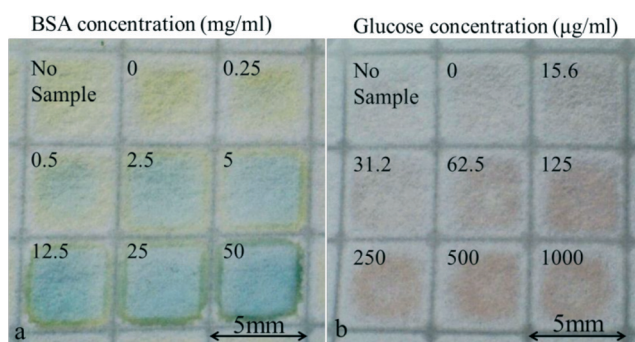


Fig. 11 a) Patterned cellulose paper after completion of the BSA detection assay showing different shades of the blue-green colour, corresponding to the different concentrations of BSA pipetted in each well, b) patterned cellulose paper after completion of the glucose assay showing different shades of the pink-brown colour, corresponding to the different concentrations of glucose pipetted in each well.

we pipetted $3 \mu\text{L}$ of a 250 mM citrate buffer solution at pH 1.8 in each square well of the test-pattern. The test paper was then allowed to dry for 1 hour before $3 \mu\text{L}$ of a 3.3 mM solution of the second reagent, tetrabromophenol blue (TBPB) (Sigma Aldrich 199311) in 95% ethanol was added into each well. After further drying at room temperature for 1 hour, the test-pattern was ready for use in the detection of BSA *via* the addition of sample solutions into the respective square wells of the test-pattern. We pipetted sample solutions made up in de-ionised water, with BSA concentrations ranging from 0.25 – 50 mg mL^{-1} into each well. Introduction of the sample solutions resulted in a colour change in each well showing different concentration-dependent shades of blue-green colour (as seen in Fig. 11a.) which were fully developed after ~ 10 minutes. The concentration of protein in each sample is labeled in Fig. 11a. Comparing the colour change observed for an unknown concentration with a known calibration curve would then allow determination of the concentration for that unknown sample. Using such test patterns with nine wells, it should be possible to quantify nine unknown samples illustrating the utility and simplicity of using such low-cost paper-patterns to perform multiplexed quantitative analysis.

The detection of glucose was implemented using an identical square-well pattern, where $3 \mu\text{L}$ of glucose oxidase/peroxidase reagent (Sigma Aldrich G3660) at a 5:1 ratio and 15 units of protein per ml of solution, were pipetted into each well. As with the BSA test, the reagents were left to dry at room temperature for 1 hour before further use. The test was then executed by addition of sample solutions with different concentrations of glucose into each well of the test-pattern. The concentration of glucose in the artificial solutions made up in de-ionised water ranged from 15.6 – $1000 \mu\text{g mL}^{-1}$ of D-glucose (Sigma Aldrich G3285). Introduction of the sample solutions into the wells resulted in a change of colour from white to different shades of pink-brown (Fig. 11b). The colours were fully developed after ~ 10 minutes. The concentration of glucose in each sample is labeled in Fig. 11b.

The final part of our experimental validation involved the use of a fluidic device shaped as a T-junction, for the simultaneous detection of BSA and glucose in the same sample solution, as shown in Fig. 12. The lower end of the vertical arm of the T served as the sample inlet point, and the two ends of the horizontal arm of the T served as the test zones. The reagents required for the assays were first pipetted at these two test zones and were allowed to dry. A sample solution ($15 \mu\text{L}$) containing both BSA and glucose (in concentrations of 50 mg mL^{-1} and $1000 \mu\text{g mL}^{-1}$ respectively in de-ionised water), when pipetted at the inlet of the device, flowed towards the test areas, and produced a colour change (blue-green) for BSA and (pink-brown) for glucose with the level of colour change depending on the concentrations of the biomolecules in the sample solution at the respective specified test zones. The dark area, circled in red, (Fig. 12a) in the initial section of the vertical arm of the T is the trace produced by the introduction of the fluidic sample solution, and the pale yellow colour of

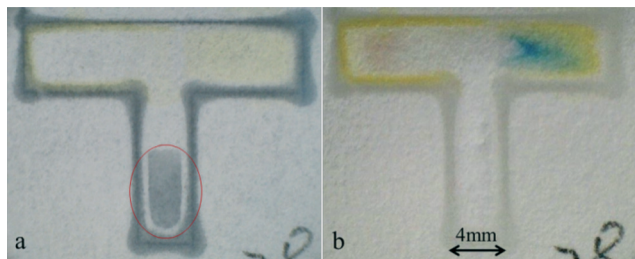


Fig. 12 Camera images of the patterned device, designed for the simultaneous detection of glucose and BSA, a) at the time of introduction of the sample solution and b) after detection was completed and measurements taken.

the right end of the horizontal arm of the T is from the dried reagents pipetted into the test zones. Fig. 12b is an image of the T after completion of the detection assay. For an unknown sample, the concentration of the BSA and glucose in the sample solution can be evaluated by capturing a picture of the T-sensor with a camera, then measuring the intensities of the RGB colours at the test zones²⁵ and comparing these to a pre-defined calibration curve.

4. Conclusions and future work

We have demonstrated laser-based patterning of paper for the creation of fluidic structures *via* photo-polymerisation. This LDW procedure is non-contact, non-lithographic and mask-less and we have demonstrated its utility in the fabrication of diagnostic tests for protein and glucose detection. The width of the walls/barriers and the width of the channels are at the level of $\sim 100\ \mu\text{m}$, the smallest that have been reported so far, which will allow for miniaturisation of the diagnostic sensor, and a corresponding minimal use of reagents. The process is ideal for rapid prototyping at preliminary trial-device fabrication stage and also for final device optimisation.

As future work, we will be investigating the implementation of curved walls and chicanes to control flow dynamics, and also trialing the patterning of nitrocellulose. Our final goal is to demonstrate fully automated paper-based biosensors that do not require any handling from the user apart from introducing the sample.

Acknowledgements

The authors acknowledge the funding received *via* the EPSRC grant no. EP/J008052/1 and EP/K023454/1, and the funding received *via* a Knowledge Mobilisation Fellowship for Dr. Collin Sones from the Institute for Life Sciences and the Faculty of Health Sciences of the University of Southampton. The authors are thankful to Photon Lines for the loan of the 375 nm laser. They also acknowledge valuable discussions with Prof. Andreas Dietzel of University of Braunschweig, Germany.

Notes and references

- 1 P. Yager, T. Edwards, E. Fu, K. Helton, K. Nelson, M. R. Tam and B. H. Weigl, *Nature*, 2006, **442**, 412–418.
- 2 D. R. Ballerini, X. Li and W. Shen, *Microfluid. Nanofluid.*, 2012, **13**, 769–787.
- 3 X. Li, D. R. Ballerini and W. Shen, *Biomicrofluidics*, 2012, **6**, 011301.
- 4 R. Pelton, *TrAC, Trends Anal. Chem.*, 2009, **28**, 925–942.
- 5 A. K. Yetisen, M. S. Akram and C. R. Lowe, *Lab Chip*, 2013, **13**, 2210–2251.
- 6 Chemstrip10 Test Strips, <http://www.poc.roche.com>, Accessed 3rd Jan, 2014.
- 7 Multistix110 SGReagent Strips, <http://www.medical.siemens.com>, Accessed January 12, 2013.
- 8 Medi-Test Combi 10 SGL, <http://www.mn-net.com>, Accessed January 3rd 2014.
- 9 YD Diagnostics URiSCAN Strips, <http://www.yd-diagnostics.com>, Accessed January 3rd, 2014.
- 10 CLINITEK1 Microalbumin Reagent Strips, <http://www.medical.siemens.com>, Accessed January 5th, 2014.
- 11 A. W. Martinez, S. T. Phillips, G. M. Whitesides and E. Carrilho, *Anal. Chem.*, 2010, **82**, 3–10.
- 12 A. W. Martinez, S. T. Phillips, M. J. Butte and G. M. Whitesides, *Angew. Chem., Int. Ed.*, 2007, **46**, 1318–1320.
- 13 D. A. Bruzewicz, M. Reches and G. M. Whitesides, *Anal. Chem.*, 2008, **80**, 3387–3392.
- 14 K. Abe, K. Suzuki and D. Citterio, *Anal. Chem.*, 2008, **80**, 6928–6934.
- 15 X. Li, J. F. Tian, T. Nguyen and W. Shen, *Anal. Chem.*, 2008, **80**, 9131–9134.
- 16 E. M. Fenton, M. R. Mascarenas, G. P. Lopez and S. S. Sibbett, *ACS Appl. Mater. Interfaces*, 2009, **1**, 124–129.
- 17 Y. Lu, W. W. Shi, L. Jiang, J. H. Qin and B. C. Lin, *Electrophoresis*, 2009, **30**, 1497–1500.
- 18 E. Carrilho, A. W. Martinez and G. M. Whitesides, *Anal. Chem.*, 2009, **81**, 7091–7095.
- 19 X. Li, J. F. Tian, G. Garnier and W. Shen, *Colloids Surf., B*, 2010, **76**, 564–570.
- 20 J. L. Delaney, C. F. Hogan, J. F. Tian and W. Shen, *Anal. Chem.*, 2011, **83**, 1300–1306.
- 21 J. Olkkonen, K. Lehtinen and T. Erho, *Anal. Chem.*, 2010, **82**, 10246–10250.
- 22 W. Dungehai, O. Chailapakul and C. S. Henry, *Analyst*, 2011, **136**, 77–82.
- 23 G. Chitnis, Z. W. Ding, C. L. Chang, C. A. Savran and B. Ziaie, *Lab Chip*, 2011, **11**, 1161–1165.
- 24 X. E. Fang, S. S. Wei and J. L. Kong, *Lab Chip*, 2014, **14**, 911–915.
- 25 I. N. Katis, J. A. Holloway, J. Madsen, S. N. Faust, S. D. Garbis, P. J. S. Smith, D. Voegeli, D. L. Bader, R. W. Eason and C. L. Sones, *Biomicrofluidics*, 2014, **8**, 036502.

Laser-based patterning for fluidic devices in nitrocellulose

Peijun J. W. He, Ioannis N. Katis, Robert W. Eason, and Collin L. Sones

Citation: *Biomicrofluidics* **9**, 026503 (2015); doi: 10.1063/1.4919629

View online: <http://dx.doi.org/10.1063/1.4919629>

View Table of Contents: <http://scitation.aip.org/content/aip/journal/bmf/9/2?ver=pdfcov>

Published by the [AIP Publishing](#)

Articles you may be interested in

[Ion concentration polarization on paper-based microfluidic devices and its application to preconcentrate dilute sample solutions](#)

Biomicrofluidics **9**, 014122 (2015); 10.1063/1.4913366

[Probing the dynamic responses of individual actin filaments under fluidic mechanical stimulation via microfluidics](#)
Appl. Phys. Lett. **102**, 193704 (2013); 10.1063/1.4806975

[Cyclic olefin copolymer based microfluidic devices for biochip applications: Ultraviolet surface grafting using 2-methacryloyloxyethyl phosphorylcholine](#)

Biomicrofluidics **6**, 012822 (2012); 10.1063/1.3682098

[Optofluidic in situ maskless lithography of charge selective nanoporous hydrogel for DNA preconcentration](#)

Biomicrofluidics **4**, 043014 (2010); 10.1063/1.3516037

[Observation of hydrophobic-like behavior in geometrically patterned hydrophilic microchannels](#)

Biomicrofluidics **4**, 044103 (2010); 10.1063/1.3499416

Did your publisher get
18 MILLION DOWNLOADS in 2014?
AIP Publishing did.



THERE'S POWER IN NUMBERS. Reach the world with AIP Publishing.



Laser-based patterning for fluidic devices in nitrocellulose

Peijun J. W. He,^{a)} Ioannis N. Katis, Robert W. Eason, and Collin L. Sones
*Optoelectronics Research Centre, University of Southampton, Highfield,
 Southampton SO17 1BJ, United Kingdom*

(Received 30 January 2015; accepted 21 April 2015; published online 29 April 2015)

In this report, we demonstrate a simple and low cost method that can be reproducibly used for fabrication of microfluidic devices in nitrocellulose. The fluidic patterns are created via a laser-based direct-write technique that induces polymerisation of a photo-polymer previously impregnated in the nitrocellulose. The resulting structures form hydrophobic barriers that extend through the thickness of the nitrocellulose and define an interconnected hydrophilic fluidic-flow pattern. Our experimental results show that using this method it is possible to achieve microfluidic channels with lateral dimensions of $\sim 100\ \mu\text{m}$ using hydrophobic barriers that form the channel walls with dimensions of $\sim 60\ \mu\text{m}$; both of these values are considerably smaller than those that can be achieved with other current techniques used in the fabrication of nitrocellulose-based fluidic devices. A simple grid patterned nitrocellulose device was then used for the detection of C-reactive protein via a sandwich enzyme-linked immunosorbent assay, which served as a useful proof-of-principle experiment.

© 2015 AIP Publishing LLC. [<http://dx.doi.org/10.1063/1.4919629>]

I. INTRODUCTION

In recent years, the requirements for simple, accurate, and low-cost diagnostic solutions in both developing and developed countries have led to a rapid progress in the fabrication of point-of-care (POC) devices. Microfluidic engineering technology has been widely used for implementing lab-on-chip (LOC) type point-of-care devices since its origins in the 1990s.¹ One of the main reasons behind the use of this LOC-type microfluidic technique for POC diagnostics is the possibility of reducing the quantity of valuable samples or reagents that would be needed and also the possibility to shorten the detections times, which would result primarily from the compact structure and small size of such LOC devices. However, although this technology is promising and there have been a large number of achievements in this field, there is still a bottleneck in the development of commercialized products, which can be attributed to a disconnect between users, academic researchers, and manufacturers.²

This situation is changing, however, with the emergence of capillary-based microfluidic devices and, in particular, with the relatively recent adoption of paper, one of the most simple and widely used capillary structures. Paper as the functional substrate has already been widely researched as an alternative to other commonly used substrates such as glass, silicon, SU8, and PDMS (Polydimethylsiloxane), and many different kinds of microfluidic devices with a range of structures and applications have been reported.³ This is a direct result of the many advantages offered by paper, namely, its low cost, availability, ease of storage and transport, and finally being easily disposable in a non-hazardous manner. Paper-based fluidics, therefore, presents itself as a LOC technology that could become the technique of choice for mass-market commercialized POC diagnostic devices.

In addition, when compared with other solid-material-based LOC-type microfluidic devices, those based on porous paper do not require any additional pumps because of the inherent ability of paper to wick fluids via capillary forces. This provides a real advantage with regards to both

^{a)}E-mail: ph3e12@soton.ac.uk. Tel.: 44 2380 599091

the cost and manufacturability of any such device and has hence led to the development of many paper-based POC devices based on simple colorimetric bio-assays.^{3–5} In addition, porous nitrocellulose membranes, since their first demonstration in the 1960s, have been widely used, due to some key features, such as their smooth surface, uniform pore size, and high protein-binding capability.⁶ A large number of biological assays, namely, blotting assays, flow-through assays, and lateral flow tests have been developed on these porous nitrocellulose membranes, and hence nitrocellulose-based microfluidic devices are currently regarded as the alternative of choice for improving the performance of existing POC assays.

Several methods have already been reported for fabricating fluidic patterns/devices in such materials, and these can be classified into two broad categories: 2D cutting/shaping and physical blocking of pores. The techniques so far reported include the use of photolithography,⁷ ink-jet printing,^{8,9} printing of wax,^{10,11} plasma oxidation,^{12,13} laser-cutting,¹⁴ and shaping,¹⁵ each of which has its own merits and drawbacks. In general, the ideal technique should be as simple, cheap, and fast to implement as possible, and therefore multiple printing steps, the use of specialist chemicals, or complex post-processing procedures are to be avoided. The other factor is the feature sizes achievable, which is where procedures such as plotting or wax printing may present restrictions in this context.

Here, we report a new concept to pattern nitrocellulose membranes for low-cost microfluidic devices. We employ a laser-based direct-write (LDW) procedure to create fluidic patterns using the concept of light-induced photo-polymerisation. The fluidic channel patterns are formed by hydrophobic photo-polymer barriers that demarcate the flow regions within the hydrophilic paper. In contrast to the most widely used methods for patterning paper, our approach not only eliminates the requirements for cleanroom-based steps, expensive masks, specialist reagents, and custom-designed equipment, but is also amenable to large-scale commercialization. Since LDW is a non-contact procedure, it minimizes any chances of cross-contamination, an essential criterion in fabrication of microfluidic devices for biological and biomedical applications. As shown later, using this approach, we have successfully demonstrated that it is possible to create microfluidic channels with barrier-walls that have dimensions of $\sim 60\ \mu\text{m}$ —a size which has not yet been achieved using other reported methods. Finally, this LDW process is also suitable for a roll-to-roll process, and we believe that this technique presents itself as a promising methodology that can be used for fabricating nitrocellulose-based POC devices.

II. EXPERIMENTAL SECTION

A. Laser setup and materials

The laser used for our LDW patterning process was a 405 nm continuous wave (c.w.) diode-laser (Cobolt MLD, Cobolt AB, Sweden) with a maximum output power of $\sim 110\ \text{mW}$.

The substrates used were Protran[®] nitrocellulose membranes BA85 from Whatman, USA, and the photo-polymer used was DeSolute[®] 3471-3-14 from DSM Desotech, Inc., USA. For this specific photopolymer, the fluence required (for 90% curing) is $\sim 0.4\ \text{J/cm}^2$. By varying both the laser scan speed and the laser power, a range of experiments was performed in order to find the optimum conditions for forming fluidic structures.

B. Methods

Paper-based microfluidic devices were fabricated by creating hydrophobic barriers in the nitrocellulose membranes via the effect of light-induced photo-polymerisation. The LDW technique we use to create fluidic patterns is described as follows (Figure 1). A laser beam is first scanned across the nitrocellulose membrane which has been pre-soaked with a light-sensitive photo-polymer (DeSolute) which induces light-induced cross-linking of the photo-polymer along the exposed regions. This laser-scanned substrate is then developed in a solvent to wash away any un-polymerised material, leaving behind a user-defined pattern of polymerised photo-polymer in the laser-exposed regions. These polymerised barriers extend throughout the

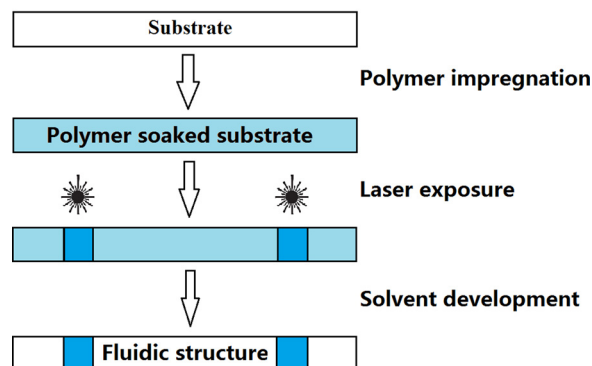


FIG. 1. Schematic of the LDW-based paper-patterning procedure.

thickness of the substrate and serve as hydrophobic barrier-walls that can contain and guide liquids introduced onto the substrate.

As the extent of the photo-polymerisation process is directly dependent on the incident laser fluence, the widths, depths, and the quality of polymerised patterns can be easily controlled by changing the fluence along the exposed area. Thus, any desired fluidic pattern can be produced by simply modifying the laser exposure parameters during the LDW process via the laser scan speed and/or laser power.

C. Procedure

As shown in the schematic in Figure 2, during the first LDW step, the laser beam is focused onto the nitrocellulose substrate using a spherical lens ($f = 15$ cm). The substrate was mounted on an xyz-stage, and by controlling the positions in the x and y directions, a user-defined 2D design is patterned on the substrate. The third axis, z , was used to position the substrate at the optimum position (usually, at the focal plane of the lens). For experiments performed in this report, the nitrocellulose substrates were positioned at the focal point, and the corresponding laser spot diameter was $\sim 8 \mu\text{m}$, and the Rayleigh range was $\sim 125 \mu\text{m}$. The range of substrate translational speeds trialed varied from 0.05 mm/s to 10 mm/s, while the incident average powers ranged from 0.3 mW through 10 mW. The corresponding incident fluences can hence be calculated using the equation:

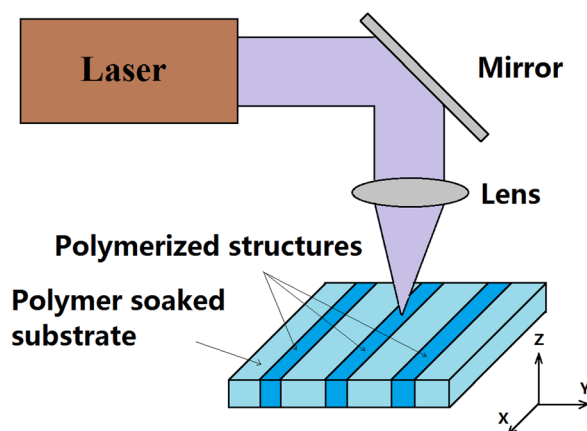


FIG. 2. Schematic of the laser-based direct-write process used to form polymerised hydrophobic structures in paper.

$$\text{Incident fluence} = \frac{\text{Energy}}{\text{Area}} = \frac{\text{Laser incident power}}{\text{Beam diameter} \times \text{Scanning speed}}$$

which, therefore, ranged from $\sim 0.375 \text{ J/cm}^2$ to $\sim 2500 \text{ J/cm}^2$.

The final developing step was to wash off any un-polymerised photo-polymer from the substrate through immersion in a suitable solvent (in this case toluene), which does not affect the intentionally polymerised regions.

III. RESULTS AND DISCUSSION

The choice of an appropriate photo-polymer that does not alter the properties of the nitrocellulose substrates is vital, and several, such as SubG from Maker Juice, USA, Norland 61 & 68 from Norland Products, Inc., USA, and Ablelux A4061T & A4086 from Henkel AG & Co., Germany, were tested in order to find the most suitable. Specifically, photo-polymers that reacted with the nitrocellulose substrate and either dissolved or decomposed it, visibly degraded it, or transformed it into an extremely hydrophobic “plastic-like” material were rejected. Our current choice, DeSolite is, however, extremely viscous, having a viscosity of $\sim 10\,000 \text{ mPa s}$ at 25°C , and so we diluted it in toluene in the ratio of 5:3 (v/v) to enable it to soak into the nitrocellulose substrates. These were then left to dry under ambient laboratory conditions, prior to the laser-patterning step.

A. Writing of fluidic channels

The first structures to be investigated were simple straight-line channels which would allow determination of some of the basic parameters of laser exposure (scan speed and laser power) required. As shown in Figure 3(a), two parallel channels were written by scanning at laser powers of 10 and 5 mW under the same scan speed of 10 mm/s, and the fluid containing properties of these channels was tested by flowing red ink (Parker, France) through them. As can be seen in Figure 3(b), the scanned lines form the barrier walls that contain and guide the flow of red ink through these fluidic channels without any observed sideways leakage.

Because toluene is volatile and easily evaporates under ambient laboratory conditions, it proved difficult to uniformly soak the substrates with the photo-polymer. As the width, depth, and uniformity of the polymerised lines are directly dependent on the polymer concentration in the substrate, any variations would thus translate into lines having undesirable variations. To circumvent this, we chose to soak the nitrocellulose paper directly with the undiluted photo-polymer. However, due to its high viscosity it took $\sim 20 \text{ s}$ for the paper to fully absorb the photo-polymer.

Figure 4 shows a nitrocellulose substrate that has undergone LDW to polymerise a set of parallel lines, written with different scan speeds (0.05, 0.1, 0.5, 1, 5, and 10 mm/s) but with a fixed laser power of 10 mW. The lines shown, after development in toluene, appear as transparent regions of the otherwise white nitrocellulose substrate. This relatively good level of optical transparency of the lines within the otherwise scattering medium is as a result of the induced polymerisation. Lines written with a scan speed less than 5 mm/s have poor definition with irregular edges, which is the result of over-polymerisation due to the unnecessarily high exposures used. However, for scan speeds greater than 5 mm/s, we see that the lines are increasingly

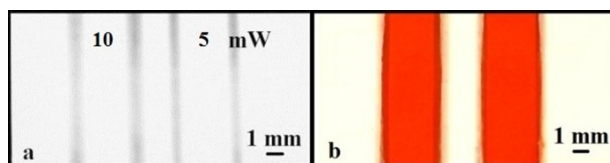


FIG. 3. Images showing two fluidic channels formed by writing parallel lines with two different laser powers of 10 and 5 mW at a speed of 10 mm/s.

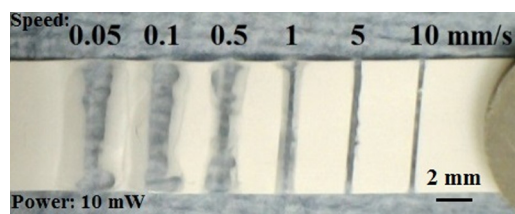


FIG. 4. Photographic image showing a nitrocellulose substrate with a set of parallel lines that were polymerised using different scan speeds of 0.05–10 mm/s at an incident laser power of 10 mW.

well-defined and, as shown in a subsequent figure, perform well as barriers to contain and guide fluids.

To further identify the optimum condition in terms of the width and the quality of the patterned lines, we performed a subsequent study by varying the laser power as well as the laser scan speed. The plots in Figure 5 show the relationship between the widths of the polymerised lines and the laser power for three different scan speeds. The line widths obtained increase from $\sim 70\ \mu\text{m}$ and $\sim 50\ \mu\text{m}$ to $\sim 340\ \mu\text{m}$ and $\sim 270\ \mu\text{m}$ at scan speeds of 5 mm/s and 7 mm/s, respectively, for an increase in the laser power from 0.2 mW to 10 mW. Similarly, for a scan speed of 10 mm/s, the widths of the polymerised lines increase from $\sim 50\ \mu\text{m}$ to $\sim 220\ \mu\text{m}$ as the laser power increases from 0.3 mW to 10 mW.

As our final goal was to pattern the nitrocellulose membranes for implementation of LOC fluidic devices, our aim was to identify the optimum conditions for the fabrication of fluidic channels that are able to reliably contain and guide the flow without leakage. Figure 6(a) shows a set of straight channels having a common width of 3 mm, written with a constant laser scan speed of 10 mm/s for varying laser powers ranging from 10 mW to 0.3 mW. Figure 6(b) is an image of the same set of channels after introduction of red ink into each channel. As can be seen from this figure, the ink solution only leaks out of the channel written with the lowest laser power of 0.3 mW, and all other channels contain and guide the flow without any leakage. Using the proposed LDW photo-polymerisation technique, the smallest size of barrier line, which we can form in nitrocellulose and which is able to contain and guide the flow, is $\sim 60\ \mu\text{m}$ —the smallest dimensions reported in literature when compared with other techniques reportedly used to fabricate microfluidic devices such as photolithography, inkjet etching, and wax printing.¹⁶

The final step was to determine the minimum width for a fluidic channel that can be patterned via LDW that will successfully allow fluid flow. While the typical widths achieved with the wax printing procedure, which is currently one of the most widely implemented techniques,

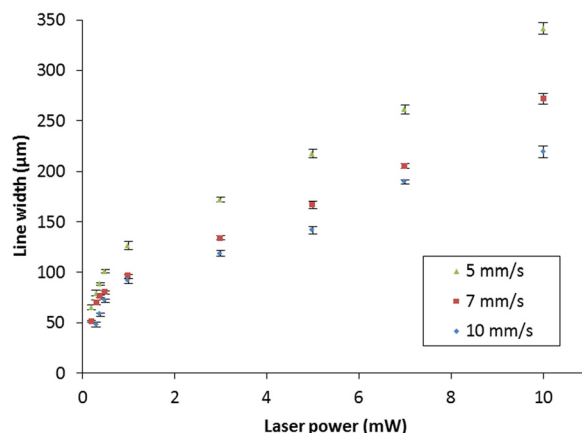


FIG. 5. Plots showing the variations in the widths of the polymerised lines for different laser powers at three scan speeds. Error bars indicate the standard deviation for 5 measurements along each line.

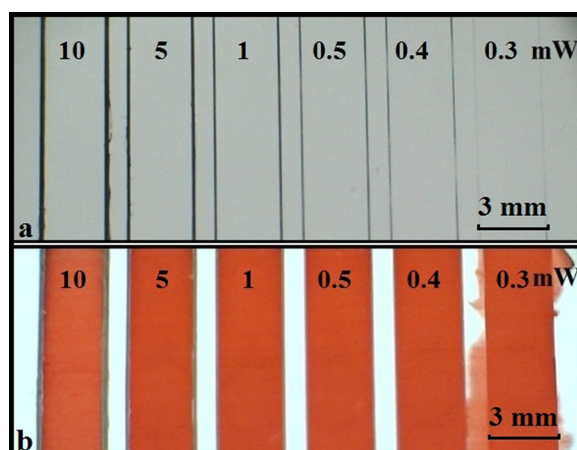


FIG. 6. (a) Image showing a set of fluidic channels formed with pairs of parallel polymerised barrier-walls that were written with different incident laser powers of 10–0.3 mW at a constant scan speed of 10 mm/s; (b) after introduction of red ink into each channel.

ranges from 0.5 mm to 4 mm,¹⁷ we anticipated that our LDW technique could produce channel widths that might be around one order of magnitude lower. To identify the smallest widths such fluidic channels can have, as shown in Figure 7(a), we patterned several pairs of parallel lines with different channel widths which were fed by the open U-shaped structures that would form the fluid reservoirs for the ink used. All these lines were scanned at the same laser scan speed of 10 mm/s and an incident laser power of 1 mW, a condition we knew produced barrier-walls that reliably contained the fluid. As shown in Figure 7(b), after introduction of the ink, channels down to a width as small as $\sim 100\ \mu\text{m}$ could reliably guide the fluid. This, to our knowledge, is the smallest dimension for any paper-patterned structures reported so far.¹⁶

B. Writing of fluidic wells

The second set of experiments relates to the writing of wells in paper and their ability to contain fluid. Figure 8(a) shows a set of square wells with dimensions of $5\ \text{mm} \times 5\ \text{mm}$ with barrier-walls written using laser powers ranging from 0.3 mW to 10 mW at a fixed scan speed of 10 mm/s. Red ink was again introduced in a fixed volume of $3\ \mu\text{l}$ that was sufficient to fill each square completely. As shown in Figure 8(b), we similarly observed leakage only for the wells written with a laser power of 0.3 mW, which we have determined to be the lower threshold value.

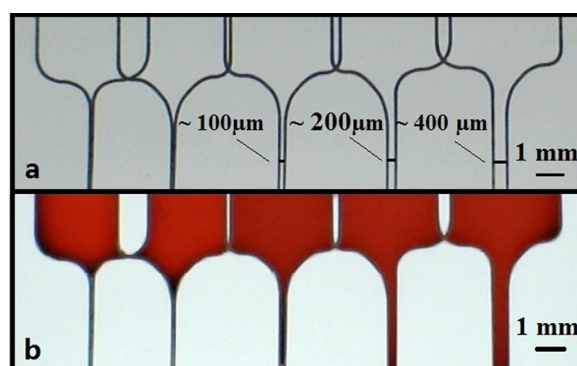


FIG. 7. Photographic image showing a set of parallel fluidic channels having different channel widths, patterned with a laser power of 1 mW, and a scan speed of 10 mm/s (a) before and (b) after introduction of $3\ \mu\text{l}$ of red ink into the reservoirs at the top-end of each of these channels.

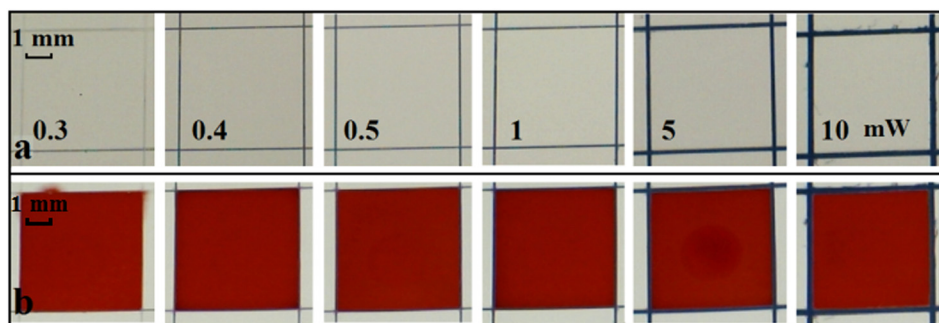


FIG. 8. Photographic image showing (a) a series of 5 mm \times 5 mm square-shaped wells patterned with different laser powers of 0.3, 0.4, 0.5, 1, 5, and 10 mW at a constant scanning speed of 10 mm/s; (b) after introduction of 3 μ l of red ink into each square.

The final step was to determine the maximum volume of liquid that these wells could contain without any sideways leakage, a parameter which is important when dealing with actual samples under test, where loss of potentially expensive samples of reagents outside the test area must be avoided. A similar set of squares was written (shown in Figure 9(a)) into which red ink of different volumes ranging from 1 μ l to 15 μ l (Figure 9(b)) was introduced. Even when the volume increased to a value of 15 μ l, the wells were still able to hold the ink solutions without any overflow.

On further investigation, we observed that a surface-relief ridge was formed along and above the patterned lines because of the polymerisation of the photopolymer that was present on the surface of the nitrocellulose membranes prior to the laser-patterning step and has been investigated through surface-profile imaging measurements. The trace in Figure 9(c) is a surface-profile scan across a laser-polymerised line and clearly shows the presence of a ridge (having a width of ~ 120 μ m and a height of ~ 8 μ m) along the polymerised line. Hence, it can

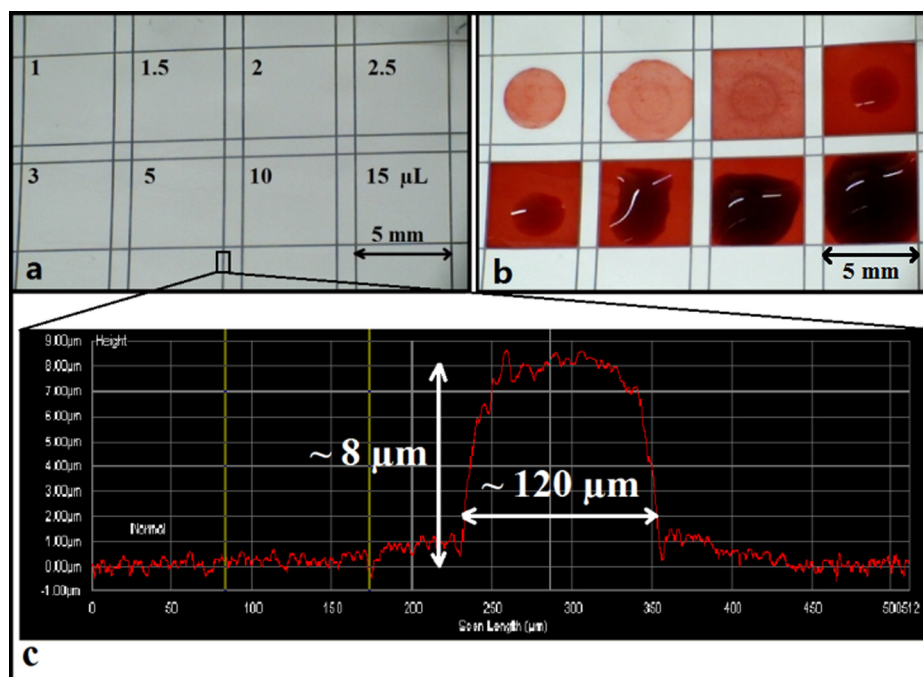


FIG. 9. Image showing (a) a series of 5 mm \times 5 mm wells patterned with a laser power of 1 mW and a scan speed of 10 mm/s; (b) after introduction of red ink in different volumes of 1–15 μ l into each square; (c) a surface-profiler scan across a polymerised barrier-wall.

be concluded that the polymerised patterns defined in nitrocellulose using the LDW method not only show excellent ability in containing small liquid volumes but also show the capability to contain larger liquid volumes without any undesired spill-over, a characteristic that is of immediate interest for practical diagnostic assays.

Following these characterization experiments, we chose to validate the effectiveness of our devices as sensors that can be used for the detection of CRP (C-reactive protein), which is an annular protein found in blood plasma and is mainly used as a marker of inflammation. Measuring and charting CRP levels can provide useful information in determining disease progress or the effectiveness of treatments. This experiment served as a useful proof-of-principle and we performed this detection via the sandwich ELISA (enzyme-linked immunosorbent assay), which is one of the most common reactions used for medical diagnostics.

The grid pattern that formed the square-well detection zones was patterned at a laser power of 1 mW and a scan speed of 10 mm/s, as described earlier. The solution of mouse IgG primary antibody ($2\ \mu\text{l}$ at $360\ \mu\text{g/ml}$) was first pipetted into each square-well of the grid-like structure (as shown in Figure 10(a)) in the nitrocellulose paper, which was then left to dry at room temperature for at least 1 h. The whole paper-device was blocked using a blocking solution of 5% bovine serum albumin (BSA), in phosphate buffered saline (PBS) for 1 h. Following this, the device was washed 3 times with PBS. Sample solutions of CRP were prepared at dilutions of 1 ng/ml, 10 ng/ml, 100 ng/ml, 1000 ng/ml, 10 000 ng/ml, and 100 000 ng/ml. The samples ($2\ \mu\text{l}$) were then pipetted on individual squares and were incubated for 1 h. Then, the device was washed again for 3 times with PBS and a solution of anti-human CRP antibody ($2\ \mu\text{l}$ at $22.5\ \mu\text{g/ml}$) was pipetted into each square-well. The whole device was again left for 1 h for incubation and this was followed by washing 3 times with PBS. In the next step, the HRP

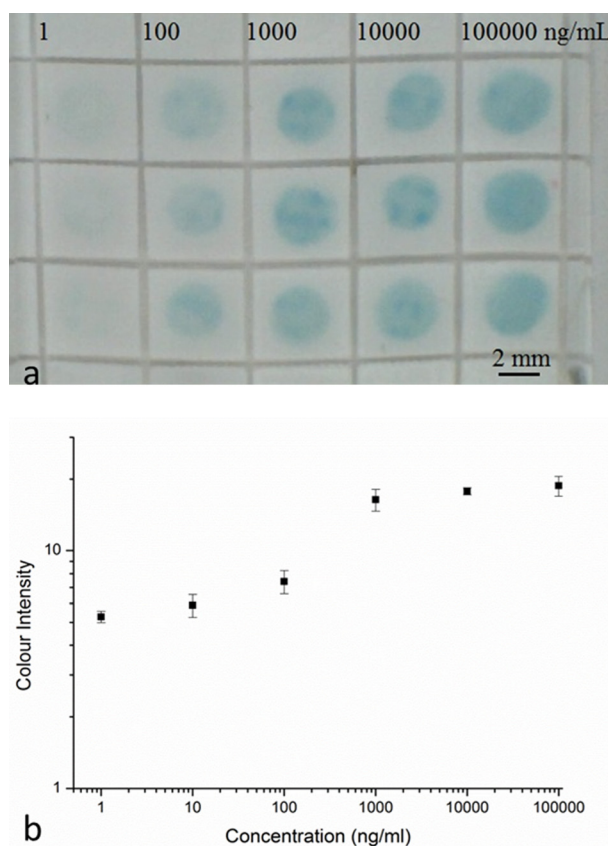


FIG. 10. (a) Selected area of 5×5 mm well structure patterned with a laser power of 1 mW and a scan speed of 10 mm/s and results for the detection of CRP by the sandwich ELISA. (b) Calibration curve constructed using the grayscale intensity values taken from the image shown in (a). Error bars indicate the standard deviation for 4 individual measurements.

(horseradish peroxidase) conjugated streptavidin was added into each well and the device was left in the dark for 20 min of incubation and then washed again using PBS. Finally, the chromogenic reagent TMB (3,3',5,5'-Tetramethylbenzidine) was pipetted on the whole device and the colour change produced was imaged by taking a photograph (as seen in Figure 10(a)) of the paper-device after 2 min with a USB camera.

The image was then processed with the ImageJ software (National Institutes of Health, USA) to extract the respective colour intensities of the blue colour produced within the square-well detection zones. The average grayscale intensities of each detection zone and of the background of the image were measured, and the background intensity was subtracted from the intensity of each detection zone to obtain the actual colour intensity of each spot to eliminate the influence of the background. By measuring the colour intensities of the known concentrations, we were then able to plot the curve (as seen in Figure 10(b)) that can then be used for calibration.

IV. CONCLUSION

We have demonstrated that a simple, low-cost laser-based direct-write technique based on the principle of light-induced polymerisation can be used for the rapid fabrication of fluidic structures in nitrocellulose membranes. The laser polymerised patterns form the hydrophobic barrier-walls of interconnected hydrophilic fluidic structures such as channels and wells. This approach is non-lithographic and mask-less, and being non-contact in nature, offers the advantage of minimizing cross-contamination that could arise during fabrication. Compared with other methods used in the production of microfluidic devices in nitrocellulose, the technique is also well-suited for up-scaling to mass-production. We have shown that using this method it is possible to create microfluidic channels and barrier-walls with dimensions of $\sim 100\ \mu\text{m}$ and $\sim 60\ \mu\text{m}$, respectively, the smallest values that have been reported so far. We believe that this technique could be an ideal choice for rapid fabrication of nitrocellulose-based microfluidic devices that can be used for a variety of applications such as clinical diagnostics and analytical chemistry.

ACKNOWLEDGMENTS

The authors acknowledge the funding received via the Engineering and Physical Sciences Research Council (EPSRC) Grant Nos. EP/J008052/1 and EP/K023454/1, and the funding received via a Knowledge Mobilisation Fellowship for Dr. Collin Sones from the Institute for Life Sciences and the Faculty of Health Sciences of the University of Southampton.

¹G. M. Whitesides, "The origins and the future of microfluidics," *Nature* **442**, 368–373 (2006).

²G. M. Whitesides, "Cool, or simple and cheap? Why not both?," *Lab Chip* **13**, 11–13 (2013).

³A. W. Martinez, S. T. Phillips, M. J. Butte, and G. M. Whitesides, "Patterned paper as a platform for inexpensive, low-volume, portable bioassays," *Angew. Chem., Int. Ed.* **46**, 1318–1320 (2007).

⁴A. W. Martinez, S. T. Phillips, E. Carrilho, S. W. Thomas, H. Sindi, and G. M. Whitesides, "Simple telemedicine for developing regions: Camera phones and paper-based microfluidic devices for real-time, off-site diagnosis," *Anal. Chem.* **80**, 3699–3707 (2008).

⁵Y. Lu, W. W. Shi, L. Jiang, J. H. Qin, and B. C. Lin, "Rapid prototyping of paper-based microfluidics with wax for low-cost, portable bioassay," *Electrophoresis* **30**, 1497–1500 (2009).

⁶J. L. Tonkinson and B. A. Stillman, "Nitrocellulose: A tried and true polymer finds utility as a post-genomic substrate," *Front. Biosci.* **7**, C1–C12 (2002).

⁷A. W. Martinez, S. T. Phillips, B. J. Wiley, M. Gupta, and G. M. Whitesides, "FLASH: A rapid method for prototyping paper-based microfluidic devices," *Lab Chip* **8**, 2146–2150 (2008).

⁸J. L. Delaney, C. F. Hogan, J. F. Tian, and W. Shen, "Electrogenerated chemiluminescence detection in paper-based microfluidic sensors," *Anal. Chem.* **83**, 1300–1306 (2011).

⁹X. Li, J. F. Tian, G. Garnier, and W. Shen, "Fabrication of paper-based microfluidic sensors by printing," *Colloid Surf. B* **76**, 564–570 (2010).

¹⁰E. Carrilho, A. W. Martinez, and G. M. Whitesides, "Understanding wax printing: A simple micropatterning process for paper-based microfluidics," *Anal. Chem.* **81**, 7091–7095 (2009).

¹¹V. Leung, A. A. M. Shehata, C. D. M. Filipe, and R. Pelton, "Streaming potential sensing in paper-based microfluidic channels," *Colloid Surf. A* **364**, 16–18 (2010).

¹²C. D. Souza, O. C. Braga, I. C. Vieira, and A. Spinelli, "Electroanalytical determination of sulfadiazine and sulfamethoxazole in pharmaceuticals using a boron-doped diamond electrode," *Sens. Actuator, B* **135**, 66–73 (2008).

- ¹³X. Li, J. F. Tian, T. Nguyen, and W. Shen, "Paper-based microfluidic devices by plasma treatment," *Anal. Chem.* **80**, 9131–9134 (2008).
- ¹⁴E. Fu, P. Kauffman, B. Lutz, and P. Yager, "Chemical signal amplification in two-dimensional paper networks," *Sens. Actuator, B* **149**, 325–328 (2010).
- ¹⁵E. M. Fenton, M. R. Mascarenas, G. P. Lopez, and S. S. Sibbett, "Multiplex lateral-flow test strips fabricated by two-dimensional shaping," *ACS Appl. Mater. Interfaces* **1**, 124–129 (2009).
- ¹⁶A. K. Yetisen, M. S. Akram, and C. R. Lowe, "Paper-based microfluidic point-of-care diagnostic devices," *Lab Chip* **13**, 2210–2251 (2013).
- ¹⁷X. Li, D. R. Ballerini, and W. Shen, "A perspective on paper-based microfluidics: Current status and future trends," *Biomicrofluidics* **6**(1), 011301 (2012).



CrossMark
click for updates

Cite this: *Lab Chip*, 2015, 15, 4054

Engineering fluidic delays in paper-based devices using laser direct-writing

P. J. W. He,^{*} I. N. Katis, R. W. Eason and C. L. Sones

We report the use of a new laser-based direct-write technique that allows programmable and timed fluid delivery in channels within a paper substrate which enables implementation of multi-step analytical assays. The technique is based on laser-induced photo-polymerisation, and through adjustment of the laser writing parameters such as the laser power and scan speed we can control the depth and/or the porosity of hydrophobic barriers which, when fabricated in the fluid path, produce controllable fluid delay. We have patterned these flow delaying barriers at pre-defined locations in the fluidic channels using either a continuous wave laser at 405 nm, or a pulsed laser operating at 266 nm. Using this delay patterning protocol we generated flow delays spanning from a few minutes to over half an hour. Since the channels and flow delay barriers can be written via a common laser-writing process, this is a distinct improvement over other methods that require specialist operating environments, or custom-designed equipment. This technique can therefore be used for rapid fabrication of paper-based microfluidic devices that can perform single or multistep analytical assays.

Received 27th May 2015,
Accepted 21st August 2015

DOI: 10.1039/c5lc00590f

www.rsc.org/loc

Introduction

Ever since the first proposal from the Whitesides' group in 2007,^{1,2} the field of paper-based microfluidics has been widely researched and many different lab-on-chip (LOC) type devices have been developed for implementing a wide range of analytical assays. The demand for low-cost alternatives to conventional diagnostic tools has been the driving force that has spurred significant developments in this field. A range of diagnostic assays, ranging from lateral flow type semi-quantitative diagnostic assays to multiplexed tests have already been implemented using such paper-based fluidic devices.^{3–6}

Several approaches which include photolithography,⁷ followed by wax printing,^{8,9} inkjet printing,^{10,11} plasma oxidation,^{12,13} laser cutting¹⁴ and flexographic printing¹⁵ have been used for fabricating paper-based fluidic devices. We have recently reported the use of a laser direct-write (LDW) approach for creating fluidic patterns in porous media, namely cellulose paper and nitrocellulose membranes.^{16,17} When compared to alternative techniques, the LDW method presents important advantages: it does not need expensive and fixed patterning masks, custom-modified equipment, specialist chemicals or inks, and it overcomes the limitation on achievable feature size that can result from the lateral spreading of the hydrophobic material used to form the

fluidic channel walls. Finally, and most importantly, it is suitable for scale-up towards mass-production, possibly on a roll-to-roll basis. Using this approach, we have shown that it is possible to fabricate paper-based fluidic devices, which consist of interconnected hydrophilic channels demarcated by hydrophobic polymerised barrier walls that extend through the thickness of the paper, with feature dimensions below a value of 100 μm .

Research into the development of methodologies to control, and in particular delay the flow of fluids in these devices is a much needed requirement that would enable greater functionalities in such paper-based devices. The introduction of control over the transport of fluid could enable a number of other diagnostic detection tests that have multiple timed analytical steps, for example a multistep test such as the enzyme-linked immunosorbent assay (ELISA), which is most often performed under controlled laboratory environments and has a protocol that requires either a machine or skilled personnel to perform the sequential steps at specific time intervals.^{18,19} In addition to this, a number of additional attributes could be incorporated though controllable fluid flow, such as fluidic diodes and valves,^{20,21} timers and metering,^{22,23} fluidic batteries,²⁴ and such desirable multistep sample processing sequences have already been reported in the literature.^{25,26}

Current methods that have already been reported for manipulating fluid flow in paper-based fluidic devices can be classified into four main categories: manually activated control,^{12,21} modification of the topology and geometry,^{18,27}

Optoelectronics Research Centre, University of Southampton, Highfield, Southampton, SO17 1BJ UK. E-mail: ph3e12@soton.ac.uk; Tel: +44 (0)2380 599091

addition of dissolvable chemicals,^{19,20} and creation of physical barriers,²⁸ and each of these procedures has its own advantages, as well as some characteristic limitations. Techniques that use manually activated control and physical barriers require additional fabrication steps while adding dissolvable chemicals has the dual drawback of additional processing steps and introduction of chemicals such as sugar in the flow-path which might alter or limit the intended function of the devices. Implementation of a similar flow-delay might be possible through careful considerations of the geometry of the fluidic channels. However, to introduce a flow-delay through changes to the channel geometry will require either an increase of the channel width or an increase of the channel length, both of which would have the undesired effect of either increasing the foot-print of the device or increasing the volume of the reagents used. Our method instead allows the introduction of flow-delay to any pre-designed device without any change to the channel geometries, thus keeping the device compact and requiring smaller reagent volumes.

In this work, to control fluid flow or delivery, we report the use of a new approach that is an extension of the basic LDW technique that we have earlier reported for creating fluidic patterns and devices made up of interconnected channels and reaction chambers. The LDW method (described in ref. 16 and 17) uses lasers to create fluidic patterns in paper via the light-induced polymerisation of a photopolymer previously impregnated in the paper. Laser-scanning of the paper substrate results in the creation of hydrophobic photopolymer tracks that extend throughout the thickness of the paper, and form the boundary walls of the laser-defined fluidic patterns. To produce flow-control, the approach presented here relies on use of physical barriers that run across the flow-path (i.e. perpendicular to the fluidic channels) and hence introduce a delay in the fluid flow. As was the case for our LDW method where we demonstrated the use of laser light to form patterns in paper through light-induced photo-polymerisation, the flow delay barriers in this report are created using the same principle of light-induced photo-polymerisation.

The schematic in Fig. 1a shows a simple fluidic geometry that can be used to produce delay barriers via either of the

two following methods, (1) by controlling the depth of solid/impermeable barriers (as shown in Fig. 1b) that are patterned across the flow and which simply impede the fluid flow by reducing the depth of the fluidic channel or, (2) by forming porous barriers (as shown in Fig. 1c) that allow controlled leakage of the fluids. As described and discussed in the later sections, control over the depth of the barriers of the first type or the porosity of the barriers of the second type is obtained by simply adjusting the laser-writing parameters such as the laser output power and scan speed. Unlike other fluid flow control methods reported for paper-based microfluidics, the approach presented here does not require any additional processing equipment or specialist materials and as described earlier uses the same fabrication approach that defines the fluidic channels themselves.

Experimental section

Laser setups and materials

The lasers used for the direct-writing process were a Q-switched Nd: YVO₄ laser (B M Industries, Thomson CSF Laser, France) operating at 266 nm, with a pulse duration of 10 ns, a maximum single pulse energy of 2 mJ, and a repetition rate of 20 Hz (used for method 1 as outlined above, and shown in Fig. 1b) and a 405 nm continuous wave (c.w.) diode laser (MLD™ 405 nm, Cobolt AB, Sweden) with a maximum output power of ~110 mW (for method 2, shown in Fig. 1c).

The paper substrates used were Whatman® no. 1 filter paper from GE Healthcare Inc. The photopolymer chosen for these experiments was Sub G, from Maker Juice, USA. The sample solution used for characterising the flow delivery delay was Tris Buffered Saline (TBS, 20 mM Tris, pH approx. 7.4, and 0.9% NaCl), which is a buffer commonly used in diagnostic assays. The inks we used for validating the fluid delay in our patterned devices were blue, black and red bottled-inks from Parker, UK.

Creating fluidic delays

We first patterned fluidic channels with the design geometry shown in the schematic of Fig. 1d, using the LDW technique, which we have previously optimised via a systematic study. The width and length of the fluidic channel was 5 mm and 15 mm respectively, and the inlet end of the channel was designed to replicate the shape of a funnel. These fluidic channel patterns were defined using the c.w. laser operating at 405 nm.¹⁷ We subsequently patterned the fluidic barriers within the channels using either of the two lasers described previously.

The channels were patterned using the c.w. laser due to the much higher writing speeds achievable (almost three orders of magnitude greater than that for the pulsed 266 nm source). To ensure that there was sufficient fluid to wick the entire length of the channel, we cut and stacked multiple (8 in this example) pieces of paper (of 3 mm × 5 mm), and positioned them at the wider end of the funnel-shaped inlet of the channel, and loaded it with a comparatively large volume

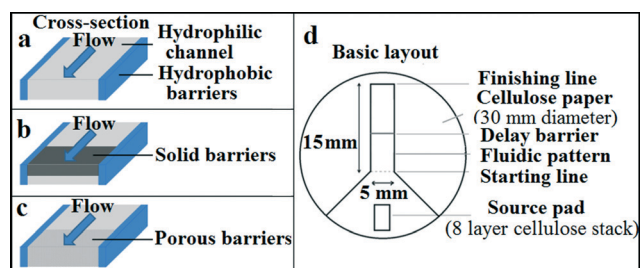


Fig. 1 Schematic representation of: a) cross-section of a fluidic channel; b) cross-section of a fluidic channel with solid barriers; c) cross-section of a fluidic channel with porous barriers; d) layout of a pre-defined fluidic structure.

of fluid ($\sim 40\ \mu\text{L}$) – the stack serving as a continuous reservoir of liquid.

During our earlier studies into the fabrication of fluidic channels using pulsed laser irradiation, we observed that by controlling the scanning speed (and therefore the effective exposure) of the laser beam, we could polymerise lines of various depths inside the paper substrate as illustrated schematically in Fig. 2a. Slower scanning speeds produced polymerisation through the full depth of the paper, while faster scanning speeds led to photo-polymerisation only in the upper portion of the paper, thus creating partial barriers that the liquid had to overcome. These fluidic ‘delay barriers’ can therefore decrease the flow by a rate that is proportional to their depth, and hence this principle can be used to impose a user-defined variable time-delay in the wicking of the liquids and test samples.

An alternative approach, as illustrated in Fig. 2b allows the writing of barriers via manipulation of the extent or degree of polymerisation using c.w. laser exposure. In this case however, the barriers produced extend throughout the full paper thickness, but the degree of polymerisation can be engineered to form barriers whose porosity can be controlled

by varying incident laser fluence, which is determined by the incident laser power and the laser scan speed. For these less dense, leaky barriers, we believe the polymerised material does not completely fill the voids within the paper matrix, thus forming permeable barriers.

Fig. 3 illustrates the difference between such solid and porous polymerised barriers. As shown in Fig. 3a, the polymerised regions for solid barriers written with a pulsed laser could only be observed on the top, and not the lower face of the paper, suggesting partial polymerisation through the thickness of the paper. However, the polymerised regions for porous barriers written with a c.w. laser always extended throughout the entire paper thickness, as shown in Fig. 3b. Blue ink was added to the sample in Fig. 3a to enhance the contrast between the paper substrate and the lines.

As described below, we compare both of these methods for generating controllable flow delay in fluidic channels. The study was aimed at characterising the influence of the laser fluence and exposure on the depths and porosity of the barriers for methods 1 and 2 respectively, including an investigation of delay as a function of position and number of barriers. Since both the fluidic channel walls and delay barriers can be patterned using the same LDW process, this technique should have immediate appeal to manufacturers wishing to develop such paper-based devices on a large scale where production speed and cost are two of the main considerations.

Results and discussion

Method 1: delay via solid barriers created by pulsed laser writing

In order to explore the relationship between the depth of the solid barriers and the incident fluence, which depends on both the laser average power and the laser scan speed, we first fabricated a set of polymerised barriers written with a fixed incident average power ($7\ \text{mW}$) but different speeds from $0.1\ \text{mm s}^{-1}$ to $1.5\ \text{mm s}^{-1}$. We then measured the depth of these barriers by cutting the paper substrates along a line that intersects the barriers, and then imaged the cross-sections of the paper using an optical microscope. The relationship between the depth and the barrier writing speed is

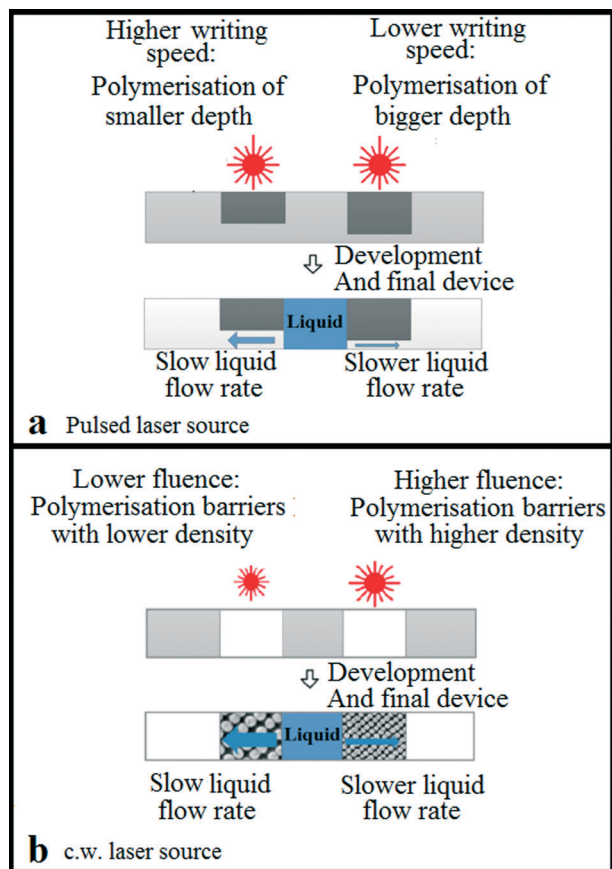


Fig. 2 Schematic of the fabrication of polymerised barriers of: a) variable depth inside the paper substrate, created using pulsed laser exposure; b) variable degree of polymerisation extending throughout the full thickness of the paper, created using c.w. laser exposure. Both methods allow for controlled wicking, and variable flow delays.

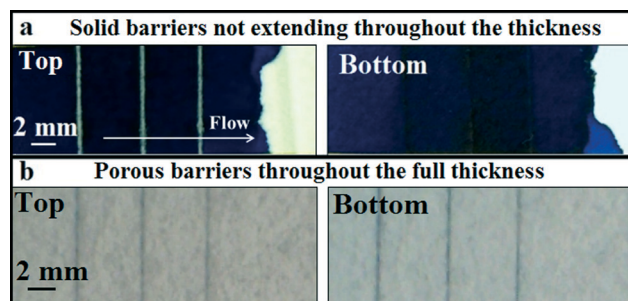


Fig. 3 Images showing the delay barriers from both sides of the cellulose paper. a) Depth-variable solid barriers formed by pulsed laser exposure; b) porosity-variable barriers formed by c.w. laser exposure.

plotted in Fig. 4, which shows that an increase in the writing speed from 0.3 mm s^{-1} to 1.5 mm s^{-1} leads to a decrease in the depth of the barrier from $82 \pm 6\%$ to $17 \pm 6\%$ of the thickness of the paper.

To understand and quantify the usefulness of these solid barriers with variable depths in both delaying and even completely stopping the fluid flow, we fabricated a set of 4 channels, as shown in Fig. 5a, and then patterned barrier lines perpendicular to the flow direction. Each of the fluidic channels was inscribed with two barriers, both of which had been written under the same writing conditions. Importantly, for each of the fluidic channels (1–4) these pairs of horizontal lines were written with the same incident average power (7 mW) but different speeds namely, 1 mm s^{-1} , 0.7 mm s^{-1} , 0.5 mm s^{-1} and 0.3 mm s^{-1} , thus forming solid barriers with differing depths, which can be calculated from the plot in Fig. 4.

As shown in Fig. 5b and c, blue coloured ink introduced from the inlet of the channels (marked in the image) experiences a flow rate that is a clear function of the presence and strength of the inscribed barriers, with channel 4 being the slowest, and channel 1 the fastest. The ink was introduced at the same time in each of the four channels. Fig. 5b and c are images taken 2 minutes and 3 minutes after the introduction of ink, and as seen in Fig. 5b, the ink has already flowed past the two barriers of channel 1, is leaking past the second barrier of channel 2, has just reached the second barrier in channel 3, while it has just crossed the first barrier in channel 4.

To quantify the flow delay versus writing conditions, we used the arrangement of Fig. 1(d), which is shown in greater detail in Fig. 6, using TBS (pH = 7.4), a reagent conventionally used as a buffer in bio-chemical assays, as the liquid medium. The fluid 'delivery time' was defined and measured as the time the TBS solution needed to travel from the starting line to the finishing line, a distance of 15 mm in total. The channel walls were written with the 405 nm c.w. laser (20 mW , 10 mm s^{-1}), whereas the barriers were written with a pulsed laser at writing speeds from 1 mm s^{-1} to 0.3 mm s^{-1} .

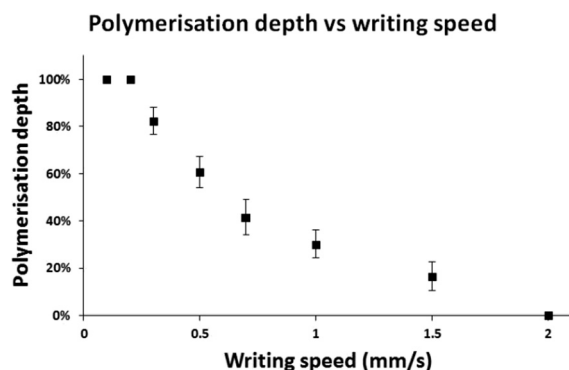


Fig. 4 Comparison between the depth of the polymerisation in the paper and the delay barrier writing speed. Error bars indicate the standard deviation for 5 measurements.

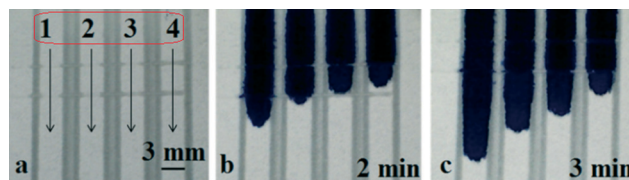


Fig. 5 Sequential images a), b) and c) that demonstrate the delay of the liquid flow after introduction of blue ink in fluidic channels with barriers created using different writing speeds.

First, we studied the consequence of having solid barriers with different depths in the flow-path, however with only one delay barrier at position P1 (as shown in Fig. 6) in each of the pre-defined devices. Several devices, each with one single delay barrier were written under different writing conditions, by changing the scan speed (from 1 mm s^{-1} to 0.3 mm s^{-1}) at a constant laser average power of 7 mW, which corresponded to creation of solid barriers with depths ranging from $30 \pm 6\%$ to $82 \pm 6\%$ of the thickness of the paper (as shown in Fig. 4). We have quantified the ability of the barriers to delay the fluid flow using a normalised 'delay factor', which we define as the time to flow (from the starting line to the finishing line) in a channel that has barriers, divided by the time to flow in a channel without barriers:

$$\text{Delay factor} = \frac{\text{Flow time for a channel with barriers}}{\text{Flow time for a channel without barriers}}$$

The flow time for the channel with the same geometry as that in Fig. 6 but without any barriers is approximately 2 minutes and 40 seconds.

The results for the delay factor are plotted in Fig. 7 which show an increase in the delay factor from ~ 1.1 to ~ 1.6 with an increase in the barrier depth from $17 \pm 6\%$ to $82 \pm 6\%$.

Method 2: delay using porous barriers created by a c.w. laser

In this case, both the fluidic channels and the flow delay barriers were written with the same c.w. laser (in a common programmed writing step) by simply changing either the laser output power or writing speed. To allow for a direct comparison with the results for the solid barriers, fluidic devices that were tested had the same design as in Fig. 6.

In this case however, four porous barriers were written across the fluidic channels, to explore the role of number and position of barriers as shown in Fig. 6. A

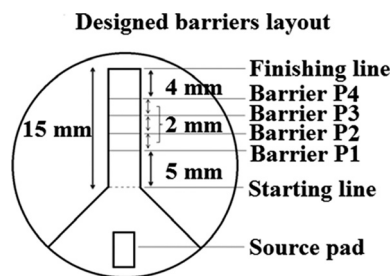


Fig. 6 Schematic representation of designed barrier layout showing the position of delay barriers (P1, P2, P3 and P4).

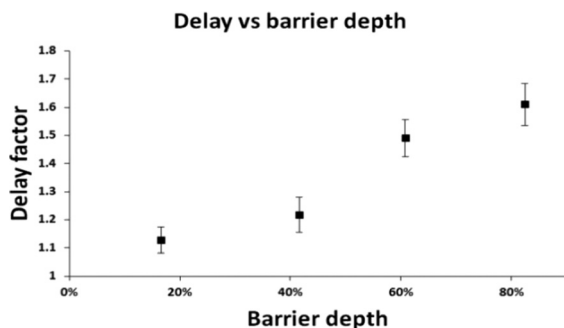


Fig. 7 Plots showing the delay factor for devices with barriers having different depths. Barriers were written with different writing speeds at a fixed average power of 7 mW. Error bars indicate the standard deviation for 5 measurements.

comprehensive study was performed to explore the flow delay induced through barriers written with a range of different writing conditions. The fluid delivery time and the percentage delay were calculated as for method 1.

We first did a comparative study for barriers patterned with different writing conditions, namely different laser powers and scan speeds. Subsequently, we changed the

number of barriers to explore the relationship between the delay and the number of barriers in the flow path. As in Fig. 6, a one barrier design refers to a device with a single barrier patterned at position P1 in the channel; a two barrier device refers to a channel with two barriers patterned at P1 and P2; and so on.

As shown in Fig. 8a, for barriers written with a fixed scan speed of 100 mm s^{-1} , the fluid delay gradually increased with an increase of the laser power, and progressively decreased for barriers written with an increasing scan speed at a fixed laser output power of 20 mW, as shown in Fig. 8b. These results show that the porosity of these barriers is a clear function of the laser fluence used and that any targeted delay (within the experimental error) can be achieved by choosing the correct fluence. Similarly, for the plots shown in both Fig. 8c and d, which are based on the use of multiple barriers, we observe identical trends – for barriers written with the same writing conditions, the delay increases with an increase in the number of barriers.

In addition to this dependence on the porosity of the barriers and the number of barriers, we observed that the fluid delay also depended on the position of the porous barrier.

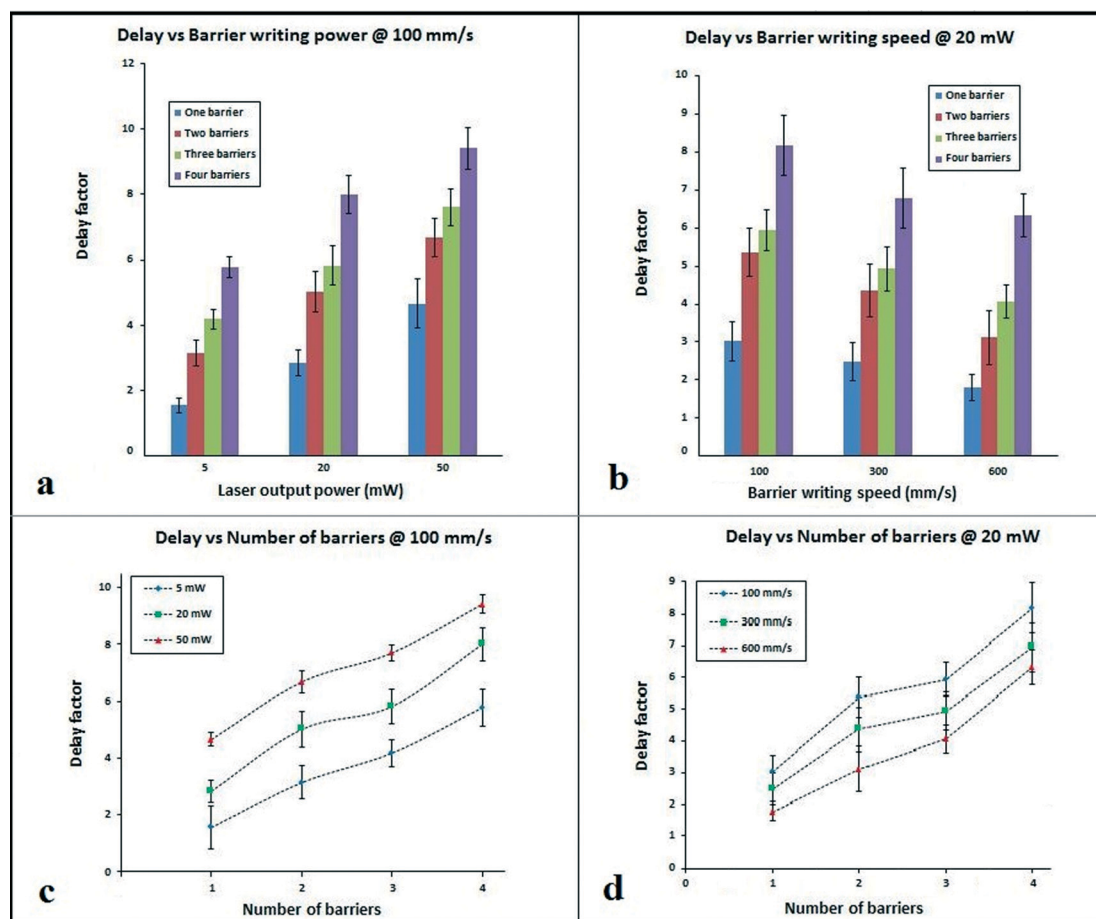


Fig. 8 Plots showing the delay factor of delay-barrier-designed devices. a) Barriers written with different laser output powers at a fixed scan speed; b) barriers written with different scan speeds at a fixed laser output power; c) different number of barriers written at a fixed scan speed; d) different number of barriers written at a fixed laser output power. Error bars indicate the standard deviation for 5 measurements, and lines are a simple guide for the eye.

We introduced a single porous delay barrier written under the same writing conditions (200 mm s^{-1} scan speed and 20 mW laser output power) at different positions (P1–P4) as shown in Fig. 6, and then studied the fluid delay. The plot of the fluid delay versus the position of the porous barrier is shown in Fig. 9. As the delay barrier was shifted further from the starting line towards the finishing line, the delay factor rapidly dropped from ~ 2.5 (for position P1) to ~ 1.3 (for position P4). We believe this is because of the geometry of the device, since the volume of the paper that serves as the reservoir for the fluid flow changes with a shift in the position of the delay barrier. The volume before the delay barrier acts as a pump for subsequent flow, thus affecting the flow rate after the barrier. As shown in Fig. 6, the closer the barrier is to the starting line, the smaller the source paper volume is, and this leads, we suggest, to a lower pump force and hence a lower flow rate and larger fluid delay.

Multiple fluid delivery using delaying barriers

Implementation of automated paper-based devices (as described by Lutz *et al.*,¹⁹ and Apilux *et al.*,¹⁸) that are user-friendly and need minimal intervention from the patient or an unskilled user need strategies that allow control over the flow of several liquids (reagents and sample) along their pathways. Such devices allow the implementation of a multi-step assay (such as an ELISA), and in this section, using fluid delay strategies effected using the flow-barriers described earlier, we demonstrate the usefulness of our method to fabricate such automated paper-based tests. Fig. 10 shows a device that uses a network of three identical channels for sequential delivery of three fluids to a common detection or reaction point. As shown in Fig. 10, sequential delivery of each of these fluids is made possible by introducing (a set of three identical) porous barriers written with a c.w. laser across the fluid channels. By changing the porosity of each set of delay barriers through simple adjustments of the laser parameters, different delays can be introduced into each channel.

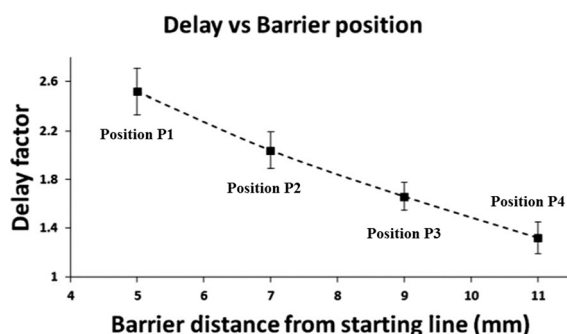


Fig. 9 Plots showing the relationship between the fluid delay factor and the position of the delay barriers (distance to the starting line) with the same condition of 200 mm s^{-1} scan speed and 20 mW laser output power. Error bars indicate the standard deviation for 5 measurements, and the line is a guide for the eye.

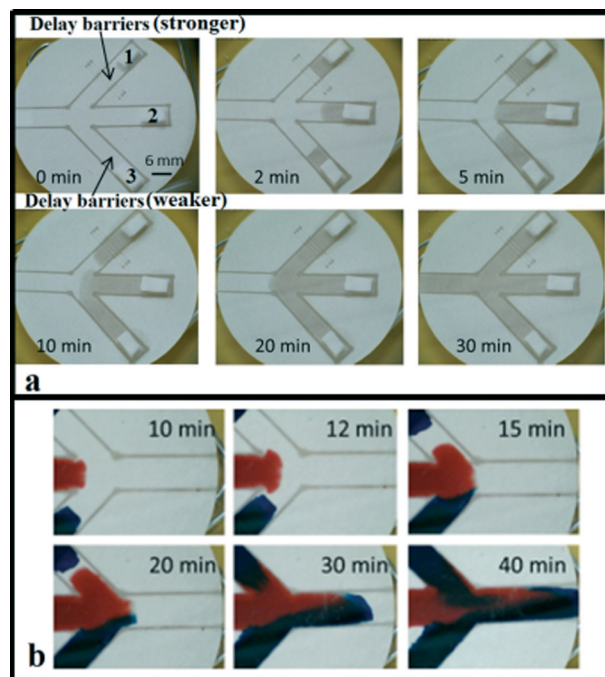


Fig. 10 Image showing a 2D multi-channel fluidic device used for sequential delivery of three fluids. It has three identical channels (6 mm width and 23 mm length) modified with different delay barriers (1. stronger delay barriers; 2. no barriers; 3. weaker delay barriers). a) Sequential images showing the arrival of TBS from each channel at different times; b) sequential images showing the arrival and mixing of blue and red ink from three separated channel and the subsequent mixing of the inks.

To show the operation of our devices, as also described earlier, we first introduced a source pad (a stack of 8 cellulose papers) into each channel that allows us to load a comparatively large volume of fluid ($\sim 40 \mu\text{L}$) in to each channel, and also serves as a continuous reservoir of liquid (Fig. 10). We first tested the performance of our devices using TBS as the test-fluid which was introduced into the source pad in each of the three channels. Fig. 10a is a set of images that are snapshots taken sequentially at different times after introducing the TBS into the source pads. The fluid in channel 2 (that does not have any delay barriers) arrived at the intersection zone first (after 5 minutes) and continued to flow onwards until the fluid in channel 3 (with weaker delay barrier) arrived at the intersection (after 10 minutes). Thereafter, the fluids from these two channels mixed and flowed forward until the arrival of the fluid from channel 1 (with the stronger delay barriers) after 20 minutes. Finally, the mixture of three fluids then wicks through the reaction pathway in the following 10 minutes.

To further illustrate the dynamics related to the mixing of the different fluids and to make the concept of flow delay more obvious, we instead used two different coloured inks to source the three separate channels (blue for channel 1 and 3 and red for channel 2). The sequential images that show the flow through the device are shown in Fig. 10b. When compared to the (blank) channel 2 that did not have any delay

barriers, the fluid delivery through channel 1 and channel 3 were delayed by 15 and 5 minutes respectively. The results for both of the devices that were either tested using TBS or the coloured inks show clear evidence that our laser-patterned delayed-fluid flow strategy can be used to make paper-based automated devices. As a final step, we demonstrate the use of this strategy to fabricate devices that can implement multi-step ELISA protocols.

Automated multistep assay for CRP detection by sandwich ELISA

This section describes the use of our fluid delay strategy to implement a multiple step ELISA that enables the detection of CRP (C-reactive protein). We have chosen CRP as an example for evaluating this automated paper-based device because it is an important and realistic analyte which is frequently measured for early-stage diagnosis.^{29,30} Devices (with the 2D multi-channel geometries) identical to that shown in Fig. 10 were used to realise a multistep enzyme-based immunoassay that allowed for the detection of CRP. As shown in Fig. 11a, the three individual arms of the device were used to sequentially deliver the three different reagents – channel 1 delivered streptavidin-HRP; channel 2 delivered the sample; channel 3 delivered the detection antibody through to the capture antibody which was immobilized in the detection zone (identified in the image with a rectangular frame). As mentioned earlier, the device geometry and the delay mechanism used were the same as those in Fig. 10, except that an additional cellulose absorbent pad was attached at the end of the detection pathway for collection of the excess fluid.

The ELISA kit used in the implementation of the CRP detection (DuoSet® Human C-Reactive Protein/CRP) was purchased from R&D Systems, Inc. (UK). All the antibodies used were from this kit and were diluted to the working concentrations of $3.6 \mu\text{g mL}^{-1}$ and 162 ng mL^{-1} for capture antibody

and conjugated antibody respectively. The CRP human standard (C1617) was purchased from Sigma-Aldrich (UK) and diluted to working concentrations using calibrator diluent (1% BSA (bovine serum albumin) in PBS (phosphate-buffered saline)).

The capture antibody was pipetted at four distinct spots (1 μL per spot) within the detection zone, and then left to dry for one hour at room temperature. The whole device was then immersed in a blocking solution (5% BSA in PBS) for one hour at room temperature, followed by three sequential washing steps using PBS. After subsequent drying, the device was ready to use.

In order to implement the assay, 40 μL of each reagent was sequentially pipetted onto the source pads within a period of a few seconds in each channel and the device was left in a covered petri dish at room temperature to allow for the timed, sequential delivery of the individual solutions along each channel, into the detection zone for reaction with the capture antibodies immobilized therein. The devices were held along their edges by a specially designed holder that suspended them in air thus eliminating any contact with the petri dish surface underneath which otherwise would have altered the flow of the reagents. After 30 minutes, the whole device was washed three times using PBS for five minutes each. Finally, 10 μL of the colorimetric substrate TMB (tetramethylbenzidine) was added at the detection zone and the result was read after 20 minutes. Ideally, such a device should also enable the sequential delivery of TMB to the detection zone *via* another fluid flow channel, and that would then be a true example of a sample-in-result-out type device, however, for this initial proof-of-principle experiment where we intend to show the usefulness of delays, we have not yet manufactured such a test. In the case of several routinely employed assays, the detection antibodies are tagged either with a gold nanoparticle or coloured beads, and if we choose to use detection antibodies labelled in this fashion, then there would not be the need to have this additional delivery path. Fig. 11b–d show the results for the detection of different concentrations of CRP, and the clearly visible and distinct blue spots that appear in the detection zone (with minimal background colour ‘noise’) confirm the presence of CRP in the sample. Fig. 11e shows the result for a control device tested with a sample solution that did not have CRP. As shown in the figure, for this negative result, we do not observe any specific blue spots in the detection zone. The colour intensity of the spots in Fig. 11b is greater than that in Fig. 11c, and this relates to the higher concentration of CRP in the corresponding samples that were used in the two different cases. For some of the spots, their non-symmetric circular shape is as a result of the spotting of the capture antibodies more towards one edge of the channel walls, resulting in a clipping of their circular shape. The images in Fig. 11b–d clearly demonstrate the successful detection of CRP on our laser-patterned paper-based device with incorporated fluid delay mechanisms. This device is an example of a semi-automatic type test that still requires intervention from a user, but we are planning on developing this concept further

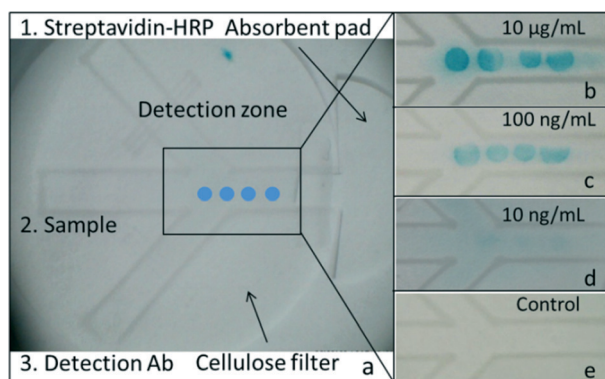


Fig. 11 Automated multi-step ELISA for CRP detection in a 2D multi-channel fluidic device. a) Image of a device showing its design and indicating reagent locations for the assay. Four blue spots, shown schematically in a), represent the position of immobilized capture antibody in the detection zone. b), c), d) and e) are photos of the CRP ELISA result on the device for different sample concentrations of $10 \mu\text{g mL}^{-1}$, 100 ng mL^{-1} , 10 ng mL^{-1} and no sample respectively.

in the immediate future to enable a fully-automated device which would then be a true example of a sample-in-result-out type device. In addition, using our devices, we were also able to detect CRP with concentrations of less than $\sim 10 \text{ ng mL}^{-1}$, which we believe is close to the limit of detection.

Conclusions

In this work, we report a new method based on our LDW technique that allows the fabrication of pre-programmed or timed fluid delivery in paper-based fluidic devices without any additional equipment or minimal actions from the user. Barriers, aligned perpendicular to the flow-path, and used to control the fluid flow in a channel were either solid barriers with differing depths, or barriers with differing porosity, and these could be fabricated by simple adjustments of the laser patterning parameters, such as the laser power and the writing speed. Both types of barriers yield similar results for control over the fluid flow. These programmable fluid delay techniques should help to further improve the functionalities of paper-based microfluidic devices as such control can be used to enable semi-automated multi-step fluidic protocols. In contrast to other methods reported for controlling fluidic transport, our approach eliminates the requirements for cleanroom-based steps, or custom-designed equipment, or the need for long flow paths, which can then translate into requirements for larger analyte volumes. Most importantly, since the delay-mechanism can be an integral part of the fabrication of the fluidic devices themselves, we believe this integrated process presents a considerable manufacturing and hence commercial advantage. With our existing laser-writing setup, it is possible to pattern devices, using a c.w. laser, at speeds of one metre per second, and accounting for the time required for the pre- and post-processing steps needed to make a complete device, our estimate is that it is possible to fabricate at least one device per second. Above all, we believe that this method could be an ideal choice for rapid fabrication of custom-designed paper-based microfluidic devices for realizing single or multistep analytical tests.

Acknowledgements

The authors acknowledge the funding received *via* the Engineering and Physical Sciences Research Council (EPSRC) Grant No. EP/J008052/1 and EP/K023454/1, and the funding received *via* a Knowledge Mobilisation Fellowship for Dr. Colin Sones from the Institute for Life Sciences and the Faculty of Health Sciences of the University of Southampton. The data for this paper can be found at 10.5258/SOTON/377463.

Notes and references

- 1 A. W. Martinez, S. T. Phillips, M. J. Butte and G. M. Whitesides, *Angew. Chem., Int. Ed.*, 2007, **46**, 1318–1320.
- 2 A. W. Martinez, S. T. Phillips and G. M. Whitesides, *Proc. Natl. Acad. Sci. U. S. A.*, 2008, **105**, 19606–19611.
- 3 I. N. Katis, J. A. Holloway, J. Madsen, S. N. Faust, S. D. Garbis, P. J. S. Smith, D. Voegeli, D. L. Bader, R. W. Eason and C. L. Sones, *Biomicrofluidics*, 2014, **8**, 9.
- 4 A. W. Martinez, S. T. Phillips, G. M. Whitesides and E. Carrilho, *Anal. Chem.*, 2010, **82**, 3–10.
- 5 E. Carrilho, S. T. Phillips, S. J. Vella, A. W. Martinez and G. M. Whitesides, *Anal. Chem.*, 2009, **81**, 5990–5998.
- 6 X. Li, D. R. Ballerini and W. Shen, *Biomicrofluidics*, 2012, **6**, 13.
- 7 A. W. Martinez, S. T. Phillips, B. J. Wiley, M. Gupta and G. M. Whitesides, *Lab Chip*, 2008, **8**, 2146–2150.
- 8 E. Carrilho, A. W. Martinez and G. M. Whitesides, *Anal. Chem.*, 2009, **81**, 7091–7095.
- 9 V. Leung, A. A. M. Shehata, C. D. M. Filipe and R. Pelton, *Colloids Surf., A*, 2010, **364**, 16–18.
- 10 X. Li, J. F. Tian, G. Garnier and W. Shen, *Colloids Surf., B*, 2010, **76**, 564–570.
- 11 J. L. Delaney, C. F. Hogan, J. F. Tian and W. Shen, *Anal. Chem.*, 2011, **83**, 1300–1306.
- 12 X. Li, J. F. Tian, T. Nguyen and W. Shen, *Anal. Chem.*, 2008, **80**, 9131–9134.
- 13 C. D. Souza, O. C. Braga, I. C. Vieira and A. Spinelli, *Sens. Actuators, B*, 2008, **135**, 66–73.
- 14 E. Fu, P. Kauffman, B. Lutz and P. Yager, *Sens. Actuators, B*, 2010, **149**, 325–328.
- 15 J. Olkkonen, K. Lehtinen and T. Erho, *Anal. Chem.*, 2010, **82**, 10246–10250.
- 16 P. J. W. He, I. N. Katis, R. W. Eason and C. L. Sones, *Biomicrofluidics*, 2015, **9**, 26503–26503.
- 17 C. L. Sones, I. N. Katis, P. J. W. He, B. Mills, M. F. Namiq, P. Shardlow, M. Ibsen and R. W. Eason, *Lab Chip*, 2014, **14**, 4567–4574.
- 18 A. Apilux, Y. Ukita, M. Chikae, O. Chailapakul and Y. Takamura, *Lab Chip*, 2013, **13**, 126–135.
- 19 B. Lutz, T. Liang, E. Fu, S. Ramachandran, P. Kauffman and P. Yager, *Lab Chip*, 2013, **13**, 2840–2847.
- 20 H. Chen, J. Cogswell, C. Anagnostopoulos and M. Faghri, *Lab Chip*, 2012, **12**, 2909–2913.
- 21 A. W. Martinez, S. T. Phillips, Z. H. Nie, C. M. Cheng, E. Carrilho, B. J. Wiley and G. M. Whitesides, *Lab Chip*, 2010, **10**, 2499–2504.
- 22 H. Noh and S. T. Phillips, *Anal. Chem.*, 2010, **82**, 8071–8078.
- 23 H. Noh and S. T. Phillips, *Anal. Chem.*, 2010, **82**, 4181–4187.
- 24 N. K. Thom, K. Yeung, M. B. Pillion and S. T. Phillips, *Lab Chip*, 2012, **12**, 1768–1770.
- 25 J. L. Osborn, B. Lutz, E. Fu, P. Kauffman, D. Y. Stevens and P. Yager, *Lab Chip*, 2010, **10**, 2659–2665.
- 26 E. L. Fu, S. Ramsey, P. Kauffman, B. Lutz and P. Yager, *Microfluid. Nanofluid.*, 2011, **10**, 29–35.
- 27 E. Fu, B. Lutz, P. Kauffman and P. Yager, *Lab Chip*, 2010, **10**, 918–920.
- 28 D. L. Giokas, G. Z. Tsogas and A. G. Vlessidis, *Anal. Chem.*, 2014, **86**, 6202–6207.
- 29 T. B. Ledue and N. Rifai, *Clin. Chem. Lab. Med.*, 2001, **39**, 1171–1176.
- 30 N. Rifai, R. P. Tracy and P. M. Ridker, *Clin. Chem.*, 1999, **45**, 2136–2141.


 CrossMark
click for updates

Cite this: DOI: 10.1039/c6lc00789a

Laser direct-write for fabrication of three-dimensional paper-based devices

 P. J. W. He,^{*} I. N. Katis, R. W. Eason and C. L. Sones

We report the use of a laser-based direct-write (LDW) technique that allows the design and fabrication of three-dimensional (3D) structures within a paper substrate that enables implementation of multi-step analytical assays via a 3D protocol. The technique is based on laser-induced photo-polymerisation, and through adjustment of the laser writing parameters such as the laser power and scan speed we can control the depths of hydrophobic barriers that are formed within a substrate which, when carefully designed and integrated, produce 3D flow paths. So far, we have successfully used this depth-variable patterning protocol for stacking and sealing of multi-layer substrates, for assembly of backing layers for two-dimensional (2D) lateral flow devices and finally for fabrication of 3D devices. Since the 3D flow paths can also be formed via a single laser-writing process by controlling the patterning parameters, this is a distinct improvement over other methods that require multiple complicated and repetitive assembly procedures. This technique is therefore suitable for cheap, rapid and large-scale fabrication of 3D paper-based microfluidic devices.

 Received 21st June 2016,
Accepted 13th July 2016

DOI: 10.1039/c6lc00789a

www.rsc.org/loc

Introduction

Paper-based microfluidic devices have drawn considerable attention over the last few years, as they possess many intrinsic advantages such as low cost, capability of mass production, and are disposable, equipment-free, and require no external power to operate.^{1–4} However, there are also some disadvantages and limitations, such as issues with the control of flow rate, multiplexed detection of assays on a single device and there is a constant drive to further reduce the size in order to achieve compact devices that require a smaller volume of reagents with shorter fluid distribution times.^{5–7} As a result, 3D microfluidic paper analytical devices, which enable fluid distribution in both lateral and vertical directions, have also been proposed in recent years.^{4,8–10}

Compared with a conventional 2D geometry, 3D devices provide a number of unique characteristics which are advantageous for certain applications.¹¹ As an example, in the case of a multi-layered 3D device, which is a stack of substrates that can be of dissimilar materials, fluid-flow can be in all three dimensions, *i.e.* both laterally in the plane of any substrate layer, and vertically through the thickness of all layers that form the composite, and such devices would thus enable a user to perform several assays within the same device footprint.⁸ When compared to a lateral flow device (LFD), such

flow-through geometries provide flow paths that are comparatively shorter and therefore provide the capability for implementation of multiple-step assays via more compact device geometries.⁸ Additionally, such compact 3D devices can minimise the quantity of reagents that are either required or wasted, in the case of 2D devices, as a result of soaking of the greater lengths and volumes of the porous substrates. Lastly, shorter flow paths obviously translate into a reduced fluid distribution or delivery time leading to likely reductions in times for operation of such tests.¹¹

So far, for almost all of the reports in the literature, 3D paper-based microfluidic devices have been fabricated by sequential assembly of individual layers of 2D devices. Therefore, in addition to the critical requirement for correct alignment of individual layers, another key challenge encountered in the fabrication of such 3D devices is ensuring sufficient contact between the hydrophilic sections of each layer that constitute the flow-path because any lack of contact will result in an interrupted flow-path.⁷ Three general solutions have been reported for avoiding this problem, which include: 1) forming the structure in a layer-by-layer manner with use of either double-sided tape or a hydrophilic spray adhesive;^{8,11} 2) applying an outer adhesive, clamp, or protective coating to pre-assembled layers thus holding the layers in contact with each other;^{9,12} and, 3) by forming 3D structures in a single layer of paper substrate which therefore circumvents this problem completely.¹³

3D paper-based microfluidic devices were first reported by the Whitesides' group who used double-sided tape to

Optoelectronics Research Centre, University of Southampton, Highfield, Southampton, SO17 1BJ UK. E-mail: ph3e12@soton.ac.uk; Tel: +44 (0)2380 599091

physically attach individual 2D devices together, which had been pre-patterned using a photolithographic method.⁸ At places where the desired flow through is required, laser-drilled holes were created in the tape and filled with cellulose powder in order to create hydrophilic connections between the adjacent layers of paper. However, this method is somewhat labour-intensive as there are several sequential assembly processes that must be accomplished and hence it does not readily lend itself to mass fabrication. An alternative technique reported the use of hydrophilic spray adhesive to glue layers of pre-patterned 2D devices together, which then allows more rapid laboratory-based fabrication of 3D devices.¹¹ As this method relies on cold lamination techniques to hold and seal together layers of stacked 2D devices, it is only able to produce 3D devices that incorporate two or three layers of paper, and so is not practicable for devices requiring more layers.^{14,15} Subsequent work by Crooks *et al.* reported an alternative method for creation of 3D paper-based devices based on the principle of origami, the traditional Japanese paper-folding art.^{9,12,13} In this approach, a 3D device is achieved by laying and folding a single piece of pre-patterned paper and then the stack is held together with a clamp. The origami technique allows patterning of different layers of paper in one go and additionally eliminates complex alignment steps. Such a folded design also enables opening and altering the device during the reagent preparation step and even during the course of an assay.^{13,16} However, this method can cause issues of reproducibility as it relies on the individual performing the test following the instructions given and there is then the possibility of an incorrect procedure occurring, particularly if the person is performing the assembly for the first time. Overall, most of these reported methods were based on fabrication of 3D devices using cellulose paper. However, other porous materials, such as threads,^{17,18} cloth,¹⁹ and silk fabric,²⁰ have also been explored by different groups for fabrication of 3D microfluidic devices.

Unlike all the methods discussed above, in this article, we report a new approach for the fabrication of 3D devices, which is a simple extension of the basic LDW technique that has been described in our previous publications for both fabrication of 2D microfluidic devices and implementation of flow-control.^{21–23} In brief, by controlling the laser patterning conditions, we have shown that we can produce solid hydrophobic structures either partially inside a single layer of paper or all the way through several layers of paper (we have so far demonstrated 3 separate layers). Also, by selectively patterning from both sides of the composite substrate, we have fabricated 3D devices based on both a single layer as well as a multi-layer stacked arrangement. Unlike other 3D device fabrication methods, the approach presented here does not require any additional processing equipment, alignment or assembly steps and, as described earlier, uses the same proven fabrication approach that we have demonstrated for 2D fluidic flow path devices.

Experimental section

Laser setup and materials

The laser used for the LDW process was a 405 nm continuous wave diode laser (MLD™ 405 nm, Cobolt AB, Sweden) with a maximum output power of ~110 mW. The basic LDW setup is the same as described in our previous publications for fabrication of 2D microfluidic devices and implementation of flow-control and has been fully optimised via a series of systematic studies.^{21–23} The results we have achieved and will report in the following sections are therefore based on the same patterning procedure with appropriate adjustment of the patterning conditions such as laser power and scan speed.

The paper substrates used were Whatman® no. 1 filter paper and polyvinylidene fluoride (PVDF) from GE Healthcare Inc., UK was used for realizing stacking and sealing. Ahlstrom® grade 320 and 222 chromatography paper from Ahlstrom, Finland, were used for fabrication of backing and 3D structures described below. The photopolymer chosen for these experiments was Sub G, from Maker Juice, USA. The solvent used in development step was acetone from Sigma Aldrich Co Ltd., UK. The inks used for validating our patterned devices were blue and red bottled inks from Parker, UK.

Results and discussion

Stacking and sealing of multi-layer papers

During our earlier LDW studies for fabrication of 2D paper-based microfluidic devices, we observed that the photopolymerization process is not restricted to a single substrate but can also extend further into a composite formed from several layers. In order to understand and further explore this phenomenon, we prepared samples with different numbers of layers (two to five) and investigated their patterning using the same LDW method. The schematic for this is shown in Fig. 1: firstly, different numbers of cellulose papers were stacked together and then soaked with the photopolymer. The same LDW patterning process was applied to form simple structures in these multi-layered samples. After the final

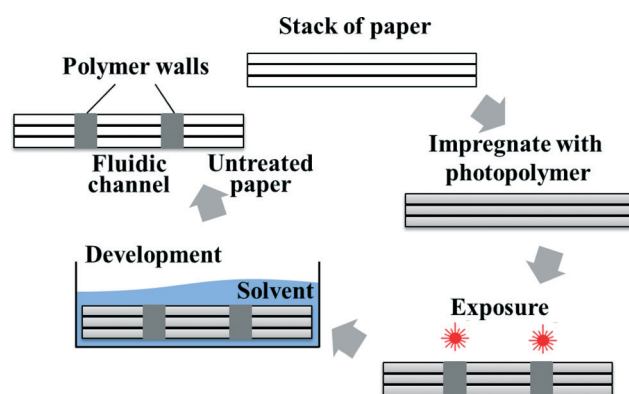


Fig. 1 Schematic of patterning multi-layer stacks using the LDW technique.

development process, it was then observed that these multi-layers had been efficiently bonded together to form a single composite structure.

Based on our current setup with a 405 nm c.w. laser, we found that a maximum of three layers of cellulose paper (each with thickness of 180 μm) can be bonded together using a laser output power of 100 mW at a scan speed of 10 mm s^{-1} . The polymerised lines were evident throughout all three layers of paper and as shown in Fig. 2a and b, can be clearly observed on both sides of the three-layer stack. We then tested these structures by applying different volumes of blue ink, from 3 μL to 7 μL , into these square wells from the top surface as shown in Fig. 2c. The ink was well-confined within the square wells defined by the polymerised walls and flowed vertically from the upper layer to the layers underneath. The result is shown in Fig. 2d: 3 μL of blue ink is just enough to reach the third layer, while the whole square well of all three layers get fully inked with a volume of 6 μL and 7 μL is seen to produce slight overflowing. It is clear therefore that the polymerised structures that extend from the top layer all the way to the bottom layer perform the dual function of bonding and forming walls that contain and hold the fluid without any leakage, as seen for the image using 6 μL in Fig. 2d.

Using the same parameters, we then attempted to pattern stacks with four layers but although the layers were indeed bonded together, leakage was much more of an issue, so under our normal patterning process conditions, we did not pursue composites with greater than three layers. However, stacked structures with more layers would indeed be possible through choosing different patterning parameters, such as lower scan speed and higher incident power.

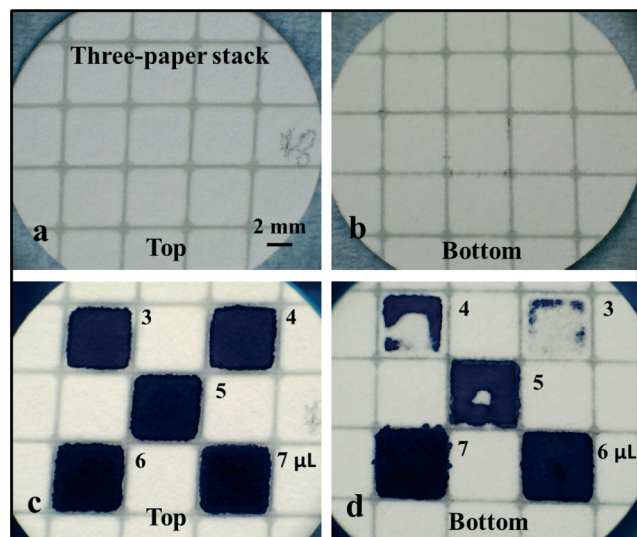


Fig. 2 Images showing the polymerised structures from both sides a) top side, b) bottom side) of a stack with three layers of cellulose paper and images of both sides of the device c) top side, d) bottom side) after introduction of blue ink of different volumes (3–7 μL) into the designated well.

Following these first trials we then trialled assembly of multi-layer stacks but this time composed of dissimilar substrate materials. The schematic image in Fig. 3a shows our first realisation of a stacked structure using different materials: two layers of cellulose paper with a PVDF layer in between that have been bonded together via a common photo-polymerization process. The rectangular channel and a T-junction shown in the schematic were patterned on the top and bottom surface respectively with a laser power of 50 mW at a scan speed of 10 mm s^{-1} . The four sealing points which extend throughout all of the three layers and enable their bonding were formed by illuminating each point with a stationary laser beam (100 mW) for 5 seconds. To test the device, red and blue inks were separately introduced onto the top and the bottom surfaces of this stack, and as shown in Fig. 3b and c the inks were guided in the channel and T-junction respectively. From Fig. 3b and c it can also be clearly observed that both inks flow only within their respective layers and did not penetrate through to the opposite layer, due to the presence of the intermediate blocking layer (hydrophobic PVDF). This innovative result presents a solution for not only sealing of paper-based devices by isolating the device between dissimilar outer cladding layers but also, most importantly, permitting 3D pathways to be engineered through judicious assembly of several layers, possibly combined with holes and voids in some layers. In our earlier publications using the same laser-direct write technique,^{21,22} we have demonstrated the patterning of varied porous materials such as nitrocellulose membranes, printing paper, fabrics,

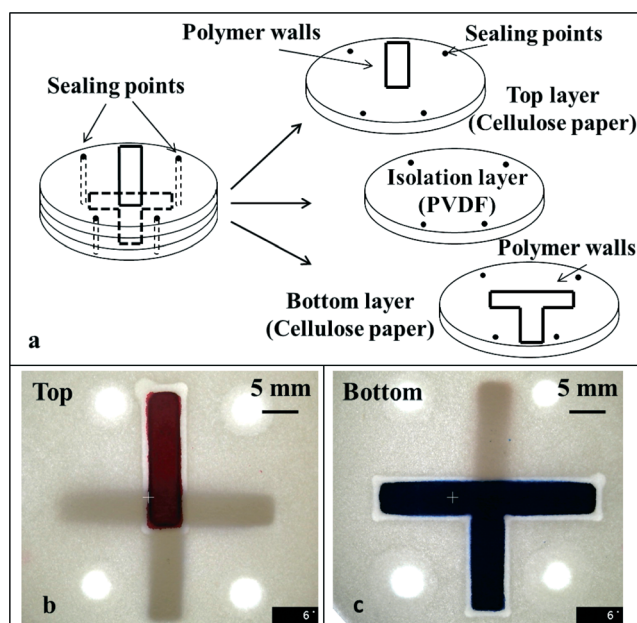


Fig. 3 a) Schematic image showing the arrangement of a stacked device with different structures in top and bottom layers, which are isolated with a hydrophobic film in between. b) Top and c) bottom images showing the device described in a) after the introduction of different inks from top and bottom surfaces without any cross-contamination or mixing.

and we therefore believe that any such material which is porous in nature would be suited for use in the production of the above described multi-layer devices. There are no other requirements that we believe would limit the use of a specific type of material for the creation of multi-layered devices.

Any paper-based device is normally intended for operation under ambient conditions, which can lead to a number of limitations when compared to fully enclosed microfluidic devices. Two of the main drawbacks are: a) the device is at risk of contamination during the fabrication, transportation and operation, and b) possible evaporation of the fluid in the open air which may lead to change of the sample concentration, or an altered flow rate due to change in sample viscosity.^{24,25} We believe that the results we have achieved above should contribute to a reduction of these two limitations by sandwiching a conventional paper-based microfluidic device with two outer layers of hydrophobic material. The LDW technique can be further extended to develop a new approach that helps with sealing in microfluidic paper-based analytical devices (μ PAD). Additionally, the technique could also be further employed for permitting 3D pathways through carefully designing the patterning protocol and subsequent assembly of several layers for realisation of a practical 3D paper-based device.

Single-sided polymerisation – for backing a paper-based device

To our knowledge, all or most of the presently reported paper-based microfluidic devices have another important limitation – operation of these unbacked devices requires that their bottom faces remain isolated from contact with any surface to prevent fluid flow along the interface which would provide an alternative undesirable flow path. In addition to the loss of the fluid (an expensive reagent or valuable sample present in small volumes for example) this unwanted flow can also lead to cross-contamination which in turn may produce a false result or failed test.²⁴ On the other hand, as paper is normally very fragile and more so especially after getting wet, a backing support to provide mechanical strength would normally be desirable. For the case of nitrocellulose (NC) membrane-based devices, the support to the membrane can be provided by an impermeable polyester layer.²⁶ While it is easy to procure such pre-backed NC membranes which are extensively used in LFD, it is not yet possible to source similar backed versions of paper substrates from the market. As an alternative, tape is widely used to back paper-based devices,²⁶ but this has certain drawbacks as the adhesion becomes poor when the paper gets wet following the introduction of the sample; additionally, the adhesives in tapes can diffuse into paper over time, which can lead to contamination as well as affecting the paper's hydrophilicity.²⁴ Another method of backing paper-based devices is based on flexography printing: a thin layer of polystyrene is printed on one side of the paper to form a hydrophobic backing,²⁷ but this

method requires additional equipment and adds cost to the final devices.

We therefore introduce here the use of our LDW technique as a new solution for backing paper-based devices. From the experiments we have done previously, we have observed that by controlling the patterning parameters, (laser incident power and scan speed), we could alter the depth of polymerised structures inside the substrate which thereby forms a hydrophobic polymerised layer within the substrate itself, which could be used as the backing layer. Compared with the methods currently used for backing, our LDW method allows formation of a backing structure inside the substrate during the device fabrication procedure without any need for extra materials or equipment, which would then lead to cost reduction and simplicity of fabrication. The schematic illustrating this is shown in Fig. 4: the paper substrate is first impregnated with photopolymer, then during the exposure step the laser parameters are selected to polymerise only to a certain depth inside the substrate. After the final development process, the un-polymerised material is washed away, leaving behind a polymer layer with a specified depth inside the substrate, which thereby serves as the required backing.

We therefore performed a parametric study to understand the influence of different patterning parameters, which also included the number of repetitive scans. The basic LDW setup is the same as described previously and the paper substrates used were Ahlstrom® grade 320 chromatography paper with a thickness of 2.48 mm. As a proof-of-principle, in order to form a backing structure, we scanned the laser beam across the substrate in a line-by-line manner with a centre-to-centre separation of 1 mm (as shown in Fig. 5a), which was appropriate for the lines to just touch each other without any significant overlap or gaps. By forming adjacent polymerised lines under the same writing conditions, it was possible to create a 2D polymerised layer inside the substrate.

The cross-sectional images in Fig. 5b and c show examples of a patterned paper with different thicknesses of polymerised layers formed at the bottom of the substrate that was achieved by simply altering the patterning parameters. As shown in Fig. 5b and c, after introducing red ink from the un-polymerised side, we could clearly identify the polymerised layers (white region). As seen in the images: the

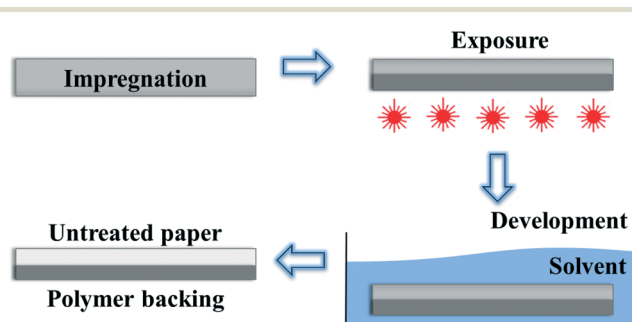


Fig. 4 Schematic of patterning a backing layer inside the paper substrate using the LDW technique.

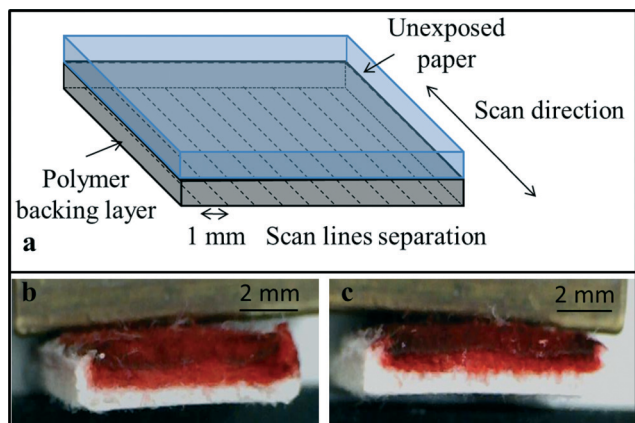


Fig. 5 a) Schematic of patterning a backing structure by scanning the laser beam across the substrate in a line-by-line manner with a separation of 1 mm. Cross-section images showing polymerised layers (un-inked white layers) on one side of thick cotton fibre filter paper with different thickness of: b) $\sim 700\ \mu\text{m}$ and c) $\sim 1\ \text{mm}$, after introduction of red ink from the other side.

thickness of the polymerised structures increases from $\sim 700\ \mu\text{m}$ to $\sim 1\ \text{mm}$ with an increase of laser output power from 30 mW to 70 mW at a fixed scan speed of $5\ \text{mm s}^{-1}$. As shown in both images, the polymerised layer, although written in a line-by-line manner was continuous and uniformly thick, and the demarcating interface between the un-polymerised and polymerised section is clearly defined.

To determine the depth of the polymerised layers as a function of the patterning parameters, we performed a study with the results shown in Fig. 6. For a fixed scan speed, as expected, the depth of the polymerised layer increases with an increase of the incident laser power. For example, at a fixed scan speed of $10\ \text{mm s}^{-1}$, the depth of the polymerised layer increases from $\sim 400\ \mu\text{m}$ to $\sim 950\ \mu\text{m}$ with an increase of laser output power from 10 mW to 100 mW. Similar behaviour was observed with a layer depth increase from $\sim 450\ \mu\text{m}$ to $\sim 1050\ \mu\text{m}$ and $\sim 1200\ \mu\text{m}$ to $\sim 2050\ \mu\text{m}$ at a fixed scan

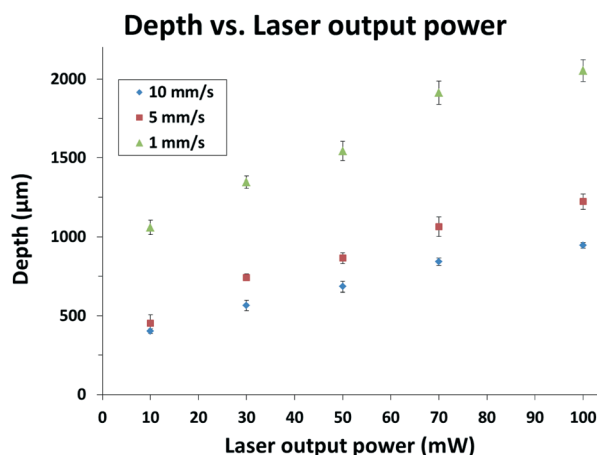


Fig. 6 Plots showing the variation in the depth of the polymerised layers for different laser powers at three different scan speeds. Error bars indicate the standard deviation for 5 measurements.

speed of $5\ \text{mm s}^{-1}$ and $1\ \text{mm s}^{-1}$ respectively for incident laser power ranging from 10 mW to 100 mW. As expected, we can also observe from the same plots that the depth of the polymerised layers increases with the decrease of the scan speed at fixed laser powers.

Additionally, we observed that the depth of a single polymerised line also depends on the number of scans performed under the same writing conditions, which thereby alters the resulting thickness of the polymerised backing layers. In order to study how the number of scans affects the polymerised depth, we scanned the beam once, twice and three times respectively under the same writing conditions. The histogram in Fig. 7 shows that the depth of the polymerised layer increases monotonically with an increasing number of repeat scans. As shown in the plots, the depth of the polymerised layer increases from $\sim 400\ \mu\text{m}$ to $\sim 800\ \mu\text{m}$ with an increase of the number of scans from one to three at a patterning condition of 10 mW of incident power at $10\ \text{mm s}^{-1}$ scan speed. Similar trends were observed for all laser powers used (30, 50, 70 and 100 mW) for the same scan speed of $10\ \text{mm s}^{-1}$.

Single-sided polymerisation – for reduction in the dead-volume of a paper-based device

An additional benefit of this technique lies in the reduction of the active paper volume that can be produced routinely for all such test substrates, which leads to a corresponding reduction of reagent/sample volume required. Due to the opacity of the substrate, the observable signals (the colour change) that provide the test results originate only from the top region or plane of the substrate (which for an NC membrane extends below the surface to a depth of $\sim 10\ \mu\text{m}$), and any colour change from deeper regions (the so-called dead-volume) makes a negligible contribution to the observable signal, and is therefore redundant.²⁸ Reduction of the thickness of the substrate at the detection area will therefore not only help with saving of reagent/sample but will also help increase the limit of detection. Because the amount of the

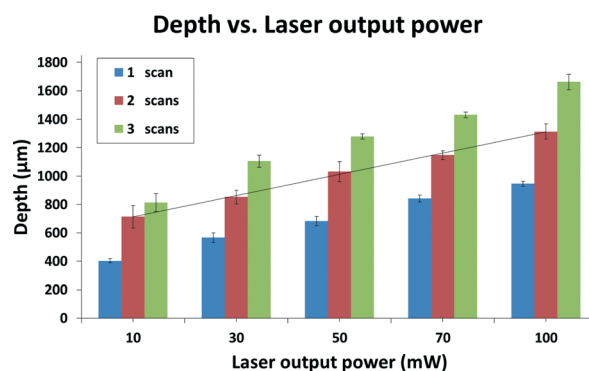


Fig. 7 Plots showing the variations in the depths of the polymerised layers for different laser powers at a fixed scan speed of $10\ \text{mm s}^{-1}$ for three different numbers of scans. Error bars indicate the standard deviation for 5 measurements and a linear line for the case of 2 scans is a simple guide for the eye.

sample which previously would have soaked the entire volume of the substrate will now instead fill up a comparatively smaller volume of the substrate, the sample concentration will be relatively higher and thus will lead to an improved limit of detection.

To test this hypothesis, as shown in Fig. 8a, a simple proof-of-principle experiment was performed by introducing different volumes (1, 2 and 3 μL) of red ink into 4×5 mm well structures patterned on samples 1 and 2, which were backed with layers that had different thickness of ~ 400 μm and ~ 600 μm , using the LDW method. These backing layers were first formed by scanning the laser in a line-by-line format using laser powers of 10 mW and 40 mW respectively at a scan speed of 10 mm s^{-1} . The line-patterns of the grid-structures were patterned by scanning the laser once along the paper surface with a power of 20 mW at a scan speed of 10 mm s^{-1} . The paper substrates used for both samples were Ahlstrom® grade 222 chromatography paper with a thickness of 0.83 mm. As shown in Fig. 8a, the colour intensities change in each well with different ink volumes and also differ between the two samples with different thickness of backing for the same volume. The images were processed with the ImageJ software (National Institutes of Health, USA) to extract the respective grayscale colour intensities of the red colour produced within the central area of each well and the results are plotted in Fig. 8b. The conclusion here is that the detected colour intensity increases with an increase of the ink volume, but more importantly, also increases with an increase of the backing thickness, *i.e.* the signal is enhanced with a reduction of the dead-volume. We therefore believe that by designing and choosing the appropriate thickness of the backing, we should be able to control the volume of sub-

strate and hence reduce the dead-volume thereby increasing the sensitivity and saving on sample or reagent needed.

In summary, we have proved that by simply changing the patterning parameters, we can polymerise lines with different depths in the substrate, and therefore, by scanning in a line-by-line manner we could form polymerised layers with the desired depths, and these can be used either as backing for paper-based devices or to alter the volume of the paper-based fluidic device. Here, for our first simple proof-of-principle experiment, we have used an un-optimised line-by-line scanning procedure in order to cover a large area. Alternatively, instead of repetitive multiple scanning protocols, a single-step process that uses a cylindrical lens could also be employed. In this case the lens focuses the beam only in one direction and leaves the other direction wide enough to cover an extended lateral region and this is an intended future approach.

Dual-sided polymerisation – for fabrication of a 3D paper-based device

In order to exploit fully the true potential of this approach we have explored the possibility of creating such polymerised patterns though exposure from either side of a single substrate. The objective here was to use this dual-sided polymerisation protocol to fabricate a 3D device in a single paper substrate. The concept is explained through the schematic depicted in Fig. 9a. As shown in this figure, by patterning via exposure from both the top and bottom faces of a single paper substrate it should be possible to create polymerised blocks that extend partially from both faces of the substrate and define an enclosed flow-path that is embedded within the substrate. By selectively positioning and connecting such polymerised areas, we can then construct arbitrarily-shaped connected 3D flow paths that guide the fluid both in the

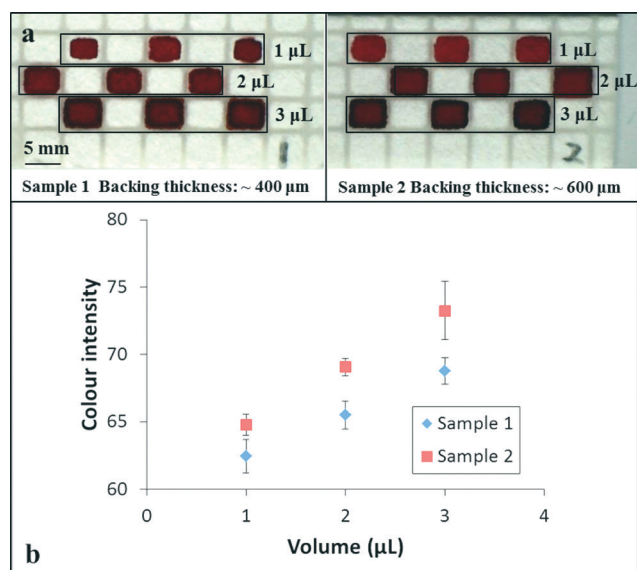


Fig. 8 (a) Images showing the results of introduction of different volumes of red ink into 4×5 mm well structures patterned in two samples with different backing thickness. (b) Plots constructed using the grayscale intensity values taken from the images shown in (a). Error bars indicate the standard deviation for 3 measurements.

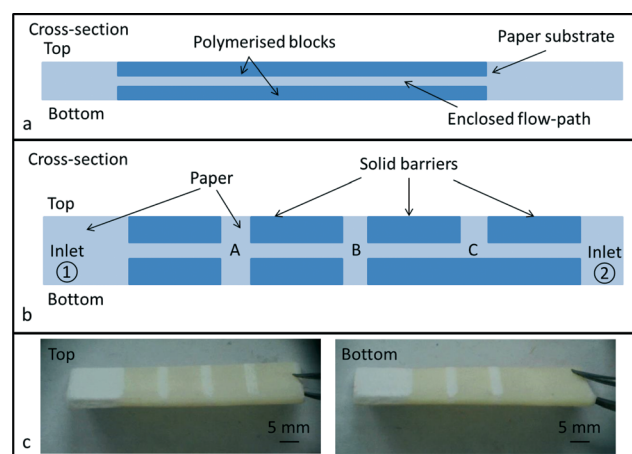


Fig. 9 a) Schematic showing an enclosed flow-path formed by creating polymerised blocks from both faces of a single paper substrate. b) Schematic representation of cross-section of a 3D fluidic device with two inlets (1, 2) from either end. c) Photographic images taken from the top and bottom of the device described in b).

horizontal and vertical directions. The schematic in Fig. 9b shows an example of such 3D paper-based devices created in a single substrate with several fully enclosed and interconnected channels. As shown in the cross-section schematic, solid polymerised barriers were formed from both top and bottom, leaving gaps in both vertical and horizontal directions. The gaps in the vertical direction form three open windows A, B and C, where the reagent/sample will appear after passing through the enclosed channels between the two inlets (①②). The enclosed channels that connect the inlets and three open windows are defined by gaps between the solid barriers in the horizontal direction. Photographic images of the top and bottom views of a real device with the illustrated arrangement are shown in Fig. 9c: the white areas are bare/un-polymerised sections of paper and the pale yellow areas are the hydrophobic polymerised regions. All of the polymerised blocks shown in the schematic in Fig. 9 and the devices in Fig. 10–12, were patterned by scanning the laser in a line-by-line manner to create lines with a centre-to-centre separation of 1 mm using a laser output power of 100 mW at a scan speed of 10 mm s⁻¹. The resultant blocks had thicknesses of ~950 μm and hence for a substrate that had a thickness of 2.48 mm, the enclosed flow-path had a height of 580 μm.

In order to test these 3D structures, we first introduced red ink from the inlet ① of the device described in Fig. 9b. The sequential images in Fig. 10 show the flow of red ink, which were taken from both top and bottom faces of the device. After the introduction of the ink, it flowed into the first enclosed channel between inlet ① and the open window A. The red shaded areas were observed from both sides of the device and illustrate the ink flow inside the channel. After a short period of time, the ink flowed through the first section of the enclosed channel and reached the open area A: as shown in the images the red ink has filled in the area A and is visible from both top and bottom.

We have also introduced red ink from the inlet ② and the result is shown in Fig. 11. The ink again flowed through the enclosed channel between inlet and the open area B and finally reached the open window C and hence appeared on the top side. The difference of the structures in the right and the

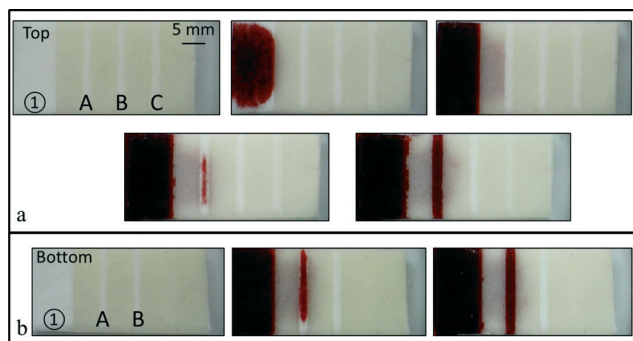


Fig. 10 Sequential images taken from the a) top and b) bottom showing the device described in Fig. 9b after introduction of red ink from the inlet ①.

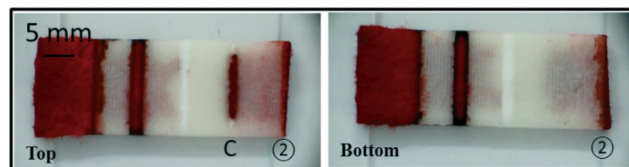


Fig. 11 Photographic images showing the top and bottom of the device described in Fig. 9b after introduction of red ink from the inlet ②.

left sections of the device is that the polymerised structures at the bottom cover the whole area without having an open window. It can be regarded as a 3D device with an enclosed channel and an open window just on the top plus a backing structure underneath, which helps to provide support to the device.

Finally, the cross-section image in Fig. 12 illustrates the flow process of the red ink inside this 3D device. The narrow red lines inside the substrate, which connect the inlets and open areas, show the flow of the red ink inside the enclosed channels. The ink from inlet ① flowed and filled up the open area A, which allows the ink to be seen from both top and bottom, through an enclosed channel in between and then kept flowing towards the open area B along another enclosed channel. Similarly, the ink filled in the open area C and shows up only from the top with the source from the inlet ② again through an enclosed channel inside the substrate that was formed with solid blocks on both sides. Such fully enclosed channels can be achieved easily with our LDW method, which prevents liquid exchange between the exterior and the interior of the channel.

Above all, the approach reported here for fabrication of 3D paper-based devices is a simple extension of the basic LDW technique that has been used for fabrication of 2D microfluidic devices.^{21,22} Through selectively designing and patterning polymerised structures from both sides of the substrate, we could fabricate 3D structures inside a single substrate. Unlike other 3D device fabrication methods, the approach presented here does not require any additional processing equipment or alignment/assembling step and uses the same fabrication approach described earlier for producing a 2D fluidic device.

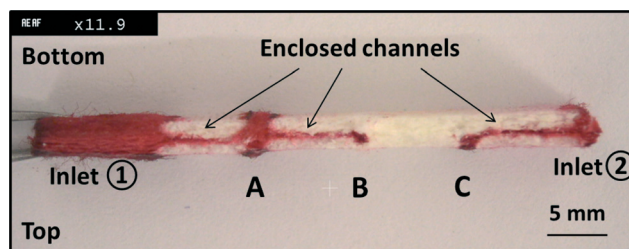


Fig. 12 Cross-section image showing the enclosed channels and flow of the red ink in the device described in Fig. 9b after introduction of ink from both inlets.

Conclusions

In summary, we have proposed and demonstrated a novel method, which can be used for stacking and sealing, fabrication of backing structures and construction of 3D structures in paper or porous substrates. The method is based on the same LDW technique we have reported previously with simple modification of the patterning parameters during the fabrication procedure, so that the polymerization process can extend through a few layers of substrate that are stacked together. This can be used for sealing the devices in order to solve potential evaporation and contamination problems. By simply changing the patterning parameters, a polymer backing layer with a specific thickness can be patterned within the paper substrate itself, which can be used as backing for paper-based devices instead of the currently used tape or polyester film. In addition, the thickness of this polymerised layer can be controlled to reduce the paper volume, which in turn allows reduction of the required reagent/sample volume and most importantly, can be used to increase the limit of detection.

Finally, we showed the possibility of fabrication of 3D paper-based devices as the polymerised structure can be formed inside the substrate with a controllable thickness. As a result, through selectively designing and patterning some of these polymerised structures from both sides of the substrate, we could fabricate 3D structures inside a single layer of substrate. Unlike other 3D device fabrication methods, our LDW approach does not require any additional processing equipment or alignment/assembling steps and uses the same fabrication approach that is applied for producing a 2D fluidic device by simply altering the patterning parameters.

Acknowledgements

The authors acknowledge the funding received *via* the Engineering and Physical Sciences Research Council (EPSRC) Grant No. EP/J008052/1, EP/K023454/1, EP/N004388/1 and EP/M027260/1, and the funding received via a Knowledge Mobilisation Fellowship for Dr. Collin Sones from the Institute for Life Sciences and the Faculty of Health Sciences of the University of Southampton. The data for this paper can be found at 10.5258/SOTON/387247.

Notes and references

- 1 J. L. Osborn, B. Lutz, E. Fu, P. Kauffman, D. Y. Stevens and P. Yager, *Lab Chip*, 2010, **10**, 2659–2665.
- 2 A. C. Siegel, S. T. Phillips, M. D. Dickey, N. S. Lu, Z. G. Suo and G. M. Whitesides, *Adv. Funct. Mater.*, 2010, **20**, 28–35.
- 3 K. Abe, K. Suzuki and D. Citterio, *Anal. Chem.*, 2008, **80**, 6928–6934.
- 4 D. Sechi, B. Greer, J. Johnson and N. Hashemi, *Anal. Chem.*, 2013, **85**, 10733–10737.
- 5 N. Hashemi, J. S. Erickson, J. P. Golden and F. S. Ligler, *Biomicrofluidics*, 2011, **5**, 9.
- 6 N. Hashemi, J. S. Erickson, J. P. Golden, K. M. Jackson and F. S. Ligler, *Biosens. Bioelectron.*, 2011, **26**, 4263–4269.
- 7 A. K. Yetisen, M. S. Akram and C. R. Lowe, *Lab Chip*, 2013, **13**, 2210–2251.
- 8 A. W. Martinez, S. T. Phillips and G. M. Whitesides, *Proc. Natl. Acad. Sci. U. S. A.*, 2008, **105**, 19606–19611.
- 9 H. Liu and R. M. Crooks, *J. Am. Chem. Soc.*, 2011, **133**, 17564–17566.
- 10 L. Ge, J. X. Yan, X. R. Song, M. Yan, S. G. Ge and J. H. Yu, *Biomaterials*, 2012, **33**, 1024–1031.
- 11 G. G. Lewis, M. J. DiTucci, M. S. Baker and S. T. Phillips, *Lab Chip*, 2012, **12**, 2630–2633.
- 12 H. Liu, Y. Xiang, Y. Lu and R. M. Crooks, *Angew. Chem., Int. Ed.*, 2012, **51**, 6925–6928.
- 13 C. Renault, J. Koehne, A. J. Ricco and R. M. Crooks, *Langmuir*, 2014, **30**, 7030–7036.
- 14 S. J. Vella, P. Beattie, R. Cademartiri, A. Laromaine, A. W. Martinez, S. T. Phillips, K. A. Mirica and G. M. Whitesides, *Anal. Chem.*, 2012, **84**, 2883–2891.
- 15 N. R. Pollock, J. P. Rolland, S. Kumar, P. D. Beattie, S. Jain, F. Noubary, V. L. Wong, R. A. Pohlmann, U. S. Ryan and G. M. Whitesides, *Sci. Transl. Med.*, 2012, **4**, 10.
- 16 A. V. Govindarajan, S. Ramachandran, G. D. Vigil, P. Yager and K. F. Bohringer, *Lab Chip*, 2012, **12**, 174–181.
- 17 M. Reches, K. A. Mirica, R. Dasgupta, M. D. Dickey, M. J. Butte and G. M. Whitesides, *ACS Appl. Mater. Interfaces*, 2010, **2**, 1722–1728.
- 18 X. Li, J. F. Tian and W. Shen, *ACS Appl. Mater. Interfaces*, 2010, **2**, 1–6.
- 19 A. Nilghaz, D. H. B. Wicaksono, D. Gustiono, F. A. A. Majid, E. Supriyanto and M. R. A. Kadir, *Lab Chip*, 2012, **12**, 209–218.
- 20 P. Bhandari, T. Narahari and D. Dendukuri, *Lab Chip*, 2011, **11**, 2493–2499.
- 21 C. L. Sones, I. N. Katis, P. J. W. He, B. Mills, M. F. Namiq, P. Shardlow, M. Ibsen and R. W. Eason, *Lab Chip*, 2014, **14**, 4567–4574.
- 22 P. J. W. He, I. N. Katis, R. W. Eason and C. L. Sones, *Biomicrofluidics*, 2015, **9**, 10.
- 23 P. J. W. He, I. N. Katis, R. W. Eason and C. L. Sones, *Lab Chip*, 2015, **15**, 4054–4061.
- 24 K. M. Schilling, A. L. Lepore, J. A. Kurian and A. W. Martinez, *Anal. Chem.*, 2012, **84**, 1579–1585.
- 25 E. da Silva, M. Santhiago, F. R. de Souza, W. K. T. Coltro and L. T. Kubota, *Lab Chip*, 2015, **15**, 1651–1655.
- 26 E. M. Fenton, M. R. Mascarenas, G. P. Lopez and S. S. Sibbett, *ACS Appl. Mater. Interfaces*, 2009, **1**, 124–129.
- 27 J. Olkkonen, K. Lehtinen and T. Erho, *Anal. Chem.*, 2010, **82**, 10246–10250.
- 28 R. L. F. S.-c. *f. p. development*, Millipore Corporation, Billerica, MA, pp. 9–10.